Charmonium studies at LHC energies using the ALICE Muon Spectrometer

by

Biswarup Paul

PHYS05201004010

Saha Institute of Nuclear Physics
Kolkata, India

A thesis submitted to the
Board of Studies in Physical Science Discipline
In partial fulfillment of requirements
For the Degree of

DOCTOR OF PHILOSOPHY

of

HOMI BHABHA NATIONAL INSTITUTE

May, 2015

Homi Bhabha National Institute

Recommendations of the Viva Voce Committee

As members of the Viva Voce Committee, we certify that we have read the dissertation prepared by Biswarup Paul entitled "Charmonuim studies at LHC energies using the ALICE Muon Spectrometer" and recommend that it may be accepted as fulfilling the thesis requirement for the award of Degree of Doctor of Philosophy.

Date :

Chairman : **Prof. Pradip Kumar Roy**, SINP

Date :

Guide & Convener : **Prof. Sukalyan Chattopadhyay**, SINP

Date :

Examiner : **Prof. Raghava Varma**, IITB

Date :

Member : **Prof. Tapan Kumar Nayak**, VECC

Date :

Member : **Prof. Debasish Das**, SINP

Final approval and acceptance of this thesis is contingent upon the candidate's submission of the final copies of the thesis to HBNI.

I hereby certify that I have read this thesis prepared under my direction and recommend that it may be accepted as fulfilling the thesis requirement.

Date :
Place : **Guide**

STATEMENT BY AUTHOR

This dissertation has been submitted in partial fulfillment of requirements for an advanced degree at Homi Bhabha National Institute (HBNI) and is deposited in the Library to be made available to borrowers under rules of the HBNI.

Brief quotations from this dissertation are allowable without special permission, provided that accurate acknowledgement of source is made. Requests for permission for extended quotation from or reproduction of this manuscript in whole or in part may be granted by the Competent Authority of HBNI when in his or her judgment the proposed use of the material is in the interests of scholarship. In all other instances, however, permission must be obtained from the author.

BISWARUP PAUL

DECLARATION

I, hereby declare that the investigation presented in the thesis has been carried out by me. The work is original and has not been submitted earlier as a whole or in part for a degree / diploma at this or any other Institution / University.

BISWARUP PAUL

"Thinking should become your capital asset, no matter whatever ups and downs you come across in your life."

A. P. J. Abdul Kalam

List of Publications arising from the thesis

Journal

1. **"Measurement of quarkonium production at forward rapidity in pp collisions at $\sqrt{s}$ = 7 TeV"**,
   B. Abelev *et al.* [ALICE Collaboration],
   Eur. Phys. J. C **74**, 2974 (2014),
   [arXiv:1404.3648 [nucl-ex]].

2. **"Suppression of ψ(2S) production in p-Pb collisions at $\sqrt{s_{\rm NN}}$ = 5.02 TeV"**,
   B. Abelev *et al.* [ALICE Collaboration],
   JHEP **12**, 073 (2014),
   [arXiv:1405.3796 [nucl-ex]].

3. **"Systematic study of charmonium production in pp collisions at LHC energies"**,
   Biswarup Paul, Mahatsab Mandal, Pradip Roy and Sukalyan Chattopadhyay,
   J. Phys. G: Nucl. Part. Phys. **42** 065101 (2015),
   [arXiv:1411.6783 [nucl-ex]].

Conference Proceedings

1. **"Inclusive J/ψ and ψ(2S) production in pp and p-Pb collisions at forward rapidity with ALICE at LHC"**,
   Biswarup Paul for the ALICE Collaboration,
   Proceedings of the Indian National Science Academy, Vol 81 (2015), p. 179,
   [arXiv:1409.8077 [nucl-ex]].

2. **"Suppression of inclusive J/ψ and ψ(2S) production in p-Pb collisions with ALICE at the LHC"**,
   Biswarup Paul for the ALICE Collaboration,
   DAE Symposium on Nuclear Physics, Vol 59 (2014), p. 696,
   [arXiv:1405.3796 [nucl-ex]].

3. **"Charmonium production in pp collisions at energies available at the CERN Large Hadron Collider within the NRQCD framework"**,
   Biswarup Paul, Mahatsab Mandal, Pradip Roy and Sukalyan Chattapadhyay,
   DAE Symposium on Nuclear Physics, Vol 59 (2014), p. 690.

4. **"Inclusive J/ψ and ψ(2S) production in pp collisions at $\sqrt{s}$ = 7 TeV at forward rapidity with ALICE at LHC"**,
   Biswarup Paul for the ALICE Collaboration,
   DAE Symposium on Nuclear Physics, Vol 58 (2013), p. 784,
   [arXiv:1410.3075 [nucl-ex]].

5. **"Measurement of ψ(2S)/ψ(1S) ratio in pp collisions at $\sqrt{s}$ = 7 TeV"**, Biswarup Paul and Sukalyan Chattopadhyay for the ALICE Collaboration, DAE Symposium on Nuclear Physics, Vol 57 (2012), p. 794.

ALICE Analysis Notes

1. **"Inclusive J/ψ and ψ(2S) production cross sections in pp collisions at $\sqrt{s}$ = 7 TeV"**,
   Biswarup Paul, Roberta Arnaldi, Livio Bianchi, Sukalyan Chattopadhyay, Martino Gagliardi, Enrico Scomparin, Diego Stocco and Lizardo Valencia Palomo,
   ANA-812, CERN-PH-EP-2014-042.

2. **"ψ(2S) production in pA collisions at $\sqrt{s_{\rm NN}}$ = 5.02 TeV"**,
   Laurent Aphecetche, Roberta Arnaldi, Cynthia Hadjidakis, Igor Lakomov, Marco Leoncino, Biswarup Paul and Enrico Scomparin,
   ANA-1171, CERN-PH-EP-2014-092.

3. **"$p_{\rm T}$ dependence of the inclusive ψ(2S) production in pA collisions at $\sqrt{s_{\rm NN}}$ = 5.02 TeV"**,
   Roberta Arnaldi, Marco Leoncino, Biswarup Paul and Enrico Scomparin,
   ANA-1405, CERN-PH-EP-2014-092.

4. **"Measurement of inclusive charmonium production cross section at forward rapidity in pp collisions at $\sqrt{s}$ = 8 TeV"**,
   Das Indranil, Lardeux Antoine Xavier, Paul Biswarup, Pillot Phillipe,
   ANA-2400.

BISWARUP PAUL

Dedicated to My Parents

ACKNOWLEDGMENTS

First and foremost, I would like to express my deepest and sincere gratitude to my supervisor Prof. Sukalyan Chattopadhyay. I have been amazingly fortunate to have a supervisor who gave me the freedom to explore on my own, and at the same time the guidance to recover when my steps faltered. He taught me how to question thoughts and express ideas. His patience, caring, motivation, enthusiasm and immense knowledge helped me in all the time of research and writing of this thesis. I hope that one day I would become as good a supervisor to my students as he has been to me.

SINP and CERN both have such an excellent atmosphere for doing research and working in a project like LHC is a life changing opportunity. I am grateful to Indranil da for his help and support during the early stages of my research, both at SINP and at CERN, irrespective of whether it was academic or non-academic.

I am grateful to Roberta Arnaldi, Enrico Scomparin and Ermanno Vercellin for giving me the opportunity to work with them in Torino. My sincere thanks to Roberta for the analysis which I learned from her. I feel privileged to be able to work with her on the analysis of charmonium of which she is a renowned expert and for the helps and discussions throughout my Ph.D.

Theoretical work discussed in chapter 7 would not have been possible without the help of Prof. Pradip Kumar Roy, Prof. Abhee K. Dutt-Mazumdar and Mahatsab da. They have been always there to listen and give advice whether it was academic or non-academic. Prof. Abhee K. Dutt-Mazumdar lived his life well, acting upon his spiritual beliefs conscientiously by assisting both friends and strangers in need. He was a very good scientist as well as a well known social activist. He faced his too

early death bravely. His example kept me working and taught me to never give up.

I would like to convey my sincere thanks to Prof. Tapan Kumar Nayak, Prof. Sunanda Banerjee, Debasish Da and Tinku di for extending their hand of support whenever needed.

I am also indebted to the members of PWG-DQ Jpsi2mumu group of ALICE with whom I have interacted throughout my research studies. Their valuable comments, suggestions and discussions helped me to understand and learn different techinques of data analysis and physics interpretation of results. I am grateful to them for holding me to a high research standard.

In my daily work I have been blessed with a friendly and cheerful group of fellow students and staff. It is my greatest pleasure to have Sanjoy da, Pradip da, Indranil da, Santosh da, Kushal da, Palash da, Arindam da, Lusaka di, Mahatsab da, Sreemoyee di, Niyaz, Kalyanmoy da, Atanu, Swagata, Debarati, Kuntal, Ashim, Suvankar, Sourav, Biswarup, Anisa, Rajarshi, Arnab, Shamik, Saswati, Amit, Chandrachur, Kamakshya, Uttam, Dipankar, Dubey ji, Ashis da, Bijoy da, Lipy di, Dipankar da, Sampa di, Pappu da, Sudam da and Sanjib da around all the time, whenever I needed them.

I would like to convey my sincere thanks to my housemates Mayukh da, Moin and Subhendu. Their support and care helped me overcome setbacks and stay focused on my research study. I greatly value their friendship.

Most importantly, none of this would have been possible without the love and patience of my parents, elder brother, elder sisters, brother-in-laws and their childrens. They have been a constant source of love, concern, support and strength all these years. I would like to express my heart-felt gratitude to them.

Finally, I appreciate the financial support from Council of Scientific and Industrial Research (CSIR) and Department of Atomic Energy (DAE) of India that funded parts of the research discussed in this thesis.

Contents

SYNOPSIS

Theoretical calculations based on quantum chromodynamics (QCD) predict that at high baryonic density and/or high temperature a deconfined quark and gluon phase can be formed, in which chiral symmetry is restored. This phase of matter is called the quark gluon plasma (QGP) and it exists for a short time and then the process of hadronization takes place. The characterization of QGP is the main goal of ultra-relativistic heavy-ion collision studies. The quarkonium (bound states of quark and anti-quark) suppression is one of the most prominent probes used to investigate and quantify the properties of the QGP. The in-medium dissociation probability of the different quarkonium states could provide an estimate of the temperature of the system since the dissociation is expected to take place when the medium reaches or exceeds the critical temperature for the phase transition ($T_{\rm c}$), depending on the binding energy of the quarkonium state. For charmonium ($c\overline{c}$) states, the J/ψ is likely to survive significantly above $T_{\rm c}$ (1.5 - 2 $T_{\rm c}$) whereas $\chi_{\rm c}$ and ψ(2S) melt near $T_{\rm c}$ (1.1 - 1.2 $T_{\rm c}$). At LHC energies, due to the large increase of the $c\overline{c}$ production cross-section with the collision energy, there is a possibility of J/ψ enhancement via recombination of c and $\overline{c}$. Thus, this observation of J/ψ enhancement in nucleus-nucleus collisions via recombination could also constitutes an evidence of QGP formation. On the other hand, the ψ(2S) production has drawn considerable attention of both experimentalists and theorists since the ψ(2S) yield is less affected by higher mass charmonium decays with respect to the J/ψ. In addition, the [ψ(2S)/J/ψ] ratio is predicted to be very sensitive to the QGP temperature and to the details of the recombination mechanism. On the other hand, experimentally this ratio is interesting as most of the systematic uncertainties cancel out and the systematic uncertainties are only due to signal extraction and the efficiency evaluation.

The suppression or enhancement of charmonium production is obtained by

comparing the heavy-ion collision data with those obtained in pp collisions where it is believed that the partonic medium is not created. In addition, charmonium production in p-Pb collisions is also investigated in order to understand cold nuclear matter (CNM) effects which is necessary to disentangle hot and cold nuclear matter effects in Pb-Pb collisions. The name cold matter arises because these effects are observed in proton-nucleus or deuteron-nucleus interactions where no hot or dense matter effects are expected.

Thus, in order to characterize the matter created in ultra-relativistic heavy-ion collisions, it is necessary to analyze the experimental data on pp, p-Pb and Pb-Pb coliisions. These data are being analyzed by four experiments at the Large Hadron Collider (LHC) namely, ALICE (A Large Ion Collider Experiment), ATLAS (A Toroidal LHC Apparatus), CMS (Compact Muon Solenoid) and LHCb (LHC-beauty). The results presented in this thesis are from the analysis of the data obtained from the forward Muon Spectrometer of ALICE. The ALICE Muon Spectrometer is designed to detect muons in the extreme forward angles from $\theta = 171^{\circ}$ to 178° which corresponds to a rapidity range $-4 \leq \eta \leq -2.5$ and can measure a wide range of transverse momentum down to $p_{\mathrm{T}} = 0$. The production of quarkonia, low mass vector mesons, open heavy-flavours and weak bosons have been studied using the ALICE Muon Spectrometer in pp, p-Pb and Pb-Pb collisions. It is the only detector at LHC which is capable to study quarkonia at forward rapidities in Pb-Pb collisions.

The Muon Spectrometer consists of five distinct components, namely, (1) a ten interaction length thick front absorber to absorb hadrons and photons from the interaction vertex; (2) a high granularity tracking system of 10 tracking planes with about 1.1 millions pad readout; (3) a 3 Tm dipole magnet; (4) four planes of trigger chambers behind a passive muon filter wall of 1.2 m thick iron; (5) an inner beam shield up to 2^0 to protect the tracking and trigger chambers from particles and secondaries produced at very large rapidities. The Cathode Pad Chambers (CPC) are

used for tracking and have a position resolution ∼70 μm for J/ψ while the Resistive Plate Chambers (RPC), used in streamer mode, are capable of providing single and dimuon triggers with two different p_{T} thresholds within ∼25 ns.

The following important results will be reported in the thesis:

(A) Results from 2011 pp run at $\sqrt{s} = 7$ TeV:

- Production cross-section of J/ψ and ψ(2S) as a function of transverse momentum, p_{T} and rapidity y.
- The ratio of ψ(2S) to J/ψ production cross-section.
- Comparison of the cross-sections and the ψ(2S)/J/ψ ratio with the theoretical predictions.

(B) Results from 2013 p–Pb and Pb–p run at $\sqrt{s_{\mathrm{NN}}} = 5.02$ TeV:

- Production cross-section of J/ψ and ψ(2S) as a function of p_{T} and y.
- The double ratio $[\psi(2\mathrm{S})/\mathrm{J}/\psi]_{\mathrm{pPb}}/[\psi(2\mathrm{S})/\mathrm{J}/\psi]_{\mathrm{pp}}$.
- R_{pPb} of J/ψ and ψ(2S) as a function of p_{T} and y.
- Comparison of the cross-sections and R_{pPb} with the theoretical predictions.

(C) Results from 2011 Pb–Pb run at $\sqrt{s_{\mathrm{NN}}} = 2.76$ TeV:

- Fractional double differential cross-section of J/ψ as a function of rapidity.

The following numerical calculations based on the framework of NRQCD have also been carried out during the course of this thesis work:

(D) Quarkonium production cross-section:

- Differential cross-section of charmonium as a function of $p_{\rm T}$.
- Differential cross-section of bottomonium as a function of $p_{\rm T}$.

The ALICE Muon Spectrometer has measured the inclusive production cross-sections of J/ψ and ψ(2S) at forward rapidity ($2.5 < y < 4$) in pp collisions at a center of mass energy $\sqrt{s} = 7$ TeV. The analysis has been carried out on a data sample corresponding to an integrated luminosity $\mathcal{L}_{\rm int} = 1.35$ pb^{-1}. The inclusive cross-sections, integrated over transverse momentum ($p_{\rm T}$) and rapidity (y) are: $\sigma_{\rm J/\psi} = 6.69 \pm 0.04 \pm 0.63$ μb and $\sigma_{\psi(\rm 2S)} = 1.13 \pm 0.07 \pm 0.19$ μb, where the first uncertainty is statistical and the second is systematic (assuming no quarkonium polarization). Since these cross-sections have been measured with the same apparatus and the same data set, it is possible to extract the ψ(2S) to J/ψ cross-section ratio and the fraction of inclusive J/ψ that comes from ψ(2S) decay with reduced systematic uncertainties. The values are: $\sigma_{\psi(\rm 2S)}/\sigma_{\rm J/\psi} = 0.170 \pm 0.011 \pm 0.013$ and $f^{\psi(2S)} = 0.103 \pm 0.007 \pm 0.008$, respectively. The J/$\psi$ and ψ(2S) differential cross-sections as a function of $p_{\rm T}$ and y have also been measured. The results have been compared with the measurement performed by LHCb collaboration as shown in Fig. 1. This has been done since the results obtained by LHCb is also in the same rapidity range ($2 < y < 4.5$). The ψ(2S) to J/ψ cross-section ratio have also been measured as a function of $p_{\rm T}$ and y. The ratio as a function of $p_{\rm T}$ has been compared with the LHCb measurement as shown in Fig. 2. In all the cases, there is a good agreement between the results from ALICE and LHCb. These results are also in good agreement with the theoretical calculations from CSM and NRQCD framework.

In case of p-Pb and Pb-p collisions, the inclusive J/ψ and ψ(2S) production was measured with the ALICE Muon Spectrometer in the p-going ($2.03 < y_{\rm cms} < 3.53$) and Pb-going ($-4.46 < y_{\rm cms} < -2.96$) directions with the integrated luminosities for the two data samples being $L_{\rm int}^{\rm pPb} = 5.01$ nb^{-1} and $L_{\rm int}^{\rm Pbp} = 5.81$ nb^{-1}, respectively. The production cross sections, the double ratios with respect to the J/ψ in p-Pb

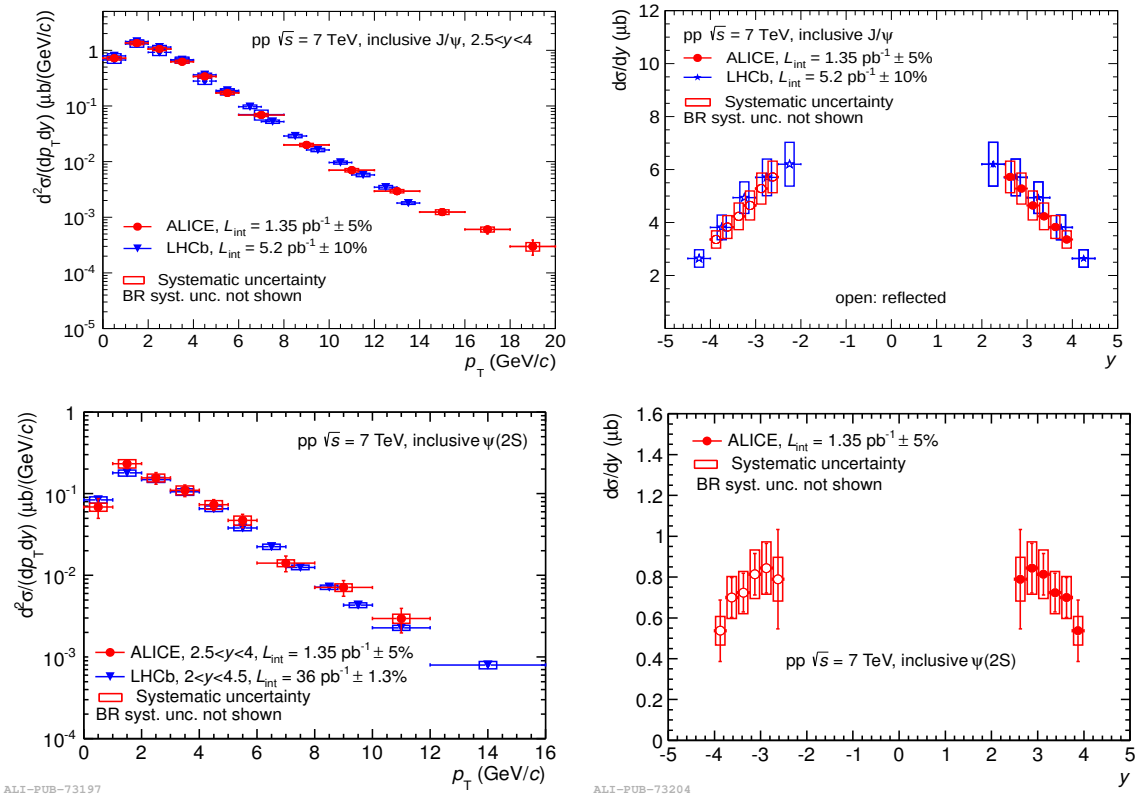

Figure 1: (Color online) Differential production cross-section of J/ψ (top) and ψ(2S) (bottom) as a function of $p_{\rm T}$ (left) and y (right) compared to the LHCb measurements.

and pp ($[\sigma_{\psi(2S)}/\sigma_{J/\psi}]_{\rm pPb}/[\sigma_{\psi(2S)}/\sigma_{J/\psi}]_{\rm pp}$) and the nuclear modification factors ($R_{\rm pPb}$) were estimated. The results show that ψ(2S) is significantly more suppressed than J/ψ in both rapidity regions and the $R_{\rm pPb}$ for ψ(2S) does not exhibit any significant $p_{\rm T}$ dependence. These observations imply that the initial state nuclear effects alone cannot account for the modification of the ψ(2S) yields. This is confirmed by the poor agreement of the ψ(2S) $R_{\rm pPb}$ with models based on shadowing and/or energy loss as shown in Fig. 3. The final state effects, such as the pair break-up by interactions with cold nuclear matter, might lead to the observed effect, but the extremely short crossing times for the $c\bar{c}$ pair, in particular at forward rapidity, make such an explanation unlikely. Thus, other final state effects should be considered, such as the interaction of the $c\bar{c}$ pair with the final state hadronic system created in the proton-nucleus

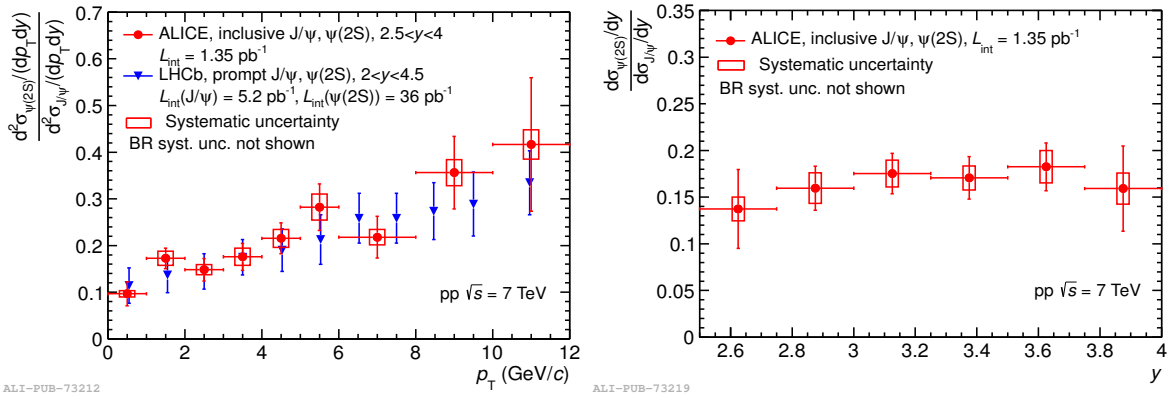

Figure 2: (Color online) The $\psi(2S)/J/\psi$ cross-section ratio as a function of p_T (left) compared to LHCb measurement and as a function of y (right).

collision.

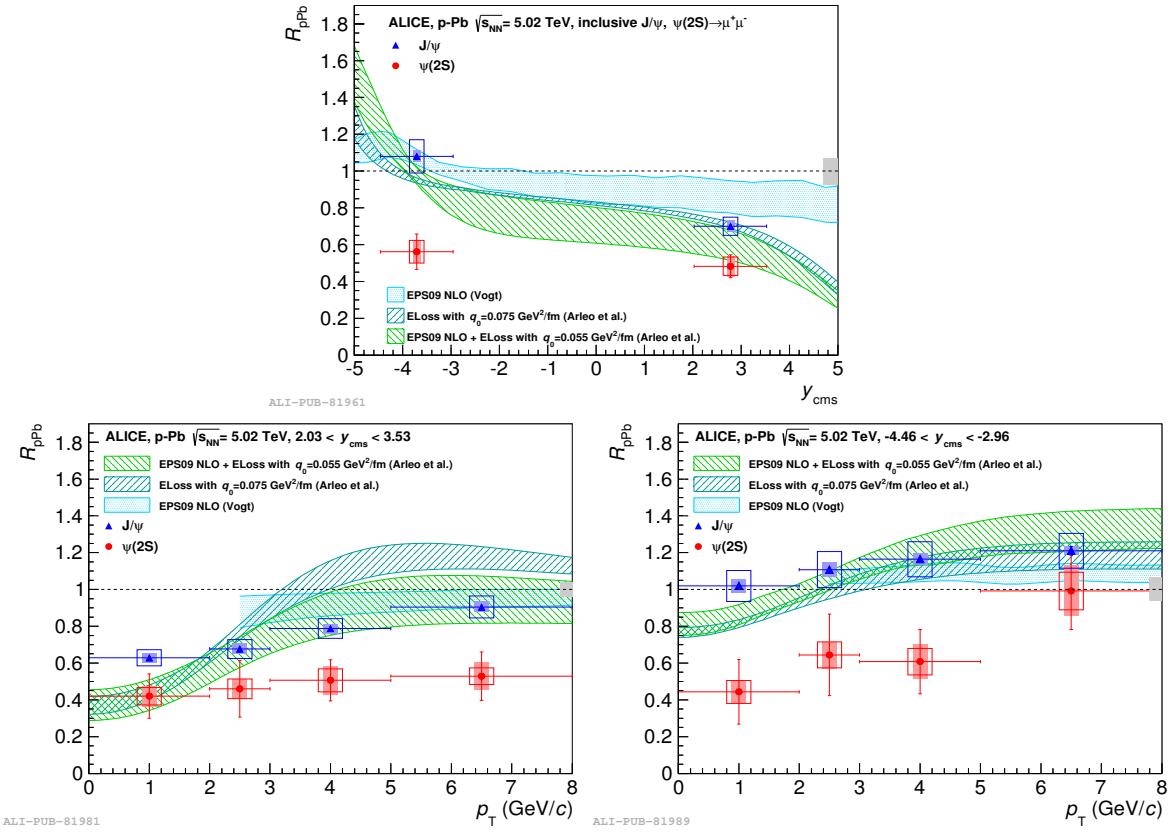

Figure 3: (Color online) The nuclear modification factor $R_{\rm pPb}$ of J/ψ and ψ(2S) as a function of $y_{\rm cms}$ (top) and p_T (bottom) compared to the theoretical models.

In case of inclusive Pb-Pb collisions at $\sqrt{s_{\rm NN}}$ = 2.76 TeV, ALICE Muon Spectrometer has reported the value of nuclear modification factor ($R_{\rm AA}$) to be $0.58 \pm 0.001 \pm 0.09$ integrated over centrality range corresponding to 90%. However, at low transverse momentum ($p_{\rm T} < 3$ GeV/c), the value of $R_{\rm AA}$ are significantly higher compared to the measurements at lower energy at RHIC. This feature tends to indicate a sizable contribution to the J/ψ yield from charm quark recombination in the deconfined partonic medium. Thus, it may be interesting to study the fractional double differential cross-section in two $p_{\rm T}$ bins, namely 0< $p_{\rm T}$ <3 GeV/c and $p_{\rm T}$ >3 GeV/c where the baseline behaviour is to be determined from the pp data. In this study, the fractional double differential cross-section of J/ψ integrated over centrality has been measured as a function of y for two different $p_{\rm T}$ bins, one is low $p_{\rm T}$ bin ($0 < p_{\rm T} < 3$ GeV/c) and other is high $p_{\rm T}$ bin ($p_{\rm T} > 3$ GeV/c). Fig. 4 shows the ratio of the fractional double differential cross-sections of J/ψ in Pb-Pb to that in pp. The two distributions are similar for $y > 3$ but for $2.5 < y < 3$, the distributions seems to be distinct. It will be interesting to compare these results with theoretical predictions in order to understand the reason for this difference.

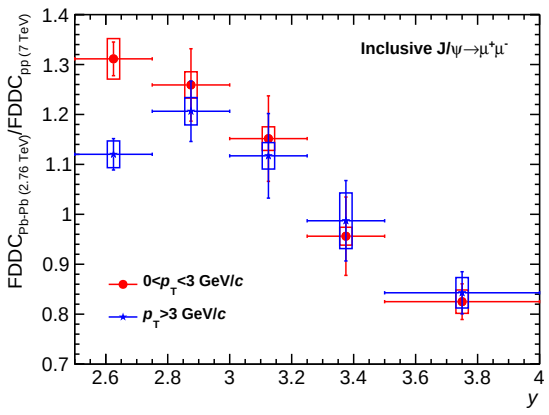

Figure 4: (Color online) Ratio of the fractional double differential cross-section of J/ψ in Pb-Pb to pp.

A systematic study of J/ψ, ψ(2S), Υ(1S), Υ(2S) and Υ(3S) production in pp collisions at different LHC energies and at different rapidities using the leading order

(LO) non-relativistic QCD (NRQCD) model of heavy quarkonium production have been performed. In these calculations, the feed-down contributions from χ_{cJ} ($J = 0$, 1, 2) and ψ(2S) decays to J/ψ have been considered while for Υ(1S), the feed-down from Υ(2S), Υ(3S) and χ_{bJ} has been taken into account. The calculated values have been compared with the available data from the four experiments at LHC namely, ALICE, ATLAS, CMS and LHCb. For ALICE data, the inclusive J/ψ and ψ(2S) cross-sections have been calculated by including the feed-down from B meson using Fixed-Order Next-to-Leading Logarithm (FONLL) formalism. It has been found that all the experimental cross-sections are well reproduced for $p_{\rm T} > 4$ GeV/c within the theoretical uncertainties arising due to the choice of the factorization scale. The transverse momentum distributions of J/ψ and ψ(2S) both for the direct and feed-down processes have been calculated at the upcoming LHC energies of $\sqrt{s} = 5.1$ TeV and 13 TeV.

The thesis consists of eight chapters and these are as follows,

Chapter 1. Physics motivation :

In this chapter the general understanding of the QGP from the view point of QCD and different probes of QGP will be discussed. The quarkonium production mechanisms will also be discussed.

Chapter 2. ALICE Experiment at the LHC :

Different detectors of ALICE with specific emphasis on Muon Spectrometer will be presented in this chapter. The detector layout, data taking and analysis framework will be discussed.

Chapter 3. Experiment and data analysis :

In this chapter different types of data, trigger and their defination will be discussed which were relevant for the first run period of LHC. The data statistics and various set of cuts will also be discussed.

Chapter 4. J/ψ and ψ(2S) production in pp collisions :

In this chapter the analysis of inclusive J/ψ and ψ(2S) production at forward rapidity in pp collisions at $\sqrt{s} = 7$ TeV will be discussed. The integrated and differential production cross-sections of J/ψ and ψ(2S) and ψ(2S)/J/ψ cross-section ratio as a function of p_{T} and y, will be reported.

Chapter 5. ψ(2S) production in p-Pb collisions :

In this chapter, the inclusive production cross-sections of J/ψ and ψ(2S), both integrated and as a function of p_{T}, for the two y_{cms} domains, will be presented. The ratio of the production cross sections, as well as the double ratios between p-Pb and pp collisions and the nuclear modification factor of J/ψ and ψ(2S) will be discussed.

Chapter 6. Fractional double differential cross-section of J/ψ in pp and Pb-Pb collisions :

In this chapter, the fractional double differential cross-section of J/ψ in pp and Pb-Pb collisions as a function of y in two p_{T} domains integrated over centrality will be reported.

Chapter 7. Quarkonium production cross-section calculation within the framework of NRQCD :

In this chapter, the prompt and inclusive production cross-sections of J/ψ, ψ(2S), Υ(1S), Υ(2S) and Υ(3S) at different LHC energies and at different rapidities have been calculated within the framework of LO NRQCD and FONLL. The predictions of production cross-sections of J/ψ and ψ(2S) at $\sqrt{s} =$ 5.1 and 13 TeV will be presented.

Chapter 8. Summary :

In this chapter the summary of the thesis, and the future directions will be discussed.

List of Figures

List of Tables

Chapter 1

Physics Motivation

In this chapter the Standard Model of particle physics, quantum chromodynamics (QCD) and Quark-Gluon Plasma (QGP) [1] will be described in brief. The quarkonia as a probe to QGP will be discussed. Different kinds of effects in heavy-ion collisions such Cold Nuclear Matter (CNM) effects and Hot Matter effects or QGP related effects on the productions of quarkonia will be discussed in greater details. The time evaluation of the matter produced in heavy-ion collisions and the kinematic variables related to these collisions and used in this thesis will be described.

1.1 The Standard Model of Particle Physics

Particle physics is the branch of physics which aims to study the fundamental constituents of matter and the forces which govern their interactions. To the present knowledge, there are four fundamental forces or interactions as listed in Table 1.1. The Standard Model (SM) is the theory of the strong, the weak, and the electromagnetic forces. The SM as we know it today has evolved over many years, beginning with the

unification of the electromagnetic and weak forces in the late 1960's.

Force	Relative Strengh	Range [m]	Mediators	Current Theory
strong	10^{38}	10^{-15}	gluon (g)	Quantum Chromodynamics (QCD)
electromagnetic	10^{36}	∞	photon (γ)	Quantum Electrodynamics (QED)
weak	10^{25}	10^{-18}	Z^0, W^+, W^-	Electroweak Theory
gravity	1	∞	graviton	General Relativity (GR)

Table 1.1: The four fundamental forces and their effective strengths relative to gravity.

The SM is based on the framework of group theory and the overall symmetries of the SM are given by the combined group SU(3)⊗SU(2)⊗U(1). Each group corresponds to the symmetries of one of the three forces. U(1) represents the electromagnetic, SU(2) represents the weak while the strong interaction is represented by SU(3). Each force is mediated by a number of spin-1 gauge bosons. The photon is the mediator for electromagnetic, the weak interaction has three mediating bosons (the Z and $W^{\pm}$ bosons) and the eight gluons are mediators for the strong interaction. These gauge bosons interact with the fermions and also with each other except for the photon. There are two types of fundamental fermions: quarks and leptons. The quarks make up the strongly-bound particles, called hadrons, like the proton and neutron, and interact via all three forces. The leptons interact electromagnetically and weakly, but not strongly. The only stable charged lepton is the electron, which pairs up with protons and neutrons to make atoms. There are three generations of fermions, and each one has identical properties, except that the masses are different. For each lepton generation there are two particles: the charged lepton and the neutral lepton. The neutral leptons are called neutrinos and in SM, they are massless. The charges given in the Fig. 1.1 are for the particles. For each particle there is an oppositely charged antiparticle (e.g. antielectron, antitau). Due to a process called spontaneous symmetry breaking, the SU(2)⊗U(1) symmetry is broken by the Higgs potential. This generates along with the three massive bosons (the Z and $W^{\pm}$) and one massless boson (the photon) as discussed above and at least one massive

Higgs particle. The Higgs particle is a prediction of the SM which has been observed experimentally. The elementary particles in the SM are shown in the Fig. 1.1.

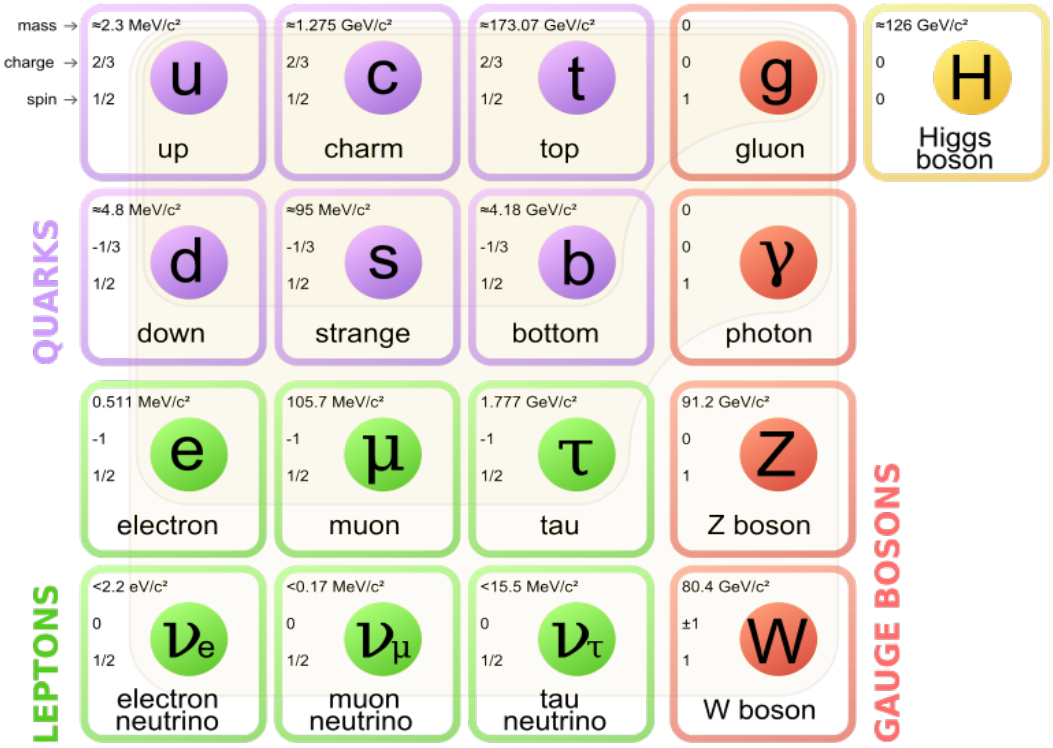

Figure 1.1: The elementary particles in the Standard Model [2].

1.2 QCD and Asymptotic Freedom

The mathematical formulation of the strong interaction is quantum chromodyanamics (QCD). The strong charge is called color. Each quark carries a color which can be of three types – red, green and blue, in an analogy to the three colors in optics. The gluon has a combination of a color and anticolor. Unlike in quantum electrodynamics (QED) where the electric field diminishes with distance, the strength of the strong force increases with the distance. Thus, as two quarks separate, the force between them increases with the increase in the distance between them due to the self interaction of the gluons. When a quark-antiquark ($q\bar{q}$) pair separate, it becomes

energetically favorable at some point to create a new $q\bar{q}$ pair out of the vacuum and the original $q\bar{q}$ pair becomes two independent $q\bar{q}$ pairs. This mechanism is responsible for the lack of experimental observation of free quarks as well as the color neutral property of hadrons, and is known as confinement.

Color neutrality can exist in two configurations. First, the hadron can consist of a quark and antiquark pair where one quark carries a color and the other carries the corresponding anticolor. Such a state is called meson; the lightest meson is the pion ($u\bar{d}$, $\bar{u}d$ or $u\bar{u}/d\bar{d}$) and other examples include the J/ψ meson ($c\bar{c}$), the Υ ($b\bar{b}$) meson, the K^+ ($u\bar{s}$) and K^- ($\bar{u}s$) etc. Second, the hadron can consist of three quarks or anti-quarks where each quark carries a different color. States of three quarks are called baryons. Examples are the proton and neutron. Other exotic hadrons are predicted by QCD such as the tetraquark (made of two quark-antiquark pairs), the pentaquark (made of a color-anticolor quark pair and three quarks of color red, green, and blue) and glueballs (made of only gluons). Experiments are actively searching for their definite experimental signatures.

In QCD, $q\bar{q}$ provides a screening effect on the bare color charge. On the otherhand, the color-carrying gluon creates an antiscreening effect due to self interaction, which ends up dominating the screening coming from $q\bar{q}$ pairs. This means that the closer one gets to a bare charge, the strong force gets weaker, this phenomenon is called asymptotic freedom. Mathematically, this is directly manifested in the dependence of the coupling constant α_s on the scale of the momentum transfer Q, according to the following equation for 1-loop corrections [3]:

$$\alpha_{\mathrm{s}}(Q) = \frac{12\pi}{\beta \ln\left(\frac{Q^2}{\Lambda^2_{\mathrm{QCD}}}\right)} \tag{1.1}$$

$\Lambda_{\rm QCD}$ is the QCD energy scale, approximately 200 MeV [4], and $\beta = 11n_c - 2n_f$, where n_c and n_f are the number of colors and number of quark flavours, respectively. As shown in the Fig. 1.2, when Q is high (i.e. the scale of the interaction is very small) the coupling constant is small. This is the asymptotic freedom regime where the quarks can be thought of as moving freely. The perturbative QCD (pQCD) approach can be applied to make predictions for observables expressed in terms of powers of $\alpha_{\rm s}$ since in this regime $\alpha_{\rm s} \ll 1$. Perturbative QCD cannot be used when Q is low as $\alpha_{\rm s}$ becomes large. In this regime Lattice QCD (lQCD) [5] calculations or some effective phenomenological models like color glass condensate (CGC), are used.

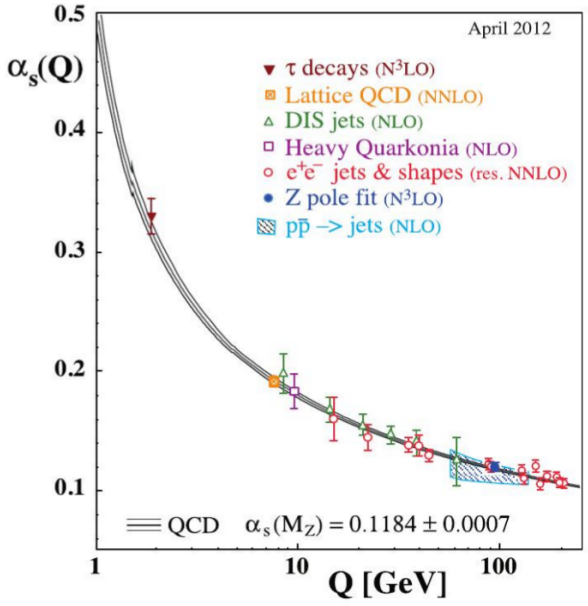

Figure 1.2: The summary of $\alpha_{\rm s}$ measurements as a function of respective energy scale Q.

1.3 QCD Phase Diagram

The above discussion suggests that if the temperature (T) or net baryon density (μ) is high enough, a transition should occur from normal nuclear matter where quarks

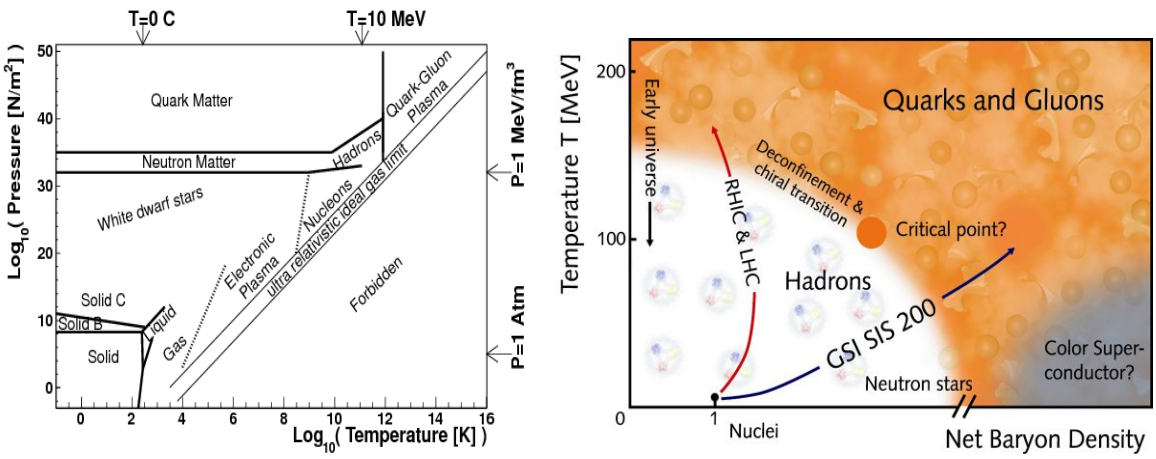

Figure 1.3: (Color online) Left: Phase diagram of matter in the pressure versus temperature plane for a non zero baryonic potential. Right: A schematic QCD phase diagram.

and gluons are confined in hadrons, to a new state of matter where the quarks and gluons are deconfined. Analogous to electric plasmas, the abundance of color charge creates a Debye screening effect which limits the interaction length of the strong force, allowing the deconfinement of the quarks and gluons. This state of deconfined quarks and gluons is called the quark gluon plasma (QGP). It is expected that during the first few microseconds after the Big Bang, the universe would have existed in a QGP state with zero net baryon density and it is possible that neutron stars, which have a low temperature but high net baryon number, might contain a QGP at their core. At even higher chemical potential and low temperature a state may emerge, where two quarks of same color will form a cooper pair, called Color Superconductor. The model calculations and the studies of this color superconducting phase strongly suggest a first order phase transition between the hadronic and QGP phases at large baryon chemical potential and lower temperature. On the other hand, recent extensive Lattice QCD calculations have conclusively demonstrated that the temperature driven transition at zero baryon chemical potential is an analytic crossover. These two features would require existence of a critical point, at which, as the chemical potential is decreased

and the temperature is increased, the first order transition line terminates and turns into a crossover. At the critical point the hadronic and the QGP phases, coexisting along the first-order line, fuse into one phase where striking physical phenomena, analogous to critical opalescence, are expected. A schematic view of the QCD phase diagram is shown in the right panel of Fig. 1.3.

The left panel of Fig. 1.3 shows the lay-out of the phase diagram of matter as is known today. We clearly distinguish two regions, one for temperatures below 10^9 K (1 MeV) and pressures below 10^{32} Pa (1 MeV/fm^3), where the electromagnetic interaction between atoms (or ions) provides the degrees of freedom of matter, and a second region, for temperatures above 10^9 K and/or pressures above 10^{32} Pa, where the strong interaction between nucleons, hadrons or quarks dominates and as shown in the figure at sufficiently high temperatures and pressures, QGP exist.

Since the transition between quark confinement and deconfinement is a non-perturbative process, so normal perturbative QCD approaches are no longer valid. Lattice QCD (lQCD) is used to perform calculations in this regime. In lQCD, numerical non-perturbative QCD calculations are performed on a discrete grid of space time points. In the limit of infinitely small lattice spacings this approach regains continuum QCD. Practically, this approach is computationally limited, as increasingly small lattice spacing involves increasingly intensive numerical calculations. The lQCD calculations predict that the transition to a QGP should occur at a critical temperature of $T_c \sim 170$ MeV for zero net baryon density.

1.4 Time evolution of QGP matter in Heavy-Ion Collisions

The only way to access the region with low chemical potential (μ_B) and high temperature of the QCD phase diagram is through the particle accelerators by means of heavy-ion collisions. To fulfill this purpose, the ultra-relativistic heavy-ion collisions are performed at Brookhaven National Laboratory (BNL) in USA and at Large Hadron Collider (LHC) at CERN in Switzerland.

In heavy-ion collisions, the two beams of heavy ions (like Au, Pb) are accelerated quite close to that of speed of light and then allowed to collide. In the center of mass frame of the colliding nuclei, these two nuclei can be seen as two thin disks due to Lorentz contraction. During collisions a nucleon in one nucleus may collide with many nucleons in the other nucleus and deposits large amount of energy in the collision region. The energy density generated can be measured by measuring the charge particle produced per unit rapidity range:

$$\epsilon = \frac{\langle m_{\mathrm{T}} \rangle}{\tau_f A} \frac{dN}{dy} \tag{1.2}$$

where $\langle m_{\mathrm{T}} \rangle = \sqrt{(E^2 - p_z^2)}$, is the average transverse mass of the charged particle, τ_f is the formation time of the charged particle, A is the overlapping area of the colliding nuclei and $\frac{dN}{dy}$ is the charge particle multiplicity in the rapidity range covered.

The time evolution of the collision is shown in Fig. 1.4. The collision takes place at $\tau = 0$. In this initial stage, called "pre-equilibrium" very hard processes with high momentum transfer occur within partons. As an example, the creation of heavy $q\bar{q}$

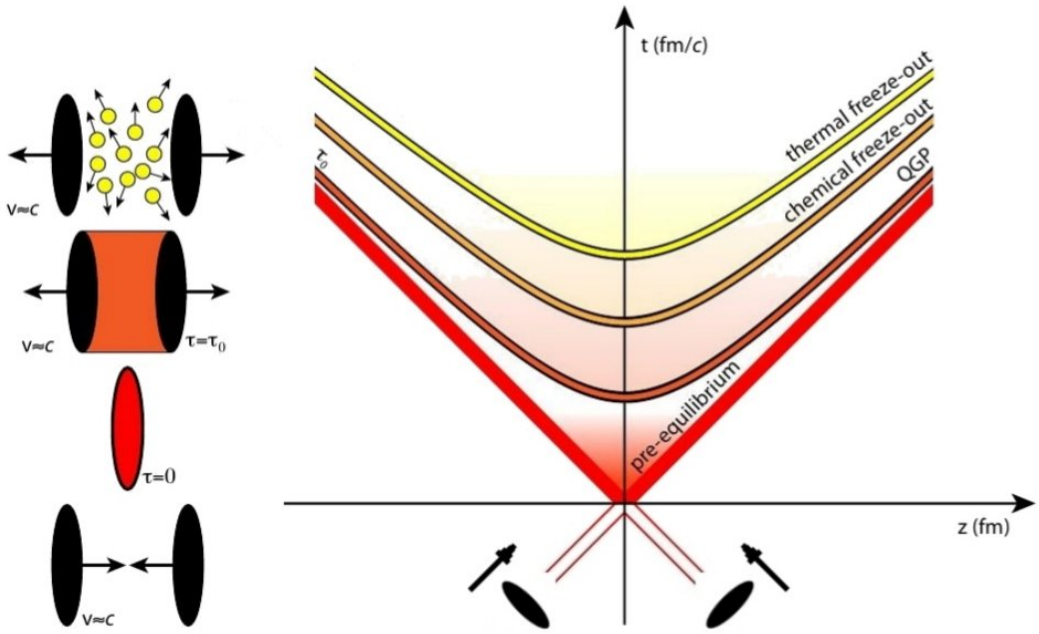

Figure 1.4: Time evolution of space-time diagram in heavy-ion collisions.

pairs predominantly happens for gluon fusion in this phase. At $\tau = \tau_0 \sim 1$ fm/c ($\sim 3{\times}10^{-24}$ sec), multiple scattering processes among the nucleons and their constituents lead to a thermal equilibration of the medium and a hot dense fireball of quark-gluon matter of energy density $\epsilon \sim 10$ GeV/fm^3 (approximately 50 times more than normal matter) [6] with a dimension of ~ 300 fm^3 [7] is produced and the temperature reaches to T ~ 550 MeV (approximately $5.5{\times}10^{12}$ K) at LHC. The fireball expands due to pressure gradient and after few fm/c (about 10^{-23} sec) "hadronization" takes place. The life time of the plasma depends on the energy density reached in the collision, which is few fm/c in case of LHC. The kinetic energy of the produced particles becomes too low for inelastic collisions and at this point all abundances and particle ratios becomes fixed, this stage is called "chemical freeze-out". Finally, after the "thermal freeze-out" elastic collisions also stops and the kinematic distribution of the produced particles get fixed.

1.5 The quarkonium and QGP

The meson comprising of a heavy quark and a heavy antiquark is called a quarkonium. Due to the large mass of the constituent quarks, the quarkonium spectroscopy can be described by non-relativistic potential models [8]. While $c\bar{c}$ pairs are further called charmonia and $b\bar{b}$ pairs bottomonia, the life time of the top quark is too small to allow for the formation of bound states and so no such state has been measured yet. Furthermore, again due to their high masses, heavy-quark pairs are expected to be created predominantly in the early stage of ultra-relativistic hadronic collisions which can be used to produce the extreme temperatures necessary for the deconfinement. Thus, the quarkonium can be utilized as a very promising probe to study the QGP. The evolution of this state of matter is expected to take place in later stages of the collision and is therefore believed to modify the measured rates of quarkonia.

Depending on the angular momentum state of the quark pair, quarkonium states have different masses, due to the hyperfine splitting. Quarkonium states can be described using spectroscopic notation $n^{2S+1}L_J$, where n, S, L and J are the principal quantum number, the spin angular momentum, the orbital angular momentum and the total angular momentum of the quarkonium system, respectively. The different angular momentum states give the quarkonium different parity. Charge parity (the parity under charge inversion) is given by $C = (-1)^{L+S}$ and parity under spatial coordinate inversion is given by $P = (-1)^{L+1}$. The spectroscopic notation, mass, decay width and average radius of various qaurkonium are summerized in Table 1.2. The verious decay modes of charmonium and bottomonium are shown in Fig. 1.5 and Fig. 1.6, respectively.

Meson	$n^{2S+1}L_J$	J^{PC}	Mass (MeV)	Width (MeV)	r_0 (fm)
$\eta_c(1S)$	1^1S_0	0^{-+}	2981.0 ± 1.1	29.7 ± 1.0	
$J/\psi(1S)$	1^3S_1	0^{--}	3096.916 ± 0.011	0.0929 ± 0.0028	0.50
$\chi_{c0}(1P)$	1^3P_0	0^{++}	3414.75 ± 0.31	10.4 ± 0.6	
$\chi_{c1}(1P)$	1^3P_1	1^{++}	3510.66 ± 0.07	0.86 ± 0.05	
$h_c(1P)$	1^1P_1	1^{+-}	3525.41 ± 0.06	< 1	
$\chi_{c2}(1P)$	1^3P_2	2^{++}	3556.20 ± 0.09	1.98 ± 0.11	
$\eta_c(2S)$	2^1S_0	0^{-+}	3638.9 ± 1.3	10 ± 4	
$\psi(2S)$	2^3S_1	1^{--}	3686.109 ± 0.034	0.304 ± 0.009	0.90
$\Upsilon(1S)$	1^3S_1	1^{--}	9460.30 ± 0.26	0.05402 ± 0.00125	0.28
$\chi_{b0}(1P)$	1^3P_0	0^{++}	9859.44 ± 0.42 ± 0.31	Undertermined	
$\chi_{b1}(1P)$	1^3P_1	1^{++}	9892.78 ± 0.26 ± 0.31	Undertermined	
$h_b(1P)$	1^1P_1	1^{+-}	9898.6 ± 1.4	Undertermined	
$\chi_{b2}(1P)$	1^3P_2	2^{++}	9912.21 ± 0.26 ± 0.31	Undertermined	
$\Upsilon(2S)$	2^3S_1	1^{--}	10023.26 ± 0.321	0.03198 ± 0.00263	0.56
$\chi_{b0}(2P)$	2^1P_0	0^{++}	10232.5 ± 0.04 ± 0.05	Undertermined	
$\chi_{b1}(2P)$	2^1P_1	1^{++}	10255.46 ± 0.022 ± 0.05	Undertermined	
$\chi_{b2}(2P)$	2^1P_2	2^{++}	10268.65 ± 0.022 ± 0.05	Undertermined	
$\Upsilon(3S)$	3^3S_1	1^{--}	10355.2 ± 0.05	0.02032 ± 0.000185	0.78

Table 1.2: Properties and standard notation for all quarkonium states. The average radius (r_0) are taken from [9].

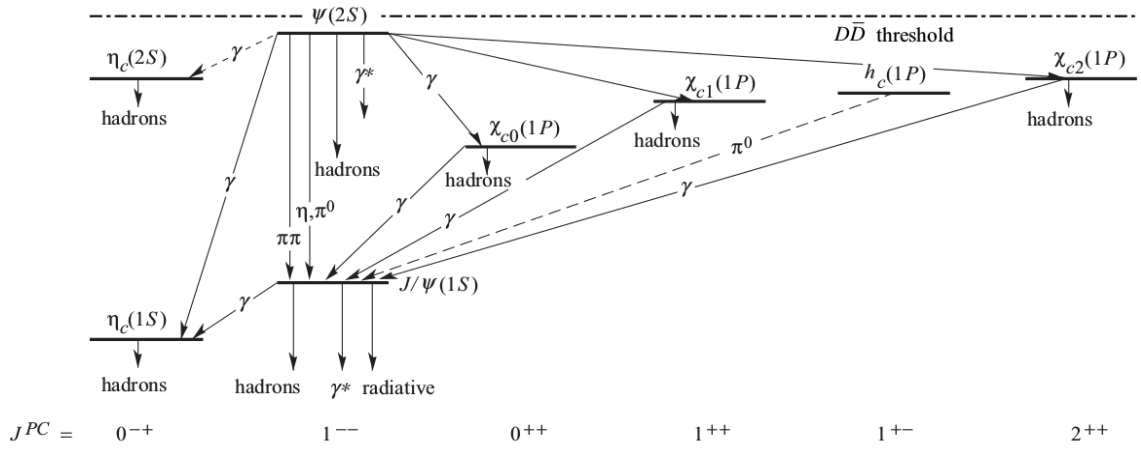

Figure 1.5: Charmonium decay modes with spectroscopy notation [10].

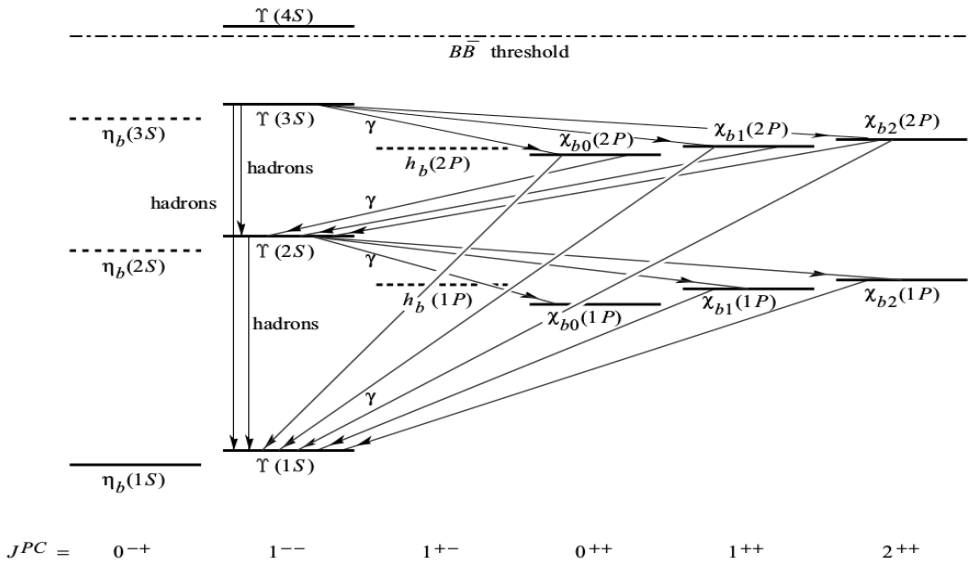

Figure 1.6: Bottomonium decay modes with spectroscopy notation [10].

1.6 Cold Nuclear Matter (CNM) Effects

The name cold matter arises because these effects are observed in proton-nucleus or deuteron-nucleus interactions where no hot or dense matter effects are expected. They can either suppress or enhance the quarkonium production. The CNM effects are broadly classified as initial and final state effects.

1.6.1 Initial-state effects

The initial state effects are nuclear shadowing, gluon saturation, parton energy loss and Cronin effect, affect the partons before the hard scattering.

Nuclear shadowing

The parton distribution functions (PDF's) describe the probability density of quarks and gluons inside a free proton as a function of their longitudinal momentum fraction (x) and energy scale (Q^2). An example of PDF for an energy transfer of $Q^2 = 10$ GeV^2 (roughly the scale relevant for J/ψ production) is shown in Fig. 1.7. These PDF's are phenomenological parametrization of data taken mostly from deep inelastic scattering (DIS) experiments and Drell-Yan (DY) production. Both DIS and DY directly probe only the quark and antiquark distributions, while the gluon distribution is probed only indirectly. This leads to a larger uncertainty on the gluon distribution compared to those for the quark [11]. This is important, as the gluon distribution dominates the hard scattering processes in the high energy collisions at RHIC and LHC.

The PDF of a free nucleon differs from that of a nucleon bound in a nucleus. It

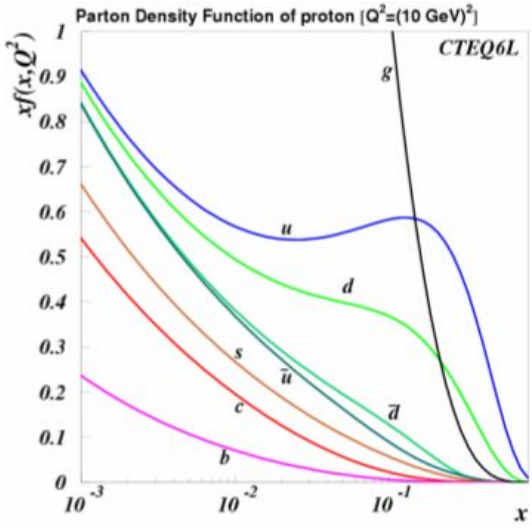

Figure 1.7: An example of a parton distribution function for the quarks and gluons at $Q^2 = 10$ GeV^2 from the CTEQ collaboration [11].

has been observed that the parton distribution functions extracted from nuclear DIS experiments [12] are modified for protons bound in a nucleus. This has led to the development of nuclear parton distribution functions (nPDF's). The modification of the PDF's is typically quantified by the ratio

$$R_i^A(x, Q^2) = \frac{f_i^A(x, Q^2)}{f_i(x, Q^2)}, \tag{1.3}$$

where $f_i(x, Q^2)$ is the free proton PDF for parton flavor i and $f_i^A(x, Q^2)$ is the PDF for parton flavor i of a proton bound in nucleus A. A purely schematic example of this ratio is shown in Fig. 1.8. The modification is generally broken into four regions:

- *Shadowing* refers to the low-x ($x \leq 0.03$) region where $R_i^A(x, Q^2) < 1$. This signifies a decrease in the number of partons when compared to the free proton case. In the case of the gluon distribution, where this effect is largest, it is believed to be caused by fusion of gluons into a single high-x gluon due to the

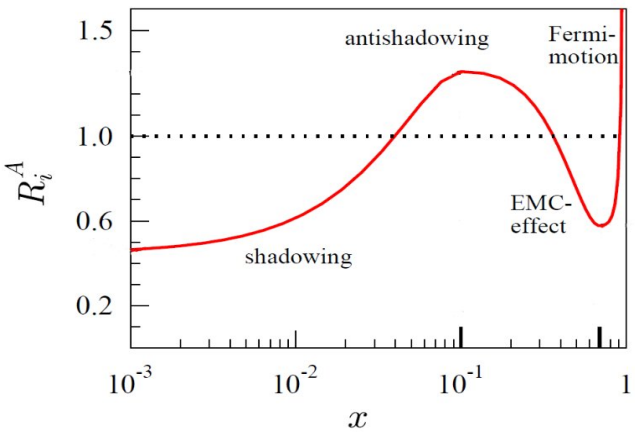

Figure 1.8: A purely schematic example of the modification of the parton distribution function in nuclei.

greater density of gluons present in the nucleus.

- *Anti-shadowing* refers to the intermediate x region ($0.03 \leq x \leq 0.3$) where $R_i^A(x, Q^2) > 1$. This is due to the fusion of low-x gluons, creating an excess in this region and a deficit in the lower x region.

- *EMC Region* refers to the higher x region ($0.3 \leq x \leq 0.7$) where $R_i^A(x, Q^2) < 1$ and is named after the European Muon Collaboration (EMC) experiment which discovered this phenomenon in DIS experiments with nuclei [12]. No strong consensus has been reached as to the cause of this suppression.

- *Fermi-motion* refers to the highest x region where $R_i^A(x, Q^2) \gg 1$. This is due to Fermi motion of the nucleons in the nucleus.

In the present thesis, the phenomenon of the modification of the PDF's will be referred to as nuclear shadowing, while shadowing alone (or the shadowing region) will refer to low-x suppression of the parton distribution.

Since the cross sections of quarkonium directly depend on these PDF's, the modifications have to be accounted to compare the different collision systems such as

pp, p-A or A-A. The region of very small x is accessible at the LHC [13] and therefore significant shadowing effect is expected.

Gluon saturation

From the Fig. 1.7, we can see that as one goes to smaller values of the x, (alternatively higher momentum transfer Q^2) the density of gluons begins to quickly dominate that of the quarks. The density of gluons per unit transverse area becomes so large that the individual gluons begin to overlap and can no longer be resolved. This happens at a scale, known as the saturation scale (Q_s). The evolution of x with Q^2, along with the evolution of Q_s, is schematically shown in Fig. 1.9. This leads to a saturation of the gluon distribution where non-linear corrections to the normal evolution equations dominate. When $Q_s \gg \Lambda_{\mathrm{QCD}}$, then weak coupling techniques can be employed which led to the development of an effective field theory known as the Color Glass Condensate (CGC). The CGC attempts to explain the small-x behavior of QCD [14, 15].

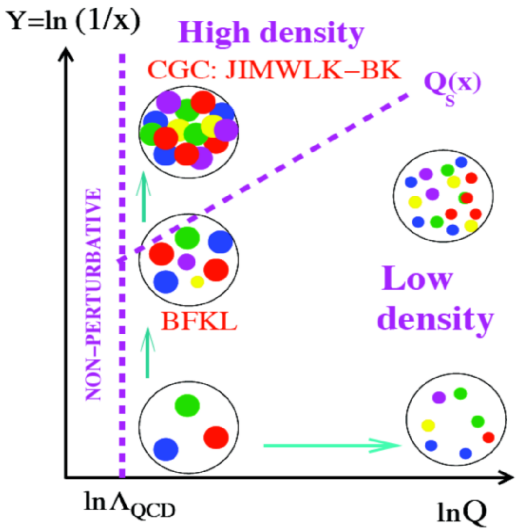

Figure 1.9: A schematic picture of the evolution of proton parton density with x and Q^2.

The nuclear shadowing and gluon saturation are not so clearly separated because both deal with the modification of the x and Q^2 dependence of parton distributions. It may be argued that the gluon saturation and the nuclear shadowing are two different interpretations of the same physical phenomenon. In the gluon saturation picture this is interpreted as arising from coherent interactions of gluons above some scale, while the nuclear shadowing assumes the nucleus is simply a collection of bound nucleons and parametrizes the collective modification.

One of the limitation of the CGC framework is that it is limited in its range of applicability through the saturation scale Q_s. Calculations indicate that CGC is valid for low-p_{T} process at forward rapidity at RHIC, however it breaks down near mid-rapidity. At the LHC, however, the CGC should be applicable over a much wider range of rapidity and p_{T} due to the significant increase in collision energies, and will be a good theory to employ in the calculations for the production cross-sections of quarkonia at forward rapidity. In a recent publication [16], it has been shown that the J/ψ production for $p_{\mathrm{T}} < 5$ GeV/c both in mid and forward rapidity regions can be well reproduced by employing the CGC + NRQCD formalism.

Coherent parton energy loss

An incoming parton can scatter elastically and lose energy by radiating gluon as it traverses the nucleus, before the hard scattering process occurs. This decreases the incoming partons x, effectively causing a shift in the parton distribution relative to pp collisions which is responsible for a suppression of the hadrons in p-A collisions.

Cronin effect

In p-A collisions, an incoming parton can undergo a multiple scattering processes in the nucleus before undergoing a hard collision. In this case, the parton survives to the medium and in its random walk it acquires an extra transverse momentum which modifies the p_{T} differential spectrum of the hadrons with respect to pp collisions. This modification is known as the Cronin effect. This effect is believed to be responsible for the enhanced hadron production in d-A collisions as measured by the STAR Collaboration at RHIC Fig. 1.10 [17].

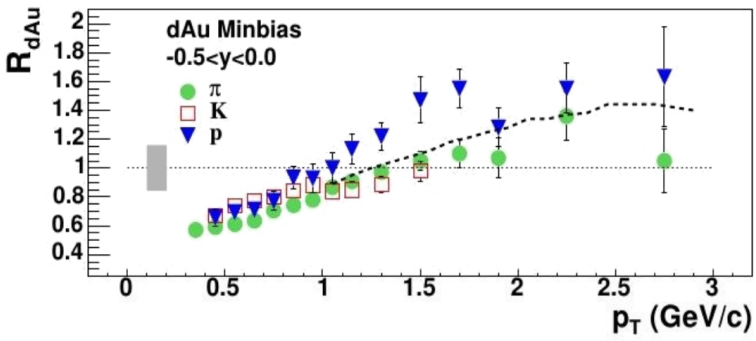

Figure 1.10: Hadron yields in d-Au collisions at $\sqrt{s_{\mathrm{NN}}} = 0.2$ TeV normalized to pp collisions. Dashed line is the R_{dAu} of inclusive charged hadrons [17].

1.6.2 Final-state effects

Nuclear absorption

The breakup of pre-resonant $Q\bar{Q}$ pairs due to multiple scattering with nuclear matter surrounding the collision region is called nuclear absorption. It is a final-state effect. In this picture, the J/ψ production cross section is obtained as a function of a parameter L which is defined as the mean path length of the pre-resonant $Q\bar{Q}$ through cold nuclear matter. It depends on the colliding beams and their centrality. The

nuclear absorption can be characterized by the cross section $\sigma_{\rm abs}$ which is determined by an exponential fit to the data: $\sim \exp(-\rho_{\rm nm}\sigma_{\rm abs}L)$, where $\rho_{\rm nm}$ is the density of normal nuclear matter. Recent studies [18–20] show that the absorption cross section $\sigma_{\rm abs}$ is strongly dependent both on the quarkonium kinematics (rapidity), as seen in the left panel of Fig. 1.11, as well as on the nucleon-nucleon collision energy. The right panel of Fig. 1.11 shows a compilation of measurements of $\sigma_{\rm abs}$ at mid-rapidity in the centre-of-mass system at various collision energies. The effect of absorption decreases with collision energy and will have a smaller impact at LHC energies. This observation holds regardless of the specific shadowing parameterization used to obtain the remaining absorption cross section.

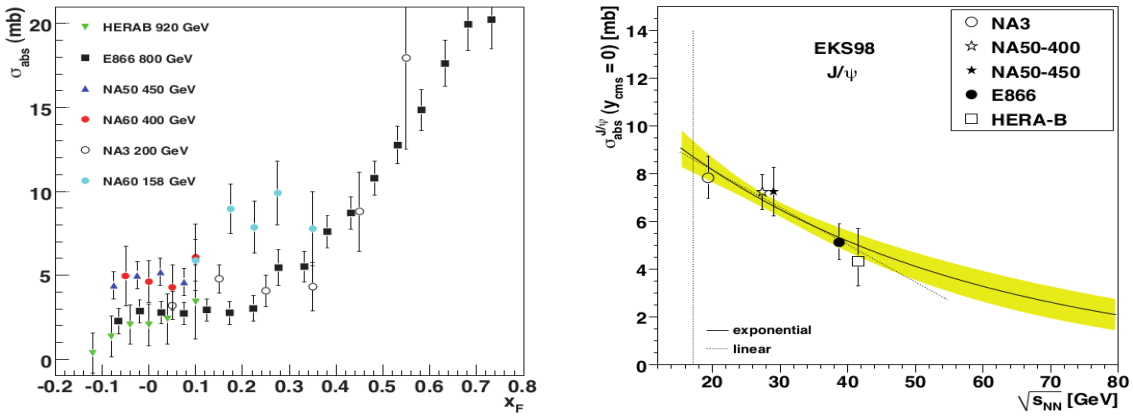

Figure 1.11: (Color online) Left: the J/ψ absorption cross section $\sigma_{\rm abs}$ as a function of x_F [20] from various experimental compilation. Note that measurements from fixed target experiments at different energies are compared. Right: compilation of data from various experiments for $\sigma_{\rm abs}$ around $y_{\rm cms}$ versus $\sqrt{s_{\rm NN}}$ [18]. The curves correspond to linear (dotted line) and exponential (solid line with yellow error band) fits to the data.

Comovers absorption

The quarkonium could be suppressed in a hot and dense gas system formed by conventional hadrons like pions and kaons by the processes like J/$\psi + \pi = D + \bar{D} + X$. This is called suppression by hadronic comovers.

1.7 Hot Matter Effects or QGP-Induced Effects

Color screening and regeneration are two well known QGP-induced effects. The current status on the theoretical understanding of hot-medium effects is briefly discussed below:

1.7.1 Color screening

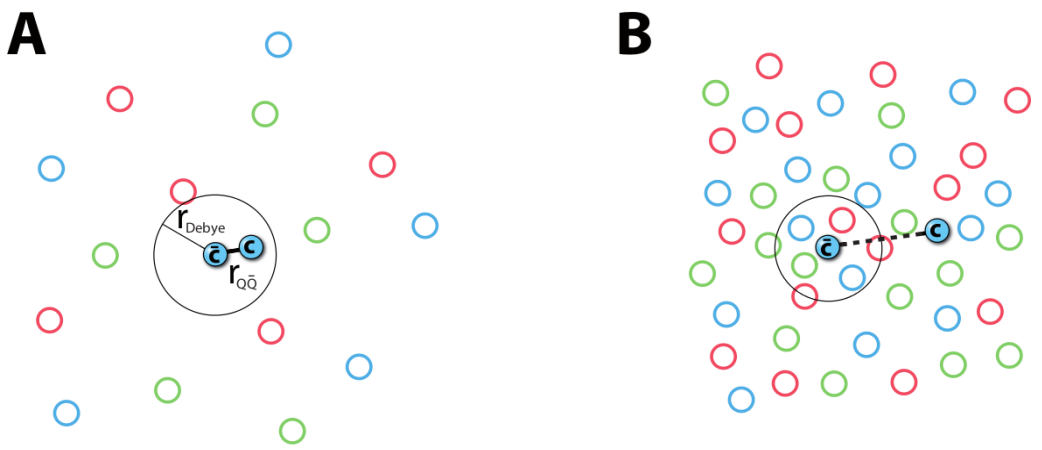

Figure 1.12: Debye screening in a medium of quasi-free color charges. Left: the Debye radius is larger than the binding radius of the quarkonium state, the state survives. Right: the Debye radius becomes much smaller than the $Q\bar{Q}$ binding radius, the state may melt.

In 1986 Matsui and Satz [21] predicted for the first time a modification of J/ψ yields in heavy-ion collisions. The break-up of $Q\bar{Q}$ pairs in the hot environment of a QGP via Debye screening by free color charges is the central idea which is analogous to the well-known QED process in electro-dynamic plasmas. The QED potential of two opposite sign charges gets screened exponentially with the distance r between

them as:

$$V(r) = -\frac{q^2}{4\pi r} e^{-r/\lambda_D}. \tag{1.4}$$

Here the parameter λ_D is known as Debye length and it depends on the temperature T_e and density ρ_e of the electrons in the electromagnetic plasma:

$$\lambda_D = \sqrt{\frac{\epsilon_0 k_B T_e}{\rho_e e^2}}. \tag{1.5}$$

Here e, ϵ_0 and k_B are the electron charge magnitude, the permittivity of free space and the Boltzmann constant, respectively. In analogly with that a similar effect in plasmas of quasi-free color charges can be expected where the effective QCD potential can be written as [22]:

$$V_{Q\bar{Q}}(r, T) \sim -\frac{4}{3}\frac{\alpha_s}{r} e^{-r/\lambda_D(T)}. \tag{1.6}$$

In Fig. 1.12, the effect of the screening is depicted schematically. The left panel (A) shows the Debye radius is larger than the binding radius of the quarkonium state, the state survives. The right panel (B) shows the case where the Debye radius becomes much smaller than the $Q\bar{Q}$ binding radius (Bohr radius) what may lead to a melting of that state. When the QGP freeze out occurs, the dissociated heavy quarks will arbitrarily bind with other nearby quarks most likely light quarks making up D or B mesons that will be measured in the experiment instead of quarkonia. This is indeed the case for collisions where only few heavy-quark pairs are created.

Different quarkonium states have different radii between the bound quark and

antiquark. The formation of such a state of matter would lead to a suppression of quarkonia rates in heavy-ion collisions depending on the temperature of the QGP and the corresponding Debye length λ_D. The yields of different quarkonia states might even reflect the temperature of the quark-gluon plasma [23, 24] due to their varying radii.

1.7.2 Regeneration

It has also been theorized that there are effects of the QGP which could actually enhance quarkonia production, known as recombination or regeneration or coalescence. This occurs at ultra-relativistic heavy-ion collisions, where many $c\bar{c}$ pairs are produced in one collision (see Fig. 1.13 for illustration). After the diffusion of the c and $\bar{c}$ through the medium as shown in the panel B if Fig. 1.13, the uncorrelated c and $\bar{c}$ may create bound states at some stage of the medium evolution which is shown in panel C of Fig. 1.13. This effect might lead to an enhancement of the yields, especially of the J/ψ, as depicted in panel C, Fig. 1.13. The sketch drawn in that latter panel is inspired by a statistical model [25, 26] assuming that all hadrons including the quarkonia are created almost simultaneously during the chemical freeze-out at the QGP phase boundary. A key prediction of this model is that the charmonium yields scale with the squared of the number of $c\bar{c}$ pairs. As this number increases dramatically towards LHC energies and the LHC results are expected to provide an important test for this statistical model. At LHC energies, the recombination effects have been observed at low p_{T} region ($0 < p_{\mathrm{T}} < 4$ GeV/c) [27].

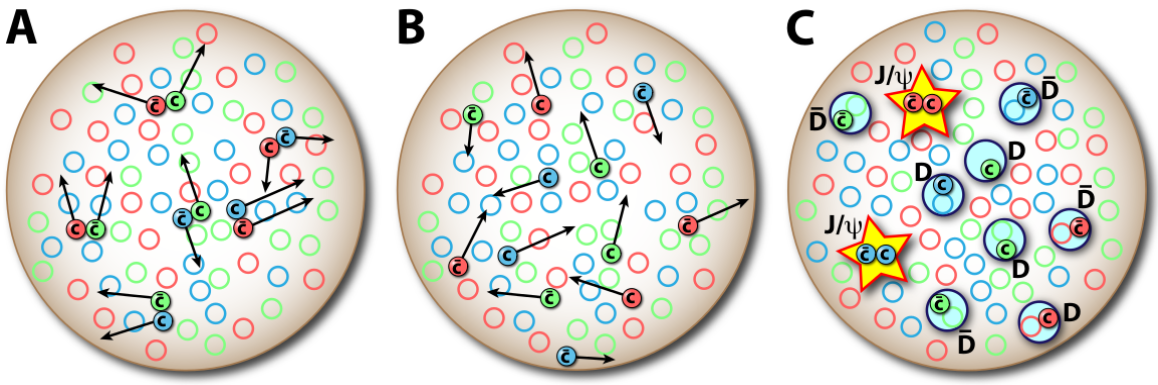

Figure 1.13: Sketch of the dissociation of correlated $c\bar{c}$ pairs (A), their diffusion (B) and the statistical production (C) of uncorrelated $c\bar{c}$ pairs in the QGP in heavy-ion collisions.

1.8 Kinematic variables

The transverse momentum (p_{T}), transverse mass (m_{T}), rapidity (y) and pseudo-rapidity (η) are the kinematic variables used frequently in the high energy experiments. These variables follow simple transformation rules under Lorentz transformation.

For a particle with 4-momentum $p^{\mu} = p^{\mu}(E, p_x, p_y, p_z)$ the kinematic variables are defined as:

- **Transverse momentum :**

$$p_{\mathrm{T}} = \sqrt{p_x^2 + p_y^2}$$

- **Transverse mass :**

$$m_{\mathrm{T}} = \sqrt{p_{\mathrm{T}}^2 + m^2}$$

- **Rapidity :** The rapidity of a particle is defined in terms of its energy E and

longitudinal momentum component p_z by,

$$y = \frac{1}{2} \ln \left(\frac{E + p_z}{E - p_z} \right). \tag{1.7}$$

It is a dimensionless quantity and it can be either positive or negative. In the nonrelativistic limit, the rapidity of a particle travelling in the longitudinal direction is equal to the velocity of the particle in units of the speed of light.

The rapidity variable depends on the frame of reference. It is not an Lorentz invariant quantity, but changes by an additive constant. If y_A and y_B represents the rapidity of a particle in two reference frames A and B, respectively, under Lorentz boost along the z-direction, they are related as,

$$y_A = y_B + y_\beta$$

Where,

$$y_\beta = \frac{1}{2} \ln \left(\frac{1 + \beta}{1 - \beta} \right)$$

with $\beta = v/c$.

- **Pseudorapidity :** In order to measure the rapidity, it is necessary to calculate E and p_z. In many experiments, it is only possible to measure the angle of the detected particle with respect to the beam axis. In that case, the kinematic properties of the particles are expressed in terms of pseudorapidity variables instead of rapidity, which is defined as,

$$\eta = -\ln \left[\tan \left(\frac{\theta}{2} \right) \right] = \frac{1}{2} \ln \left(\frac{|\vec{p}| + p_z}{|\vec{p}| - p_z} \right). \tag{1.8}$$

where, θ and $|\vec{p}|$ are the angle of particle trajectory with respect to beam axis and magnitude of momentum, respectively.

Using Eqn. 1.7 and 1.8 the rapidity y can be expressed in terms of pseudorapidity η as,

$$y = \frac{1}{2} \ln \left[\frac{\sqrt{p_{\mathrm{T}}^2 \cosh^2 \eta + m^2} + p_{\mathrm{T}} \sinh \eta}{\sqrt{p_{\mathrm{T}}^2 \cosh^2 \eta + m^2} - p_{\mathrm{T}} \sinh \eta} \right].$$

and vice-verse as,

$$\eta = \frac{1}{2} \ln \left[\frac{\sqrt{p_{\mathrm{T}}^2 \cosh^2 y + m^2} + p_{\mathrm{T}} \sinh y}{\sqrt{p_{\mathrm{T}}^2 \cosh^2 y + m^2} - p_{\mathrm{T}} \sinh y} \right].$$

If the particle have a distribution $dN/dydp_{\mathrm{T}}$ in terms of the rapidity variable y, then the distribution in terms of the pseudorapidity variable η is

$$\frac{dN}{d\eta dp_{\mathrm{T}}} = \sqrt{1 - \frac{m^2}{m_{\mathrm{T}}^2 \cosh^2 y}} \frac{dN}{dydp_{\mathrm{T}}}. \tag{1.9}$$

For a particle, if the momentum $|\vec{p}|$ is very large compared to its rest mass, then $|\vec{p}| \approx$ E. In that case from Eqn. 1.7 and 1.8 it is evident that $y \approx \eta$.

Center-of-mass energy

Consider a collision of two particles with 4-momentum,

$$P_1 = (E_1, \vec{p}_1), \qquad P_2 = (E_2, \vec{p}_2) \tag{1.10}$$

The center-of-mass (CMS) is defined by $\vec{p}_1 = -\vec{p}_2$

The Mandelstam varible s is defined as $s = (P_1 + P_2)^2$ and it is a Lorentz-invariant. The center-of-mass energy $\sqrt{s}$ is the total energy available in the CMS.

In centre-of-mass,

$$s = (P_1 + P_2)^2 = (E_1 + E_2)^2 - (\vec{p}_1 + \vec{p}_2)^2 = (E_1 + E_2)^2. \tag{1.11}$$

Also note that,

$$s = (E_1 + E_2)^2 - (\vec{p}_1 + \vec{p}_2)^2 = m_1^2 + m_2^2 + 2(E_1 E_2 - \vec{p}_1.\vec{p}_2). \tag{1.12}$$

With $m_1, m_2 \ll E_1, E_2$,

$$s \simeq 4E_1 E_2. \tag{1.13}$$

For the centre-of-mass energy of a collision of two different systems with charge Z_1, Z_2 and atomic numbers A_1, A_2, we have $E_1 = E.(Z_1/A_1)$ and $E_2 = E.(Z_2/A_2)$. Hence, $\sqrt{s} \simeq 2E\sqrt{\frac{Z_1 Z_2}{A_1 A_2}}$.

- **pp collisions :** for proton $A = Z = 1$. Hence $\sqrt{s} \simeq 2E$. If energy of the proton beam $E = 3.5$ TeV then $\sqrt{s} = 7$ TeV.
- **p-A collisions :** $\sqrt{s_{\rm NN}} \simeq 2E\sqrt{\frac{Z}{A}}$ (the subindex NN refers to the energy per nucleon inside the colliding nucleus). For p-Pb collisions at LHC, the energy of the proton beam was $E = 4$ TeV and for Pb, $Z = 82$ and $A = 208$. Hence $\sqrt{s_{\rm NN}} = 5.02$ TeV.
- **A-A collisions :** $\sqrt{s_{\rm NN}} \simeq 2E\frac{Z}{A}$. For Pb-Pb collisions at LHC, the energy of the proton beam was $E = 3.5$ TeV for Pb, $Z = 82$ and $A = 208$. Hence $\sqrt{s_{\rm NN}} = 2.76$ TeV.

Additionally, for non-symmetric systems such as p-A collisions there is a rapidity

shift

$$\Delta y \simeq 0.5 \ln \frac{Z_1 A_2}{Z_2 A_1} \tag{1.14}$$

due to the fact that the CMS frame of the p-A collision does not coincide with the laboratory frame. For p-Pb collisions at LHC the rapidity shift was $\Delta y_{\mathrm{NN}} = 0.465$.

Bibliography

[1] E.V. Shuryak. "Theory of Hadronic Plasma", Sov. Phys. JETP **47**, 212 (1978).

[2] `https://en.wikipedia.org/wiki/Standard_Model`

[3] M. E. Peskin et al. "An Introduction to Quantum Field Theory", Addison-Wesley Publishing Company, 1995.

[4] J. Beringer et al. "Review of Particle Physics", Phys. Rev. D **86**, Jul 2012.

[5] T. Hatsuda et al. "QCD phenomenology based on a chiral effective Lagrangian", Phys. Rep. **247**(5-6), 221-367 (1994).

[6] H. Satz. "Colour deconfinement and quarkonium binding", J. Phys. G **32**, R25 (2006).

[7] K. Aamodt et al. "Two-pion Bose-Einstein correlations in central Pb-Pb collisions at $\sqrt{s_{\mathrm{NN}}} = 2.76$ TeV", Phys. Lett. B **696**(4), 328-337 (2011).

[8] S. Jacobs et al. "Comparing the Schrodinger and spinless Salpeter equations for heavy-quark bound states", Phys. Rev. D **33**, 3338 (1986).

[9] H. Satz. "Charm and beauty in a hot environment", arXiv:hep-ph/0602245.

[10] C. Amsler et al. (Particle Data Group) "The Review of Particle Physics", Phys. Lett. B **667**, 1 (2008).

[11] J. Pumplin, D.R. Stump, J. Huston, H.L. Lai, Pavel M. Nadolsky, et al. "New generation of parton distributions with uncertainties from global QCD analysis". JHEP **0207**, 012 (2002).

[12] J.J. Aubert et al. "The ratio of the nucleon structure functions F_n^2 for iron and deuterium", Phys. Lett. B **123**, 275 (1983).

[13] M. Malek. "Low-x QCD at the LHC with the ALICE detector", arXiv:0911.1458, Nov 2009.

[14] L.V. Gribov, E.M. Levin, and M.G. Ryskin. "Semihard Processes in QCD", Phys. Rept. **100**, 1-150 (1983).

[15] Alfred H. Mueller and Jian-wei Qiu. "Gluon Recombination and Shadowing at Small Values of x", Nucl. Phys. **B268**, 427 (1986).

[16] Y. Q. Ma and R. Venugopalan, "Comprehensive Description of J/ψ Production in Proton-Proton Collisions at Collider Energies", Phys. Rev. Lett **113**, 192301 (2014).

[17] J. Adams et al. "Pion, kaon, proton and anti-proton transverse momentum distributions from p+p and d+Au collisions at $\sqrt{s_{\rm NN}} = 200$ GeV", Phys. Lett. B **616**(1-2), 8-16 (2005).

[18] C. Lourenco et al. "Energy dependence of J/ψ absorption in proton-nucleus collisions", JHEP **014**, 02 (2009), arXiv:0901.3054.

[19] R. Arnaldi et al. (NA60 Collaboration). "J/ψ production in proton-nucleus collisions at 158 and 400 GeV", arXiv:1004.5523.

[20] R. Arnaldi (NA60 Collaboration). "J/ψ production in p-A and A-A collisions at fixed target experiments", Nucl. Phys. **A830**, 345c (2009), arXiv:0907.5004.

[21] T. Matsui and H. Satz. "J/ψ Suppression by Quark-Gluon Plasma Formation", Phys. Lett. B **178**, 416 (1986).

[22] K. Yagi et al. "Quark-Gluon Plasma", Cambridge University Press (2005).

[23] H. Satz. "Charm and beauty in a hot environment", arXiv:hep-ph/0602245

[24] M. Asakawa et al. "J/ψ and η_c in the Deconfined Plasma from Lattice QCD", Phys. Rev. Lett. **92**, 012001 (2004).

[25] P. Braun-Munzinger et al. "Charmonium from Statistical Hadronization of Heavy Quarks - a Probe for Deconfinement in the Quark-Gluon Plasma", arXiv:0901.2500.

[26] A. Andronic et al. "Statistical hadronization of charm in heavy-ion collisions at SPS, RHIC and LHC", Phys. Lett. B **571**, 36 (2003).

[27] B. Abelev et al. (ALICE Collaboration), Phys. Lett. B **734**, 314 (2014).

Chapter 2

ALICE at the LHC

This thesis aims to probe the matter produced in ultra-relativistic collisions at the Large Hadron Collider (LHC) with the ALICE detector. In this chapter, a brief introduction of LHC have been given. Thereafter, the ALICE (A Large Ion Collider Experiment) detector is discussed with more emphasis on the detectors related to the analysis presented in this thesis. The second half of this chapter addresses the methods for the reconstruction of particle trajectories and tracks.

2.1 The Large Hadron Collider (LHC) at CERN

The LHC [1] at CERN [1] has been built in the circular tunnel with a circumference of 27 km and was previously used by the Large Electron Positron collider (LEP). It is located between 45 and 170 meters underground between Switzerland and France. It delivered the first proton-proton collisions at $\sqrt{s} = 900$ GeV on 23$^{\text{rd}}$ November, 2009 and it is now the most powerful accelerator ever

[1] CERN, the European Organization for Nuclear Research was founded in 1951 as a council named Conseil Européen pour la Recherche Nucléaire.

constructed. Like all other colliders, the LHC consists of acceleration cavities, bending magnets and two beam lines plus a large set of beam optics and diagnostics instruments. The two counter-rotating beams circulate in two separated pipes inside the same yoke of the superconducting dipole magnets and can intersect at eight points. Their field provides a Lorentz force $F_L = qvB$ matching the centrifugal force $F_C = mv^2/r$ of the accelerated particles. The magnetic field of 8.3 T and the collider radius of about 4.3 km leads to a proton-proton centre-of-mass collision energy of 14 TeV. The dipole magnets are cooled at the temperature of 1.9 K with super-fluid Helium at atmospheric pressure.

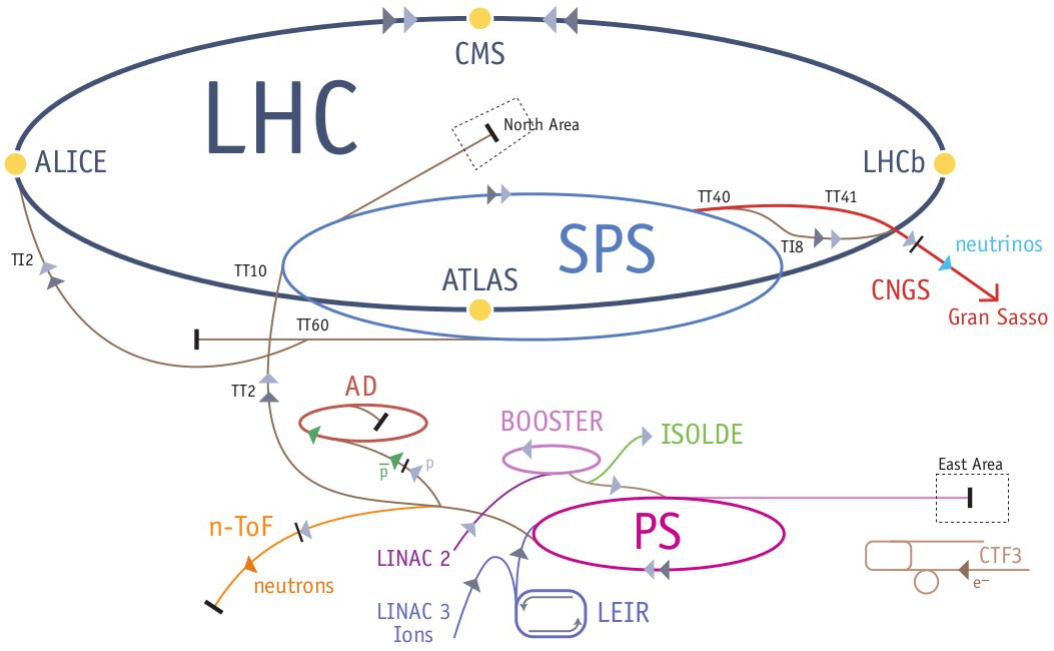

Figure 2.1: Schematic view of the CERN accelerator complex.

The whole accelerating chain is shown in Fig. 2.1. First, protons are accelerated inside the linear accelerator (LINAC) and the Proton Synchrotron Booster before they are injected in the Proton Synchrotron (PS), where they are accelerated up to a momentum of 25 GeV/c. Then protons are injected in the Super Proton Synchrotron (SPS), where protons reach the momentum of 450 GeV/c and are finally injected in

the LHC. The ions acceleration procedure is more complex, as it includes additional stripping and accumulation phases at the beginning of the chain. When the desired beam energy is reached, the two opposite directional beams are collided in four of the eight intersection points: ALICE [2], ATLAS [3], CMS [4] and LHCb [5]. The beam intensity goes down after several interactions and the interaction rates starts to decrease. This period is about 3 - 4 hours. At that point a new fill is prepared and injected into the collider.

The LHC has delivered pp collisions at energies $\sqrt{s}$ = 0.9, 2.36, 2.76, 7 and 8 TeV during the first period of operation (2009-2013). In order to investigate the hot nuclear matter effect in heavy-ion collisions, LHC also delivered two Pb-Pb collisions (around four weeks in 2010 and 2011) at energy $\sqrt{s_{\mathrm{NN}}}$ = 2.76 TeV. However there is also cold nuclear matter effects present in the heavy-ion collisions. In order to study these cold nuclear matter effects a p-Pb collisions at $\sqrt{s_{\mathrm{NN}}}$ = 5.02 TeV were provided by the LHC at the beginning of 2013. The different collision systems with integrated lumonisity deliverd to ALICE are listed in Table 2.1.

Year	System	Energy (TeV)	Running mode	Delivered Luminosity
2009	pp	0.9	MB	19.6 μb^{-1}
	pp	2.36	MB	0.87 μb^{-1}
2010	pp	0.9	MB	0.31 nb^{-1}
	pp	7	MB+rare (mixed)	0.5 pb^{-1}
	Pb-Pb	2.76	MB	9 μb^{-1}
2011	pp	2.76	rare	46 nb^{-1}
	pp	7	rare	4.9 pb^{-1}
	Pb-Pb	2.76	rare	146 μb^{-1}
2012	pp	8	MB rare	9.7 pb^{-1} (altogether)
	p-Pb	5.02	MB (pilot)	1.5 μb^{-1}
2013	p-Pb	5.02	MB rare	0.891 nb^{-1} 14 nb^{-1}
	Pb-p	5.02	rare	17.1 nb^{-1}
	pp	2.76	rare	129 nb^{-1}

Table 2.1: ALICE data taking in Run 1 (2009-2013).

2.2 A Large Ion Collider Experiment (ALICE)

The main goal of ALICE [2] is to study the properties of matter at extremely high temperatures and densities in ultra-relativistic proton-proton and heavy-ion collisions. In contrast to the other big experiments, ATLAS and CMS, its design has been optimized for high precision measurements in very high track densities (up to 8000 charged particles per rapidity unit at midrapidity) down to very low transverse momenta (of the order of 100 MeV/c).

The global coordinate system of ALICE is defined by a right-handed orthogonal cartesian system [6]. Its origin $x, y, z = 0$ is the beam interaction point (IP). The x axis is perpendicular to the mean beam direction at the IP, aligned with the local horizontal accelerator plane and pointing with positive values of x to the LHC ring center. The y axis is perpendicular to the x axis and the mean beam direction at

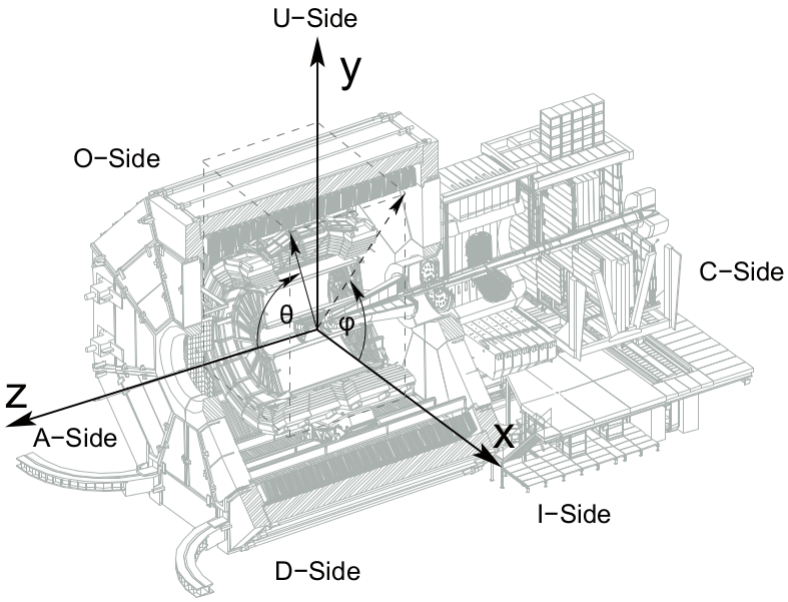

Figure 2.2: The ALICE global coordinate system.

the IP, pointing upwards. The z axis is parallel to the mean beam direction, with negative values of z in direction of the muon spectrometer. The ALICE coordinate system is shown in Fig. 2.2.

Furthermore, the directions from the IP, i.e. the detector sides, have been named A, C for positive and negative z, I and O at positive (inside the accelerator ring) and at negative x (outside the accelerator ring) and U and D at positive (upwards) and negative y (downwards).

The ALICE layout is shown in Fig. 2.3. The different detectors can be broadly group as: the central barrel detectors, the forward detectors and the the muon spectrometer. The analysis described in this thesis has been carried out using the data from the forward muon spectrometer. The other detectors involved in the analysis are: (i) Silicon Pixel Detector (SPD) of Inner Tracking System (ITS); (ii) the two V0 scintillator hodoscopes; (iii) the Zero Degree Calorimeter (ZDC). These detectors will be described in more details in the following sections.

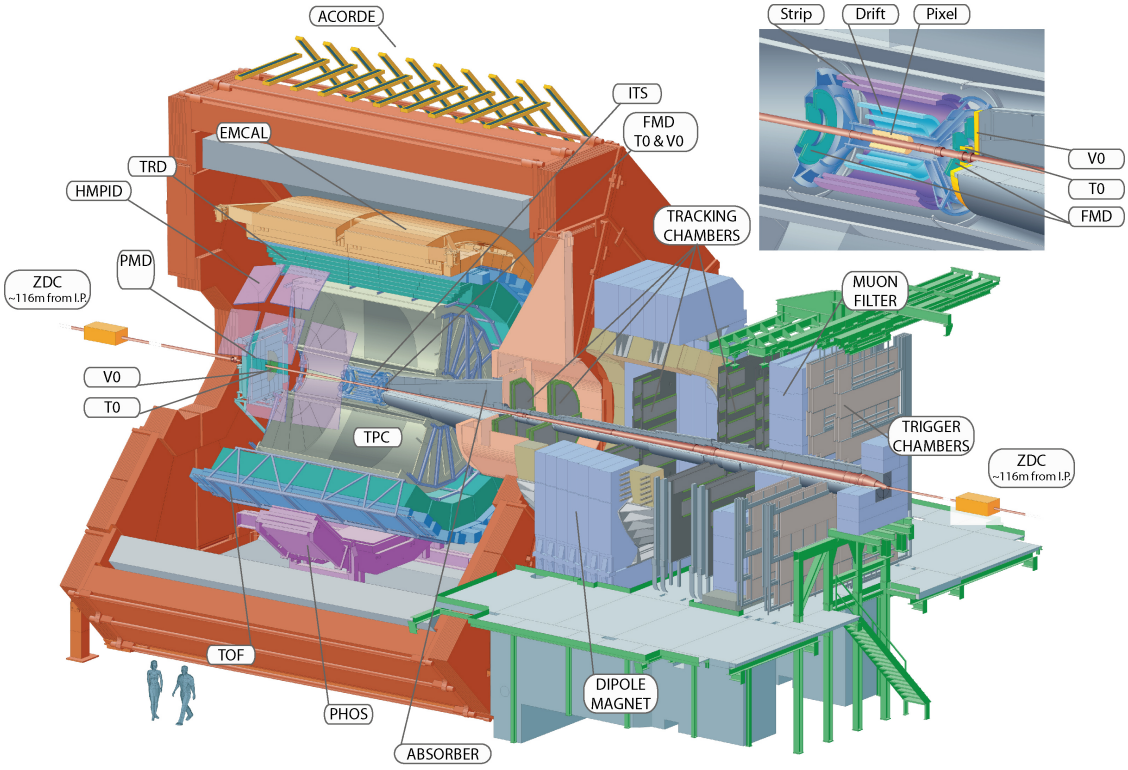

Figure 2.3: Schematic view of the ALICE experiment.

2.3 Central Barrel Detectors

The central barrel detectors are placed inside the L3 magnet and they cover a rapidity $-0.9 \leq \eta \leq 0.9$. These detectors are used in wide variety of measurements such as vertex reconstruction and particle identification and are dedicated detectors to study the matter produced in the central region after collision. The different central barrel detectors are shown in Fig. 2.3 and Fig. 2.4, listed below:

The detectors which detects the particles over full azimuth angle are,

- ITS : Inner Tracking System [7]
- TPC : Time Projection Chamber [8]
- TRD : Transition Radiation Detector [9]

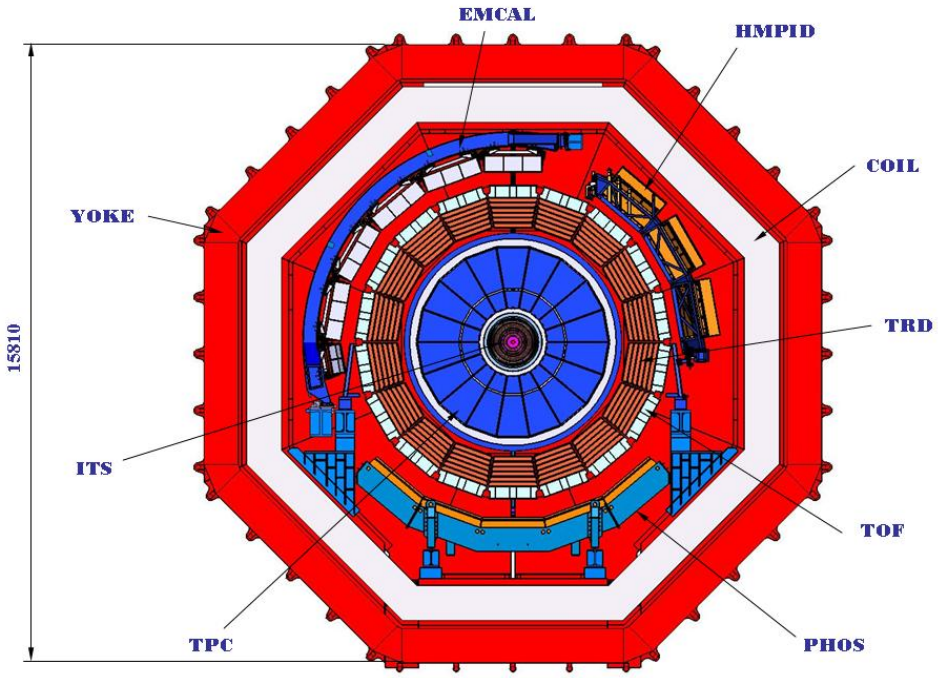

Figure 2.4: The front view of central barrel showing the layout of different detectors.

- TOF : Time of Flight [10]

  and the rest of the central barrel detectors covering partial azimuth angle are,

- PHOS : Photon Spectrometer ($|\eta| \leq 0.12$, $\Delta\varphi = 100°$) [11]

- EMCAL : Electromagnetic Calorimeter ($|\eta| \leq 0.7$, $60° \leq \varphi \leq 180°$) [12]

- HMPID : High-Momentum Particle Identification Detector ($|\eta| \leq 0.6$, $\Delta\varphi = 57.61°$) [13]

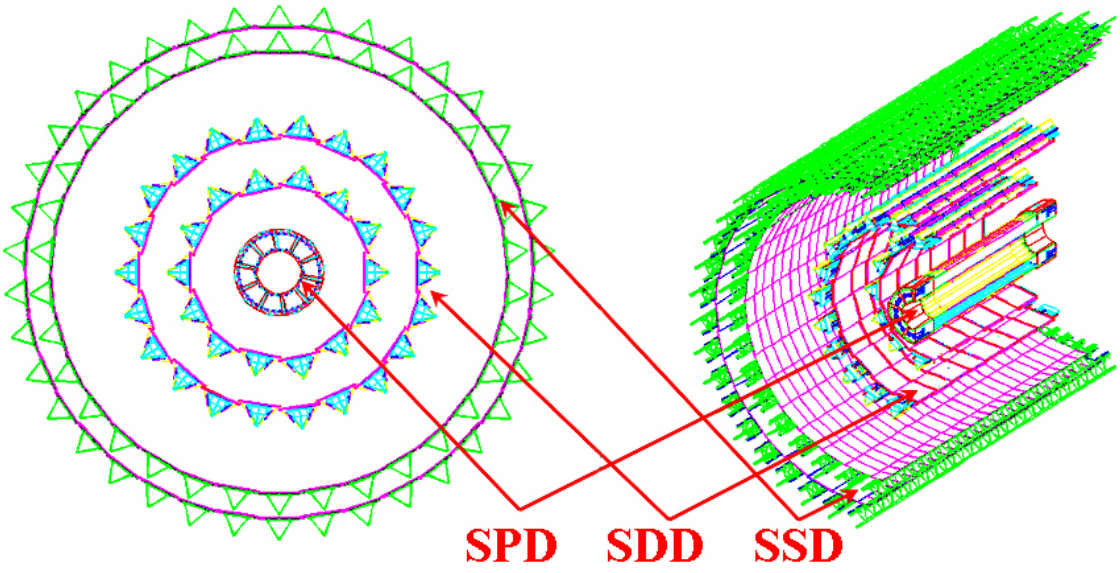

Figure 2.5: Layout of the Inner Tracking System (ITS).

2.3.1 Silicon Pixel Detector (SPD) of ITS

The ITS, shown in Fig. 2.5, is the closest detector to the interaction point. It has inner diameter of 8 cm and outer diameter of 86 cm and covers an acceptance of $|\eta| \leq 1.98$. It consists of six cylindrical layers of silicon detectors, located at radii, $r =$ 3.9, 7.6, 15.0, 23.9, 38.0 and 43.0 cm. The six layers of ITS are grouped in three pairs, which form three different detectors systems. The innermost two layers are silicon pixel detectors and therefore it is called Silicon Pixel Detector (SPD). It can handle up to 80 particles per cm^2 and it can run at higher rate (about 1 kHz) to provide the vertex information for events triggered by the Forward Muon Spectrometer.

Parameter	Silicon Pixel Detector
Spatial precision rφ (μm)	12
Spatial precision z (μm)	100
Two track resolution rφ (μm)	100
Two track resolution z (μm)	850
Total number of readout channels (k)	9 835
Total number of cells (M)	9.84
Average occupancy (inner layer) (%)	2.1
Average occupancy (outer layer) (%)	0.6

Table 2.2: Parameters of the Silicon Pixel Detector [7]

2.4 Forward Detectors

The ALICE forward detectors are generally used for the centrality determination in AA collision and the calculation of the total multiplicity of the produced particles in pp, pA and AA collisions. These measurements of the centrality and multiplicity is useful to understand the global characteristic of the event. The following are forward detectors:

- FMD: Forward Multiplicity Detector [14]
- V0: VZERO detector [14]
- T0: TZERO Detector [14]
- PMD: Photon Multiplicity Detector [15]
- ZDC: Zero Degree Calorimeter [16]
- ACORDE: ALICE Cosmic Ray Detector

2.4.1 V0 Detector

The V0 detector [14] is a small angle detector consisting of two arrays of scintillator counters, called V0A and V0C, located asymmetrically on each side of the interaction point. It provides the L0 (zeroth level) trigger for ALICE. The V0A is located 340 cm from the vertex on the side opposite to the muon spectrometer and the V0C is fixed at the front face of the front absorber, 90 cm from the vertex. They cover the pseudorapidity ranges $2.8 < \eta < 5.1$ (V0A) and $-3.7 < \eta < -1.7$ (V0C)

The V0A/V0C are segmented (Table 2.3, Fig. 2.6) into 32 elementary counters distributed in four rings and the rings are divided into 8 sectors of 45°. Each ring covers 0.4–0.6 unit of pseudo-rapidity. The elementary counter consists of scintillator material with embedded Wave-Length Shifting (WLS) fibres. The light from the WLS is collected by optical fibre and transported to PhotoMultiplier (PM) installed at 3–5 m from the detectors, inside the L3 magnet. The time resolution of each individual counter is better than 1 ns.

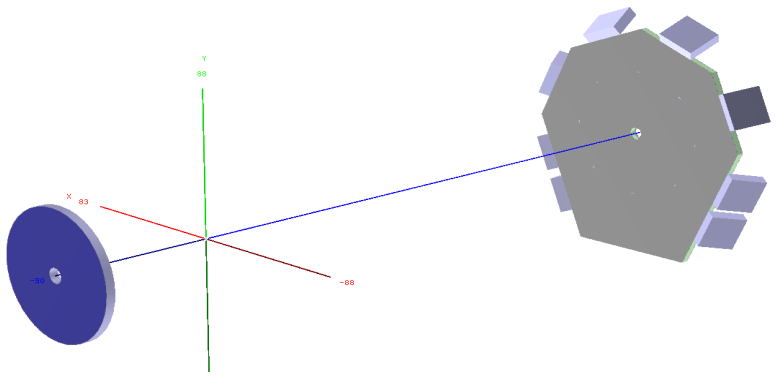

Figure 2.6: The V0 detector setup. The detector in the left side and the right side of the figure are, V0C and V0A, respectively.

The V0 detector has several functions. It provides:

- a minimum bias trigger for the central barrel detectors.

Ring	V0A		V0C	
	η_{max}/η_{min}	$\theta_{min}/\theta_{max}$	η_{max}/η_{min}	$(\pi-\theta)_{min}/(\pi-\theta)_{max}$
1	5.1/4.5	0.7/1.3	$-3.7/-3.2$	2.8/4.7
2	4.5/3.9	1.3/2.3	$-3.2/-2.7$	4.7/7.7
3	3.9/3.4	2.3/3.8	$-2.7/-2.2$	7.7/12.5
4	3.4/2.8	3.8/6.9	$-2.2/-1.7$	12.5/20.1

Table 2.3: V0A and V0C arrays. Pseudo-rapidity coverage and angular acceptance (in degrees) of the rings.

- two centrality triggers in Pb-Pb collisions.
- charged particle multiplicity, thus resulting in a centrality indicator.
- an estimate of the luminosity.
- a validation signal for the muon trigger.

2.4.2 Zero Degree Calorimeter (ZDC)

The ZDCs are placed at 112.5 m on either sides of the interaction point (IP). The ZDC system includes two small electromagnetic calorimeters (ZEM) which are located at about 7 m from the IP, on both sides of the LHC beam pipe, opposite to the muon arm. This ZEM allow to resolve ambiguities in the determination of the centrality. Each ZDC set is made up of two distint detectors. One for spectator neutrons (ZN) which is placed between the beam pipes at 0° relative to the LHC axis and its the transverse dimensions have to be smaller than 7 cm, requiring a very dense passive material (tungsten). Another for spectator protons (ZP) which is placed externally to the outgoing beam pipe on the side where positive particles are deflected. Since the stringent space constraints do not hold for ZP, it is made with a less dense material. The ZN which is segmented in four regions can also provide an estimation of the reaction plane.

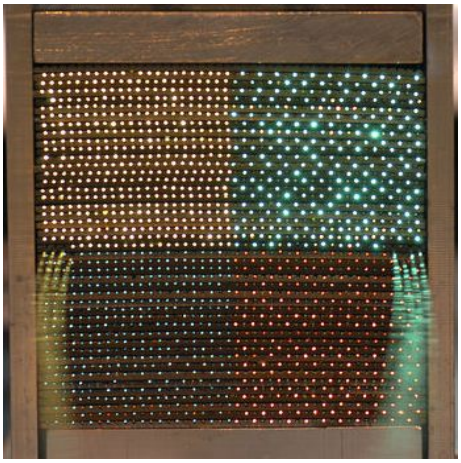

(a) The ZDC front-view shows the lights through the quartz fibres

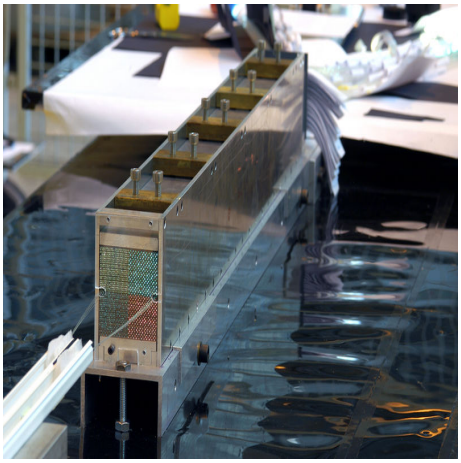

(b) A ZDC module in the laboratory

Figure 2.7: The figure shows the front view(left) and side view(right) of a Zero-Degree Calorimeters(ZDC) module

The quartz fibre calorimetry technique has been adopted for the ALICE ZDC. ZDC provide a centrality estimation and trigger in Pb–Pb collisions by measuring the energy carried in the forward direction (at zero degrees with respect to the beam direction) by noninteracting nucleons. The ZDCs cannot provide a Level-0 (L0) trigger, since they are located too far from the interaction point, but they can provide the essential Level-1 (L1) trigger for centrality. The ZEM is made of lead and quartz fibers and it is designed to measure the energy of particles mostly photons generated from π^0 decays at forward rapidities ($4.8 < \eta < 5.7$). Unlike in the ZN and ZP, the ZEM fibres are oriented at 45°. This choice maximizes the detector response. The ZDC is shown in the Fig. 2.7 and the main design features of ZDC are listed in table 2.4 .

	ZN	ZP
Dimensions (cm^3)	$7.04 \times 7.04 \times 100$	$12 \times 22.4 \times 150$
Absorber	tungsten alloy	brass
$\rho_{absorber}$ (g cm^{-3})	17.61	8.48
Fibre core diameter (μm)	365	550
Fibre spacing (mm)	1.6	4
Filling ratio	1/22	1/65

Table 2.4: Dimensions and main characteristics of absorber and quartz fibres for neutron and proton calorimeters.

2.5 The Forward Muon Spectrometer

The central interest of Muon Spectrometer [17] of ALICE is to study the properties of the charmonium (J/ψ and ψ(2S)), bottomonium (Υ resonances), low mass vector mesons (ρ and ϕ), open heavy-flavours (D and B families) and weak bosons (Z, $W\pm$) through their muon decay channel in pp, p-A and A-A collisions at LHC energies at forward rapidity $2.5 < y < 4$ and in a wide range of transverse momentum down to $p_{\mathrm{T}} = 0$ GeV/c. The Muon Spectrometer is the only LHC detector capable of quarkonium measurements at forward rapidity and down to $p_{\mathrm{T}} = 0$ GeV/c in A-A collisions. In order to resolve the different resonances, the spectrometer needs a mass resolution of 70 MeV/c^2 in the J/ψ mass region and 100 MeV/c^2 in the Υ mass region. The capability to measure charm and beauty particles in the forward rapidity makes it possible to access the momentum fraction regime down to $x \sim 10^{-6}$ [18].

The spectrometer is situated from $\sim$ 90 cm to $\sim$ 1720 cm along the negative z-direction, according to the ALICE co-ordinate system as shown in Fig. 2.2 and it has polar and azimuthal coverage of $172^\circ < \theta < 178^\circ$ ($4.0 < \eta < 2.5$) and 2π, respectively.

The layout of the muon spectrometer is shown in the Fig. 2.8. It is consists of the following components:

- Front Absorber

- Dipole Magnet
- Tracking Stations
- Muon Filter
- Trigger Stations
- Beam Shield

The present thesis utilizes the data from the muon spectrometer. Thus, it is described in details in the following section.

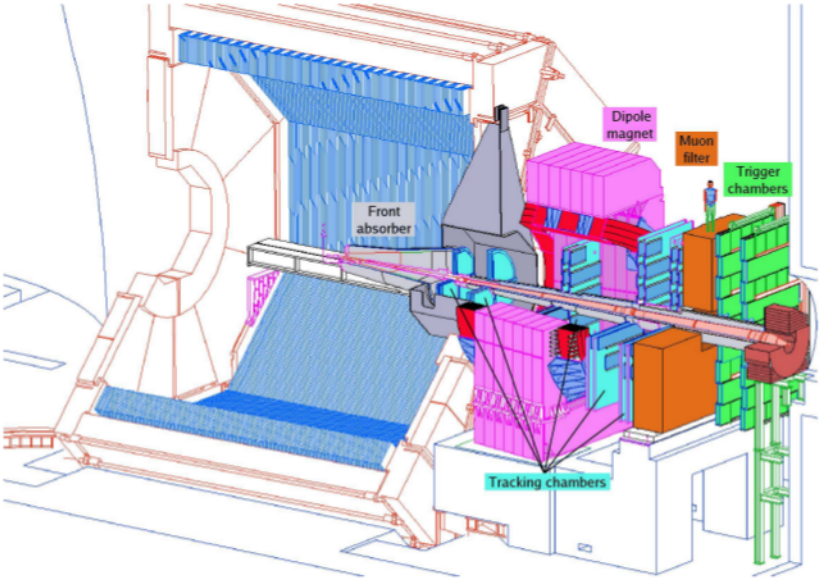

Figure 2.8: The layout of the ALICE Forward Muon Spectrometer [17, 19].

2.5.1 Front Absorber

The front absorber is located, inside the L3 magnet, at 90 cm from the IP. It has a total length of 4.13 m (corresponding to $\sim$ 10 radiation lengths) and it is made out of carbon, concrete and steel with a conical geometry as shown in Fig. 2.9.

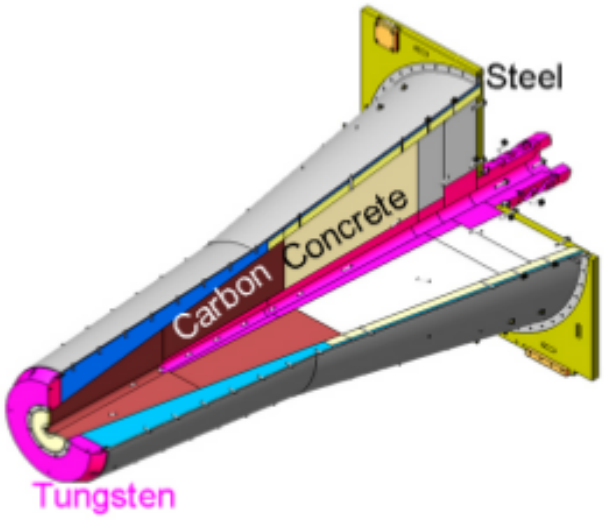

Figure 2.9: The Front Absorber of ALICE.

It is designed to limit multiple scattering and energy loss by traversing muons. In addition it also protects other ALICE detectors from secondary particles produced within the absorbing material [20]. It reduces the forward flux of primary hadrons from nucleus-nucleus collisions by at least two orders of magnitude and decreases the decay muon background by limiting the free path for primary π, $K \rightarrow \mu$ decay. It is covered by a 10 mm layer of tungsten at the front end of the cone (close to ITS) and in the sector between 10.5° and 12.5° where it faces TPC. Most of the low energetic electrons created inside the absorber, are absorbed by a tungsten cover of 100 mm thickness at the back end. To improve the shielding against particles from the beam pipe, an additional ring of 100 mm of tungsten is added to the 2° cone. Finally, to stop slow neutrons, three layers of polyethylene are placed at the end of the absorber.

During the course of this thesis work, I had carried out a study of the effects of the Front Absorber on the mass resolution of J/ψ and Υ resonances. This has been included in Appendix A.

2.5.2 Dipole Magnet

Figure 2.10: The Dipole Magnet after the first assembly.

The Dipole magnet [Fig. 2.10] is placed about 10 m away from the IP. It houses the third Muon Tracking station and provides the bending power to measure the muon momenta by muon tracking detectors. The general concept of the magnet is based on a window-frame return yoke, fabricated from low-carbon steel sheets. It is the world's largest warm dipole magnet of 850 tons (5 m in length, 7 m in width and 9 m in height) [21] with a nominal field of 0.7 T and a field integral of 3 Tm along beam axis. The magnet is also used as a support for the front absorber and beam shield. An additional radial space of 10 cm to 15 cm is provided to house the support frames of the Muon Tracking chambers inside the magnet. The dipole has an angular acceptance of $171^\circ < \theta < 178^\circ$ and is designed to provide a horizontal magnetic field perpendicular to the beam axis. The field polarity can be reverted within a short time.

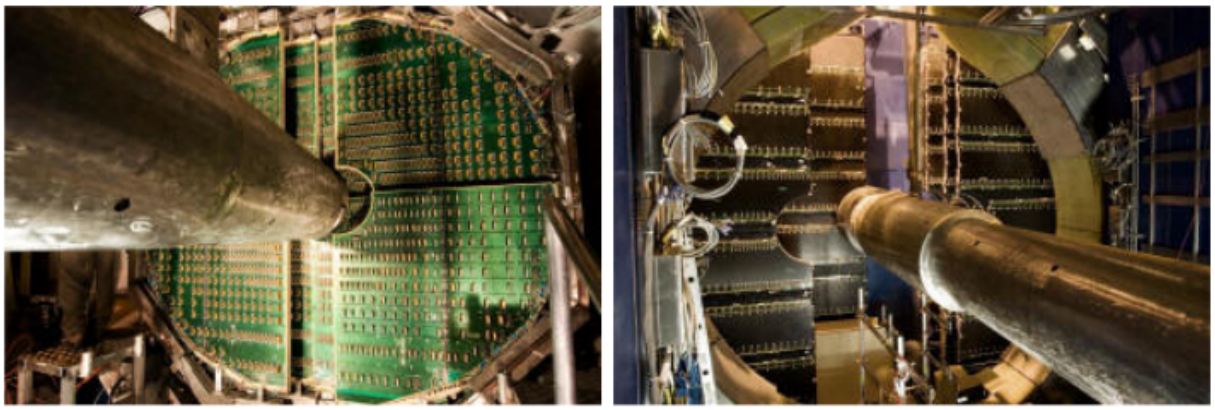

Figure 2.11: The picture of Tracking Stations of ALICE.

2.5.3 Tracking Stations

The tracking detector system of Muon Spectrometer is located at $\sim$ 5 m from the IP and it is about 10 m long. It has five stations and each station is composed of two tracking chambers, so, in all there are ten tracking chambers. The third station is situated inside the dipole magnet and on each side of the dipole magnet there are two stations as shown in Fig. 2.8 and Fig. 2.11. The second tracking station, shown on the left panel of Fig. 2.11, is indegeneously built in India. In central Pb-Pb collisions, a few hundred particles are expected to hit the muon chambers, with a maximum hit density of about 5×10^2 cm^{-2}. Moreover, the tracking system has to cover a total area of about 100 m^2. The basic design criteria of dimuon tracking chamber is to cope with such particle flux in the forward direction and to achieve a spatial resolution of about 100 μm to distinguish the members of the resonance family. Both of the conditions are found to be satisfied by Cathode Pad Chambers (CPC). Therefore, the tracking detectors are made up of segmented Cathode with anode wires in between and are operated following the principle of Multiwire Proportional Counters (MWPC) with gas mixture of Ar/CO_2 (80%/20%).

The basic geometry of CPC is shown Fig. 2.12, in which both the cathode planes are divided into sensitive pads, which are used to determine the position of particle traversing the detector. As the charge particle passes through the active gas volume of the detector, it produces ionization along its trajectories and avalanche take place when the primary electrons drift towards the nearest anode wire. The pads of specific geometric shape are used to sample the charge induced on the cathode planes. The relative values of the induced charges and the absolute positions of the pads in a charge cluster are used to determine the position of the charged particle passing through the detector.

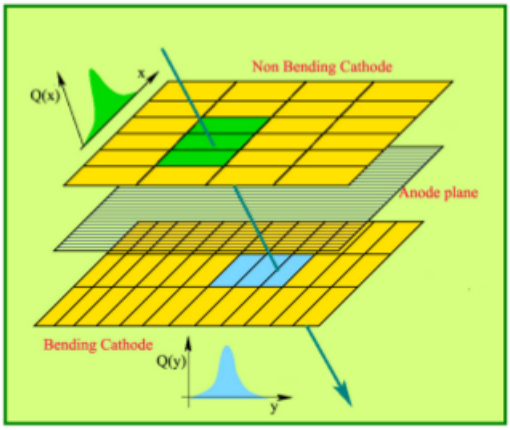

Figure 2.12: The basic working principle of cathode pad chamber.

In order to keep the number of overlapping clusters to be less than 1%, the pad occupancy should be kept below 5%. Thus a large segmentation of the readout pads is needed. For instance, pads as small as 4.2×6 mm^2 are needed for the region of the first station close to the beam pipe, where highest charged particle multiplicity is expected. Since the hit density decreases with the distance from the beam, larger pads are used at larger radii. This optimization helps to keep the total number of channels to about 1 million.

Multiple scattering of the muons in the chambers is minimised by keeping the

material budget less than 3% of the radiation length. Because of the different size of the stations, (ranging from few square metres for station 1 to more than 30 m^2 for station 5) two different designs have been adopted. The first two stations have a quadrant structure, with the readout electronics distributed on their surface. For the other stations, a slat architecture has been chosen. The maximum size of a slat is 40×280 cm^2 and the electronics is implemented on the top and bottom sides of the slats. Thus, the slats have been overlapped to avoid dead zones on the detector.

A sophisticated system of optical lines inspired by the RASNIK concept, monitors continuously the position of the tracking chambers. The main components of each optical line are a IR LED, a lens and a CCD or CMOS camera. The relative positions of the different chambers are monitored with an accuracy better than 20 μm by means of about 100 optical lines, while 160 lines are used to monitor the planarity of the chambers.

2.5.4 Muon Filter

The Muon Filter is a $5.6 \times 5.6 \times 1.2$ m^3 cast iron wall placed at 15 m from the IP. It is located between the last tracking station and the first trigger station. It reduces the background on the trigger stations by absorbing the punch-through pions, hadrons and low momentum muons. The combined effect of the front absorber and muon filter prevents muons with momentum less than 4 GeV/c from reaching the trigger station and enhance the trigger chamber performance. The muon filter along with the dipole magnet is shown in Fig. 2.13.

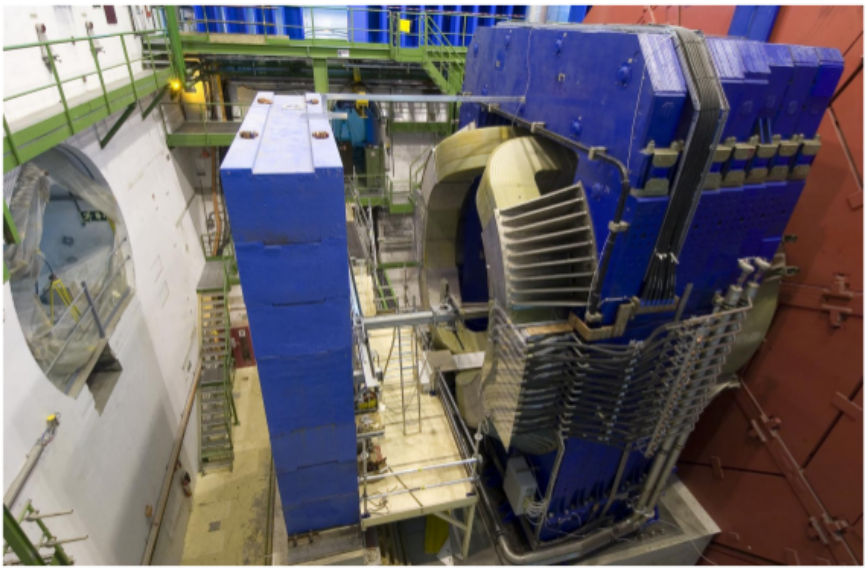

Figure 2.13: The picture of Muon Filter (left) and Dipole Magnet (right) of ALICE.

2.5.5 Trigger Stations

The trigger system has two stations (MT1 and MT2) and each station consists of two Resistive Plate Chamber (RPC) planes. The two stations are one metre apart from each other and placed behind the muon filter about 1600 cm and 1700 cm, respectively, from the IP. Each trigger station is made of two parallel detection planes of 18 single-gap RPCs separated by 15 cm, so that the total number of RPCs is 72. The active area covered by the first station and the second are 6.12×5.44 m^2 and 6.50×5.78 m^2, respectively.

The main motivation of the muon trigger system is to select unlike sign muon pairs from the decay of quarkonia resonances, single muons from heavy flavors and like sign muon pairs for combinatorial background studies. To reduce the probability of triggering on events where the low-p_{T} muons from π and K decays are not accompanied by the high-p_{T} ones (emitted in the decay of heavy quarkonia or in the semi-leptonic decay of open charm and beauty), a p_{T} cut has been applied at the

trigger level on each individual muon. A dimuon trigger signal is issued when at least two tracks above a predefined p_{T} threshold are detected in an event. To perform the p_{T} selection, a position-sensitive trigger detector with space resolution better than 1 cm has been designed which can issue trigger within a very short time interval ($\sim$ 600 ns). This is achieved by Resistive Plate Chambers (RPCs) operated in streamer mode.

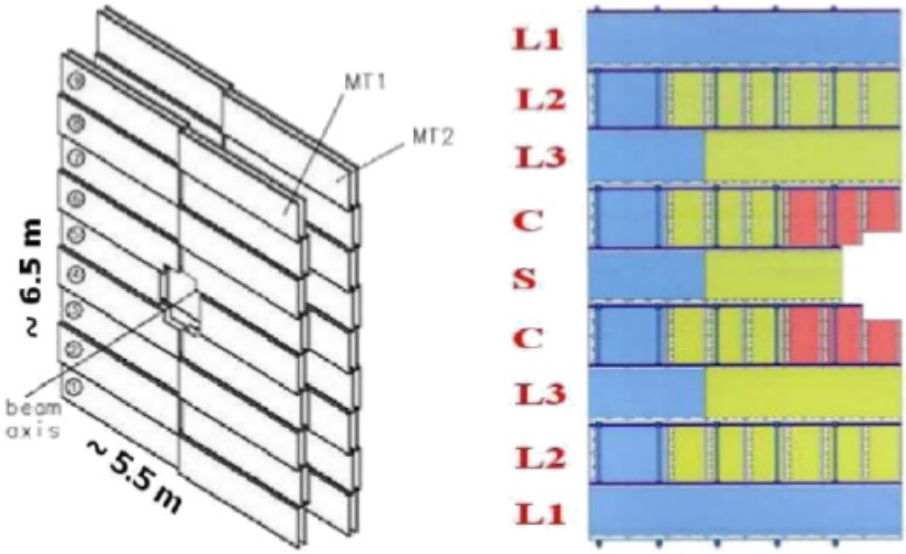

Figure 2.14: Layout of the ALICE Muon Trigger system. Different colours refer to the three strip widths.

A RPC is a planar geometry gaseous detector [Fig. 2.15], where the active gas material is flushed through the resistive electrode plates. High voltage is applied to the plate by means of a conducting layer coated on their outer surfaces. It is kept at a constant distance by plastic spacers placed inside the gas gap. The detector is filled with gas at atmospheric pressure, and kept in flow mode. The voltage required for operation is 4-5 kV/mm. When an ionising particle crosses the gas gap, the liberated electrons gives rise to a discharge on the anode, which are absorbed by organic gas and electronegative gases (Ar+$C_2H_2F_4$+isobuthane+SF_6 in a ratio 49:40:7:1). Since the duration of discharge ($\sim$ 10 ns) is much shorter than the relaxation time of the

electrodes, they behave as an insulator through out the whole discharge. The signal can be picked up by induction method using insulated conductive strips placed on the electrodes.

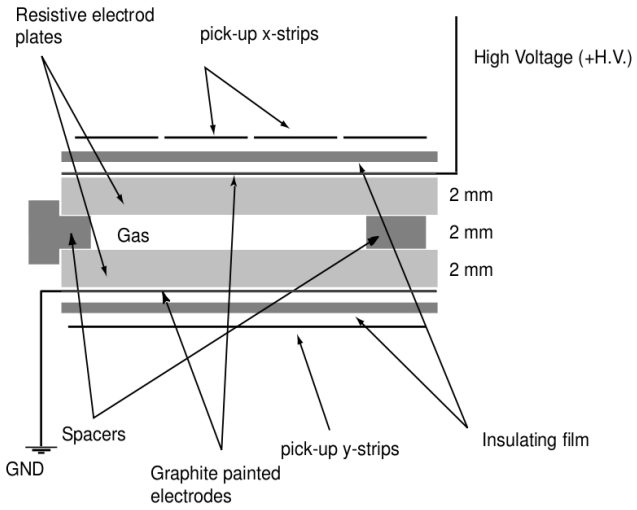

Figure 2.15: A schematic view of a Resistive Plate Chamber.

2.5.6 Beam Shield

The beam shield is used to stop the small angle particles and secondary ones emerging from the beam pipe. It is an absorber made of high Z tungsten-lead mixture embedded in a 4 cm thick stainless steel envelope, which surrounds the beam pipe along the Muon Spectrometer. Its shape follows the 178° acceptance line up to a maximum radius of 30 cm and then it stays constant.

2.6 Detector Readout

The tracking stations has front-end electronics which is based on a 16-channel chip (MANAS), which includes the following functionalities: charge amplifier, filter,

shaper and track & hold. This front end electronics for muon tracking were designed and produced in India. The channels of four such chips are fed into 12-bit ADCs which are read out by the MARC chip and includes zero suppression. This chain is mounted on front-end boards (MANUs). A total of 16,816 MANU cards are necessary to read the 1,076,224 channels of the tracking system. A maximum of 26 MANUs are connected (via PATCH bus) to the translator board which allows the data transfer to the Concentrator ReadOut Cluster Unit System (CROCUS). Each chamber is read out by two CROCUS, leading to a total number of 20 CROCUS. The main tasks of the CROCUS are to concentrate data from the chambers, to transport them to the DAQ and to perform control of the front-end electronics, including calibration and dispatching of the trigger signals. The data link that connects the top most readout element of the detector (i.e. CROCUS for dimuon tracking chambers) to the DAQ is called Detector Data Link (DDL). This scheme is shown in Fig. 2.16.

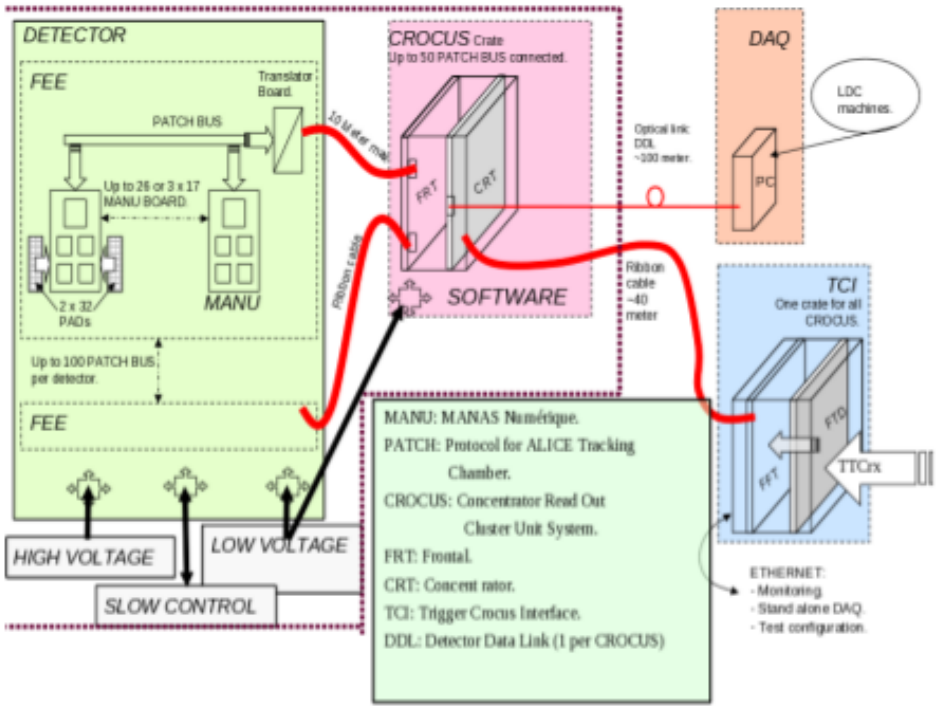

Figure 2.16: A schematic diagram for the detector readout of ALICE.

The dual-threshold front-end discriminators are used in the RPCs to adapt to the timing properties of the detector and reach the time resolution (1–2 ns) necessary for the identification of the bunch crossing. From the discriminators, the signals are sent to the trigger electronics (local trigger cards, based on programmable circuits working in pipeline mode) where the coordinates measured in the first and second stations are compared to determine the muon p_T. Due to the short decision time (600–700 ns) of the electronics, the dimuon trigger participates in the ALICE L0 trigger.

2.7 Online Control System

The data taking is supported by the Online Control System of ALICE. The various modeules of the data taking system are discussed below in brief:

2.7.1 Detector Control System (DCS)

The Detector Control System (DCS) [22] is developed by ALICE to control the detectors during data taking. It allows the shift crew to control the status of the detectors, check errors that can happen and have the possibility to recover possible failures in order to maximize the efficiency during data acquisition. In order to cope with a large variety of different subsystems and equipments, the DCS was designed to be flexible and modular, in order to give an easy environment to the sub-detector developers. The DCS configures, monitors and controls all the equipment in the experiment. It provides a graphical user interface that shows the state of the detectors and allows powering the various units controlling the detector.

2.7.2 Central Trigger Processor (CTP)

The Central Trigger Processor (CTP) [23] collects and processes the trigger signals from the participating detectors. Depending on the DAQ bandwidth and the physics requirements it can select events having different features and downscale the data taking rates. The aim of the ALICE trigger is to manage the detectors which are busy for different periods following a valid trigger and to perform trigger selection optimized for several different running conditions. The fastest trigger signal, called Level 0 (L0), arrives 1.2 μs after the collision. The input to the L0 trigger comes from the fast detectors, such as the SPD, V0, T0 and the Muon Trigger. These detectors are treated with a three states logic (asserted, not relevant and negated) combined together with logic AND and OR in order to select a certain class of events. The information of slower detectors is used to create a Level 1 trigger signal (L1) that is dispatched after 6.5 μs. The ALICE trigger system is provided with a past-future protection circuit that looks for other events of requested types in a time windows before and after the collision under investigation. It is expected to reject the pile-up events. The last level called Level 2 (L2), waits for the past-future protection and arrives after 88 μs. The CTP data are stored in the raw data stream and in dedicated scalers. In particular, there are scalers for all the inputs and for each trigger class that store the number of events passing each stage of the trigger (L0, L1, L2).

2.7.3 Data Acquisition System (DAQ)

The ALICE Data AcQusition system (DAQ) [22] was designed to handle large interaction rate and large amount of data (1.25 GB/s). Different clusters of detectors with different trigger rates can also be maintained by this DAQ. Once the CTP decides to acquire a particular event, the trigger signal is dispatched to the front-end

read-out electronics (FERO) of the involved detectors. The data are then injected in the Detector Data Link (DDL4) and sent to a farm of computers, called Local Data Concentrators (LDC), that build the event fragments from the front-end electronics into sub-events. The sub-events are then shipped through an event building network to the Global Data Collectors (GDC) that take all the sub-events from the various LDC, build the whole event and eventually send it to the storage facilities.

2.7.4 High Level Trigger (HLT)

The High Level Trigger (HLT) [24] can collect raw data from the LDC, to perform local pattern recognition, fast tracking and primary vertex localization, and to build up the global event. So, it can select interesting events as well as further reduce the data size. The trigger decision and the compressed data are sent back to the DAQ via the HLT DDL output. In order to fulfil these requirements the HLT consists of a farm of more than 1000 multi-processor computers. The HLT also has an online event display that allows visualizing the events and monitoring the goodness of the data taking.

2.7.5 Data Quality Monitoring (DQM)

The Data Quality Monitoring (DQM) [25] provides online feedback of the data being recorded to ensure the acquisition of high quality data. It typically involves the online collection of data samples, their analyses by userdefined algorithms and the visualization of the monitoring results. The final design of the DQM software framework of ALICE is AMORE (Automatic MOnitoRing Environment). This system is used to monitor the event data coming from the ALICE detectors. It allows operators and experts to access a view of monitoring elements and to detect potential

problems. Important features include the integration with the offline analysis and reconstruction framework, the interface with the electronic logbook that makes the monitoring results available everywhere through a web browser.

2.7.6 Detector Algorithms (DA)

The Detector Algorithms (DA) [26] provided by the detector teams allows to regularly measure the noise level and calibrate the readout electronics to reduce the systematic uncertainty to the maximum extent possible. Each DA grabs detector data (physics or calibration events) and produces results online. These results can be directly used (for example to configure the detector electronics or to give quality feedback to the DQM system) or shipped offline (to be processed and used in event reconstruction). A DA consists of a specific detector code to analyse events and to produce results according to a given calibration task, using a support library to interact with the external components (read configuration, grab events, log messages, export results, deal with the control system commands). There are two types of DA: the monitoring DA, which subscribe to events on the fly and the LDC DA, which analyse at the end of a run a locally recorded data file.

2.8 Offline Framework

The offline framework used by the ALICE community is a software called AliRoot. It can be used for simulation, reconstruction, detector alignment, calibration, visualization and data analysis. A short description of the ALICE offline framework is given below:

2.8.1 AliRoot

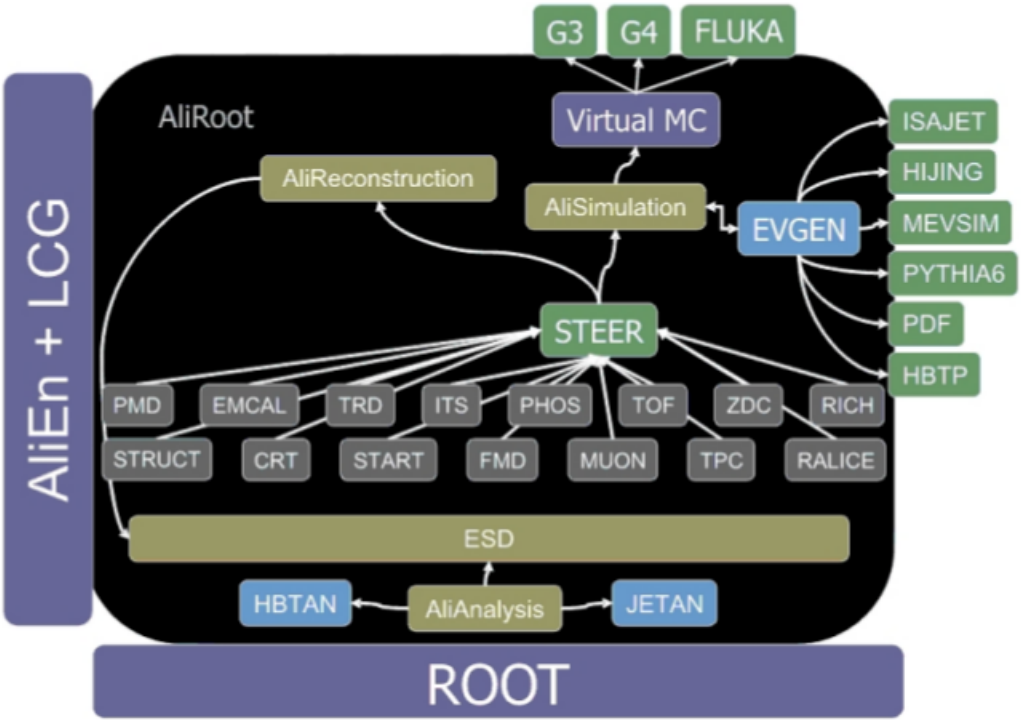

Figure 2.17: General scheme of the AliRoot architecture.

In 1998 the development of the ALICE offline project started by a software called AliRoot [27]. The AliRoot architecture is based on the ROOT [28] framework and it is designed to be extremely modular as shown in Fig. 2.17. This framework is completely based on the Object Oriented paradigm and it is entirely written in C++ with some makefiles for Fortran 90 to interface with GEANT. The STEER module provides steering, run management, interface classes and base classes. The detectors code is divided into independent modules which provide the syntax for simulation and reconstruction. The analysis code is continuously developed and progressively added to the framework. AliRoot is designed to easily interface with external Monte Carlo modules for the event generation and particle transport through the detector geometry.

Simulation: In AliRoot the main simulation class is the AliSimulation. It provides the the interface to event generators (such as PYTHIA [29] or HIJING [30]) and to geometry builder (as detectors alignment and magnetic field). Users can also force the particles to be produced and to decay in a particular acceptance region in order to speed up the processes and tune their kinematic parametrizations (basically y and p_T needed to get the phase space of the particles) in the cases they are known.

Particle Transport: The AliRoot provides different Monte Carlo packages (like GEANT3 [31], GEANT4 [32] and FLUKA [33]) to obtain the detector response for the simulated events. The geometry of ALICE detectors is built in these packages, including support structures, absorbers, shielding and beam pipe. The magnetic field of the solenoid and the warm dipole magnet can be described in the simulation as well. Ideal geometry is used as a default, but it is possible to work with a more reliable apparatus condition by retrieving the Offline Conditions Data Base objects (OCDB) which include real time pedestals, noisy or dead channels, HV values.

Reconstruction: The configuration of the reconstruction phase (for both the real data and Monte Carlo simulations) is provided by the class AliReconstruction. It gives the primary vertex reconstruction, track reconstruction and particle identification, secondary vertices reconstruction. The final output is an Event Summary Data (ESD), i.e. a ROOT file containing all the information relevant for physics analyses [27, 28]. During the reconstruction, specific processes such as the offline realignment of the tracking chambers are possible. The ESD could be further filtered for a more specific analysis and then stored in the Analysis Object Data (AOD) output files that are smaller in size and therefore results in faster access for the users. Furthermore, for the analysis presented in this work, the final stage of the filtering was the production of Muon Analysis Oriented Data (Muon AOD) which summarizes all necessary information required for physics with the Muon Spectrometer.

2.8.2 The GRID

The computing facility called Grid [34] was started in CERN to distribute the enormous amount of data produced by the LHC experiments around the world. The ALICE computing infrastructure, as those for the other LHC experiments, belongs to the program coordinated by the Worldwide LHC Computing Grid (WLCG). This infrastructure, based on the MONARC [35] model, is hierarchical and its levels are called Tiers. The real data from the experiment are stored in the very large computing center at CERN, the Tier-0, then data are replicated in regional large computing centers, called Tier-1 that also participate in the reconstruction and the storage of Monte Carlo data. The local computing centers, i.e. the resources of the participating institutes, are the Tier-2. Although with smaller data storage capabilities, they contribute with computing power for the user data analysis tasks and the Monte Carlo simulations. The lower levels of this infrastructure are the Tier-3 and Tier-4, local computing clusters of University departments and user's workstations. The interconnections between all these different facilities are possible thanks to the Grid Middleware. ALICE developed a set of Middleware services called AliEn [36]. Through the AliEn User Interface (the MonALISA [37] repository for ALICE), the user interacts with the Grid: after authentication, he can access and store files as in a Unix like system, send his tasks (jobs) for analysis or simulation purposes and monitor their execution. All the analysis presented in this thesis were carried out at SINP utilizing this GRID framework.

2.9 Future ALICE Upgrade Program

In order to improve the quality data and to collect data at higher interaction rates at the ALICE Collaboration is planning to upgrade the current detectors [38].

It is planned that after the second long shutdown in 2018, the LHC will progressively increase its luminosity with reaching an interaction rate of about 50 kHz, i.e. instantaneous luminosities of $L = 6{\times}10^{27}$ cm^{-2} s^{-1} in Pb-Pb collisions. The upgrade will include:

(i) new ITS with a factor of 3 higher resolution between a track and its primary vertex;

(ii) the replacement of TPC with Gas Electron Multiplier (GEM) detectors;

(iii) improvement of the readout electronics for TPC, TRD, TOF, EMCal and Muon Spectrometer for higher data taking rate;

(iv) new online systems (HLT, DAQ and CTP) for high data taking rates and increase the data mass storage to about 20 GB/s;

(v) the completion of EMCal for nearly 2π coverage.

(vi) to increase the secondary vertex reconstruction capabilities for the muon spectrometer, a Muon Forward Tracker (MFT) [39] has been approved.

Bibliography

[1] L. Evans and P. Bryant. "LHC Machine". JINST **3**, S08001 (2008).

[2] K. Aamodt et al. (ALICE Collaboration). "The ALICE experiment at the CERN LHC". JINST **3**, S08002 (2008).

[3] G. Aad et al. (ATLAS Collaboration). "The ATLAS Experiment at the CERN Large Hadron Collider". JINST **3**, S08003 (2008).

[4] S. Chatrchyan et al. (CMS Collaboration). "The CMS experiment at the CERN LHC". JINST **3**, S08004 (2008).

[5] A. Augusto Alves Jr et al. (LHCb Collaboration). "The LHCb Detector at the LHC". JINST **3**, S08005 (2008).

[6] L. Betev et al. "Definition of the ALICE coordinate system and basic rules for sub-detector components numbering". ALICE-INT, 2003-038 (2003).

[7] The ALICE Collaboration. "ITS Technical Design Report". CERN–LHCC, 99–12 (1999).

[8] The ALICE Collaboration. "TPC Technical Design Report". CERN–LHCC, 2000–001 (2000).

[9] The ALICE Collaboration. "TRD Technical Design Report". CERN–LHCC, 2001–021 (2001).

[10] The ALICE Collaboration. "TOF Technical Design Report". CERN–LHCC, 2000–012 (2000).

[11] The ALICE Collaboration. "PHOS Technical Design Report". CERN–LHCC, 99–4 (1999).

[12] The ALICE Collaboration. "EMCAL Technical Design Report". CERN–LHCC, 2006–014 (2006).

[13] The ALICE Collaboration. "HMPID Technical Design Report". CERN–LHCC, 98–19 (1998).

[14] The ALICE Collaboration. "Forward Detectors: FMD, T0 and V0 Technical Design Report". CERN–LHCC, 2004–25 (2004).

[15] The ALICE Collaboration. "PMD Technical Design Report". CERN–LHCC, 99–32 (1999).

[16] The ALICE Collaboration. "ZDC Technical Design Report". CERN–LHCC, 99–5 (1999).

[17] The ALICE Collaboration. "The forward muon spectrometer". Addendum to the ALICE Technical Proposal. CERN–LHCC, 96–32 (1996).

[18] D. Das for the ALICE Collaboration. "Performance and First Physics Results of the ALICE Muon Spectrometer". Nucl. Phys. **A862**, 223-230 (2011).

[19] The ALICE Collaboration. "ALICE dimuon forward spectrometer: addendum to the Technical Design Report". CERN–LHCC, 2000–46 (2000).

[20] S. Grigoryan. "Contribution of Secondary π/K Mesons, Produced in the Absorber, into the Dimuon Background in Pb–Pb Collisions". ALICE Internal Note, 2002–06 (2002).

[21] D. Swoboda. "ALICE Muon Arm Dipole Magnet". ALICE Internal Note, 1999–06 (1999).

[22] The ALICE Collaboration. "Trigger, Data Acquisition, High-Level Trigger and Control System Technical Design Report". CERN–LHCC, 2003–062 (2003).

[23] D. Evans et al. "The ALICE central trigger processor". CERN–LHCC, 2005–038 (2005).

[24] T. Alt et al. "The ALICE high level trigger". J. Phys. G **30**, S1097–S1100 (2004).

[25] A. Telesca et al. "The ALICE Data Quality Monitoring System". Real Time Conference (RT), 2010 17th IEEE-NPSS, May 2010.

[26] F. Carena et al. "Online processing in the ALICE DAQ, the Detector Algorithms". J. Phys. **219**, 022004 (2010).

[27] http://aliweb.cern.ch/Offline.

[28] http://root.cern.ch.

[29] S. Mrenna et al. "PYTHIA 6.4 Physics and Manual". JHEP **0605**, 026 (2006).

[30] M. Gyulassy et al. "HIJING 1.0: A Monte Carlo program for parton and particle production in high energy hadronic and nuclear collisions". Comp. Phys. Comm. **83**(2–3), 307–331 (1994).

[31] M. Goossens et al. "GEANT: Detector Description and Simulation Tool". CERN program library long write-up, W5013 (1994).

[32] S. Agostinelli et al. "Geant4 - a simulation toolkit". Nucl. Instrum. Meth. A **506**(3), 250–303 (2003).

[33] G. Battistoni et al. "Applications of FLUKA Monte Carlo code for nuclear and accelerator physics". Nucl. Instrum. Meth. B **269**(24), 2850–2856 (2011).

[34] I. Foster et al. Morgan Kaufmann Publishers, 1999.

[35] http://monarc.web.cern.ch/MONARC.

[36] http://alien2.cern.ch.

[37] http://monalisa.cern.ch/monalisa.html.

[38] K. Safarik. "Long-term plans of the ALICE Collaboration". Open Symposium – European Strategy Preparatory Group, Krakow 2012.

[39] The ALICE MFT Collaboration. "Letter of Intent: A Muon Forward Tracker for the ALICE Experiment".

Chapter 3

Experiment and data analysis

3.1 Data types

The LHC, in the first period of data taking (2009 − 2013), delivered three combinations of colliding beams namely, pp, p-Pb and Pb-Pb collisions. In this thesis, we have analysed the data for pp collisions at $\sqrt{s} = 7$ TeV, p-Pb collisions at $\sqrt{s_{\rm NN}} = 5.02$ TeV and Pb-Pb collisions at $\sqrt{s_{\rm NN}} = 2.76$ TeV.

3.2 Alignment

The mass resolution is primarily determined by the accuracy with which the Muon Tracking chambers can be aligned. The effects of gain dispersion of MANAS was found to be negligible compared to the alignment effects. It may be noted that all the data presented in this thesis have not been corrected for the electronic gain dispersion. This also indicates the success of MANAS chip as the front end electronics of Muon Tracking.

The chamber positions were measured after the installation with a precession of better than a millimetre through the technique of photogeometry [1]. Special runs without magnetic field have been periodically carried out at the beginning of every data taking period in order to improve the quality of the alignment. The straight tracks are used in an offline realignment, performed using the Millepede algorithm [2], thus estimating the residual misalignment for each detection element. All these corrections are then implemented in the muon track reconstruction phase.

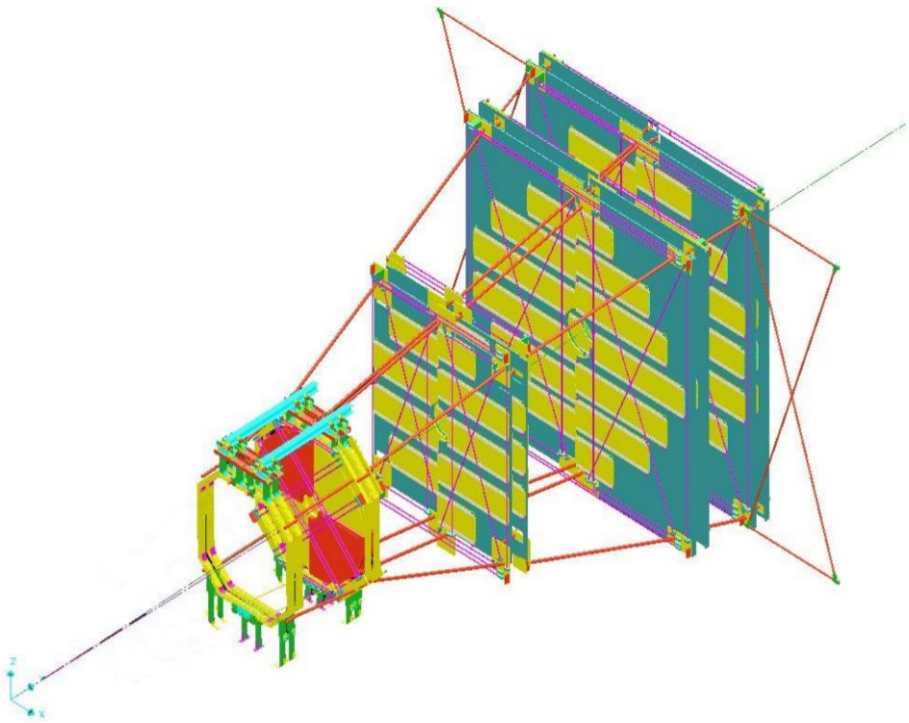

Figure 3.1: Geometry Monitoring System setup: the lines on this figure represent the optical lines.

However, these positions get modified by the magnetic field. In order to keep track of these displacements, an optical monitoring system was installed. The Geometry Monitoring System (GMS) is an array of about 460 optical sensors placed on the corners of each Muon Tracking chamber and in the ALICE cavern, as shown in Fig. 3.1.

This system monitors the relative position of two chambers of each station and between different stations, together with the flatness of the chambers and the absolute displacement of the entire Muon Spectrometer with respect to the ALICE cavern with a resolution of about 20 μm.

In the absence of this data, a new analysis class has been developed to align the chambers with online tracks. This method relies on the fact that an improvement in mass resolution implies better alignment.

3.3 Track reconstruction

Kalman Filter

The Kalman filter [3, 4] is a set of mathematical equations that provides an efficient computational (recursive) solution of the least-squares method. The tasks for charged-track reconstruction in experimental high-energy physics are pattern recognition (i.e. track finding) and track fitting. Experimentally, we observe hits on the ten tracking chambers due to the passage of charged particles through the spectrometer. The emarging pattern of a track is indentified by demanding at least one hit in each of the tracking station. The Kalman filtering method provides the technique to perform the pattern recognition and the track fitting simultaneously. The multiple scattering can be handled properly by this method too.

The algorithm starts from track candidates ("seeds"), for which vectors of initial parameters and covariance matrices are evaluated. Then each track is propagated to some surface (detector or intermediate point). The new covariance matrix can be obtained using the Jacobian matrix of the transformation, i.e. the matrix of derivatives of propagated track parameters with respect to current parameters.

If there is a new seed within a certain window around the extrapolated point with its vector of local measured parameters and covariance matrix it can be added to the track, and the Kalman filter updates the vector of parameters, covariance matrix and χ^2 value of the track.

Application to the Forward Muon Spectrometer

A Kalman track seed is created for all track segments found in detector stations 4 and 5. Tracks are parameterized as $(y, x, \alpha, \beta, q/p)$, where y is a coordinate in the bending plane, x is a non-bending coordinate, α is a track angle in the bending plane with respect to the beam line, β is an angle between the track and the bending plane, q and p are the track charge and momentum, respectively.

A track starting from a seed is followed to the station 1 or until it is lost (if no hits in a station are found for this track) according to the following procedure. It propagates the track from the current z-position to a hit with the nearest z-coordinate. Then for given z it looks for the hits within certain window around the transverse track position (the window is taken to be 4σ). After this there are two possibilities. The first one is to calculate the χ^2 contribution of each hit and consider the hit with the lowest contribution as belonging to the track. The second way is to use a so-called track branching and pick up all the hits inside the acceptance window. Efficiency and mass resolution tests have shown that the second way gives a better result and so is used in the current implementation.

Since the magnetic field is generally non-uniform, the Runge-Kutta algorithm is used for propagation of track parameters. Effect of the track chamber material is taken into account by adding a multiple scattering term to the track covariance matrix for each chamber traversed.

After propagation to the chamber 1 all tracks are sorted according to their quality, defined as

$$Quality = N_{hits} + \frac{\chi^2_{max} - \chi^2}{\chi^2_{max} + 1} \tag{3.1}$$

where χ^2_{max} is the maximum acceptable χ^2 of tracks. Then duplicated tracks are removed, where duplicated means having half or more of their hits shared with another track with a higher quality.

3.3.1 Method of the tracking efficiency calculation

The tracking algorithm described in the previous section, does not require a cluster in all the chambers to reconstruct a track. The minimum tracking conditions require one reconstructed cluster in each one of the first three stations and in three chambers of the last two stations. Assuming that the efficiency of one chamber is independent on the efficiency of the others, it is possible to exploit the redundancy between the detection planes to determine the efficiency of a given chamber.

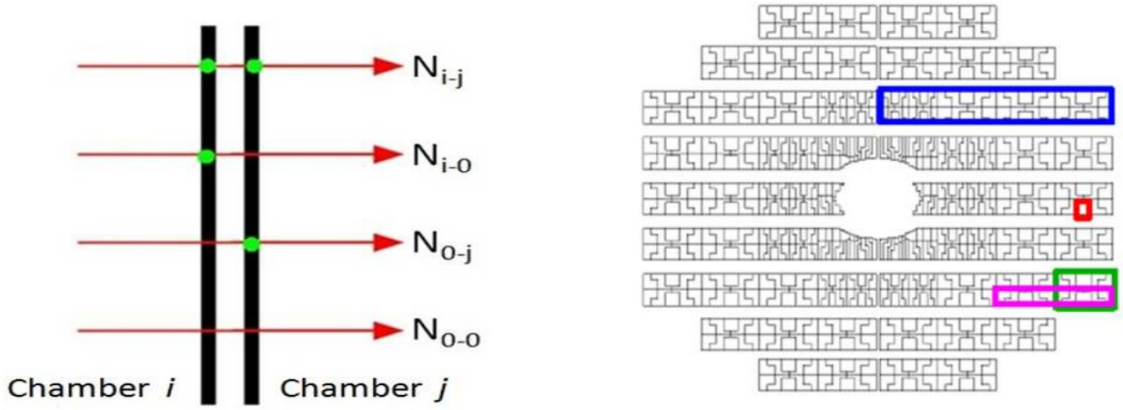

Figure 3.2: Left: possible configurations for a track going through a muon tracking station. Right: the different substructures of a tracking chambers are the Detection Elements (blue), Bus Patch (pink), PCB (green) and MANU (red).

Taking as example one of the first three stations, the reconstructed tracks can be classified into three categories: the ones with a cluster in both chambers (N_{i-j}), the ones with a cluster only in chamber i (N_{i-0}) and the ones with a cluster only in chamber j (N_{0-j}), as illustrated in the left plot of Fig. 3.2. The case N_{0-0} does not fulfil the tracking conditions so it can not be reconstructed. Considering that the efficiency of chamber i ($\varepsilon_{\mathrm{Ch}i}$) is independent of the one of chamber j ($\varepsilon_{\mathrm{Ch}j}$), it is possible to express N_{i-j}, N_{i-0} and N_{0-j} as a function of the total number of tracks crossing the station (N_{Tot}):

$$N_{i-j} = \varepsilon_{\mathrm{Ch}i}\varepsilon_{\mathrm{Ch}j}N_{\mathrm{Tot}} \tag{3.2}$$

$$N_{i-0} = \varepsilon_{\mathrm{Ch}i}(1-\varepsilon_{\mathrm{Ch}j})N_{\mathrm{Tot}} \tag{3.3}$$

$$N_{0-j} = (1-\varepsilon_{\mathrm{Ch}i})\varepsilon_{\mathrm{Ch}j}N_{\mathrm{Tot}} \tag{3.4}$$

with:

$$N_{\mathrm{Tot}} = N_{i-j} + N_{i-0} + N_{0-j} + N_{0-0} \tag{3.5}$$

Although the total number of tracks is unknown (N_{0-0} is not measured), if $\varepsilon_{\mathrm{Ch}i} = 0$ and $\varepsilon_{\mathrm{Ch}j} = 0$ it is then possible to combine the above equations to express $\varepsilon_{\mathrm{Ch}i}$ and $\varepsilon_{\mathrm{Ch}j}$ as a function of measurable quantities:

$$\varepsilon_{\mathrm{Ch}i} = \frac{N_{i-j}}{N_{i-j} + N_{0-j}}, \tag{3.6}$$

$$\varepsilon_{\mathrm{Ch}j} = \frac{N_{i-j}}{N_{i-j} + N_{i-0}}. \tag{3.7}$$

For the first three stations, the efficiency of one chamber can be obtained by using the reconstructed tracks for which the other chamber of the station responds, thus satisfying the tracking conditions irrespectively of the status of the chamber under study. Following the same recipe, it is possible to compute the efficiency of any of the last four chambers by using the tracks which contain a cluster in all of the three other chambers to fulfil the tracking conditions.

The error on the estimated efficiency of a chamber is computed considering a binomial distribution because in the previous equations the numerator (N_{Num}) is a subset of the denominator (N_{Den}):

$$\Delta\varepsilon_{\mathrm{Ch}i,j} = \frac{1}{N_{\mathrm{Den}}}\sqrt{N_{\mathrm{Num}}\left(1 - \frac{N_{\mathrm{Num}}}{N_{\mathrm{Den}}}\right)}. \tag{3.8}$$

However, when $N_{\mathrm{Num}} \approx 0$ or $N_{\mathrm{Num}} \approx N_{\mathrm{Den}}$ the binomial approach does not hold any more: efficiencies, within the uncertainties, could become inferior to zero or superior to 1. It is then necessary to employ asymmetric error ranges to avoid unphysical results: never lower than 0% nor greater than 100% [5].

The same procedure applies to measure the efficiency of only a part of a chamber like a Detection Element (DE) for instance (see right plot of Fig 3.2). As mentioned before, it is enough to count the number of tracks detected or expected to be detected in that particular element, with the same conditions on the other chambers to fulfil the tracking criteria.

The efficiency of a station is estimated according to the tracking reconstruction algorithm, that demands at least one cluster in each one of the first three stations, so

for $m \in (1, 2, 3)$:

$$\varepsilon_{\mathrm{St}m} = \varepsilon_{\mathrm{Ch}i} + \varepsilon_{\mathrm{Ch}j} - \varepsilon_{\mathrm{Ch}i}\varepsilon_{\mathrm{Ch}j}, \tag{3.9}$$

this is, the sum of efficiencies for each chamber in the station minus the combination. For the last two stations, due to the requirement of at least three clusters among the four chambers, the efficiency is computed as a single one:

$$\begin{aligned}\varepsilon_{\mathrm{St4-5}} = \varepsilon_{\mathrm{Ch7}}\varepsilon_{\mathrm{Ch8}}\varepsilon_{\mathrm{Ch9}}\varepsilon_{\mathrm{Ch10}} + (1-\varepsilon_{\mathrm{Ch7}})\varepsilon_{\mathrm{Ch8}}\varepsilon_{\mathrm{Ch9}}\varepsilon_{\mathrm{Ch10}} \\ +\varepsilon_{\mathrm{Ch7}}(1-\varepsilon_{\mathrm{Ch8}})\varepsilon_{\mathrm{Ch9}}\varepsilon_{\mathrm{Ch10}} + \varepsilon_{\mathrm{Ch7}}\varepsilon_{\mathrm{Ch8}}(1-\varepsilon_{\mathrm{Ch9}})\varepsilon_{\mathrm{Ch10}} \\ +\varepsilon_{\mathrm{Ch7}}\varepsilon_{\mathrm{Ch8}}\varepsilon_{\mathrm{Ch9}}(1-\varepsilon_{\mathrm{Ch10}}).\end{aligned} \tag{3.10}$$

The total tracking efficiency is then given by the following expression:

$$\varepsilon_{\mathrm{Tracking}} = \varepsilon_{\mathrm{St1}}\varepsilon_{\mathrm{St2}}\varepsilon_{\mathrm{St3}}\varepsilon_{\mathrm{St4-5}}. \tag{3.11}$$

In reality, the tracking efficiency measured with this method is biased because the efficiency can vary between different parts of a chamber. But due to the limited statistic in each run, we can only measure the average efficiency per chamber. The direct consequence is that we loose possible local correlations between the chambers when combining the efficiency measurements using equations 3.9, 3.10 and 3.11. The indirect effect is that the spatial distribution of the tracks that can be used in equations 3.6 and 3.7 to measure the average efficiency of one chamber is modified by the local variation of the efficiency of the others, thus affecting the measurement itself (assuming the efficiency of this chamber is also not uniform). These two effects can lead to either an overestimation or an underestimation of the tracking efficiency. As a result, we can not use this method to measure the absolute efficiency of the spectrometer. Nevertheless, since the biases are the same in data and simulations,

we can use the differences of the efficiency measurements performed in both cases to control the realism of these simulations. This comparison allowed us to identify the discrepancies that we have then been able to correct for by rejecting the faulty parts, both in data and simulations. Furthermore, when the remaining differences are small, they give a good estimate of the magnitude of the remaining discrepancies between data and simulations and can then be used to assess the corresponding systematic uncertainties. There is one exception to this: when two dead areas appear in front of each other in the two chambers of a station. In this case none of the tracks in this region can be reconstructed and used to compute the efficiency loss in any of the chambers. As a result the measured tracking efficiency is (almost) not affected, while the true tracking efficiency, obtained from simulations by comparing the reconstructed to the trackable tracks, is clearly reduced. The results of sytematic on tracking efficiency using this method will be discussed in chapter 4, 5 and 6.

3.4 Data Processing

3.4.1 Pass1

In the first step, the Event Summary Data (ESD) are produced with the standard re-alignment process (Pass1) which takes advantage of the specific sets of data previously collected in absence of magnetic field in the Muon Tracking. First, tracks are reconstructed and their positions with respect to the clusters formed by the pads hit by incoming particles are estimated. The track parameters are then tuned in order to minimize the position differences observed between tracks and clusters. Before to continue with the signal extraction, raw data need to be further treated to improve the quality suitable for analysis.

3.4.2 Pass2

The second ESD production (Pass2) is made with a much more efficient alignment procedure, first initiated for 2011 pp data. The new method takes now advantage of data collected with and without magnetic field. The new procedure can make good use of a large data sample and it is less affected by possible modifications of chamber positions due to the magnetic field.

From Pass1 to Pass2 the position becomes compatible with the nominal J/ψ mass and an improvement of about 5% of the width is observed.

3.4.3 Pass2 with refit

In the last processing step (called refit) performed at ESD level, the effects of some abnormal pad clusters of the Muon Tracking are better handled.

Each side of a tracking chamber is supposed to provide one spatial co-ordinate of the track. Accordingly, pads of the bending plane are sized to provide accurate vertical positions and vice versa. Therefore, if the charge of an incoming particle is not collected by one of the two planes of a chamber due to a malfunction, the resulting resolution will be poor corresponding to the plane where the hit was not formed. This issue does not affect the first two stations as pad dimensions are rather small in both directions. To solve the problem for the other three stations, an ad hoc resolution value is assigned to the cathode clusters in the lacking direction which is set to 10 cm instead of 2 mm. Thus in the reconstruction algorithm they basically are not taken into account and the reconstructed data quality is improved.

3.5 Trigger defination

3.5.1 Minimum Bias (MB) trigger

The minimum bias (MB) trigger for ALICE (CINT) is defined by the coincidence between a signal in the two V0 detectors (V0-A and V0-C) along with the passage of the two colliding beams.

This MB trigger has high triggering efficiency ($> 98\%$) for hadronic interaction. The integrated luminosity has been determined from the cross section of the MB trigger determined from a van der Meer (vdM) scan [6].

3.5.2 p_{T} trigger thresold

The p_{T} trigger threshold was defined as the value where the trigger efficiency for single muons was found to be 50%.

3.5.3 Dimuon trigger

The unlike sign (like sign) dimuon trigger was defined as the coincidence of the MB trigger with the detection of two opposite-sign (same-sign) muon triggers with a transverse momentum above the low p_{T} trigger thresold.

3.6 pp collisions at $\sqrt{s} = 7$ TeV

3.6.1 Data sample

The present analysis is based on Muon-AODs which are finally generated filtering ESD files obtained from raw data processing. The dataset used in this work is the AOD118 [7]. The data in AOD118 are based on a pass2-reconstruction of the muon tracks which improve the alignment of the tracking chambers, and includes a refit of the tracks which incorporate a correction on the resolution for mono-cathode clusters, so its basically Pass2 with refit AOD data.

In the present analysis two 2011 rare trigger periods, namely, LHC11c and LHC11d, were used. The compatibility of the results was checked for the two periods separately following which the analysis was carried out on the data sample which is the sum of LHC11c and LHC11d periods.

3.6.2 Event and trigger selection

The present analysis was carried out applying trigger and tracks selection, to obtain a clean sample of events. All the runs analyzed were qualified by QA tests [7]. In addition, every event of a QA qualified run was validated by physics selection criteria. This involved timing cuts on the V0 or on the Zero Degree Calorimeters which helps to remove the beam induced background.

Together with the MB trigger, data were collected with four specific muon triggers:

- Single muon with low-p_{T} threshold of 1 GeV/c (CMUS),

- Single muon with high-$p_{\rm T}$ threshold of 4.2 GeV/c (CMUSH),
- Unlike sign dimuon with both muon-$p_{\rm T}$ greater than 1 GeV/c (CMUU),
- Like sign dimuon with both muon-$p_{\rm T}$ greater than 1 GeV/c (CMUL).

The unlike sign dimuon trigger, called CMUU, was selected for this analysis. The equivalent number of MB events, which has been used in the cross section evaluation, were obtained by determining a normalization factor based on the occurrence of a CMUU trigger in the CINT sample. This evaluation was based on the trigger scalers [6]. After physics selection and CMUU trigger selection, a total of 4046537 events were analysed which corresponded to an integrated luminosity $\mathcal{L}_{\rm int}$ = 1.35 pb^{-1} (with 5% systematic uncertainty) [6].

3.7 p-Pb collisions at $\sqrt{s_{\rm NN}} = 5.02$ TeV

3.7.1 Data samples

The analysis is based on the p-Pb 2013 Muon-AODs data [8] which were generated by filtering ESD files obtained from raw data processing. The dataset used in this work was pass2 with refit.

Three rare trigger periods, namely, LHC13d, LHC13e and LHC13f, have been used. Having verified that the behavoiur of the LHC13d and LHC13e periods were very similar, the data sets were merged. There were two data sets: one was p-Pb data which consisted of LHC13d + LHC13e periods and another was Pb-p data consisted of LHC13f period.

3.7.2 Data selection

The Muon Spectrometer is situated on one side of ALICE, which is by convention considered as negative z-direction [1]. For p-Pb collisions, the colliding beams have different energies per nucleon ($E_{\mathrm{p}} = 4$ TeV, $E_{\mathrm{Pb}} = 1.58 \cdot A_{\mathrm{Pb}}$ TeV, where $A_{\mathrm{Pb}} = 208$ is the mass number of the Pb nucleus). As a result the coverage of the Muon Spectrometer becomes positive or negative depending on the direction of the higher energy beam with respect to the Muon Spectrometer. In p-Pb, beam-1 consists of protons circulating towards the Muon spectrometer in the negative z direction while beam-2 consists of fully stripped Pb ions circulating in the positive z direction. This configuration resulted in collisions at $\sqrt{s_{\mathrm{NN}}} = 5.02$ TeV and in a nucleon-nucleon center-of-mass system that moves with a rapidity of $\Delta y_{\mathrm{NN}} = 0.465$ in the direction of the proton beam. Thus, in the center-of-mass system, the Muon spectrometer cover the forward rapidity region $2.03 < y_{\mathrm{cms}} < 3.53$ in p-Pb collisions and the backward rapidity region $-4.46 < y_{\mathrm{cms}} < -2.96$ in Pb-p collisions. These two rapidity ranges overlap in the region $2.96 < |y_{\mathrm{cms}}| < 3.54$ which correspond to $3.43 < y_{\mathrm{lab}} < 4$ and $2.5 < y_{\mathrm{lab}} < 3.07$ for p-Pb and Pb-p collisions, respectively.

3.7.3 Event and trigger selection

The data passed the standard quality check for the detectors considered in the analysis (V0, SPD, ZDC, muon tracking and trigger chambers). The different triggers as discussed above were activated during data taking. During the rare trigger periods (LHC13d and LHC13e for p-Pb and LHC13f for Pb-p collisions), the MB trigger was down-scaled at the L0 level to allow more DAQ bandwidth for the rare triggers. The

[1] In the ALICE reference frame, the positive z-direction is along the counter clockwise beam direction. Thus, the muon spectrometer covers a negative pseudo-rapidity (η) range and a negative y_{lab} range. In this thesis the results will be presented with a positive y_{lab} notation keeping the η values signed.

following muon specific trigger were activated:

- Single muon low-$p_{\rm T}$ ($p_{\rm T}^{\mu} \geq 0.5$ GeV/c) or CMSL
- Single muon higt-$p_{\rm T}$ ($p_{\rm T}^{\mu} \geq 4$ GeV/c) or CMSH
- Unlike sign dimuon low-$p_{\rm T}$ ($p_{\rm T}^{\mu} \geq 0.5$ GeV/c on each muon) or CMUL
- Like sign dimuon low-$p_{\rm T}$ ($p_{\rm T}^{\mu} \geq 0.5$ GeV/c on each muon) or CMLL

For the muon candidates, the transverse momentum $p_{\rm T}^{\mu} = 0.5$ GeV/c trigger threshold was applied. The effect of this threshold was not sharp, and the single muon trigger efficiency reached its plateau value ($\sim 96\%$) for $p_{\rm T}^{\mu} \sim 1.5$ GeV/c. Beam induced background was reduced at the offline level by timing cuts on the signals from the V0 and from the ZDC. This physics selection removed up to 10% of the background events depending on the run and the collision type.

3.7.4 Integrated luminosity

In this analysis, the unlike sign dimuon low-$p_{\rm T}$ trigger or CMUL was used. Since the analysis was based on a dimuon trigger sample, the equivalent number of MB triggers was evaluated as $F.N_{\rm DIMU}$, where $N_{\rm DIMU}$ is the number of unlike sign dimuon triggered events, which amounted to 9.27×10^6 for p-Pb and 20.90×10^6 for Pb-p after applying the event physics selection. The enhancement factor F was calculated in two different ways. In the first one it was obtained as the product $F_{2\mu/1\mu}.F_{1\mu/\rm MB}$, where $F_{2\mu/1\mu}$ is the inverse of the probability of having a second muon triggered when one muon has triggered the event and, correspondingly, $F_{1\mu/\rm MB}$ is the inverse of the probability of having one triggered muon in events where the MB condition is required. The various quantities were obtained from the recorded trigger mask for the collected

events after quality cuts. This procedure of obtaining F as the product of the two factors mentioned above allowed the statistical uncertainty to be reduced. In the second approach, the information of the counters recording the number of L0 (level-0) triggers were used. In this case, statistics were much larger and F was obtained as the ratio between the numbers of MB and dimuon triggers at L0, corrected for pile-up effects (2%) and taking into account the slight difference in the fraction of events surviving the quality cuts for the two trigger samples (1%). The estimated values of F obtained from the average of the results from the two approaches are: $F_{\mathrm{pPb}} = 1129 \pm 2$ and $F_{\mathrm{Pbp}} = 589 \pm 2$, where the quoted uncertainties are statistical. A 1% systematic uncertainty was estimated on both quantities, corresponding to the difference between the values obtained in the two calculations.

The quantity $N_{\mathrm{MB}}/\sigma^{\mathrm{MB}}_{\mathrm{pPb}}$ corresponds to the integrated luminosity. As a cross-check, its value was measured independently by using a second reference trigger, issued by a Cherenkov counter [9], whose cross section was also measured in the van-der-Meer (vdM) scans. The luminosities measured with the two luminometers differ by at most 1% throughout the whole data-taking period. This small difference (identical for p-Pb and Pb-p) has been included in the systematic uncertainty on $\sigma^{\mathrm{MB}}_{\mathrm{pPb}}$. The cross section for the occurrence of the MB condition, $\sigma^{\mathrm{MB}}_{\mathrm{pPb}}$, were measured in a vdM scan [10] to be 2.09 ± 0.07 b for the p-Pb and 2.12 ± 0.07 b for the Pb-p one. The integrated luminosities measured using these values are 5.01 ± 0.17 nb^{-1} in p-Pb collisions and 5.81 ± 0.18 nb^{-1} in Pb-p collisions.

3.8 Pb-Pb collisions at $\sqrt{s_{\rm NN}} = 2.76$ TeV

3.8.1 Data sample

The analysis is based on data collected in three weeks during fall 2011 (LHC11h data). The dataset used is pass2 with refit Muon-AODs data (AOD119) [11].

3.8.2 Event and trigger selection

The data selection was done in accordance with the different trigger conditions. The MB trigger provided high trigger efficiency ($> 95\%$) for hadronic interactions. An additional threshold on the energy deposited in the ZDCs was used to reject the contribution from electromagnetic processes. The MB trigger was considerably down-scaled to open the DAQ bandwidth for more rare triggers. Beam-induced background was further reduced at the offline level by timing cuts on the signals from the V0 and from the ZDC.

The following muon specific trigger together with MB trigger were activated during the data taking:

- Single muon low-$p_{\rm T}$ ($p_{\rm T}^{\mu} \geq 1$ GeV/c) or MSL
- Single muon higt-$p_{\rm T}$ ($p_{\rm T}^{\mu} \geq 4.2$ GeV/c) or MSH
- Unlike sign dimuon low-$p_{\rm T}$ ($p_{\rm T}^{\mu} \geq 1$ GeV/c on each muon) or MUL
- Like sign dimuon low-$p_{\rm T}$ ($p_{\rm T}^{\mu} \geq 1$ GeV/c on each muon) or MLL

In particular, the unlike sign dimuon low-$p_{\rm T}$ trigger or MUL was used in this analysis. A data sample of 17.3×10^6 Pb-Pb collisions were triggered with the MUL

condition. A scaling factor $F_{\rm norm}$ was computed for each run in order to re-normalize the number of MUL triggers to the number of equivalent MB triggers. It is defined as the ratio, in a MB data sample, between the total number of events and the number of events fulfilling the MUL trigger condition. It should be noted that the MB event sample considered in this calculation has been recorded in parallel to the MUL triggers. The $F_{\rm norm}$ value, 30.56 $\pm$ 0.01(stat.) $\pm$ 1.10(syst.), was obtained by the average over runs weighted by the statistical uncertainty. A small fraction of opposite-sign dimuons were misidentified by the trigger algorithm as like-sign pairs. In the present analysis, this missing fraction of opposite-sign dimuons were recovered by extracting the number of produced J/ψ and ψ(2S) from the (MUL logical-OR MLL) data sample. On the other hand, the efficiency of the trigger algorithm to determine the sign of the muon pairs did not affect the renormalization of the collected data sample to the number of equivalent MB events described above. This was cross-checked by computing the normalization factor of the (MUL logical-OR MLL) data sample, resulting in less than 1% difference in the extracted number of equivalent MB events.

The integrated luminosity corresponding to the analyzed data sample was $L_{\rm int} = N_{\rm MUL} \times F_{\rm norm}/\sigma_{\rm Pb-Pb} = 68.8 \pm 0.9$ (stat.) $\pm$ 2.5 (syst. $F_{\rm norm}$)$^{+5.5}_{-4.5}$ (syst. $\sigma_{\rm Pb-Pb}$) μb^{-1} assuming a inelastic Pb-Pb cross-section of $\sigma_{\rm Pb-Pb} = 7.7 \pm 0.1$(stat.)$^{+0.6}_{-0.5}$ (syst.)b [12]. For the fractional double differential cross-section analysis presented in this thesis, the integrated luminosity determination was not necessary.

The criteria for the track selection in the data analysis presented in this thesis are described below.

3.9 Track selections

In order to improve the purity of the muon tracks the following selection criteria were applied:

- Both muon tracks reconstructed by the tracking chambers were matched with a track segment in the trigger chambers above low p_{T}^{μ} thresold. This selection rejects efficiently light hadrons escaping from the front absorber and also rejects a part of the low-momentum muons coming mainly from π and K decays.

- the tracks must be in the pseudo-rapidity range $-4 < \eta < -2.5$. This selection is efficiently rejects particles induced by beam-gas interactions at the edges of the detector.

- the transverse radius coordinate of the track, at the end of the hadron absorber (R_{abs}), must be in the range $17.6 \leq R_{\mathrm{abs}} \leq 89.5$ cm. The tracks crossing the high density material around the beam pipe, where multiple scattering is large, were then significantly rejected. This cut improved the mass resolution.

- the dimuon rapidity must be in the range $2.5 \leq y \leq 4.0$.

- tracks should point to the interaction vertex. This requirement can be achieved by selecting tracks according to the value of a quantity defined as the product of the track momentum (p) by the distance of the extrapolated track to the transverse plane containing the vertex (DCA: Distance of Closest Approach), known as $p \times \mathrm{DCA}$. This additional selection significantly reduced the amount of fake tracks contaminating the muon sample which increases the combinatorial background. This cut was applied only for p-Pb and Pb-Pb analysis data because number of tracks in the interaction vertex were very large. This cut had no effect in pp analysis.

Bibliography

[1] A. Behrens et al. "Positioning strategy, metrology and survey in ALICE". EDMS 884850 (2007).

[2] V. Blobel. "Software alignment for tracking detectors". Nucl. Instr. Meth. A **566**(1):5-13, 2006.

[3] P. Billoir and Q. Qian, Nucl. Instr. and Meth. A **294**, 219 (1990).

[4] R. Fruhwirth, Nucl. Instr. and Meth. A **262**, 444 (1987).

[5] C. Clopper and E. Pearson, "The use of confidence or fiducial limits ilustrated in the case of the binomial", Biometrika **26**, 404 (1934).

[6] `https://aliceinfo.cern.ch/Notes/node/162`.

[7] `https://twiki.cern.ch/twiki/bin/viewauth/ALICE/MuonppQA2011`.

[8] `https://twiki.cern.ch/twiki/bin/viewauth/ALICE/MuonpPbQA2013`.

[9] ALICE collaboration, "The ALICE experiment at the CERN LHC", JINST **3**, S08002 (2008) [INSPIRE].

[10] ALICE collaboration, "Measurement of visible cross sections in proton-lead collisions at $\sqrt{s_{\rm NN}} = 5.02$ TeV in van der Meer scans with the ALICE detector", JINST **9**, P11003 (2014)[arXiv:1405.1849] [INSPIRE].

[11] `https://twiki.cern.ch/twiki/bin/viewauth/ALICE/MuonPbPbQA2011`

[12] B. Abelev et al. [ALICE Collaboration], "Measurement of the Cross Section for Electromagnetic Dissociation with Neutron Emission in Pb-Pb Collisions at $\sqrt{s_{\rm NN}} = 2.76$ TeV", Phys. Rev. Lett. **109** (2012) 252302 [arXiv:1203.2436 [nucl-ex]].

Chapter 4

J/ψ and ψ(2S) production in pp collisions

In this chapter the analysis of J/ψ and ψ(2S) production at forward rapidity in pp collisions has been discussed. The data were collected by ALICE Muon Spectrometer at $\sqrt{s}$ = 7 TeV with specific trigger conditions. The data sample corresponds to an integrated luminosity $\mathcal{L}_{\rm int}$ = 1.35 pb^{-1}. These results have been published in ref [1].

4.1 Data Processing

The data sample, events, trigger and track selection have been described in details in chapter 3.

4.2 Signal extraction

The high statistics sample collected during the two periods (LHC11c and LHC11d) allowed a detailed study of J/ψ and ψ(2S) production cross-sections as a function transverse momentum, $p_{\rm T}$, and rapidity, y. The present data have been analyzed in 13 bins in the $0 < p_{\rm T} < 20$ GeV/c range and 9 bins in the $0 < p_{\rm T} < 12$ GeV/c range for J/ψ and ψ(2S) respectively, while both the resonances could be studied in 6 rapidity bins in the range $2.5 \leq y \leq 4.0$.

4.2.1 Fit procedure

J/ψ and ψ(2S) yields have been obtained by fitting the unlike-sign (OS) dimuon mass spectra with a combination of signal and background functions. For the J/ψ and ψ(2S) signals, two Extended Crystal Ball (CB2) functions or two so-called "NA60" functions have been used, while for the background a Variable Width Gaussian (VWG) function or a combination of a 4th order polynomial and exponential functions (Pol4 x Exp) has been adopted.

- An Extended Crystal Ball function is composed of a Gaussian core convoluted with two power-law tails (one for the lower invariant masses, the other for the higher ones). This function has seven parameters corresponding to the amplitude, the mass position, the width and to the power-law tails (×4). The CB and CB2 functions are described in Appendix B.

- The NA60 function is a pseudo-gaussian empirical shape, commonly used in previous SPS experiments. It allows a better description of the right and left J/ψ tails and its description is given in Appendix B. Also in this case the mass position, the width and the normalization of the resonance are free parameters

of the fit, while all the other parameters are fixed to the values tuned on a MC simulation.

In the fit of the experimental invariant mass spectrum the amplitude parameters of the two CB2 were considered as free parameters, together with the position and the width of J/ψ. On the other hand, the position and the width of ψ(2S) were fixed by the following prescriptions:

- The mass position of ψ(2S) was fixed to the J/ψ one by the following relation:

$$m_{\psi(2S)} = m_{J/\psi} + \left(m^{PDG}_{\psi(2S)} - m^{PDG}_{J/\psi}\right). \tag{4.1}$$

$$m_{\psi(2S)} = m_{J/\psi} + \left(m^{MC}_{\psi(2S)} - m^{MC}_{J/\psi}\right). \tag{4.2}$$

  where, $m^{PDG}_{J/\psi}$ and $m^{PDG}_{\psi(2S)}$, and $m^{MC}_{J/\psi}$ and $m^{MC}_{\psi(2S)}$ are the masses of J/ψ and ψ(2S) from PDG and MC, respectively.

- The width of ψ(2S) was fixed to the J/ψ one by two ways:

$$\sigma_{\psi(2S)} = \sigma_{J/\psi}.\frac{m_{\psi(2S)}}{m_{J/\psi}}. \tag{4.3}$$

$$\sigma_{\psi(2S)} = \sigma_{J/\psi}.\frac{\sigma^{MC}_{\psi(2S)}}{\sigma^{MC}_{J/\psi}}. \tag{4.4}$$

  where, $\sigma^{MC}_{J/\psi}$ and $\sigma^{MC}_{\psi(2S)}$ are the widths of J/ψ and ψ(2S) obtained from realistic Monte Carlo simulations. Alternative values of the ψ(2S) mass resolution have also been tested, allowing the ratio $(\sigma^{MC}_{\psi(2S)}/\sigma^{MC}_{J/\psi})$ to vary within 10% and this variation is included in systematic uncertainties.

The tail parameters for J/ψ were determined by fitting the shape of the resonance obtained from a realistic MC simulation. The same tail parameters have been assumed for ψ(2S) as the resonances are separated by only 590 MeV/c^2. Thus, it is assumed that the energy straggling and multiple coulomb scattering effects of the front absorber on the decay muons are rather similar for the two resonances. All the parameters of the VWG used for the fitting of the continuum background have been kept free.

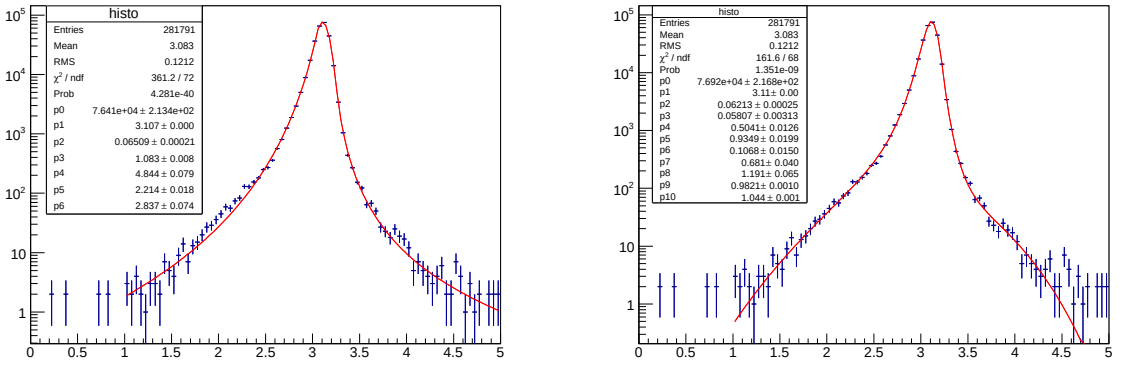

(a) MC spectrum fitted with CB2 function.

(b) MC spectrum fitted with NA60 function.

Figure 4.1: Invariant mass spectrum of J/ψ from MC simulation fitted with two different signal functions.

Fig. 4.1 (a) and (b) shows the quality of the fit to the MC shapes for J/ψ with CB2 and NA60 functions, respectively. It can be noted from the figures that on the basis of the χ^2 test, it is not possible to choose one above the other, since both shapes give a resonable description of the resonance peak. Thus, both functions were used in the signal extraction procedure and the variation in the extracted values of the signals were accounted for in the corresponding systematic uncertainty.

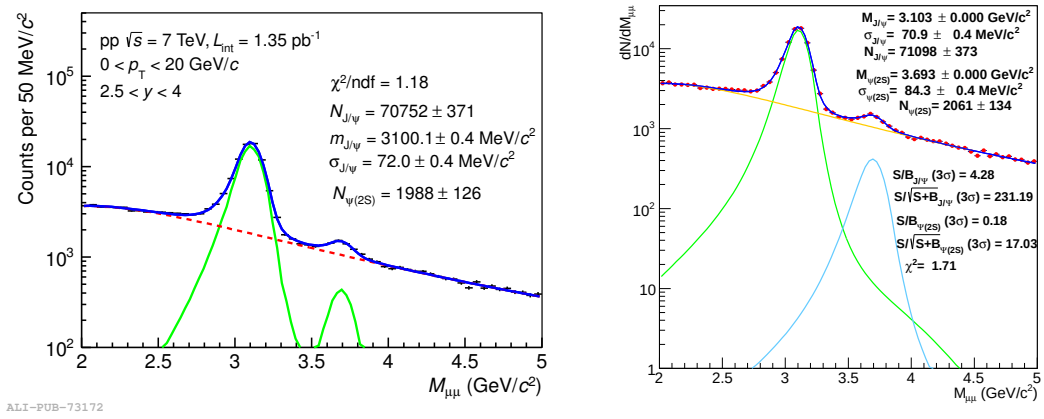

(a) Spectrum fitted with CB2+VWG. (b) Spectrum fitted with NA60+VWG.

Figure 4.2: Opposite sign dimuon invariant mass distribution for $2.5 \leq y \leq 4.0$, integrated over p_{T} fitted with two different fitting functions.

	CB2+VWG				NA60+VWG			
Signal	N ± (stat)	S/B	Significance	χ^2/ndf	N ± (stat)	S/B	Significance	χ^2/ndf
J/ψ	70910 ± 364	4.21	231.4	1.16	71098 ± 373	4.28	231.2	1.71
ψ(2S)	2056 ± 128	0.18	17.0		2061 ± 134	0.18	17.3	

Table 4.1: Fit results for integrated spectrum.

4.2.2 Fit results

Fig. 4.2 (a) and (b) show the CB2+VWG and NA60+VWG fits to the p_{T} and y integrated dimuon mass spectrum between 2 and 5 GeV/c^2. The quality of fit is similar in the two cases. Table 4.1 summarizes the results of the fits based on the two tested signal functions for J/ψ and ψ(2S). The S/B ratio computed at 3σ around the J/ψ peak is ~ 4, while for the ψ(2S) it is much smaller, of the order of ~ 0.2. It is to be noted that the NA60 fits and CB2 fits give similar results.

The statistical uncertainties for J/ψ are 0.51% and 0.52% and for ψ(2S) 6.2% and 6.5%, respectively for the two functions. These results have been used to determine the production cross-section of J/ψ and ψ(2S) at 7 TeV at forward rapidities ($2.5 \leq y \leq 4.0$).

In p_{T} bins :

The data set has been divided in 13 p_{T} bins for J/ψ and in 9 p_{T} bins for ψ(2S) in order to determine the differential cross-section as a function of p_{T}. Fig. 4.3 shows the mass spectra of different p_{T} bins fitted with CB2+VWG while Fig. 4.4 shows the fit with NA60+VWG. Table 4.2 and 4.3 summarize the results of the fit to different p_{T} bins for J/ψ and ψ(2S) respectively. The present analysis extend the p_{T} depedence up to 20 GeV/c and 12 GeV/c for J/ψ and ψ(2S), respectively. In the highest p_{T} bin, the significance is still reasonable, being ~ 5 and ~ 3.8 for J/ψ and ψ(2S).

In y bins :

From the present data set, the J/ψ and ψ(2S) signals could be extracted in six rapidity bins. Fig. 4.5 and 4.6 show the signal extraction with CB2+VWG and NA60+VWG, respectively for each of the 6 bins. Tables 4.4 and 4.5 summarize the results of these fits for J/ψ and ψ(2S), respectively.

	CB2+VWG				NA60+VWG			
p_{T} bins	$N_{J/\psi}$ ± (stat)	S/B	Significance	χ^2/ndf	$N_{J/\psi}$ ± (stat)	S/B	Significance	χ^2/ndf
[0; 1]	10898 ± 159	2.77	86.48	0.84	10942 ± 161	2.81	86.51	0.84
[1; 2]	17328 ± 189	3.17	110.95	1.53	17385 ± 193	3.23	110.94	1.30
[2; 3]	13895 ± 162	4.18	102.10	0.82	13882 ± 162	4.24	102.06	0.79
[3; 4]	10177 ± 134	5.73	89.86	1.55	10146 ± 132	5.80	89.59	1.42
[4; 5]	7038 ± 107	7.20	75.84	1.28	7000 ± 106	7.27	75.54	1.23
[5; 6]	4417 ± 81	8.25	61.04	1.17	4471 ± 83	8.87	61.04	1.45
[6; 8]	4311 ± 79	8.52	60.63	1.37	4388 ± 80	8.89	60.48	1.15
[8; 10]	1551 ± 48	8.09	36.26	1.20	1593 ± 49	8.91	36.45	1.16
[10; 12]	634 ± 32	7.85	23.04	1.12	637 ± 32	7.96	23.80	1.42
[12; 14]	284 ± 20	5.17	14.58	1.01	285 ± 30	6.59	14.74	1.77
[14; 16]	128 ± 19	4.05	9.62	1.22	129 ± 25	4.58	9.92	1.72
[16; 18]	63 ± 10	3.91	6.70	1.25	69 ± 11	4.01	6.97	1.37
[18; 20]	37 ± 8	2.19	5.14	0.69	39 ± 13	3.17	5.22	0.58

Table 4.2: Fit results in 13 p_{T} bins for J/ψ.

The significance ranges between ~ 50 (~ 3) and ~ 120 (~ 9) for the J/ψ (ψ(2S)), the maximum being reached in the middle of the covered rapidity range.

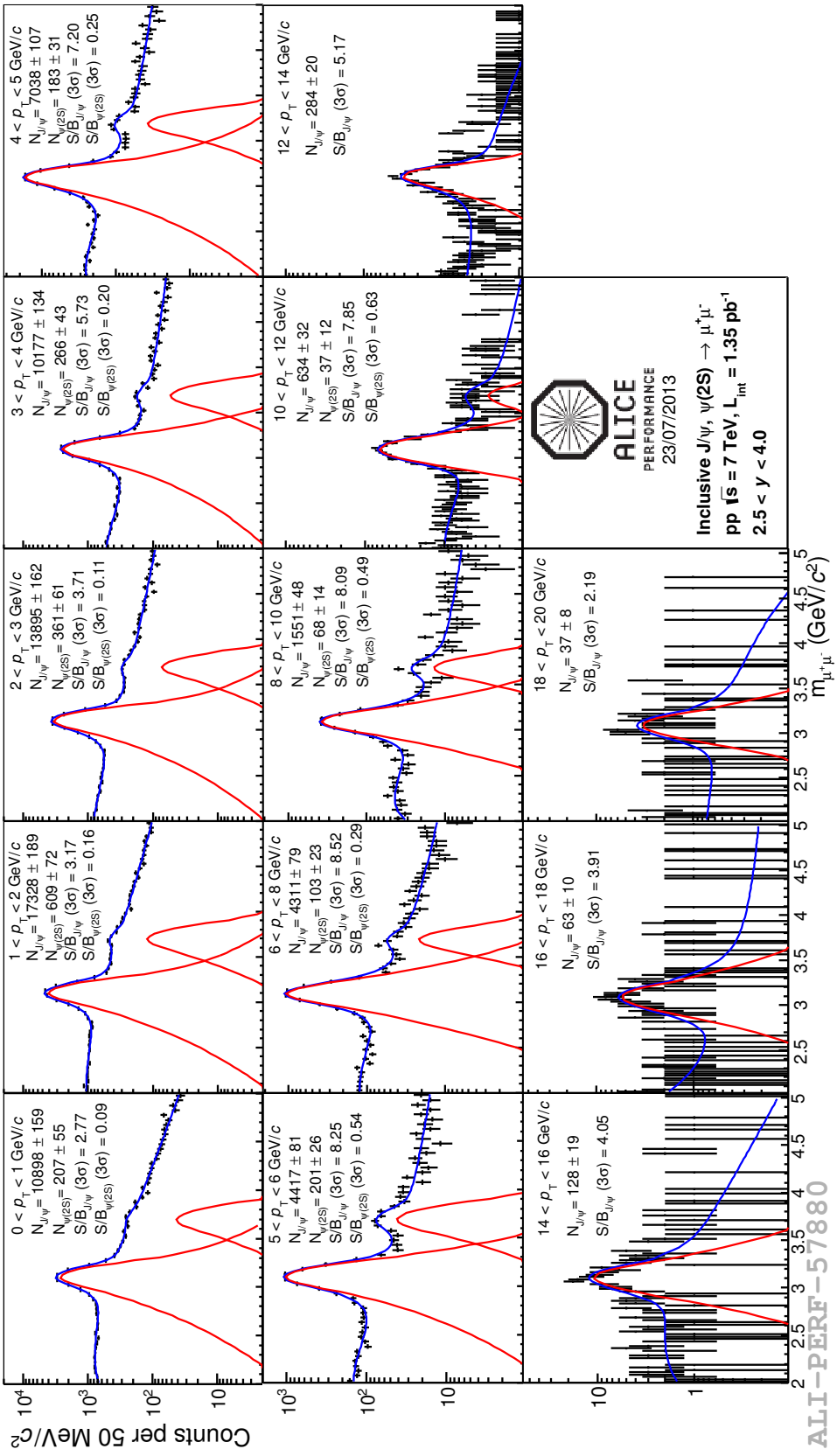

Figure 4.3: Invariant mass spectrum in various p_{T} bins fitted with CB2+VWG.

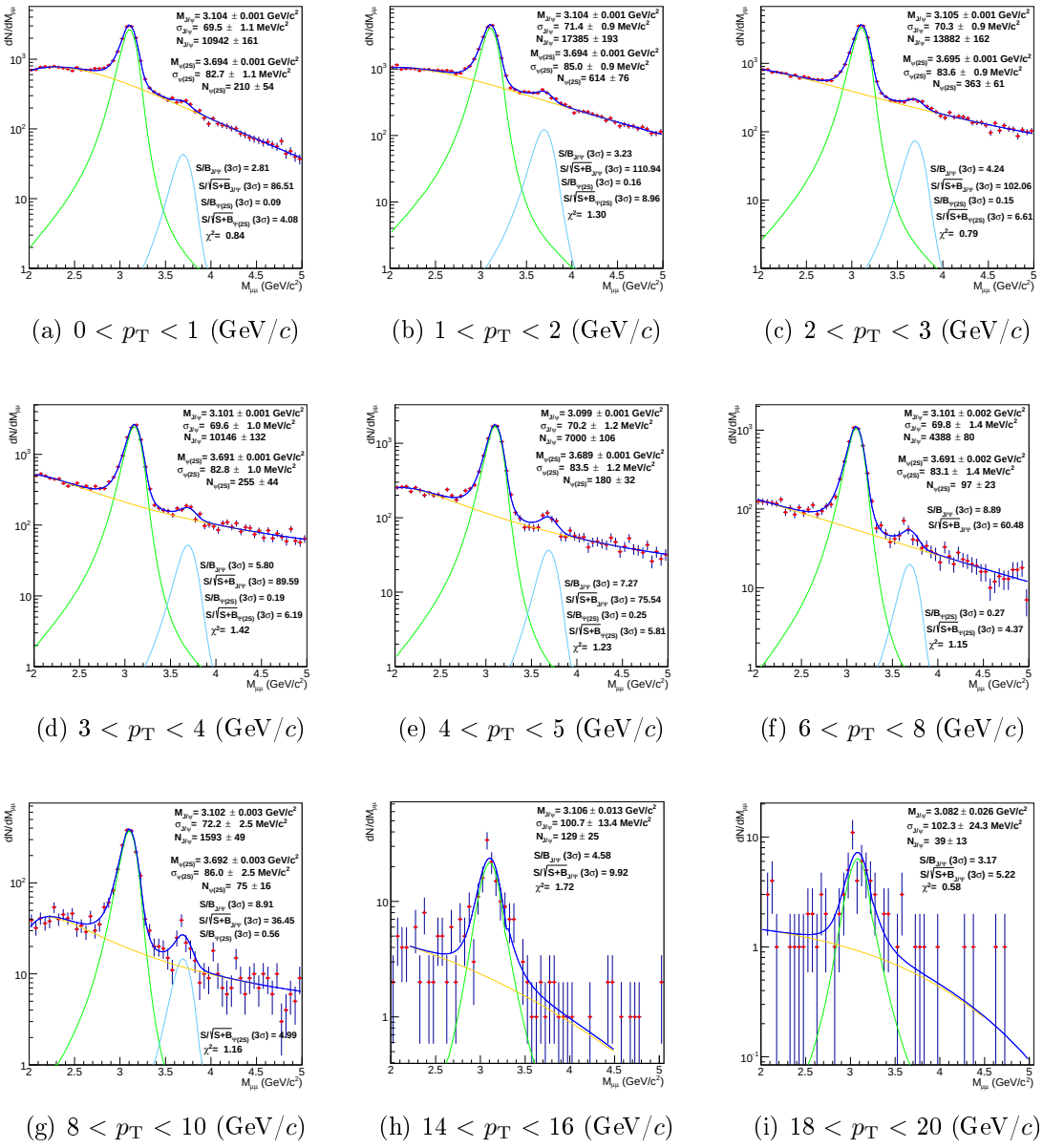

(a) $0 < p_{\mathrm{T}} < 1$ (GeV/c) (b) $1 < p_{\mathrm{T}} < 2$ (GeV/c) (c) $2 < p_{\mathrm{T}} < 3$ (GeV/c)

(d) $3 < p_{\mathrm{T}} < 4$ (GeV/c) (e) $4 < p_{\mathrm{T}} < 5$ (GeV/c) (f) $6 < p_{\mathrm{T}} < 8$ (GeV/c)

(g) $8 < p_{\mathrm{T}} < 10$ (GeV/c) (h) $14 < p_{\mathrm{T}} < 16$ (GeV/c) (i) $18 < p_{\mathrm{T}} < 20$ (GeV/c)

Figure 4.4: Invariant mass spectrum in various p_{T} bins fitted with NA60+VWG.

4.2.3 Systematic uncertainties in signal extraction

Integrated Spectra :

The systematic uncertainty on signal extraction has been determined extracting the J/ψ and ψ(2S) yields by testing two different signal fitting functions (CB2

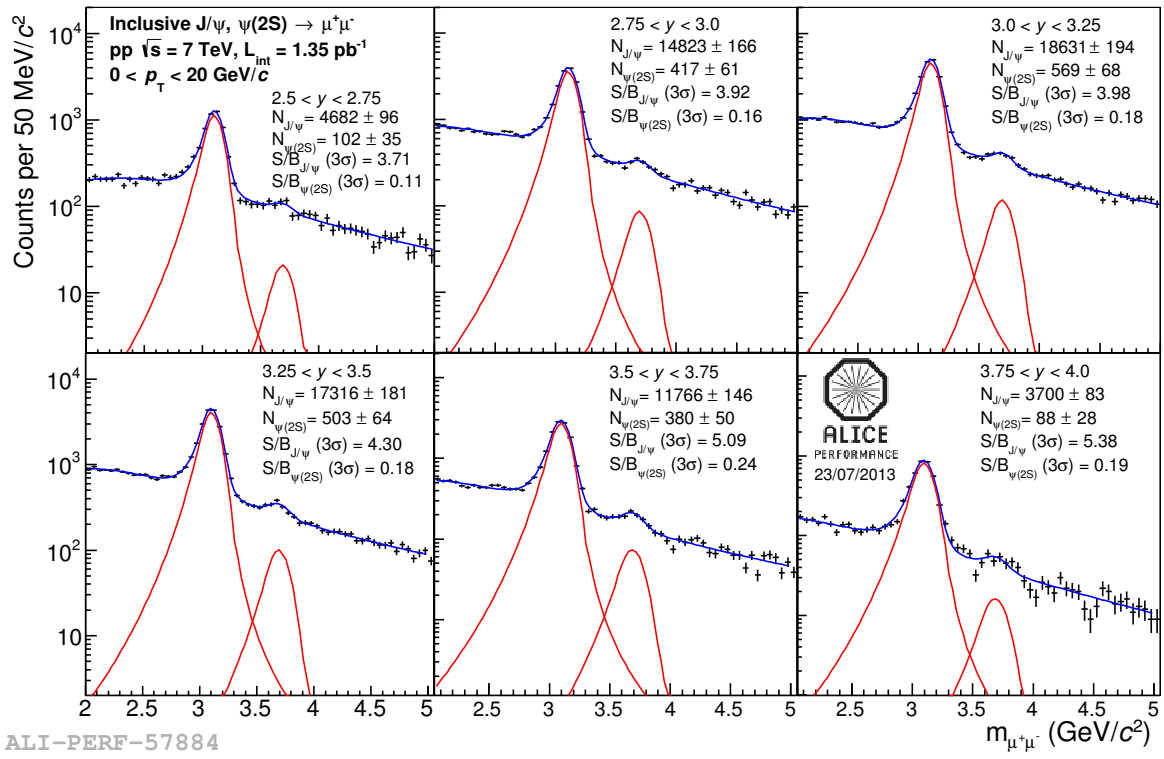

Figure 4.5: Invariant mass spectrum in 6 rapidity bins fitted with CB2+VWG.

	CB2+VWG				NA60+VWG			
p_{T} bins	$\mathrm{N}_{\psi(2S)}\pm$(stat)	S/B	Significance	χ^2/ndf	$\mathrm{N}_{\psi(2S)}\pm$(stat)	S/B	Significance	χ^2/ndf
[0; 1]	207 ± 55	0.09	4.01	0.84	210 ± 54	0.09	4.08	0.84
[1; 2]	609 ± 72	0.16	8.88	1.53	614 ± 76	0.16	8.96	1.30
[2; 3]	361 ± 61	0.15	6.53	0.82	363 ± 61	0.15	6.61	0.79
[3; 4]	266 ± 43	0.20	6.39	1.55	255 ± 44	0.19	6.19	1.42
[4; 5]	183 ± 31	0.25	5.87	1.28	180 ± 32	0.25	5.81	1.23
[5; 6]	201 ± 26	0.54	8.36	1.17	199 ± 27	0.58	8.51	1.45
[6; 8]	103 ± 23	0.29	4.73	1.37	116 ± 23	0.27	4.37	1.15
[8; 10]	68 ± 14	0.49	4.61	1.20	75 ± 16	0.56	4.99	1.16
[10; 12]	37 ± 12	0.63	3.61	1.12	37 ± 12	0.65	3.77	1.42

Table 4.3: Fit results in 9 p_{T} bins for ψ(2S).

and NA60 function), two different background functions (VWG and a 4th order polynomial multiplied by an exponential), two different fitting ranges (2 to 5 GeV/c^2 and 2.2 to 4.5 GeV/c^2) and two different ways of fixing the width of ψ(2S) by varying the $\sigma^{\mathrm{MC}}_{\psi(2\mathrm{S})}/\sigma^{\mathrm{MC}}_{\mathrm{J}/\psi}$ ratio by ± 10% (upper limit of this ratio is exactly equal to the mass ratio and lower limit is $\sigma^{\mathrm{MC}}_{\psi(2\mathrm{S})}/\sigma^{\mathrm{MC}}_{\mathrm{J}/\psi} = 1$). Thus, for each resonance the signal was

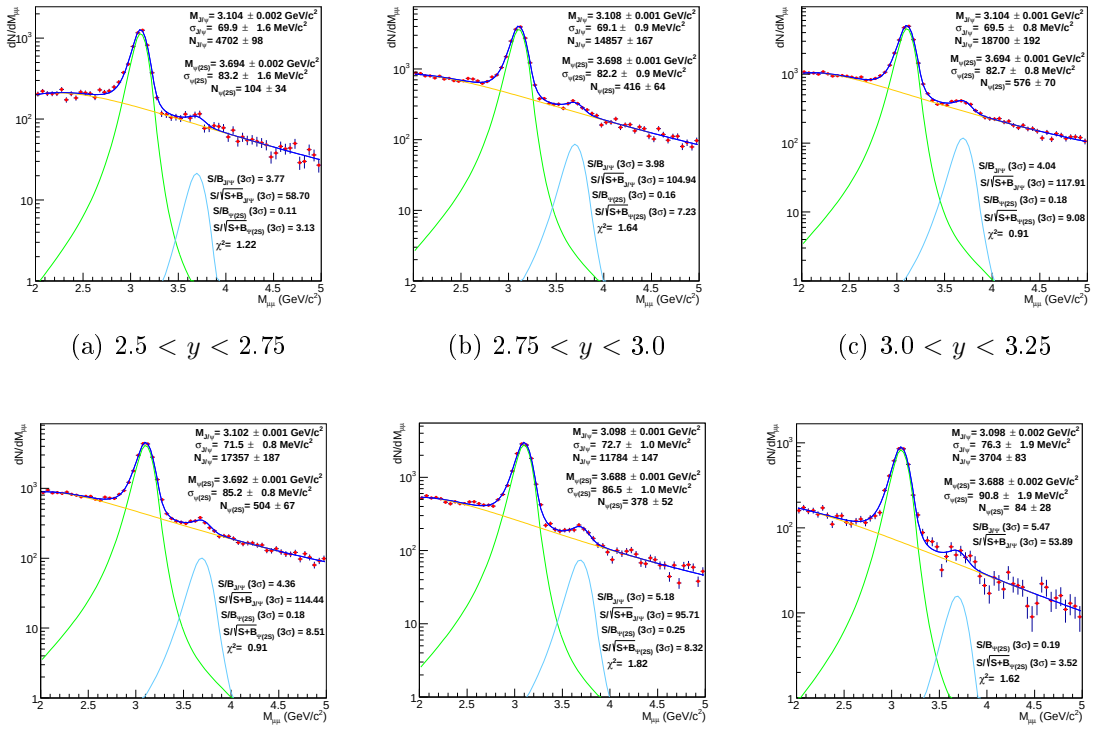

(a) $2.5 < y < 2.75$ (b) $2.75 < y < 3.0$ (c) $3.0 < y < 3.25$

(d) $3.25 < y < 3.5$ (e) $3.5 < y < 3.75$ (f) $3.75 < y < 4.0$

Figure 4.6: Invariant mass spectrum in 6 rapidity bins fitted with NA60+VWG.

	CB2+VWG				NA60+VWG			
y bins	$N_{J/\psi} \pm$ (stat)	S/B	Significance	χ^2/ndf	$N_{J/\psi} \pm$ (stat)	S/B	Significance	χ^2/ndf
[2.5; 2.75]	4682 ± 96	3.71	58.69	1.26	4702 ± 98	3.77	58.70	1.22
[2.75; 3.0]	14823 ± 166	3.92	105.05	1.70	14857 ± 167	3.98	104.94	1.64
[3.0; 3.25]	18631 ± 194	3.98	117.95	1.12	18700 ± 192	4.04	117.91	0.91
[3.25; 3.5]	17316 ± 181	4.30	114.56	0.77	17357 ± 187	4.36	114.44	0.91
[3.5; 3.75]	11766 ± 146	5.09	95.86	1.68	11784 ± 147	5.18	95.71	1.82
[3.75; 4.0]	3700 ± 83	5.38	53.99	1.67	3704 ± 83	5.47	53.89	1.62

Table 4.4: Fit results in 6 rapidity bins for J/ψ.

extracted for 2^4 combinations. The final extracted yield is the weighted average of the 16 values, while the RMS of the distribution gives the systematic uncertainty on the signal.

Fig. 4.7 shows the results of the signal extraction based on the 16 different test conditions for J/ψ and ψ(2S), together with the average value and the associated RMS.

	CB2+VWG				NA60+VWG			
y bins	$N_{\psi(2S)}\pm$(stat)	S/B	Significance	χ^2/ndf	$N_{\psi(2S)}\pm$(stat)	S/B	Significance	χ^2/ndf
[2.5; 2.75]	102 ± 35	0.11	3.06	1.26	104 ± 34	0.11	3.13	1.22
[2.75; 3.0]	417 ± 61	0.16	7.25	1.70	416 ± 64	0.16	7.23	1.64
[3.0; 3.25]	569 ± 68	0.18	8.99	1.12	576 ± 70	0.18	9.08	0.91
[3.25; 3.5]	503 ± 64	0.18	8.49	0.77	504 ± 67	0.18	8.51	0.91
[3.5; 3.75]	380 ± 50	0.24	8.35	1.68	378 ± 52	0.25	8.32	1.82
[3.75; 4.0]	88 ± 28	0.19	3.66	1.67	84 ± 28	0.19	3.52	1.62

Table 4.5: Fit results in 6 rapidity bins for ψ(2S).

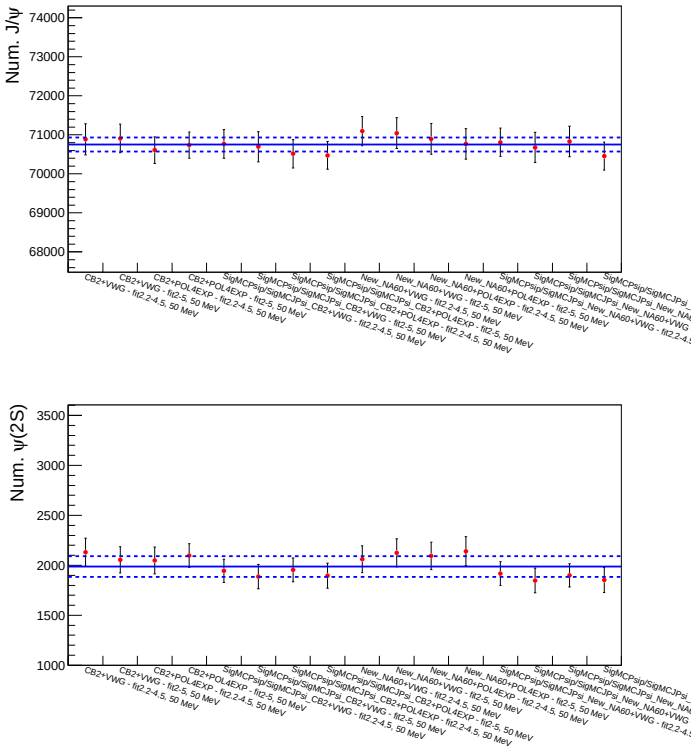

Figure 4.7: Number of J/ψ (top) and ψ(2S) (bottom) extracted for the 16 tests used for signal extraction to calculate the systematic uncertainty for integrated spectrum.The continuous line represents the weighted average, while the dotted lines correspond to the RMS of the distributions.

Table 4.6 summarizes the result on signal extraction together with the statistical and systematic errors of J/ψ and ψ(2S), respectively. The systematic uncertainty on signal extraction is $\sim 0.3\%$ for the J/ψ and $\sim 5.2\%$ for the ψ(2S).

$N_{J/\psi}$ ± (stat.) ± (syst.)	$N_{\psi(2S)}$ ± (stat.) ± (syst.)
70752 ± 371 ± 181	1987 ± 127 ± 103

Table 4.6: Results on signal extraction for integrated spectrum.

p_T bins	$N_{J/\psi}$ ± (stat.) ± (syst.)	$N_{\psi(2S)}$ ± (stat.) ± (syst.)
[0; 1]	10831 ± 161 ± 69	191 ± 52 ± 14
[1; 2]	17303 ± 196 ± 53	572 ± 73 ± 45
[2; 3]	13859 ± 162 ± 36	350 ± 57 ± 25
[3; 4]	10134 ± 133 ± 31	259 ± 42 ± 24
[4; 5]	7009 ± 103 ± 44	197 ± 30 ± 18
[5; 6]	4398 ± 81 ± 43	150 ± 28 ± 14
[6; 8]	4392 ± 80 ± 45	111 ± 24 ± 5
[8; 10]	1569 ± 47 ± 21	69 ± 15 ± 4
[10; 12]	628 ± 31 ± 7	33 ± 11 ± 3
[12; 14]	287 ± 24 ± 5	
[14; 16]	128 ± 17 ± 7	
[16; 18]	65 ± 11 ± 4	
[18; 20]	33 ± 10 ± 5	

Table 4.7: Results on signal extraction in different p_T bins for J/ψ and ψ(2S).

Differential Spectra :

The systematic uncertainties on differential spectra has been determined in the same way as described in the previous section for the p_T and y integrated result. On top of this, two different tail parameter sets (tail parameters tuned on the p_T and y integrated shapes or specific tail parameters determined for each p_T (y) bin) have been tested. Thus, for the differential yields, the signals have been extracted for 2^5 combinations.

Fig. 4.8, shows the systematic variation of the signal counts for 32 different test conditions for the analysis in p_T bins while Fig. 4.9 hows the variations for y bins.

Table 4.7, summarizes the result on signal extraction in different p_T bins for J/ψ and ψ(2S) while Table 4.8 summarizes the results for different y bins.

Systematic uncertainty on the signal extraction increases from $\sim 0.3\%$ ($\sim 4.5\%$) to $\sim 15\%$ ($\sim 9.3\%$) for the J/ψ (ψ(2S)) as a function of p_T. In the y bins, systematic uncertainty is in the range $\sim 0.5\%$ ($\sim 3\%$) to $\sim 1\%$ ($\sim 8\%$) for the J/ψ (ψ(2S)).

y bins	$N_{J/\psi}$ $\pm$ (stat.) $\pm$ (syst.)	$N_{\psi(2S)}$ $\pm$ (stat.) $\pm$ (syst.)
[2.5; 2.75]	4660 $\pm$ 93 $\pm$ 39	117 $\pm$ 36 $\pm$ 4
[2.75; 3.0]	14768 $\pm$ 165 $\pm$ 100	402 $\pm$ 58 $\pm$ 32
[3.0; 3.25]	18559 $\pm$ 196 $\pm$ 118	538 $\pm$ 67 $\pm$ 33
[3.25; 3.5]	17241 $\pm$ 185 $\pm$ 82	480 $\pm$ 63 $\pm$ 24
[3.5; 3.75]	11727 $\pm$ 148 $\pm$ 65	344 $\pm$ 48 $\pm$ 24
[3.75; 4.0]	3691 $\pm$ 82 $\pm$ 36	93 $\pm$ 26 $\pm$ 6

Table 4.8: Results on signal extraction in different rapidity bins for J/ψ and ψ(2S).

It is to be noted that the systematic uncertainty on the signal extraction is largely due to the two different signal shapes (CB2 and NA60). Additional systematic uncertainty of 2% for J/ψ, 6% for ψ(2S) and 5% for ψ(2S)/J/ψ ratio are obtained by using different tail parameter sets.

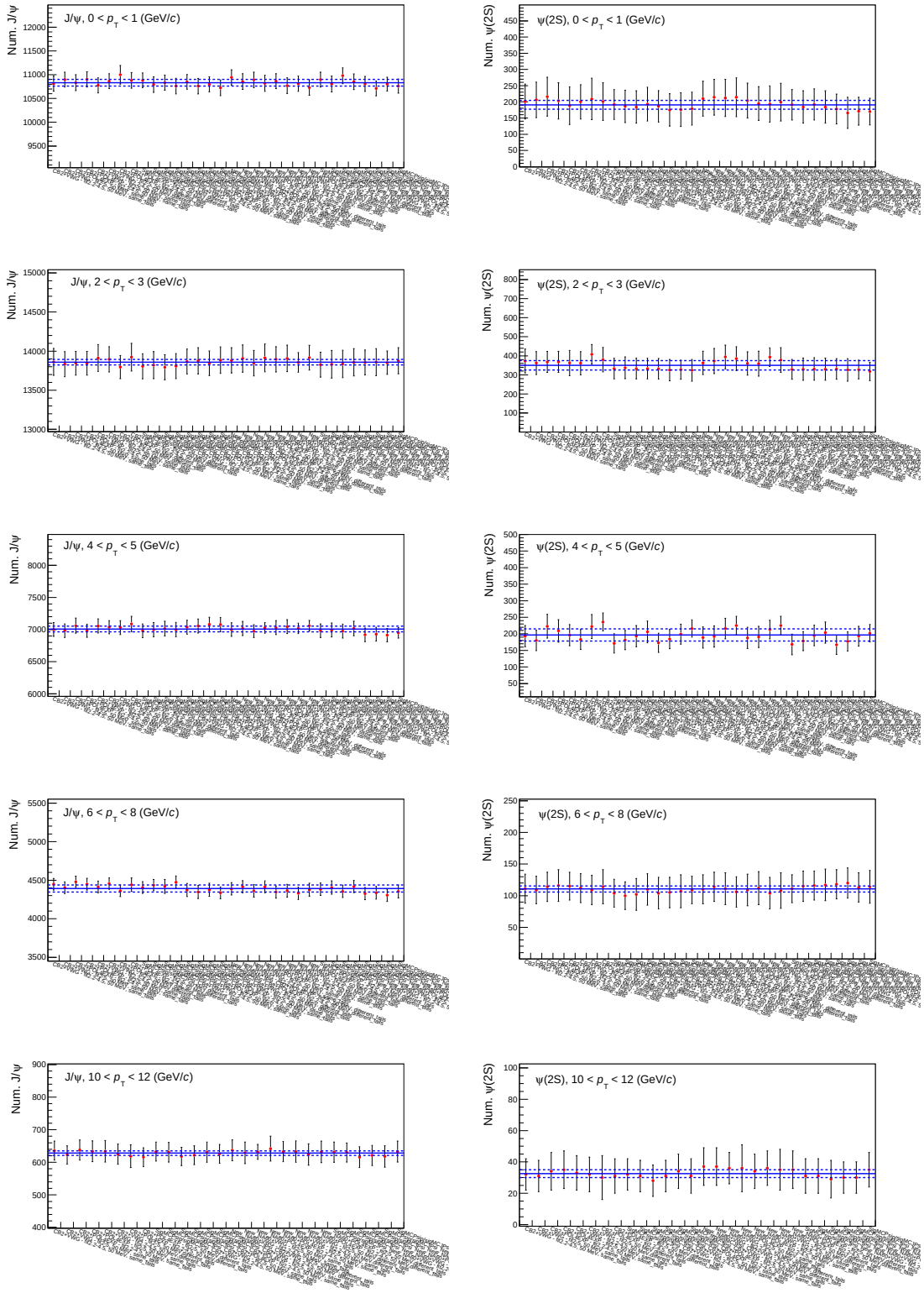

Figure 4.8: Number of J/ψ and ψ(2S) extracted for the 32 tests used for extracting the systematic uncertainty as a function of p_{T}. The continuous line represents the weighted average, while the dotted lines correspond to the RMS of the distributions.

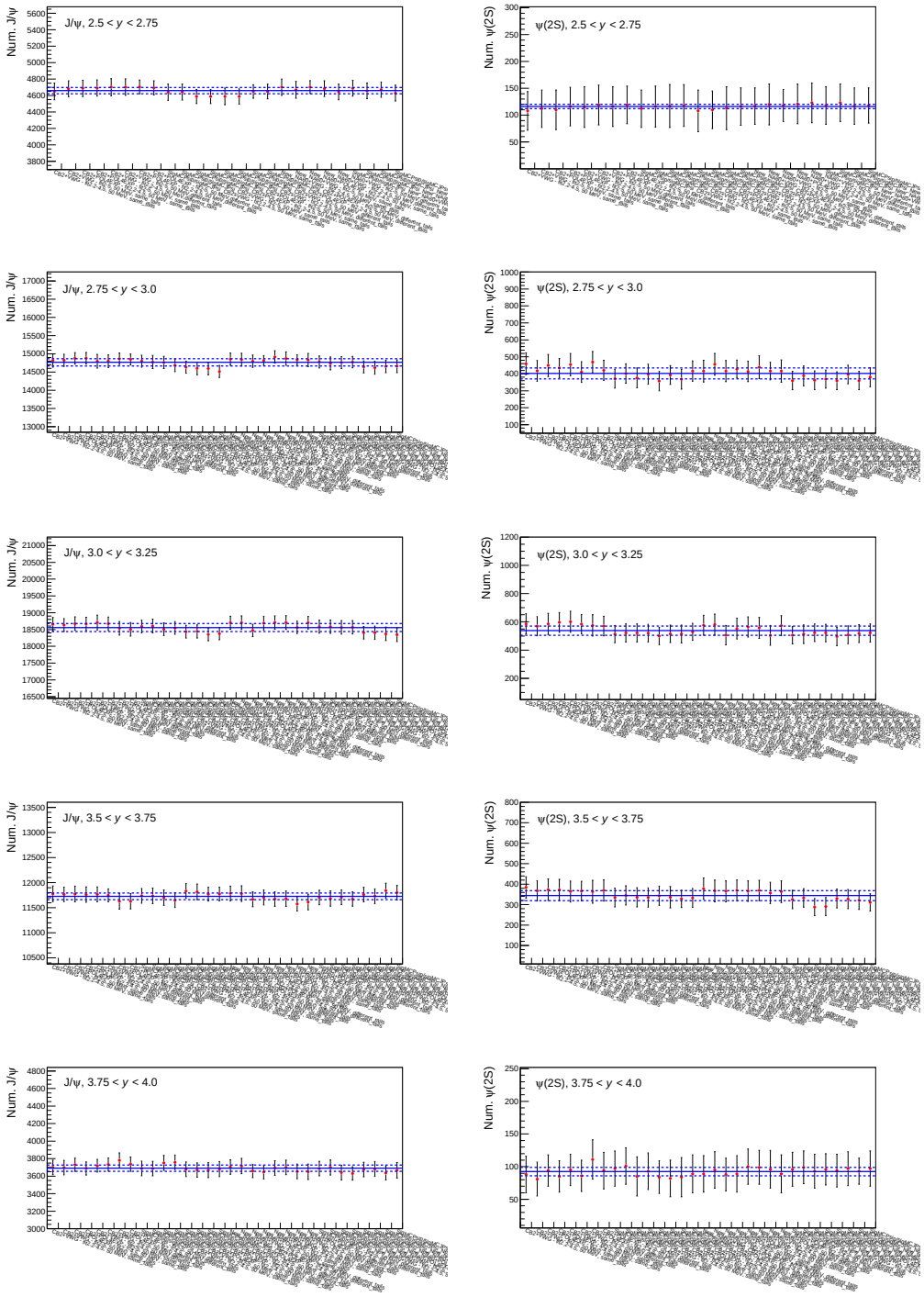

Figure 4.9: Number of J/ψ and ψ(2S) extracted for the 32 tests used for extracting the systematic uncertainty as a function of rapidity. The continuous lines represent the weighted average, while the dotted lines correspond to the RMS of the distributions.

4.3 Acceptance and efficiency corrections

The acceptance times efficiency (A×ϵ) has been determined by simulating J/ψ and ψ(2S) signals using p_{T} and y input distributions based on an interpolation of the LHC, CDF, and RHIC distributions. The signals were generated within a wider rapidity range ($2.0 \leq y \leq 4.5$) in order to account for the edge effects of the acceptance region.

The A×ϵ calculation has been performed on a run by run basis with a realistic MC simulation. It includes the experimental conditions (HV, LV and readout) of the Muon Spectrometer from Offline Calibration Data Base (OCDB). For each signal 8 million events were generated weighted by the unlike sign dimuon trigger for each run. The run by run A×ϵ for J/ψ and ψ(2S) in LHC11c and LHC11d periods was calculated. The A×ϵ factor was determined as the ratio of the number of reconstructed signals over the generated events in the muon acceptance. The average A×ϵ factor for J/ψ was found to be 0.1322 ± 0.0002 while the one for the ψ(2S) was 0.1664 ± 0.0002.

4.3.1 A×ϵ as a function of p_{T}

The A×ϵ was also estimated in bins of transverse momentum. The result is shown in Fig. 4.10 for J/ψ and ψ(2S), respectively. At lower p_{T} the A×ϵ for ψ(2S) is higher than that for J/ψ while for p_{T} greater than 5 GeV, the values are found to be similar for both of them. The higher values A×ϵ at low p_{T} for ψ(2S) is probably due to the fact that the mass of ψ(2S) is higher than J/ψ by 590 MeV.

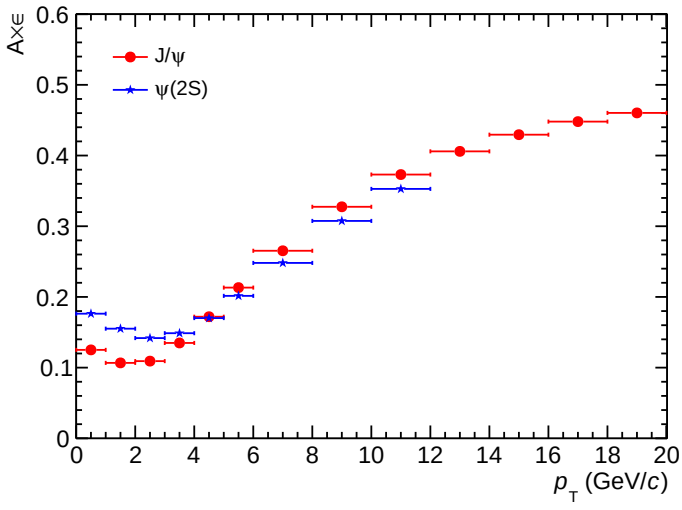

Figure 4.10: A×ϵ of J/ψ and ψ(2S) as a function of p_{T}.

4.3.2 A×ϵ as a function of y

The A×ϵ factors of J/ψ and ψ(2S) for each y bin is shown in Fig. 4.11. It can be seen from the figure that for both the resonances A×ϵ peaks around $y = 3.4$ and decreases by a factor ~ 5 at the edges.

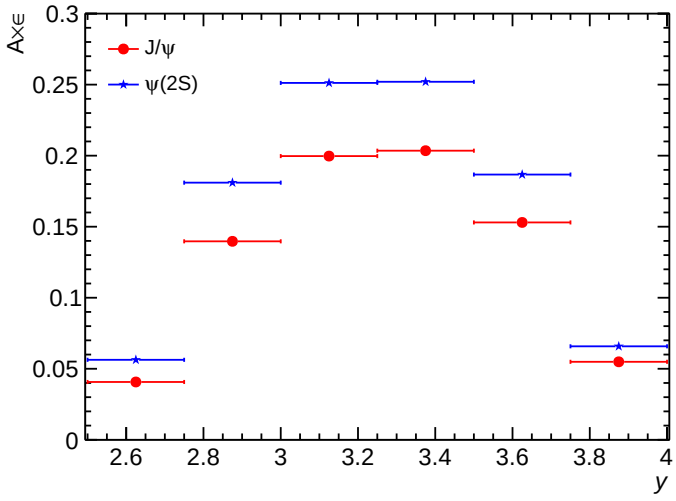

Figure 4.11: A×ϵ of J/ψ and ψ(2S) as a function of y.

4.3.3 Systematics on the MC input

The estimation of A×ϵ might depends on the $p_{\rm T}$ and y shapes of J/ψ and ψ(2S) used as input distributions in the MC simulations. In order to evaluate the sensitivity of the results on this initial choice, several MC simulations were performed, modifying the adopted $p_{\rm T}$ and y distributions of J/ψ and ψ(2S). The way in which the input distributions were varied is extensively described in reference [2] and takes into account two possible sources of bias: the precision on the experimental points used for the identification of the 1-D shapes and the correlation between $p_{\rm T}$ and y, as observed by LHCb for the J/ψ in the same rapidity region.

The systematic uncertainty on the integrated A×ϵ is 1.72% for both J/ψ and ψ(2S). The systematic uncertainty varies from 0.04% (0.42%) to 4.66% (6.44%) for J/ψ (ψ(2S)) in $p_{\rm T}$ and y bins. Table 4.9 summarizes the systematic uncertainties on A×ϵ in $p_{\rm T}$ and y bins used in this analysis.

Syst. Uncertainty on A×ϵ (%)			Syst. Uncertainty on A×ϵ (%)		
$p_{\rm T}$ bins	J/ψ	ψ(2S)	y bins	J/ψ	ψ(2S)
[0; 1]	0.04	0.42	[2.5; 2.75]	3.14	6.44
[1; 2]	0.18	0.34	[2.75; 3.0]	1.99	4.15
[2; 3]	0.22	0.35	[3.0; 3.25]	1.49	3.00
[3; 4]	0.48	0.59	[3.25; 3.5]	1.35	2.82
[4; 5]	0.65	0.75	[3.5; 3.75]	1.72	3.29
[5; 6]	0.68	0.82	[3.75; 4.0]	4.32	4.40
[6; 8]	0.74	0.88			
[8; 10]	0.69	0.86			
[10; 12]	1.02	1.14			
[12; 14]	1.58				
[14; 16]	2.29				
[16; 18]	3.33				
[18; 20]	4.66				

Table 4.9: Systematic uncertainties on A×ϵ in $p_{\rm T}$ and y bins for J/ψ and ψ(2S).

4.4 Tracking and Trigger efficiency

Considering the fact that the J/ψ and the ψ(2S) are very close in mass and their kinematics are very similar, the same systematic uncertainties are applied to both resonances.

4.4.1 Tracking efficiency and systematics

The single muon tracking efficiency integrated over p_{T} and y as obtained from real data was $\epsilon_{trk} = 87.2\%$. However, from simulation, the tracking efficiency was found to be 88.8%. This is the source of systematic error in tracking efficiency.

In order to quantify this systematic uncertainty, a pure signal simulation was performed, randomly injecting for each decay muon a survival probability of 98.2%. This value corresponded to the ratio of single muon tracking efficiencies quoted above which is also shown in Fig. 4.12. Such a probability was applied to both J/ψ decay muons and the surviving opposite sign tracks were then paired into J/ψ^S. The procedure was repeated by setting the survival probability to 100% which implies that no muon was excluded to form a J/ψ. The systematic uncertainty was obtained by taking the difference between the ratio (J/ψ^S)/(J/ψ) and unity. The p_{T} and y integrated systematic error was found to be 4%.

An additional systematic uncertainty was due to Correlated Dead Areas (CDA). The method above is blind to correlated inefficiencies of Detection Element, i.e. dead areas located in front of each other in the same station. This effect leads to an overestimation of the efficiency. A dedicated method to spot and to account for CDA led to a results of 2.5% systematic uncertainty.

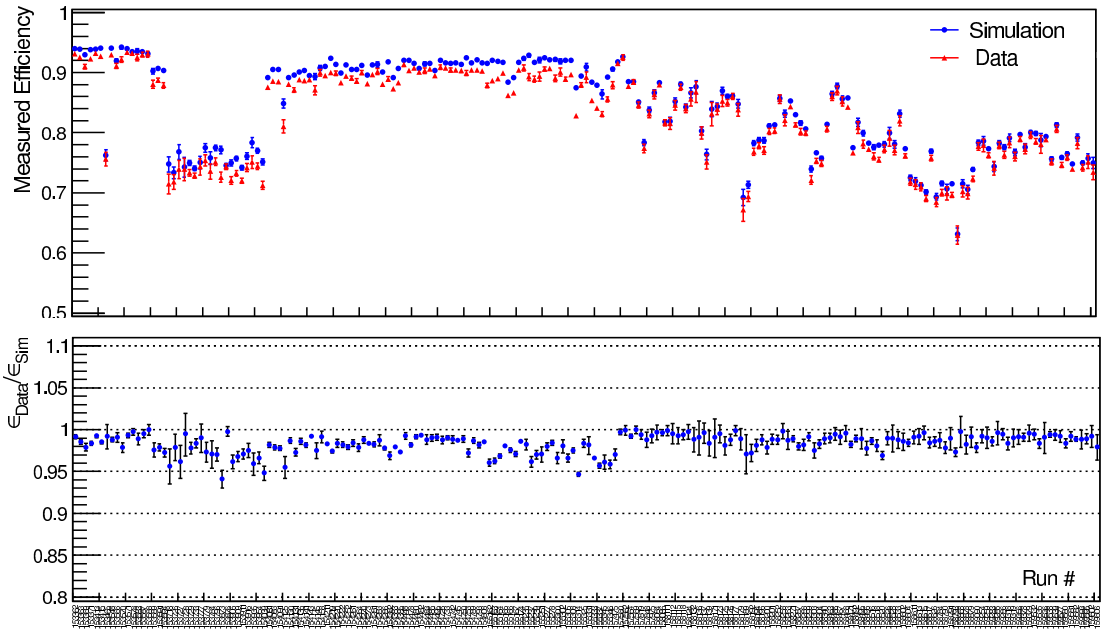

Figure 4.12: Run-per-run single muon tracking efficiency from data and MC simulation and the ratio of the two efficiency.

The total systematic uncertainty on the tracking efficiency was taken as 6.5%, by summing the two sources described above.

Uncertainty vs p_{T} and y

The same procedure has been applied to calculate tracking efficiency systematics as a function of the transverse momentum and rapidity. Fig. 4.13 shows the comparison between J/ψ^S and J/ψ in p_{T} and y bins. The ratio $\mathrm{J}/\psi^S/\mathrm{J}/\psi$ from which the systematic was extracted varies bin by bin. It is observed that the systematic uncertainty varies form $\sim 1\%$ ($\sim 5\%$) to $\sim 5\%$ ($\sim 9\%$) in p_{T} (y) bins. The additional systematic uncertainty due to CDA which is 2.5% was added to each bin.

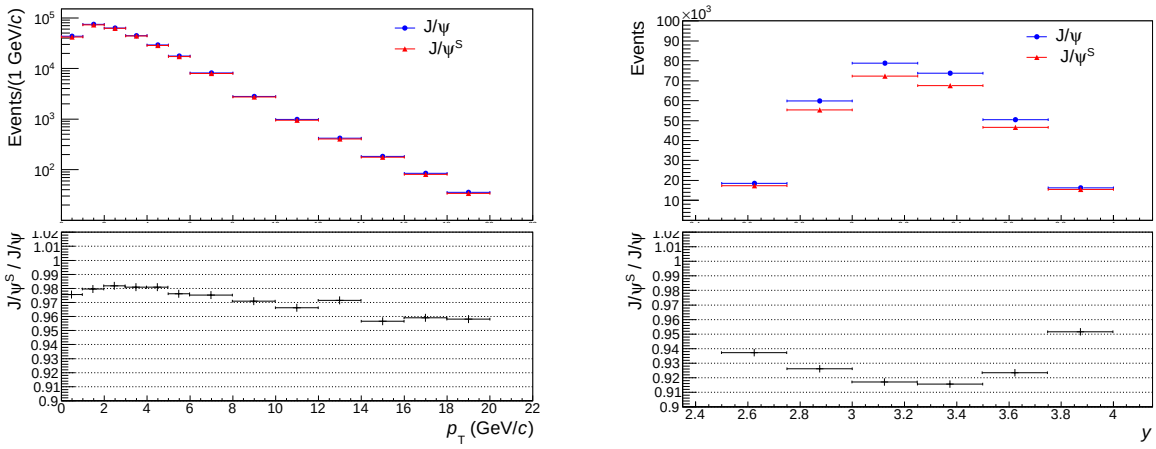

(a) $J/\psi^S/J/\psi$ ratio in p_T bins.

(b) $J/\psi^S/J/\psi$ ratio in y bins.

Figure 4.13: Tracking systematic uncertainty in p_T and y bins.

4.4.2 Trigger efficiency and systematics

The three contributions considered in the evaluation of the systematic uncertainty on trigger efficiency are: first, the difference in the shape of the trigger response function in data and MC; second, the uncertainty on the trigger chamber efficiency; third, the uncertainty from MB (V0and) trigger efficiency.

- The systematic uncertainty on the shape of the trigger response has been determined by comparing the influence of two different trigger response functions, obtained in data and in MC, on the A×ϵ of J/ψ. The trigger response functions have been obtained from the ratio of the Lpt (i.e. 1 GeV/c p_T threshold, used in this analysis) and Apt (i.e. 0.5 GeV/c p_T threshold) single muon p_T distributions. For the experimental data, single muons from LHC11c+LHC11d have been selected, while for the MC, muons from J/ψ decay have been used.

  The data and MC trigger response functions (Lpt/Apt) are shown in Fig. 4.14. Muons coming from the MC J/ψ decay were weighted according to their

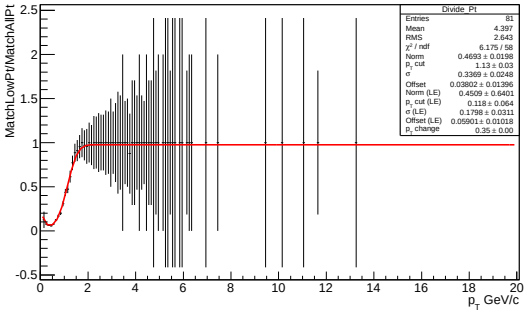

(a) Lpt/Apt from Data.

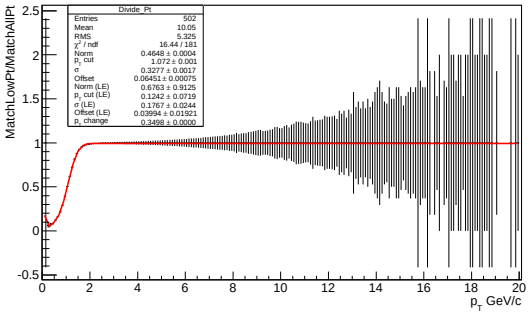

(b) Lpt/Apt from MC simulation.

Figure 4.14: Trigger response function (Lpt/Apt) in data and in MC simulation.

kinematics with the two different trigger response functions. Comparing the results obtained with the two distributions, the systematic uncertainty on the trigger has been evaluated. This integrated systematic uncertainty was found to be 2%.

- The systematic uncertainty arising from the intrinsic trigger efficiency was estimated by varying the efficiency of each local board by 2% in the simulation. This value corresponds to the uncertainty on the local board efficiency which was obtained by estimating the efficiency in different trigger classes and with different methods (in particular the response of the trigger chambers was estimated by searching for strips matching either tracks extrapolated from the tracker or the tracklets in the trigger). Using pure signal simulations, an uncertainty on dimuon of the order of 2% was found. This uncertainty is uncorrelated as a function of p_{T} and y since variations from one local board to another one may exist.

- The dimuon trigger used for this analysis was not dimuon trigger alone, but rather dimuon and V0and and it is possible that some J/ψ were produced in events where the V0and is not fired due to, e.g., low particle multiplicity. Such effect is not taken into account in the efficiency simulations, which only simulate

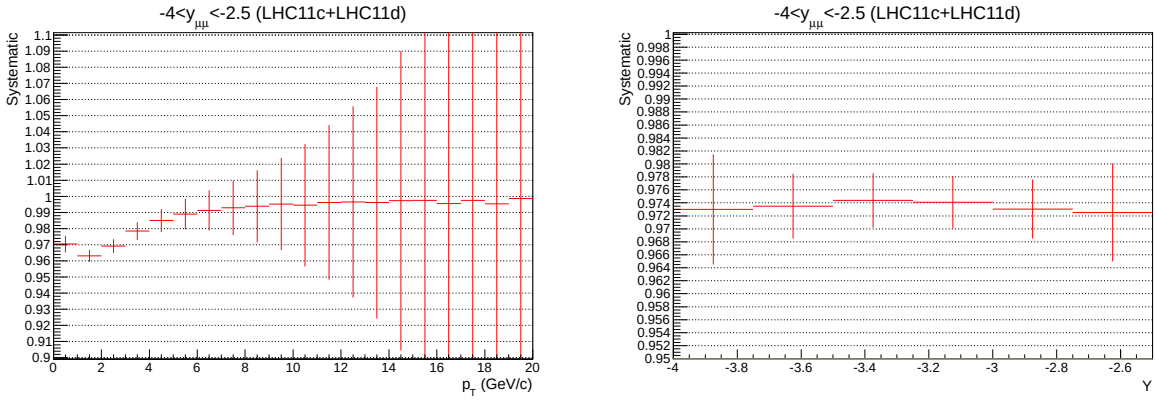

(a) Systematic in p_{T} bins.

(b) Systematic in y bins.

Figure 4.15: Trigger systematic uncertainty in p_{T} and y bins.

the dimuon trigger response to muon from J/ψ decays. In order to estimate such effect, we have extracted the J/ψ yield with and without requiring the V0and to be fired and we find that about 2% of J/ψ are lost when we require the V0and in the trigger. So, we assign 2% systematic uncertainty to our trigger efficiency due to the min bias condition.

The final trigger systematic uncertainty was found to be $\sim$ 3.5% by summing in quadrature the three contributions mentioned above.

Uncertainty vs p_{T} and y

The systematic uncertainty on the trigger efficiency as a function of p_{T} and y has been estimated bin to bin (uncorrelated uncertainty) and it amounts to 3.8% in the p_{T} range from 1 to 2 GeV/c and 1% in all the other bins. As a function of y, the variation is rather flat, with a maximum systematic uncertainty of the order of 2.8%. The systematic uncertainty as a function of p_{T} and y is shown in the Fig. 4.15. The other two systematics mentioned above were added in quadrature with this systematic.

4.5 Matching efficiency

The estimated systematic uncertainty on the matching efficiency between the tracking and the trigger tracks is 1%. Its origin lies in difference observed in simulations for different χ^2 cuts on the matching between the track reconstructed in the tracking chambers of the spectrometer and the one reconstructed in the trigger chambers. This error is uncorrelated as a function of p_{T} and y.

4.6 Summary of systematic uncertainties

The Table 4.10 summarizes the sources of various systematic uncertainties for both J/ψ and ψ(2S). The largest source of uncertainty is related to the signal extraction and the largest signal extraction uncertainty values corresponds to the highest p_{T} bin for both J/ψ and ψ(2S).

Source	J/ψ	ψ(2S)	Type
Signal extraction	2% (2%–15%)	8% (7.5%–11%)	Uncorrelated
Input MC parametrization	1.7% (0.1%–1.8%)	1.7% (0.4%–2.4%)	Uncorrelated
Trigger efficiency	3.5% (3%–5%)	3.5% (3%–5%)	Uncorrelated
Tracking efficiency	6.5% (4.5%–11.5%)	6.5% (4.5%–11.5%)	Uncorrelated
Matching efficiency	1%	1%	Uncorrelated
Luminosity	5%	5%	Correlated

Table 4.10: Systematic uncertainties on the quantities associated to J/ψ and ψ(2S) cross section measurement.

4.7 Results

The production cross-sections of J/ψ and ψ(2S) have been determined from:

$$\sigma_{\psi} = \frac{N_{\psi}}{(\mathrm{A}\times\epsilon)} \cdot \frac{1}{\mathrm{B.R.}_{\psi\to\mu^+\mu^-}} \cdot \frac{1}{\mathcal{L}_{\mathrm{int}}} \tag{4.5}$$

where:

- N_ψ is the number of J/ψ or ψ(2S) obtained from the signal extraction;
- A$\times\epsilon$ is the acceptance and efficiency correction factor of J/ψ or ψ(2S);
- BR($\psi \to \mu^+\mu^-$) is the branching ratio of J/ψ or ψ(2S) in dimuon decay channel ($J/\psi \to \mu^+\mu^-$ or $\psi(2S) \to \mu^+\mu^-$). For J/ψ the branching ratio is (5.93±0.06)% and for ψ(2S) it is (0.78±0.09)%;
- $\mathcal{L}_{\rm int}$ is the integrated luminosity [3].

4.7.1 J/ψ resonance

The inclusive J/ψ production cross sections in pp collisions at $\sqrt{s} = 7$ TeV is:
$\sigma_{\rm J/\psi}(2.5 < y < 4,\ 0 < p_{\rm T} < 20\ {\rm GeV}/c) = 6.69 \pm 0.04\ ({\rm stat.}) \pm 0.63\ ({\rm syst.})\ \mu{\rm b}$.
The systematic uncertainties on signal extraction, on the MC inputs, on the trigger and tracking efficiency, on the tracking and trigger tracks matching efficiency and on luminosity have been included.
This result is in good agreement with the previous ALICE published result [4]:
$\sigma_{\rm J/\psi}(2.5 < y < 4,\ p_{\rm T} > 0\ {\rm GeV}/c) = 6.31 \pm 0.25\ ({\rm stat.}) \pm 0.76\ ({\rm syst.})\ \mu{\rm b}$.
A comparison has been done with LHCb results [5] in terms of $\mathrm{d}\sigma_{\rm J/\psi}/\mathrm{d}y$, since the rapidity ranges are different between the two experiments.
LHCb provides the cross section for both prompt and B feed-down J/ψ. These two contributions have been added in order to compare with the ALICE inclusive measurement. The inclusive J/ψ cross section values are:
$\mathrm{d}\sigma_{\rm J/\psi}/\mathrm{d}y$ (LHCb) $= 4.82 \pm 0.02\ ({\rm stat.}) \pm 0.64\ ({\rm syst.})\ \mu{\rm b}$.
$\mathrm{d}\sigma_{\rm J/\psi}/\mathrm{d}y$ (ALICE) $= 4.46 \pm 0.03\ ({\rm stat.}) \pm 0.42\ ({\rm syst.})\ \mu{\rm b}$.

Assuming the systematic uncertainty from luminosity is fully correlated between the two experiments, ALICE and LHCb results are compatible within 1σ.

p_{T} differential production cross-section of J/ψ: $\mathrm{d}^2\sigma_{J/\psi}/\mathrm{d}p_{\mathrm{T}}\mathrm{d}y$

The previously published ALICE result was given in the range $0 < p_{\mathrm{T}} < 8$ GeV/c [4]. Due to the high statistics sample collected during the two periods (LHC11c and LHC11d) in 2011, we have now reached up to 20 GeV/c in p_{T} for J/ψ.

Fig. 4.16 shows the differential production cross-section of J/ψ in p_{T} bins. This result has been compared with the previous ALICE result, with a sizeable extension of the covered p_{T} range, and also with the measurement performed by the LHCb collaboration. In this case also, the LHCb results for both prompt and B feed-down J/ψ are summed.

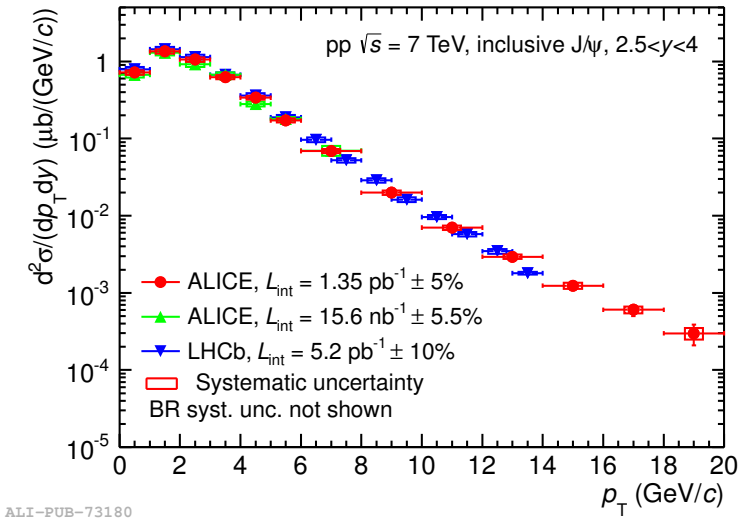

Figure 4.16: p_{T} differential production cross-section of J/ψ.

The measured p_{T} differential cross section of J/ψ is in good agreement with both previous ALICE results [4] and LHCb results [5].

p_T (GeV/c)	$N_{J/\psi}$ ± stat. ± syst.	A×ϵ ± stat. ± syst. (%)	$d^2\sigma_{J/\psi}/dp_T dy$ ± stat. (μb/(GeV/c))	$\Sigma_{syst.}$ (μb/(GeV/c))
[0; 1]	$10831 \pm 161 \pm 69$	$12.51 \pm 0.06 \pm 0.01$	0.7210 ± 0.0107	0.0491
[1; 2]	$17303 \pm 196 \pm 53$	$10.67 \pm 0.04 \pm 0.02$	1.3504 ± 0.0153	0.0930
[2; 3]	$13859 \pm 162 \pm 36$	$10.92 \pm 0.05 \pm 0.02$	1.0569 ± 0.0124	0.0682
[3; 4]	$10134 \pm 133 \pm 31$	$13.49 \pm 0.05 \pm 0.07$	0.6256 ± 0.0082	0.0383
[4; 5]	$7009 \pm 103 \pm 44$	$17.20 \pm 0.06 \pm 0.11$	0.3394 ± 0.0050	0.0202
[5; 6]	$4398 \pm 81 \pm 43$	$21.32 \pm 0.07 \pm 0.15$	0.1718 ± 0.0032	0.0108
[6; 8]	$4392 \pm 80 \pm 45$	$26.53 \pm 0.06 \pm 0.20$	0.0689 ± 0.0013	0.0044
[8; 10]	$1569 \pm 47 \pm 21$	$32.75 \pm 0.06 \pm 0.23$	0.0199 ± 0.0006	0.0013
[10; 12]	$628 \pm 31 \pm 7$	$37.31 \pm 0.07 \pm 0.38$	0.0070 ± 0.0003	0.0005
[12; 14]	$287 \pm 24 \pm 5$	$40.59 \pm 0.08 \pm 0.64$	0.0029 ± 0.0002	0.0002
[14; 16]	$128 \pm 17 \pm 7$	$42.95 \pm 0.08 \pm 0.98$	0.0012 ± 0.0002	0.0001
[16; 18]	$65 \pm 11 \pm 4$	$44.80 \pm 0.10 \pm 1.49$	0.0006 ± 0.0001	0.0001
[18; 20]	$33 \pm 10 \pm 5$	$46.03 \pm 0.11 \pm 2.15$	0.0003 ± 0.0001	0.0001

Table 4.11: Differential cross-section of J/ψ in 13 p_T bins. All uncorrelated systematic uncertainties are included in the systematic uncertainty on the differential cross-section.

Table 4.11 summarizes the number of J/ψ, A×ϵ and differential cross-sections in the 13 p_T bins.

y differential production cross-section of J/ψ: $d\sigma_{J/\psi}/dy$

The y differential cross-section has been measured in 6 rapidity bins with 0 GeV/c < p_T < 20 GeV/c. In previous ALICE result we had 5 bins in y [4].

Fig. 4.17 shows the differential production cross-section of J/ψ in rapidity bins. The result is compared with the previous ALICE result and also with the measurement performed by the LHCb collaboration. The measured y differential cross section of J/ψ is in good agreement with previous ALICE result [4] and also with LHCb values [5].

Table 4.12 summarizes the number of J/ψ, A×ϵ and differential cross-sections in 6 rapidity bins.

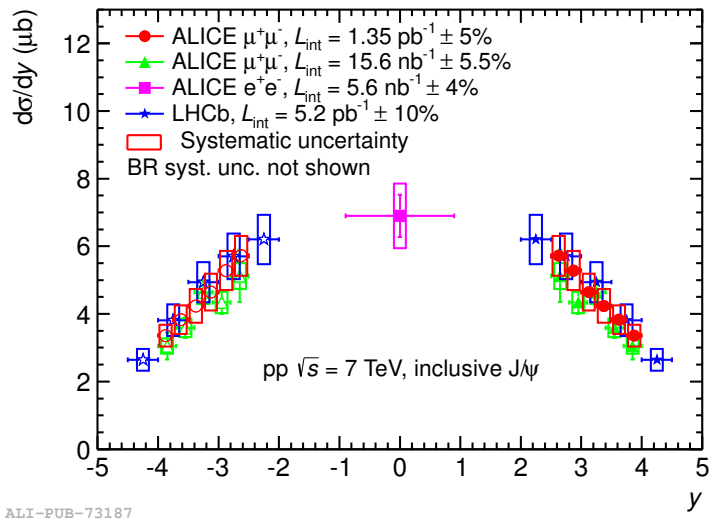

Figure 4.17: y differential production cross-section of J/ψ.

y	$N_{J/\psi}$ ± stat. ± syst.	A×ϵ ± stat. ± syst. (%)	$d\sigma_{J/\psi}/dy$ ± stat. (μb)	$\Sigma_{syst.}$ (μb)
[2.5; 2.75]	4660 ± 93 ± 39	4.07 ± 0.03 ± 0.13	5.721 ± 0.114	0.596
[2.75; 3.0]	14768 ± 165 ± 100	13.97 ± 0.05 ± 0.28	5.282 ± 0.059	0.586
[3.0; 3.25]	18559 ± 196 ± 118	19.97 ± 0.07 ± 0.30	4.644 ± 0.049	0.547
[3.25; 3.5]	17241 ± 185 ± 82	20.35 ± 0.07 ± 0.28	4.233 ± 0.045	0.503
[3.5; 3.75]	11727 ± 148 ± 65	15.30 ± 0.06 ± 0.26	3.830 ± 0.048	0.431
[3.75; 4.0]	3691 ± 82 ± 36	5.49 ± 0.03 ± 0.24	3.359 ± 0.075	0.327

Table 4.12: Differential cross-sections of J/ψ in 6 rapidity bins. All uncorrelated systematic uncertainties are included.

4.7.2 ψ(2S) resonance

The inclusive ψ(2S) production cross sections in pp collisions at $\sqrt{s} = 7$ TeV is:

$\sigma_{\psi(2S)}(2.5 < y < 4,\ 0 < p_T < 12\ \text{GeV}/c) = 1.13 \pm 0.07\ (\text{stat.}) \pm 0.14\ (\text{syst.})\ \mu\text{b}$.

A comparison has been done with LHCb results [6] in term of $d\sigma_{\psi(2S)}/dy$, since the rapidity ranges are different between two experiments:

$d\sigma_{\psi(2S)}/dy$ (LHCb) $= 0.68 \pm 0.004\ (\text{stat.}) \pm 0.048\ (\text{syst.})\ \mu\text{b}$.

$d\sigma_{\psi(2S)}/dy$ (ALICE) $= 0.75 \pm 0.05\ (\text{stat.}) \pm 0.09\ (\text{syst.})\ \mu\text{b}$.

ALICE result seems higher than the LHCb result. However, if we assume the systematic uncertainty from luminosity is uncorrelated (i.e. systematic on luminosity

is taken into account in the evaluation) between the two experiments, the discrepancy in this case is within 1σ.

It may be also noted that the ψ(2S) result of LHCb was extracted from a data sample different from the one used for the J/ψ.

p_{T} differential production cross-section of ψ(2S): $\mathrm{d}^2\sigma_{\psi(2S)}/\mathrm{d}p_{\mathrm{T}}\mathrm{d}y$

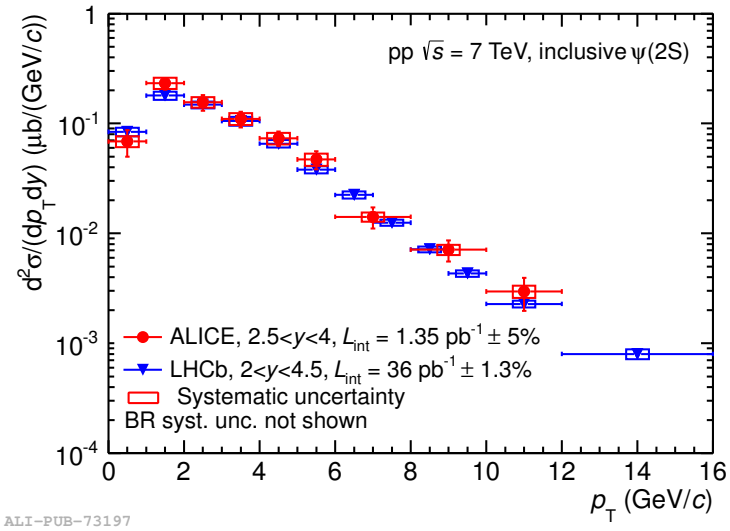

Figure 4.18: p_{T} differential production cross-section of ψ(2S).

p_T (GeV/c)	$\mathrm{N}_{\psi(2S)}$ ± stat. ± syst.	A×ϵ ± stat. ± syst. (%)	$\mathrm{d}^2\sigma_{\psi(2S)}/\mathrm{d}p_{\mathrm{T}}\mathrm{d}y$ ± stat. (μb/(GeV/c))	$\Sigma_{syst.}$ (μb/(GeV/c))
[0; 1]	$191 \pm 52 \pm 14$	$17.63 \pm 0.07 \pm 0.07$	0.0686 ± 0.0187	0.0079
[1; 2]	$572 \pm 73 \pm 45$	$15.51 \pm 0.06 \pm 0.05$	0.2335 ± 0.0298	0.0278
[2; 3]	$350 \pm 57 \pm 25$	$14.18 \pm 0.05 \pm 0.05$	0.1563 ± 0.0254	0.0174
[3; 4]	$259 \pm 42 \pm 24$	$14.87 \pm 0.06 \pm 0.09$	0.1103 ± 0.0179	0.0138
[4; 5]	$197 \pm 30 \pm 18$	$17.01 \pm 0.06 \pm 0.13$	0.0733 ± 0.0112	0.0090
[5; 6]	$150 \pm 28 \pm 14$	$20.15 \pm 0.07 \pm 0.17$	0.0471 ± 0.0088	0.0059
[6; 8]	$111 \pm 24 \pm 5$	$24.81 \pm 0.05 \pm 0.22$	0.0142 ± 0.0031	0.0014
[8; 10]	$69 \pm 15 \pm 4$	$30.75 \pm 0.06 \pm 0.26$	0.0071 ± 0.0015	0.0007
[10; 12]	$33 \pm 11 \pm 3$	$35.28 \pm 0.07 \pm 0.40$	0.0030 ± 0.0010	0.0004

Table 4.13: Differential cross-section of ψ(2S) in 9 p_{T} bins. All uncorrelated systematic uncertainties are included.

The differential cross-sections have been measured in 9 p_{T} bins between 0 - 12

GeV/c. Fig. 4.18 shows the differential production cross-sections of ψ(2S). The result has been compared with the measurement performed by the LHCb collaboration [6].

The measured p_{T} differential cross section of ψ(2S) is slightly higher than the LHCb result for some bins, for most of the bins cross sections are in good agreement.

Table 4.13 summarizes the number of ψ(2S), A$\times\epsilon$ and differential cross-sections in 9 p_{T} bins.

y differential production cross-section of ψ(2S): $\mathrm{d}\sigma_{\psi(2S)}/\mathrm{d}y$

The y differential cross-sections have been measured in 6 rapidity bins. Fig. 4.19 shows the differential production cross-section of ψ(2S) in rapidity bins. This is the first result on y differential cross section of ψ(2S) at forward rapidity at $\sqrt{s}$=7 TeV. Table 4.14 contains the number of ψ(2S), A$\times\epsilon$ and differential cross-sections in 6 rapidity bins.

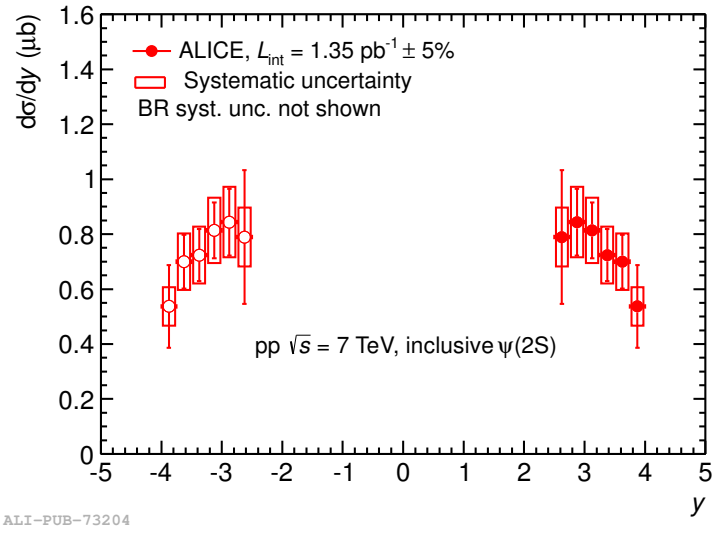

Figure 4.19: y differential production cross-section of ψ(2S).

y	$N_{\psi(2S)}$ ± stat. ± syst.	A×ϵ ± stat. ± syst. (%)	$d\sigma_{\psi(2S)}/dy$ ± stat. (μb)	$\Sigma_{syst.}$ (μb)
[2.5; 2.75]	$117 \pm 36 \pm 4$	$5.63 \pm 0.03 \pm 0.38$	0.789 ± 0.243	0.107
[2.75; 3.0]	$402 \pm 58 \pm 32$	$18.10 \pm 0.06 \pm 0.75$	0.844 ± 0.122	0.128
[3.0; 3.25]	$538 \pm 67 \pm 33$	$25.12 \pm 0.07 \pm 0.75$	0.814 ± 0.101	0.119
[3.25; 3.5]	$480 \pm 63 \pm 24$	$25.20 \pm 0.07 \pm 0.71$	0.724 ± 0.095	0.103
[3.5; 3.75]	$344 \pm 48 \pm 24$	$18.67 \pm 0.06 \pm 0.61$	0.700 ± 0.098	0.103
[3.75; 4.0]	$93 \pm 26 \pm 6$	$6.58 \pm 0.04 \pm 0.29$	0.537 ± 0.150	0.070

Table 4.14: Differential cross-section of ψ(2S) in 6 rapidity bins. All uncorrelated systematic uncertainties are included.

4.7.3 ψ(2S) to J/ψ cross-section ratio

The inclusive ψ(2S) to J/ψ cross-section ratio at $\sqrt{s} = 7$ TeV integrated over p_{T} and y is:

0.170 ± 0.011 (stat.) $\pm$ 0.013 (syst.).

The systematic uncertainty on signal extraction was directly evaluated on the ratio ψ(2S)/J/ψ, to reduce the dependence on the chosen signal function, since this is expected to be the same for J/ψ and ψ(2S). The systematic uncertainty on the acceptance input is included, while the other sources cancel out, as the two resonances under study are very close in the mass value. No polarization uncertainty is taken into account.

ψ(2S) to J/ψ cross-section ratio as a function of p_{T}

The ψ(2S) to J/ψ cross-section ratio have been measured as a function of p_{T} and a clear p_{T} dependence can be observed. In Fig. 4.20 the ALICE result is compared to LHCb [6]. The observed pattern is similar. However, it must be noted that a direct comparison with LHCb is not possible because in the present analysis the ratio is between inclusive ψ(2S) and J/ψ, while for LHCb, the ratio is between prompt ψ(2S) and J/ψ.

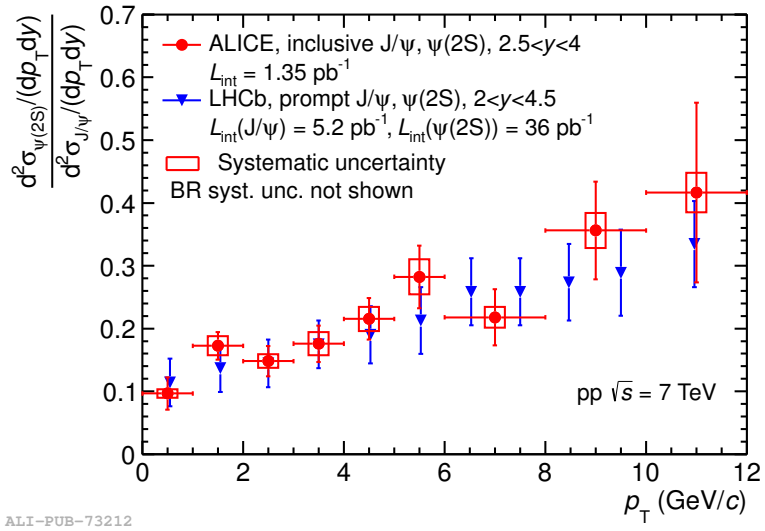

Figure 4.20: ψ(2S) to J/ψ cross-section ratio as a function of p_{T}.

Systematic uncertainty on acceptance input and signal extraction are included, while other systematics cancel out. No polarization uncertainty has been included. In LHCb, polarization uncertainty of ψ(2S) and J/ψ is also included along with the statistical and systematic errors.

ψ(2S) to J/ψ cross-section ratio as a function of y

Fig. 4.21 shows the ψ(2S) to J/ψ cross-section ratio as a function of rapidity. No strong y dependence is visible, in the y range covered by the ALICE muon spectrometer.

The inclusive $\psi(2S)$ to J/ψ cross-section ratio as a function of p_{T} and y are given in the Table 4.15.

Assuming that the ψ(2S) to J/ψ cross-section ratio is independent of y over the entire rapidity range, which is supported by our data, and multiplying it by the branching ratio of ψ(2S) decaying into J/ψ plus anything $\mathrm{BR}_{\psi(2S)\to J/\psi} = 60.3 \pm$

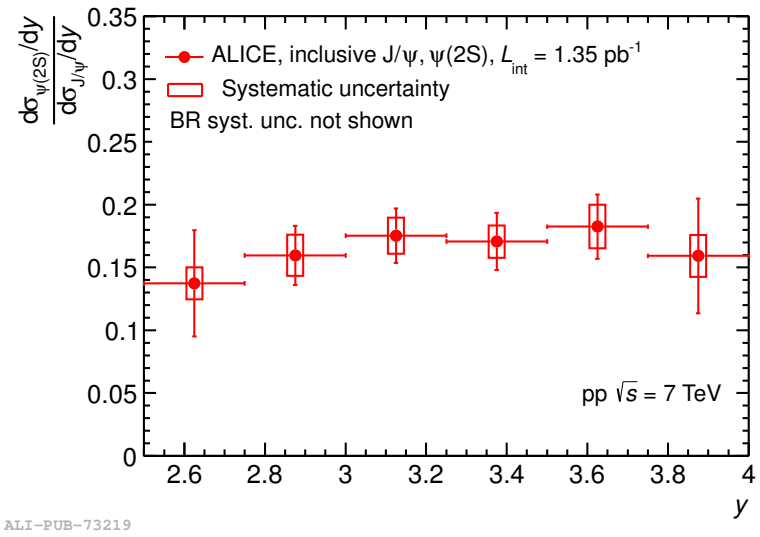

Figure 4.21: $\psi(2S)$ to J/ψ cross-section ratio as a function of y.

p_{T} (GeV/c)	$\frac{d^2\sigma_{\psi(2S)}/dp_{\mathrm{T}}dy}{d^2\sigma_{J/\psi}/dp_{\mathrm{T}}dy}$ $\pm$ stat.	$\Sigma_{syst.}$
[0; 1]	0.0966 $\pm$ 0.0259	0.0067
[1; 2]	0.1726 $\pm$ 0.0220	0.0151
[2; 3]	0.1481 $\pm$ 0.0240	0.0109
[3; 4]	0.1759 $\pm$ 0.0290	0.0185
[4; 5]	0.2152 $\pm$ 0.0331	0.0192
[5; 6]	0.2823 $\pm$ 0.0499	0.0280
[6; 8]	0.2179 $\pm$ 0.0447	0.0164
[8; 10]	0.3563 $\pm$ 0.0777	0.0278
[10; 12]	0.4165 $\pm$ 0.1431	0.0313
y	$\frac{d\sigma_{\psi(2S)}/dy}{d\sigma_{J/\psi}/dy}$ $\pm$ stat.	$\Sigma_{syst.}$
[2.5; 2.75]	0.1374 $\pm$ 0.0423	0.0128
[2.75; 3.0]	0.1596 $\pm$ 0.0235	0.0164
[3.0; 3.25]	0.1753 $\pm$ 0.0218	0.0143
[3.25; 3.5]	0.1707 $\pm$ 0.0227	0.0129
[3.5; 3.75]	0.1825 $\pm$ 0.0255	0.0174
[3.75; 4.0]	0.1592 $\pm$ 0.0457	0.0166

Table 4.15: Inclusive $\psi(2S)$ to J/ψ cross-section ratio as a function of p_{T} and y for pp collisions at $\sqrt{s}$ = 7 TeV.

0.7% [7], one gets the fraction of inclusive J/ψ coming from ψ(2S) decay $f^{\psi}(2S) = 0.103 \pm 0.007(\mathrm{stat.}) \pm 0.008(\mathrm{syst.})$.

4.8 Model Comparison

4.8.1 Differential production cross-section as a function of p_{T}

The measured inclusive J/ψ differential production cross-section as a function of p_{T} has been compared with three theoretical calculations in the framework of the CSM (Fig. 4.22): two complete calculations at LO and NLO and a third calculation that includes the contributions which are expected to dominate at NNLO [8]. In agreement with the authors, the calculations are scaled by a factor 1/0.6 to account for the fact that they correspond to direct J/ψ production, whereas they are compared to inclusive measurements. This scaling factor is obtained by assuming that about 20% of the inclusive J/ψ come from χ_c decay [9], 10% from ψ(2S) (factor f^{ψ}(2S), see previous section) and 9% from B mesons [5]. The LO calculation underestimates the data for $p_{\mathrm{T}} > 2$ GeV/c and the p_{T} dependence is much steeper than that of the measured cross-section. At NLO, the p_{T} dependence is closer to that of the data, but the calculation still underestimates the measured cross-section. The addition of some NNLO contributions further improves the agreement between the data and theory concerning the p_{T} dependence and further reduces the difference between the two, at the price of larger theoretical uncertainties.

Using a constant scaling factor for the direct-to-inclusive J/ψ production cross-sections ratio requires that the p_{T} distributions of direct and decay J/ψ are the same. This assumption is a rather crude approximation and for instance the LHCb collaboration has measured a significant increase of the fraction of J/ψ from B mesons decay with respect to p_{T} up to 30% for $p_{\mathrm{T}} > 14$ GeV/c. Properly accounting for theses variations may improve the agreement between data and theory at large p_{T}.

Fig. 4.23 presents the comparison of the inclusive J/ψ differential production

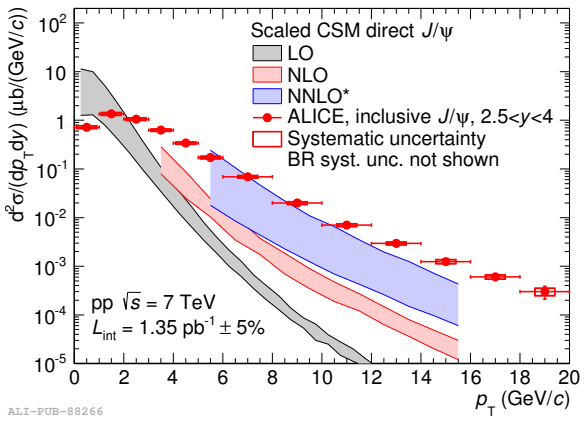

Figure 4.22: Inclusive J/ψ differential production cross-section as a function of p_{T}, compared to two scaled CSM calculations for direct J/ψ [8]

cross-section (top), the inclusive ψ(2S) differential production cross-section (middle) and the ratio between the two (bottom) as a function of p_{T} to two NRQCD calculations for prompt J/ψ and ψ(2S) production at NLO from [10] (left) and [11] (right). A number of theoretical uncertainties cancel while calculating the ψ(2S) over J/ψ ratio and the theory bands shown in the bottom panels are obtained by taking the ratio of the ψ(2S) and J/ψ upper and lower bounds from top and middle panels separately, rather than forming all four combinations.

The NRQCD calculations include both Color-Singlet (CS) contributions similar to the one shown in Fig 4.22 and Color-Octet (CO) contributions that are adjusted to experimental data by means of so-called long-range matrix elements (LRME). The two calculations differ in the LRME parametrization: the first (left panels of Fig. 4.23) uses three matrix elements whereas the second (right panels of Fig. 4.23) uses only two linear combinations of these three elements. Other differences include: the data sets used to fit these matrix elements, the minimum p_{T} above which the calculation is applicable and the way by which contributions from χ_c decays into prompt J/ψ and ψ(2S) production are accounted for. The first calculation has significantly larger uncertainties than the second for both the J/ψ cross section and the ψ(2S)-to-J/ψ

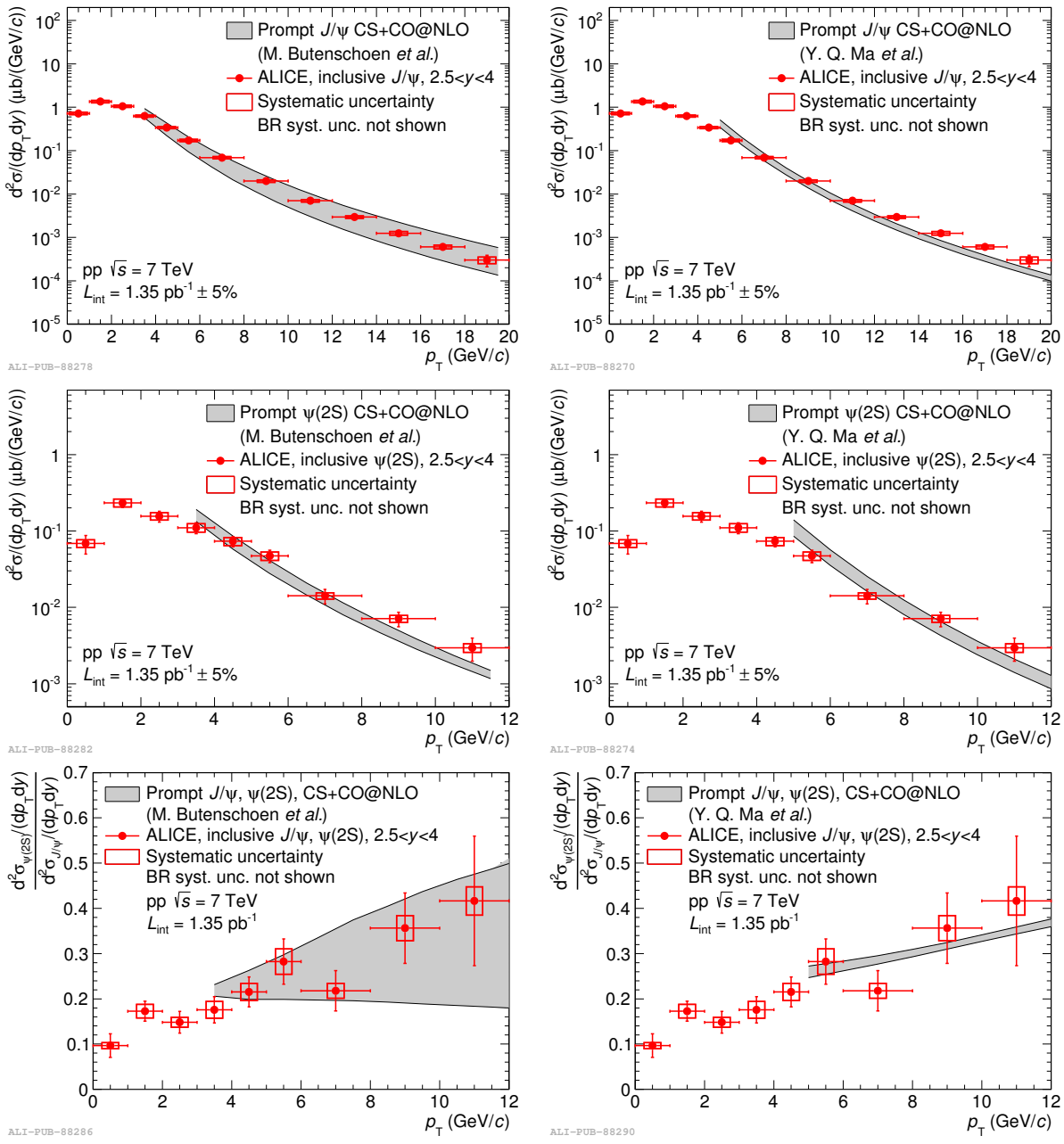

Figure 4.23: Inclusive J/ψ differential production cross-section (top), inclusive ψ(2S) differential production cross-section (middle) and inclusive ψ(2S) over J/ψ ratio (bottom) as a function of p_{T} compared to two NRQCD calculations from [10] (left) and [11] (right).

ratio. This is a consequence of the differences detailed above and in particular the fact that the fits start at a lower p_{T} and include a larger number of data sets.

Both calculations show reasonable agreement with the data for all three

observables. As is the case for the CSM calculation, properly accounting for the contribution from B meson decay to both J/ψ and ψ(2S) inclusive production in either the data or the theory would further improve the agreement between the two at high p_{T}.

In the CSM, the direct ψ(2S) over J/ψ ratio is a constant, independent of both p_{T} and rapidity. It corresponds to the ratio of the ψ(2S) and J/ψ wave functions at origin and amounts to about 0.6 [8]. This value, scaled by the appropriate direct-to-inclusive J/ψ and ψ(2S) ratios (0.6 for J/ψ, as discussed above, and 0.85 for ψ(2S) [6]), becomes 0.42. It is larger than the p_{T} integrated measurement and matches the values obtained for $p_{\mathrm{T}} > 9$ GeV/c.

Concerning the increase of the inclusive ψ(2S)-to-J/ψ cross-section ratio as a function of p_{T} observed in the data, a fraction originates from the contribution of ψ(2S) and χ_c decays. Assuming that the direct production of all three states follows the same p_{T} distribution, as it is the case in the CSM, the transverse momentum of J/ψ coming from the decay of the higher mass resonances must be smaller than the one of the parent particle. This result in an increase of the corresponding contribution to the inclusive cross-section ratio as a function of p_{T}.

The p_{T} dependence resulting from this effect on the inclusive ψ(2S)-to-J/ψ cross section ratio has been investigated using PYTHIA [12] for decaying the parent particle into a J/ψ. The result is normalized to our measured integrated ψ(2S)-to-J/ψ cross section ratio and compared to the data in Fig. 4.24. As expected, an increase of the ratio is observed with increasing p_{T} but it is not sufficient to explain the trend observed in the data. This indicates that the increase observed in the data cannot be entirely explained with sim-ple decay kinematics arguments and that other effects must be taken into account. A non-constant ratio can already be expected in the simplest case of CSM, where different dia-gram contributions to S- and P- wave

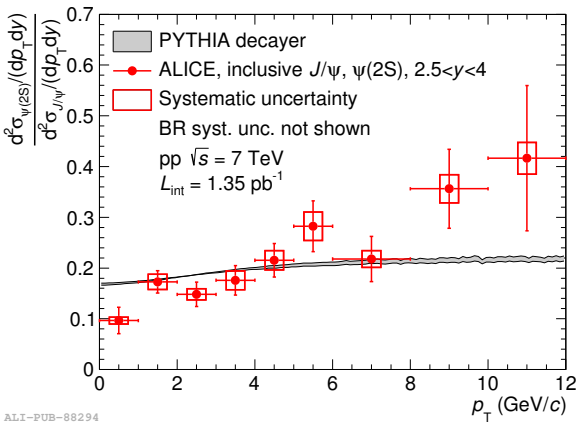

Figure 4.24: Inclusive $\psi(2S)$-to-J/ψ cross section ratio as a function of p_{T} compared to a simulation in which all direct quarkonia are considered to have the same p_{T} distribution and only kinematic effects due to the decay of higher mass resonances are taken into account, using PYTHIA [12].

charmonia production are expected, resulting in different feed-down contributions to J/ψ and $\psi(2S)$. On top of this Color-Octet contributions can also be added, as done in the NRQCD framework. The proper accounting of such contributions is sufficient to reproduce the trend observed in the data, as shown in Fig. 4.23, bottom panels.

4.8.2 Differential production cross-section as a function of rapidity

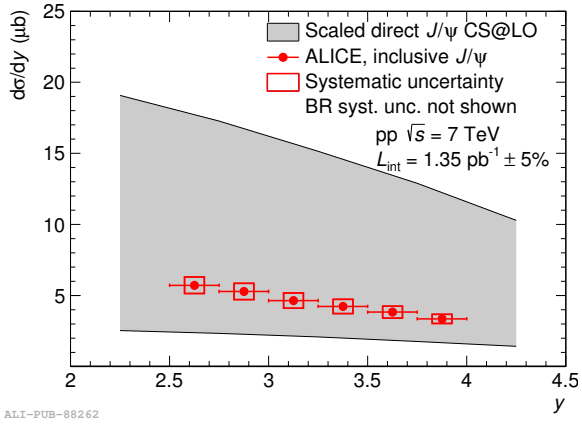

Figure 4.25: Differential inclusive production cross-section of J/ψ as a function of y compared to a CSM calculation at LO [13].

Since the LO CSM calculations described in the previous section extend down to zero p_{T} they can be integrated over p_{T} and evaluated as a function of the quarkonium rapidity. The result is compared to measured inclusive differential cross-sections of J/ψ in Fig. 4.25. As for the p_{T} differential cross-sections, the calculations are scaled by the direct over inclusive ratios described in the previous section (1/0.6 for J/ψ). Extending the calculation down to zero p_{T} results in rather large theoretical uncertainties: a factor four to five between the lower and upper bounds. The magnitude of the calculations is in agreement with the measurements. It is also worth noting that these calculations have no free parameters.

4.8.3 Theoretical work

We have also performed theoretical calculations of quarkium cross-sections within the framework of NRQCD and FONLL by taking into account all the feed-down contributions from higher quarkonium states and also from B decays [14]. These calculations are presented in detail in chapter 7.

Bibliography

[1] B. Abelev *et al.*, (ALICE Collaboration), "Measurement of quarkonium production at forward rapidity in pp collisions at $\sqrt{s}$ = 7 TeV", Eur. Phys. J. C **74**, 2974 (2014).

[2] `https://indico.cern.ch/getFile.py/access?contribId=5\&resId=0&materialId=slides&confId=246184`

[3] `https://aliceinfo.cern.ch/Notes/node/162`.

[4] K. Aamodt *et al.*, (ALICE Collaboration), "Rapidity and transverse momentum dependence of inclusive J/ψ production in pp collisions at $\sqrt{s}$=7 TeV", Phys. Lett. B **704**, 442-455 (2011).

[5] R. Aaij *et al.*, (LHCb Collaboration), "Measurement of J/ψ production in pp collisions at $\sqrt{s}$=7 TeV", Eur. Phys. J. C **71**, 1645 (2011).

[6] R. Aaij *et al.*, (LHCb Collaboration), "Measurement of ψ(2S) meson production in pp collisions at $\sqrt{s}$=7 TeV", Eur. Phys. J. C **72**, 2100 (2012).

[7] J. Beringer *et al.*, "Review of particle physics," Phys. Rev. D **86**, 010001 (2012).

[8] J.P. Lansberg. "J/ψ production at $\sqrt{s}$ = 1.96 and 7 TeV: Color-Singlet Model, NNLO* and polarisation", J. Phys. G **38**, 124110 (2011).

[9] R Aaij *et al.*, (LHCb Collaboration), "Measurement of the ratio of prompt χ_c to J/ψ production in *pp* collisions at $\sqrt{s} = 7$ TeV", Phys. Lett. B **718**, 431–440 (2012).

[10] M. Butenschoen and B. A. Kniehl. "World data of J/ψ production consolidate NRQCD factorization at NLO", Phys. Rev. D **84**, 051501 (2011).

[11] Y.Q. Ma, K. Wang, and K.T. Chao. "A complete NLO calculation of the J/ψ and ψ(2S) production at hadron colliders", Phys. Rev. D **84**, 114001 (2011).

[12] T. Sjostrand, S. Mrenna, P.Z. Skands, "PYTHIA 6.4 physics and manual", JHEP **0605**, 026 (2006). arXiv:hep-ph/0603175 [hep-ph]

[13] J.P. Lansberg. "Υ production in pp and pA collisions: from RHIC to the LHC", Nucl. Phys. **A470**, 910–911 (2013).

[14] Biswarup Paul, Mahatsab Mandal, Pradip Roy and Sukalyan Chattapadhyay, "Systematic study of charmonium production in pp collisions at LHC energies", J. Phys. G: Nucl. Part. Phys. **42** 065101 (2015).

Chapter 5

ψ(2S) production in p-Pb collisions

In this chapter, detailed analysis of ψ(2S) production in p-Pb collisions has been discussed. The data has been collected by ALICE Muon Spectrometer in specific trigger conditions at $\sqrt{s_{\rm NN}} = 5.02$ TeV in January and February 2013. The analysis has been performed at forward rapidity ($2.03 < y_{\rm cms} < 3.53$) as well as backward rapidity ($-4.46 < y_{\rm cms} < -2.96$) with data sample corresponding to an integrated luminosity of 5.01 ± 0.19 nb^{-1} and 5.81 ± 0.20 nb^{-1} respectively. These results have been published in ref [1].

5.1 Data Processing

The data sample, events, trigger and track selection have been described in details in chapter 3.

5.2 Signal extraction

The signal extraction is based on two different approaches. In the first method, charmonia yields are extracted through a fitting procedure. This approach is similar to the one followed for obtaining the J/ψ and ψ(2S) results in pp collisions. The second approach is based on a bin-counting technique ("electron-like" approach) and it has been introduced to reinforce the ψ(2S) signal extraction.

The signal extraction has been performed in two rapidity bins while $p_{\rm T}$ is integrated: $2.03 < y_{\rm cms} < 3.53$ for p-Pb and $-4.46 < y_{\rm cms} < -2.96$ for Pb-p. Also in 4 $p_{\rm T}$ bins (0-2, 2-3, 3-5, 5-8 GeV/c) with rapidity integrated both for p-Pb and Pb-p. The choice of the binning in all cases has been driven by the requirement of having a signal significance greater than 3.

5.2.1 Fitting technique

The J/ψ and ψ(2S) yields are extracted through a fit of the invariant mass spectrum, based on signal and background shapes.

As in pp collisions, in p-Pb also an extend Crystal Ball (CB2) function or new NA60 function has been used as signal shape. Due to the large background under the J/ψ region, it was not possible to fix the tails of these signal shapes by directly fitting the data. Therefore, the signal shape parameters were tuned on the J/ψ MC and then fixed in the fit procedure to the invariant mass spectra. In particular, parameters were tuned in each kinematic bin under study. Also the ψ(2S) tails were tuned, for each kinematic bin, on a ψ(2S) MC. The only signal parameters which were kept free in the final fit are the J/ψ mass, width and the absolute normalization of both resonances.

The background was described with a variable width gaussian function (VWG). As alternatives, an exponential function multiplied by a fourth order polynomials was also used as in pp case. Background parameters were directly tuned during the fit to the invariant mass spectrum. Due to the low signal over background ratio under the ψ(2S) its mass and width are linked to the J/ψ ones in the following way:

$$m_{\psi(2S)} = m_{J/\psi} + \left(m^{PDG}_{\psi(2S)} - m^{PDG}_{J/\psi}\right). \tag{5.1}$$

$$m_{\psi(2S)} = m_{J/\psi} + \left(m^{MC}_{\psi(2S)} - m^{MC}_{J/\psi}\right). \tag{5.2}$$

where, $m^{PDG}_{J/\psi}$ and $m^{PDG}_{\psi(2S)}$, and $m^{MC}_{J/\psi}$ and $m^{MC}_{\psi(2S)}$ are the masses of J/ψ and ψ(2S) from PDG and MC, respectively.

$$\sigma_{\psi(2S)} = \sigma_{J/\psi}.\frac{m_{\psi(2S)}}{m_{J/\psi}}. \tag{5.3}$$

$$\sigma_{\psi(2S)} = \sigma_{J/\psi}.\frac{\sigma^{MC}_{\psi(2S)}}{\sigma^{MC}_{J/\psi}}. \tag{5.4}$$

As an alternative, the sigma of the ψ(2S) was linked to the J/ψ through the ratio of the widths of the resonances, as obtained from the MC.

Fig. 5.1 shows the invariant mass spectra in the two rapidity ranges under study for the p-Pb (left) and Pb-p (right) data samples. Fig. 5.2 shows the invariant mass

spectra for 4 p_{T} bins for p-Pb (upper panel) and Pb-p (lower panel) collisions.

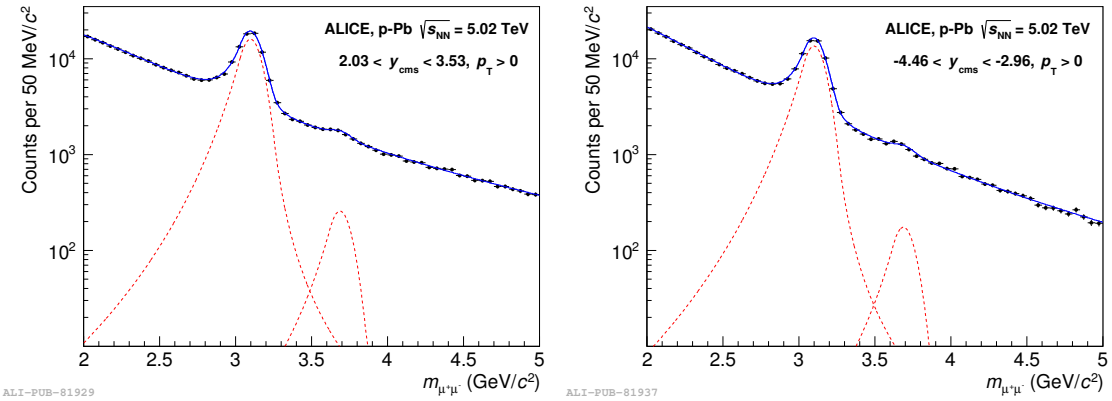

Figure 5.1: Opposite-sign dimuon invariant mass spectra for the p-Pb (left) and Pb-p (right) data samples, together with the result of a fit.

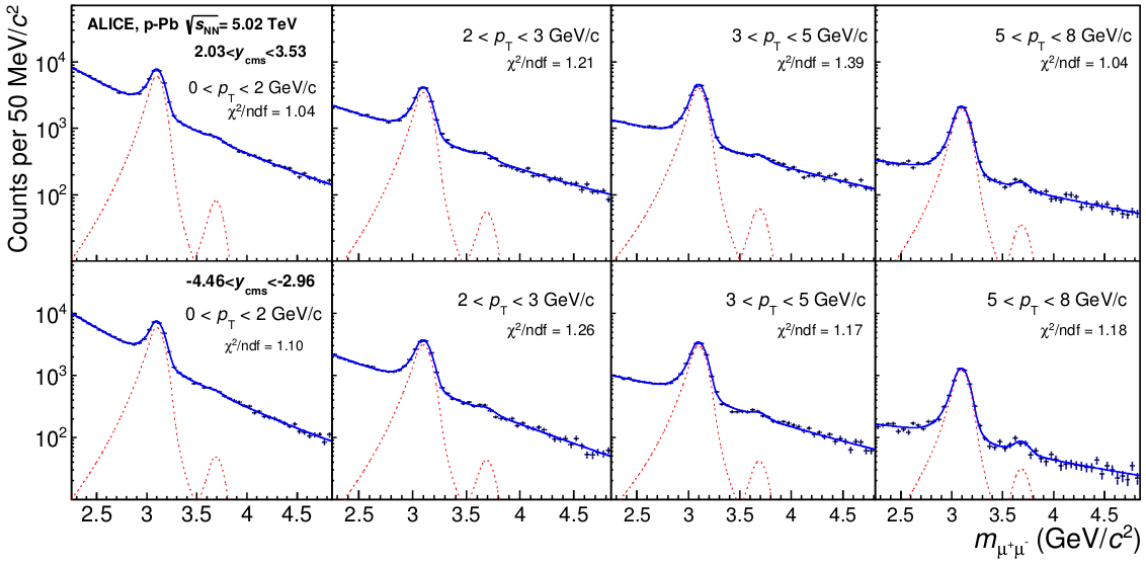

Figure 5.2: Opposite-sign dimuon invariant mass spectra, in bins of transverse momentum, for the p-Pb (upper) and Pb-p (lower) data samples.

5.2.2 "Electron-like" technique

In this method, the signal extraction is based on a bin counting technique on a background subtracted invariant mass spectrum. The procedure can be summarized in the following steps:

1. The invariant mass spectrum is fitted with a given signal and bacground shapes, in a similar way as it is done with the fitting technique. The obtained background shape is then subtracted from invariant mass spectrum (a poissonian uncertainty is associated to the background distibution).

2. The J/ψ yield is obtained by counting the signal events in the mass region 2.9-3.3 GeV/c^2, while the ψ(2S) yield is obtained by counting events in the mass range 3.5-3.8 GeV/c^2. The results are not sensitive to the specific bin counting range.

3. Since the number of J/ψ or ψ(2S) is counted in a limited mass range, a correction factor, evaluated from the signal shapes tuned on the data (obtained in step 1), allows us to obtain the total number of charmonia.

4. A further additional correction factor, again evaluated from the signal mass shape of step 1, allows us to correct for the J/ψ contribution under the ψ(2S) peak. On the contrary, the ψ(2S) contribution under the J/ψ peak can be neglected.

The procedure is repeated, choosing different signal and background shapes. In particular the same shapes introduced in the first approach are used.

5.2.3 Systematic uncertainties in signal extraction

In both the approaches, J/ψ and ψ(2S) yields were extracted slightly modifying the fitting procedure or the signal and background shapes. For each combination of signal and background shape, the fitting range was also modified, to verify the stability of the fit. For each combination, the width of the ψ(2S) was fixed either to the ratio of the J/ψ and ψ(2S) masses or to the ratio of their widths obtained in the

MC. Alternative values of the ψ(2S) mass resolution were also tested, allowing the ratio ($\sigma^{\rm MC}_{\psi(2S)}/\sigma^{\rm MC}_{J/\psi}$) to vary within 10%.

The summary of the performed tests, similar to pp case is:

- CB2 signal shape and VWG for the background.
- CB2 signal shape and 4th order polynomial $\times$ exponential for the background.
- NA60 signal shape and VWG for the background.
- NA60 signal shape and 4th order polynomial $\times$ exponential for the background.

These tests were repeated for both the standard fitting approach and the "electron-like" technique. The extracted J/ψ and ψ(2S) yields were obtained with the various performed tests for p-Pb and Pb-p collisions. Similar behaviours were observed in all the $p_{\rm T}$ bins. As discussed in pp case, the final J/ψ and ψ(2S) yields have been obtained as weighted average of different tests. The systematic uncertainty corresponds to the RMS of the yields distribution. For the ψ(2S)/J/ψ ratio, the systematic uncertainty on the signal extraction was evaluated directly on the ratio and it is dominated by the uncertainty on the ψ(2S).

Extracted yields in this approach are in very good agreement with the values obtained with the fitting technique. The systematic uncertainty on signal extraction for integrated case are 9.5% for p-Pb and 9.3% for Pb-p, while it varies from 8% (8.6%) to 11.9% (12.7%) for p-Pb (Pb-p) in $p_{\rm T}$ bins. Table 5.1 summarizes the result on signal extraction together with the statistical and systematic uncertainty for integrated case.

Collision	Rapidity	$N_{\psi(2S)}$
p-Pb	$2.03 < y_{cms} < 3.53$	1069 ± 130 (stat.) ± 102 (syst.)
Pb-p	$-4.46 < y_{cms} < -2.96$	697 ± 111 (stat.) ± 65 (syst.)

Table 5.1: Summary of signal extraction of ψ(2S) for p-Pb and Pb-p data samples.

5.3 Acceptance and efficiency corrections

In p-Pb and Pb-p collisions, the occupancy in the detector is small and no deterioration of the muon tracking chamber efficiency was observed even for most central events, justifying the use of a pure signal simulation. As in such simulation the vertex could not be reconstructed, the events were generated and reconstructed at a fixed vertex position. A run-per-run simulation, with a number of events generated proportional to the number of unlike-sign dimuon triggers after the event physics selection, was performed using a pure signal parametrization that reproduced the measured J/ψ kinematical $p_{\rm T}$ and y distributions to correct the data by the detector acceptance and efficiency (A×ϵ). The polarization of the J/ψ was assumed to be zero.

At the end of each period, hardware issues in the tracking chambers (mainly HV trips) had increased leading to a decrease of the tracking efficiency and of A×ϵ. The $p_{\rm T}$ and rapidity input distributions of the generated J/ψ were tuned directly on the raw number of J/ψ extracted from the data. Starting with a generator based on a parametrization of the J/ψ production in pp collisions at 5.02 TeV, a single iteration over the corrected data allowed to describe the $p_{\rm T}$ and rapidity distribution within 10%. The integrated A×ϵ of J/ψ was approximately 25% and 17% for the periods LHC13de and LHC13f, respectively. It was also estimated as a function of rapidity (integrated over $p_{\rm T}$) and as a function of $p_{\rm T}$.

The A×ϵ of ψ(2S) was evaluated using MC simulations in a similar way as for the J/ψ. The input $p_{\rm T}$ distributions for ψ(2S) were obtained from those used for the J/ψ [2], scaled such that $\langle p_{\rm T}\rangle^{\psi(2S)}_{\rm pPb,5.02TeV} = \langle p_{\rm T}\rangle^{\rm J/\psi}_{\rm pPb,5.02TeV} \times (\langle p_{\rm T}\rangle^{\psi(2S)}_{\rm pp,7TeV}/\langle p_{\rm T}\rangle^{\rm J/\psi}_{\rm pp,7TeV})$,

and using the $\sqrt{s}$ = 7 TeV pp values from LHCb [3, 4] obtained in the slightly larger range $2 < y_{\rm cms} < 4.5$. The input y distributions of ψ(2S) were obtained from those used for the J/ψ assuming a scaling of the widths with $y^{\psi(2S)}_{\rm max}/y^{\rm J/\psi}_{\rm max}$, where $y^{i}_{\rm max} = \log(\sqrt{s}/m_i)$ is the maximum rapidity for the resonance i at the $\sqrt{s}$ value under study. An unpolarized distribution for the ψ(2S) was assumed, according to the results obtained in pp collisions at $\sqrt{s}$ = 7 TeV by the CMS and LHCb experiments [5, 6]. The integrated A$\times\epsilon$ of ψ(2S) was approximately 27% and 18% for the periods LHC13de and LHC13f, respectively.

5.3.1 Systematics on the MC input

The systematic uncertainty on the A$\times\epsilon$ was obtained by defining y ($p_{\rm T}$) distributions for selected phase space regions, corresponding to sub-ranges in $p_{\rm T}$ (y) and centrality of the collision. The hardest and softest spectra for each variable were then used as inputs to the MC calculation and the variation with respect to the default acceptance values gives the systematic uncertainty. The systematic uncertainty amounts to 1.5% for both p-Pb and Pb-p for J/ψ and 1.8% (2.5%) for p-Pb (Pb-p) for ψ(2S).

5.4 Tracking and Trigger efficiency

The same systematic uncertainties have been applied to both J/ψ and ψ(2S) since they are very close in mass and their kinematics are very similar.

5.4.1 Tracking efficiency and systematics

The procedure to calculate the tracking efficiency and its systematics is same as for pp case and it has been explained in detail in the previous chapter. The tracking efficiency was measured on the data and amounts to approximately 90%, 85% and 74% for LHC13d, LHC13e and LHC13f respectively. It fluctuates from one run to another depending on the tracking chambers condition as illustrated in Fig. 5.3. It does not suffer any centrality dependence (the centrality is estimated using the V0M estimator), justifying the use of pure signal MC simulations to determine A$\times\epsilon$. The tracking efficiency measured on the data is also compared to the one measured on the MC in Fig. 5.3. The difference observed between the data and the MC is taken as a systematics for single muon and was found to be 2% (3%) for p-Pb (Pb-p). For dimuon, this uncertainty was assumed to be uncorrelated and the resulting uncertainty was 4% (6%) for p-Pb (Pb-p). The uncertainty was found to be uncorrelated with respect to y, p_{T} and the collision system. It represents the main uncertainty of this analysis.

5.4.2 Trigger efficiency and systematics

The trigger efficiency and its systematics calculation is similar to that described in the previous chapter. In p-Pb collisions, the trigger efficiency was measured on data and amounts to approximately 97 - 97.5% for each chamber leading to an overall trigger efficiency above 99%. At large p_{T}, the trigger efficiency originates from the intrinsic local board efficiency while at low p_{T}, it decreases due to the trigger threshold of 0.5 GeV/c .

The systematic uncertainty arising from the intrinsic trigger efficency was estimated by varying by 2% each local board in the simulation. This value corresponds

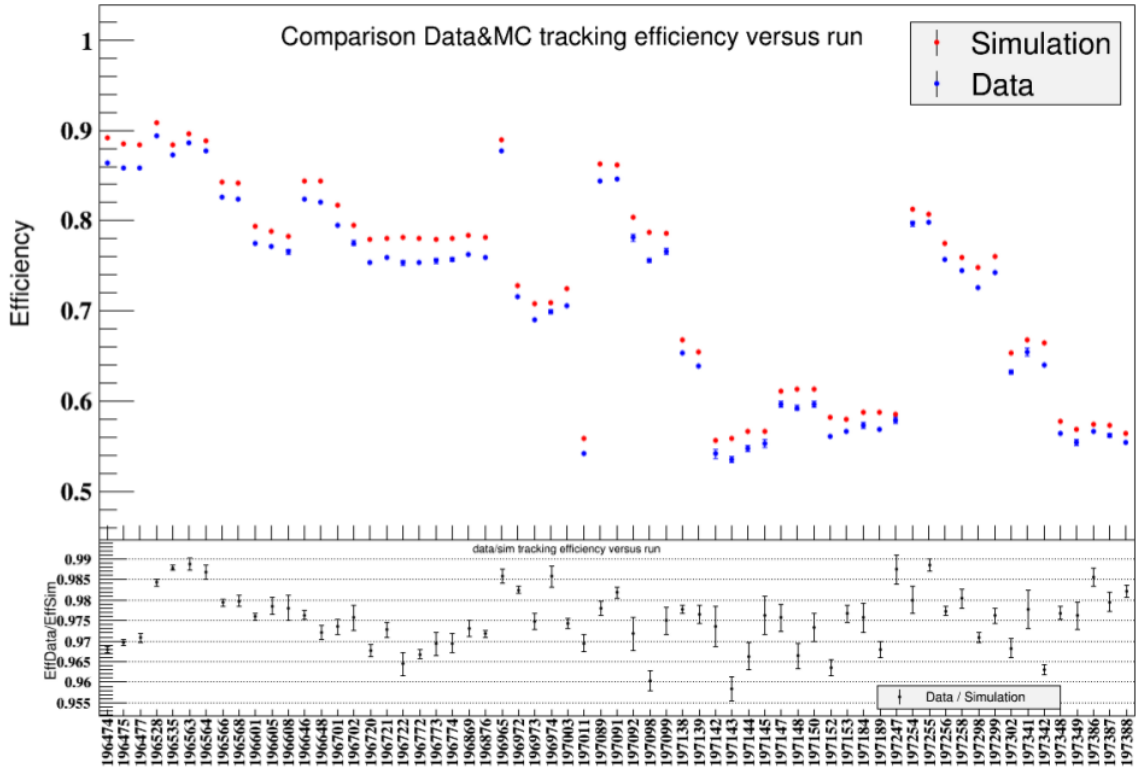

Figure 5.3: Tracking efficiency measured both on data and MC simulations for Pb-p.

to the uncertainty on the local board efficiency determined by varying the cuts on the trigger or tracker tracks used to determined the intrinsic efficiency. Using pure signal simulations, an uncertainty on dimuon of the order of 2% was found. This uncertainty is uncorrelated as a function of p_{T}, y and collision system since the variations were at the level of the local boards.

The systematic uncertainty arising from the trigger p_{T} threshold was estimated by varying the p_{T} dependence of the trigger efficiency in the simulations. In previous runs, the low trigger threshold was set to 1 GeV/c and the difference of the ratio of data/MC between the 0.5 (all) and 1 (low) GeV/c trigger thresholds was considered to estimate the systematic uncertainty on the trigger threshold. However in 2013, the low trigger threshold was set to 0.5 GeV/c and it was therefore not possible to estimate the bias using the same method. Instead, a similar variation data/MC ratio

between the 0 (i.e no trigger requirement) to 0.5 GeV/c trigger threshold in 2013 data was assumed. From this study, the systematic uncertainty is found to be of the order of 3% for the dimuon sample and which decreases with higher value of p_{T}. It is an uncorrelated uncertainty with respect to y, p_{T} and collision system.

On top of the contribution described above, which takes into account a small discrepancy of the trigger response function in data and in MC, there was an additional 2% due to the uncertainty on the evaluation of the intrinsic efficiency of the trigger chambers. This systematic uncertainty on trigger efficiency is considered to be uncorrelated between p-Pb and Pb-p.

The final trigger systematic uncertainty was found to be 2.8% and 3.2% for p-Pb and Pb-p, respectively. It varied from 2% to 3.5% in p_{T} bins both for p-Pb and Pb-p.

5.5 Matching efficiency

The systematic uncertainty on the matching efficiency between the track reconstructed in the tracking chambers and the one reconstructed in the trigger chambers was found to be 0.5 - 1% for the single muon. It was estimated as the difference observed in simulation and data when applying different χ^2 cuts on the matching between the trigger and tracker track. For large mass resonance as the J/ψ and ψ(2S), this uncertainty amounts to 1%. This uncertainty is uncorrelated as a function of p_{T}, y and the collision system. The same uncertainty applies to the J/ψ and ψ(2S).

5.6 Normalization CINT7 - CMUL7

The systematic uncertainty on this normalization amounts to 1% and is described in chapter 3. This uncertainty is correlated as a function of p_{T} and y and uncorrelated for the different collision system. However as it is small, it is also considered as uncorrelated in p_{T} and y and applied to both J/ψ and ψ(2S).

5.7 Others

The systematic uncertainty on the nuclear thickness function $\langle T_{\mathrm{pPb}} \rangle$ is 0.0035/mb (3.6%). The systematic uncertainty on the minimum bias cross sections $\sigma_{\mathrm{pPb}}^{\mathrm{MB}}$ is $\sim$ 3.2% (3%) in p-Pb (Pb-p). Both the uncertainties are correlated as a function p_{T}, y and the collision system.

5.8 Summary of systematic uncertainties

The summary of systematic uncertainties for ψ(2S) are given in Table 5.2. The uncertainties due to luminosity measurement [7] are divided in two components uncorrelated and correlated. All the other uncertainties are uncorrelated between forward and backward rapidity. Uncertainties refer to p_{T}-integrated quantities and, where they depend on p_{T}, the corresponding maximum and minimum values are also quoted. The efficiency-related uncertainties refer to muon pairs.

Source of Systematic Uncertainties	**Forward Rapidity** $2.03 < y_{\rm cms} < 3.53$	**Backward Rapidity** $-4.46 < y_{\rm cms} < -2.96$	**Type**
Signal extraction	9.5% (8% − 11.9%)	9.3% (8.6% − 12.7%)	Uncorrelated
Input MC parametrization	1.8% (1.5% − 1.5%)	2.5% (1.5% − 1.7%)	Uncorrelated
Trigger efficiency	2.8% (2% − 3.5%)	3.2% (2% − 3.5%)	Uncorrelated
Tracking efficiency	4%	6%	Uncorrelated
Matching efficiency	1%	1%	Uncorrelated
$\mathcal{L}_{\rm int}$	3.4%	3.1%	Uncorrelated
$\mathcal{L}_{\rm int}$	1.6%	1.6%	Correlated
$\langle T_{\rm pPb} \rangle$	3.6%	3.6%	Correlated
$\sigma^{\rm MB}_{\rm pPb}$	3.2%	3%	Correlated

Table 5.2: Systematic uncertainties on each quantity entering in the calculations of the inclusive ψ(2S) results. The various sources are grouped according to the degree of correlation of the uncertainties between forward and backward rapidity.

5.9 Results

5.9.1 ψ(2S) cross-section

The production cross-section times the branching ratio B.R.$(\psi(2S) \to \mu^+\mu^-)$ for inclusive ψ(2S) production in p-Pb collisions (and similarly for Pb-p) can be written as:

$$\text{B.R.}_{\psi(2S)\to\mu^+\mu^-} \cdot \sigma^{\psi(2S)}_{\rm pPb} = \frac{N^{\psi(2S)}_{\rm pPb}}{(\text{A}\times\epsilon)^{\psi(2S)}_{\rm pPb}} \cdot \frac{1}{\mathcal{L}^{\rm pPb}_{\rm int}} \tag{5.5}$$

where:

- $N^{\psi(2S)}_{\rm pPb}$ is the number of ψ(2S) obtained from signal extraction. It depends on the rapidity bin under consideration;
- $(\text{A}\times\epsilon)^{\psi(2S)}_{\rm pPb}$ is the acceptance times efficiency correction factor for ψ(2S). It depends on the considered rapidity bin;
- B.R.$_{\psi(2S)\to\mu^+\mu^-}$ is the branching ratio for $\psi(2S) \to \mu^+\mu^-$ decay and its value is

(0.78±0.09)%.

- $\mathcal{L}_{\rm int}^{\rm pPb}$ is the integrated luminosity, calculated as $N_{\rm MB}/\sigma_{\rm pPb}^{\rm MB}$, discussed in details in chapter 3. $N_{\rm MB}$ is the number of minimum bias p-Pb events. The total number of minimum bias event is obtained by re-normalising the measured number of CMUL events. The normalisation factor is 1129 ± 11 for p-Pb and 589 ± 6 for Pb-p. $\sigma_{\rm pPb}^{\rm MB}$ [7] is the cross sections for the occurrence of the MB condition, is 2.09 ± 0.07 b for the p-Pb and 2.12 ± 0.07 b for the Pb-p.

The inclusive ψ(2S) cross-section in p-Pb collisions at $\sqrt{s_{\rm NN}} = 5.02$ TeV are:

$$\text{B.R.} \cdot \sigma_{\rm pPb}^{\psi(2S)}(2.03 < y_{\rm cms} < 3.53) = 0.791 \pm 0.096(\text{stat.}) \pm 0.091(\text{syst.uncorr.}) \pm 0.013(\text{syst.corr.})\ \mu\text{b} \quad (5.6)$$

$$\text{B.R.} \cdot \sigma_{\rm Pbp}^{\psi(2S)}(-4.46 < y_{\rm cms} < -2.96) = 0.653 \pm 0.104(\text{stat.}) \pm 0.080(\text{syst.uncorr.}) \pm 0.010(\text{syst.corr.})\ \mu\text{b} \quad (5.7)$$

All the individual systematic uncertainties have been listed in Table 5.2 have been included.

The sizeable ψ(2S) statistics collected in p-Pb (Pb-p) collisions allows for a differential study of the cross-section as a function of $p_{\rm T}$, in the range $0 < p_{\rm T} < 8$ GeV/c. The analysis was carried out with the same procedure adopted for the integrated data samples. The systematic uncertainties were evaluated differentially in $p_{\rm T}$ and their range is reported in Table 5.2. The differential cross sections at forward and backward rapidity are shown in Fig. 5.4. The systematic uncertainties on signal extraction, MC input and efficiencies are considered to be uncorrelated in different bins. The uncertainties associated with luminosity measurements are correlated between the various $p_{\rm T}$ bins and partially correlated between p-Pb and Pb-p. Table 5.3 and 5.4 summarizes the ψ(2S) differential cross-sections in 4 $p_{\rm T}$ bins for p-Pb and Pb-p, respectively.

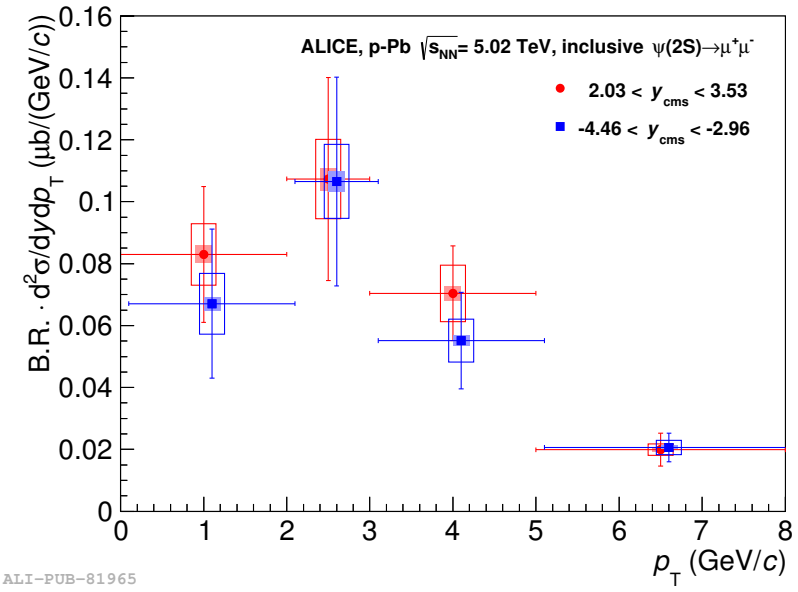

Figure 5.4: The $\psi(2S)$ differential cross sections B.R.$\cdot \mathrm{d}^2\sigma/\mathrm{d}y\mathrm{d}p_\mathrm{T}$ for p-Pb and Pb-p collisions. The horizontal bars correspond to the width of the p_T bins. The vertical error bars correspond to the statistical uncertainties, the boxes to uncorrelated systematic uncertainties and the shaded areas to p_T-correlated uncertainties. A global 1.6% uncertainty applies to both p-Pb and Pb-p results. The points corresponding to negative y are slightly shifted in p_T to improve visibility.

p_T GeV/c	$\mathrm{d}^2\sigma^{\psi(2S)}_{\mathrm{pPb}}/\mathrm{d}p_\mathrm{T}\mathrm{d}y$ [μb/(GeV/c)] Value $\pm$ stat. $\pm$ uncorr. $\pm$ p_T-corr. $\pm$ global
[0; 2]	$0.0830 \pm 0.0219 \pm 0.0028 \pm 0.0099 \pm 0.0013$
[2; 3]	$0.1074 \pm 0.0328 \pm 0.0036 \pm 0.0128 \pm 0.0017$
[3; 5]	$0.0704 \pm 0.0153 \pm 0.0024 \pm 0.0091 \pm 0.0011$
[5; 8]	$0.0199 \pm 0.0053 \pm 0.0007 \pm 0.0019 \pm 0.0003$

Table 5.3: The $\psi(2S)$ differential cross-sections as a function of p_T for p-Pb ($2.03 < y_\mathrm{cms} < 3.53$).

5.9.2 $\psi(2S)$ to J/ψ cross-section ratio

The study of the $\psi(2S)$ to J/ψ cross section ratio is very interseting in many ways. The comparison of this ratio between different systems offers a powerful tool to investigate nuclear effects on charmonium production. In addition, several systematic uncertainties cancel, or are significantly reduced in such ratios. In the present analysis, the tracking, trigger and matching efficiencies, as well as the normalization-related quantities, cancel out. For the MC input, the fraction of the uncertainty related to the

$p_{\rm T}$ GeV/c	$\mathrm{d}^2\sigma^{\psi(2S)}_{\rm Pbp}/\mathrm{d}p_{\rm T}\mathrm{d}y$ [μb/(GeV/c)] Value ± stat. ± uncorr. ± $p_{\rm T}$-corr. ± global
[0; 2]	$0.0671 \pm 0.0241 \pm 0.0098 \pm 0.0021 \pm 0.0011$
[2; 3]	$0.1065 \pm 0.0337 \pm 0.0119 \pm 0.0033 \pm 0.0017$
[3; 5]	$0.0551 \pm 0.0156 \pm 0.0069 \pm 0.0017 \pm 0.0009$
[5; 8]	$0.0206 \pm 0.0462 \pm 0.0023 \pm 0.0064 \pm 0.0003$

Table 5.4: The ψ(2S) differential cross-sections as a function of $p_{\rm T}$ for Pb-p ($-4.46 < y_{\rm cms} < -2.96$).

choice of the J/ψ kinematical distribution [2] cancels in the cross section ratios, and a remaining 1% (2%) uncertainty for p-Pb (Pb-p) is assigned to this source. Finally, the uncertainty on signal extraction is considered as uncorrelated between J/ψ and ψ(2S), and its value for the cross-section ratios amounts to 10% for both p-Pb and Pb-p. The resulting values are:

$$\frac{\mathrm{B.R.}_{\psi(2S)\to\mu^+\mu^-}\sigma^{\psi(2S)}}{\mathrm{B.R.}_{\mathrm{J}/\psi\to\mu^+\mu^-}\sigma^{\mathrm{J}/\psi}}(2.03 < y_{\rm cms} < 3.53) = 0.0154 \pm 0.0019(\mathrm{stat.}) \pm 0.0015(\mathrm{syst.}) \quad (5.8)$$

$$\frac{\mathrm{B.R.}_{\psi(2S)\to\mu^+\mu^-}\sigma^{\psi(2S)}}{\mathrm{B.R.}_{\mathrm{J}/\psi\to\mu^+\mu^-}\sigma^{\mathrm{J}/\psi}}(-4.46 < y_{\rm cms} < -2.96) = 0.0116 \pm 0.0018(\mathrm{stat.}) \pm 0.0011(\mathrm{syst.}) \quad (5.9)$$

The ψ(2S) to J/ψ cross section ratio in p-Pb collisions is shown in Fig. 5.5 where comparison with the corresponding ALICE results for pp collisions [8], obtained in slightly different centre of mass energy and rapidity regions, $\sqrt{s} = 7$ TeV, $2.5 < |y| < 4$, as no LHC pp results are available in the same kinematic conditions of proton-nucleus collisions, are also shown. The pp ratios are significantly higher than those for p-Pb and Pb-p, which are compatible within uncertainties.

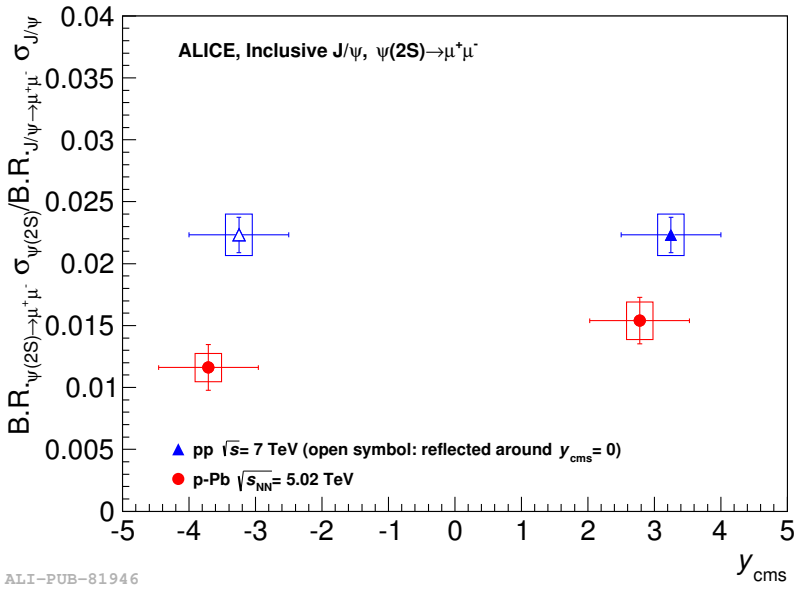

Figure 5.5: The cross section ratios $\mathrm{B.R.}_{\psi(2S)\to\mu^+\mu^-}\sigma^{\psi(2S)}/\mathrm{B.R.}_{J/\psi\to\mu^+\mu^-}\sigma^{J/\psi}$ for p-Pb and Pb-p collisions, compared with the corresponding pp results at $\sqrt{s} = 7$ TeV [8]. The horizontal bars correspond to the width of the rapidity regions under study. The vertical error bars represent statistical uncertainties, the boxes correspond to systematic uncertainties.

5.9.3 The double ratio $[\sigma_{\psi(2S)}/\sigma_{J/\psi}]_{pPb}/[\sigma_{\psi(2S)}/\sigma_{J/\psi}]_{pp}$

The double ratio is a useful quantity to directly compare the relative suppression of the two states between various experiments. Since the collision energy and the y-coverage of the p-Pb (Pb-p) and pp measurements are different in this analysis, the possible dependence of the $\sigma^{\psi(2S)}/\sigma^{J/\psi}$ vs $\sqrt{s}$ and y in pp collisions, have been estimated. The empirical observation is that this ratio is very similar at collider energies over a rather broad range of y and $\sqrt{s}$. In particular, from the LHCb data ($\sqrt{s} = 7$ TeV, $2 < y < 4.5$) [3, 4] one gets 2.11% for the inclusive ratio integrated over p_T, while the corresponding value from CDF data ($p\overline{p}$ at $\sqrt{s} = 1.96$ TeV, $|y| < 0.6$) [9] is 2.05%, i.e., only 3% smaller (the latter quantity was obtained by extrapolating the CDF $\psi(2S)$ measurement to $p_T = 0$ with the phenomenological function $f(p_T) = (p_T)/[1 + (p_T/a)^2]^b)$ [10]. The LHCb result can be extrapolated to central rapidity at $\sqrt{s} = 7$ TeV, assuming a Gaussian y-distribution for both resonances, with the

width of the J/ψ distribution tuned directly on data [3] and that for ψ(2S) obtained from the former assuming a scaling of the widths with $y_{\rm max}^{\psi(2S)}/y_{\rm max}^{J/\psi}$. The effect of this rescaling is small, leading to a 3% increase of the ratio. The central-rapidity ratio $\sigma_{\psi(2S)}/\sigma_{J/\psi}$ at $\sqrt{s}$ = 5.02 TeV is then obtained by means of an interpolation between the CDF and LHCb-rescaled values, assuming a linear dependence of the ratio vs $\sqrt{s}$. Finally, one can extrapolate the ratio to the p-Pb and Pb-p rapidity ranges by using for the J/ψ the Gaussian shape obtained with the interpolation procedure described in [11] and for the ψ(2S) the corresponding shape scaled with $y_{\rm max}^{\psi(2S)}/y_{\rm max}^{J/\psi}$. The difference between the measured value of $\sigma_{\psi(2S)}/\sigma_{J/\psi}$ for $\sqrt{s}$ = 7 TeV, $2 < y_{\rm cms} < 4.5$ and the results of the interpolation procedure to $\sqrt{s} = 5.02$ TeV, $2.03 < y_{\rm cms} < 3.53$ ($-4.46 < y_{\rm cms} < -2.96$) is -1.6% (-3.7%). When calculating the double ratio $[\sigma_{\psi(2S)}/\sigma_{J/\psi}]_{\rm pPb}/[\sigma_{\psi(2S)}/\sigma_{J/\psi}]_{\rm pp}$, the measured pp value at $\sqrt{s}$ = 7 TeV, $2.5 < y_{\rm cms} < 4$ [8] (rather than the interpolated one at $\sqrt{s} = 5.02$ TeV) has been used and a 8% systematic uncertainty on this quantity is included, i.e., about twice the maximum difference between the measured values of the ratio in pp and the results of the interpolation procedure. A similar uncertainty would be obtained using as an input for the calculation, instead of the LHCb data, the more recent pp result from ALICE on $\sigma_{\psi(2S)}/\sigma_{J/\psi}$ [8].

In Fig. 5.6, the double ratio in p-Pb collisions have been compared with the corresponding results obtained by the PHENIX experiment at $\sqrt{s_{\rm NN}}$ = 200 GeV, for $|y| < 0.35$ in d-Au collisions [12]. In this double ratio, the systematic uncertainties on the pp ratio, including the 8% contribution described in the previous paragraph, are considered as correlated between forward and backward rapidity, while the other systematic uncertainties are treated as uncorrelated. The ALICE results show that, compared to pp, the ψ(2S) is more suppressed than the J/ψ to a 2.1σ (3.5σ) level in p-Pb (Pb-p). The PHENIX result shows a similar feature, at a 1.3σ level. The numerical values of the double ratios are summarized in Table 5.5.

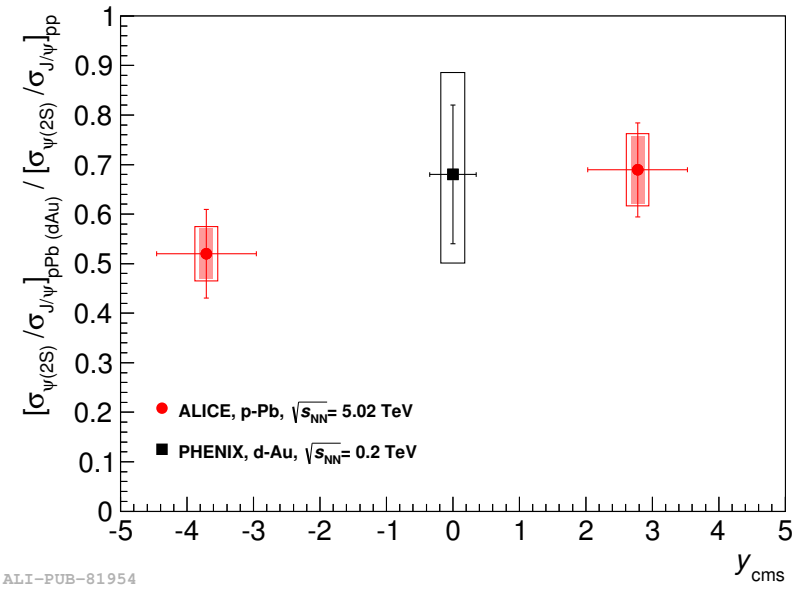

Figure 5.6: Double ratios $[\sigma_{\psi(2S)}/\sigma_{J/\psi}]_{pPb}/[\sigma_{\psi(2S)}/\sigma_{J/\psi}]_{pp}$ for p-Pb and Pb-p collisions, compared to the corresponding PHENIX result at $\sqrt{s_{NN}} = 200$ GeV [12]. The horizontal bars correspond to the width of the rapidity regions under study. For ALICE, the vertical error bars correspond to statistical uncertainties, the boxes to uncorrelated systematic uncertainties, and the shaded areas to correlated uncertainties. For PHENIX, the various sources of systematic uncertainties were combined in quadrature.

Collision Type	**Rapidity Range**	$[\sigma_{\psi(2S)}/\sigma_{J/\psi}]_{pPb}/[\sigma_{\psi(2S)}/\sigma_{J/\psi}]_{pp}$ Value $\pm$ stat. $\pm$ corr. $\pm$ uncorr.
p-Pb	$2.03 < y_{cms} < 3.53$	$0.52 \pm 0.09 \pm 0.05 \pm 0.05$
Pb-p	$-4.46 < y_{cms} < -2.96$	$0.69 \pm 0.09 \pm 0.07 \pm 0.07$

Table 5.5: The double ratio $[\sigma_{\psi(2S)}/\sigma_{J/\psi}]_{pPb}/[\sigma_{\psi(2S)}/\sigma_{J/\psi}]_{pp}$ for p-Pb and Pb-p collisions. First uncertainty is statistical, the second one is the correlated systematic, while the third is the uncorrelated systematic.

The p_T dependence of the double ratio $[\sigma_{\psi(2S)}/\sigma_{J/\psi}]_{pPb}/[\sigma_{\psi(2S)}/\sigma_{J/\psi}]_{pp}$ is shown in Fig. 5.7, with the p-Pb J/ψ cross sections taken from [2] and the pp values from [8]. As for the integrated double ratio, the systematic uncertainties related to efficiencies and to normalizations cancel out for both p-Pb and pp, while the uncertainties on signal extraction and MC input are considered as uncorrelated. The 8% uncertainty related to the $\sqrt{s}$ and y mismatch between the two systems is correlated as a function of p_T, while the uncertainties on the ratio in pp collisions are correlated, for each p_T bin, between forward and backward rapidity. Within uncertainties, no p_T dependence

of the double ratio can be seen. The numerical values of the double ratios in p_{T} bins are summarized in Table 5.6.

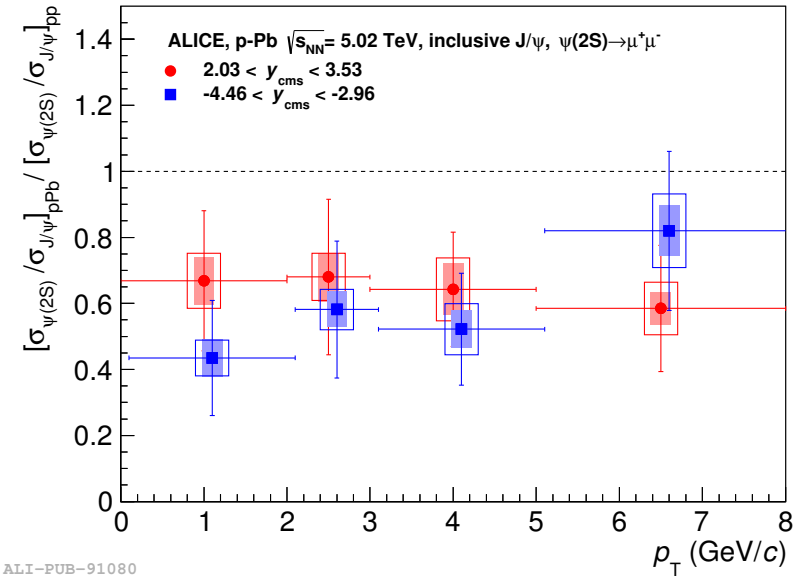

Figure 5.7: The double ratio $[\sigma_{\psi(2\mathrm{S})}/\sigma_{\mathrm{J}/\psi}]_{\mathrm{pPb}}/[\sigma_{\psi(2\mathrm{S})}/\sigma_{\mathrm{J}/\psi}]_{\mathrm{pp}}$ for p-Pb and Pb-p collisions, as a function of p_{T}. The horizontal bars correspond to the width of the p_{T} bins. The points corresponding to negative y are slightly shifted in p_{T} to improve visibility.

p_{T} GeV/c	$[\sigma_{\psi(2\mathrm{S})}/\sigma_{\mathrm{J}/\psi}]_{\mathrm{pPb}}/[\sigma_{\psi(2\mathrm{S})}/\sigma_{\mathrm{J}/\psi}]_{\mathrm{pp}}$ Value ± stat. ± corr. ± uncorr.	$[\sigma_{\psi(2\mathrm{S})}/\sigma_{\mathrm{J}/\psi}]_{\mathrm{Pbp}}/[\sigma_{\psi(2\mathrm{S})}/\sigma_{\mathrm{J}/\psi}]_{\mathrm{pp}}$ Value ± stat. ± corr. ± uncorr.
[0; 2]	$0.67 \pm 0.21 \pm 0.08 \pm 0.07$	$0.43 \pm 0.17 \pm 0.05 \pm 0.06$
[2; 3]	$0.68 \pm 0.23 \pm 0.07 \pm 0.07$	$0.58 \pm 0.21 \pm 0.06 \pm 0.05$
[3; 5]	$0.64 \pm 0.17 \pm 0.10 \pm 0.08$	$0.52 \pm 0.17 \pm 0.08 \pm 0.06$
[5; 8]	$0.58 \pm 0.19 \pm 0.08 \pm 0.05$	$0.82 \pm 0.24 \pm 0.11 \pm 0.08$

Table 5.6: The double ratio $[\sigma_{\psi(2\mathrm{S})}/\sigma_{\mathrm{J}/\psi}]_{\mathrm{pPb}}/[\sigma_{\psi(2\mathrm{S})}/\sigma_{\mathrm{J}/\psi}]_{\mathrm{pp}}$ for p-Pb (second column) and Pb-p (last column) as a function of p_{T}.

5.9.4 Nuclear Modification Factor of $\psi(2\mathrm{S})$

The nuclear modification factor is defined as the suppression of charmonium yield in proton-nucleus or nucleus-nucleus collisions with respect to the corresponding pp yield. The nuclear modification factor of $\psi(2\mathrm{S})$ ($R_{\mathrm{pPb}}^{\psi(2\mathrm{S})}$) can be obtained as a multiplication of the nuclear modification factor of J/ψ ($R_{\mathrm{pPb}}^{\mathrm{J}/\psi}$) [2] and the double

ratio evaluated above:

$$R_{\rm pPb}^{\psi(2S)} = R_{\rm pPb}^{J/\psi} \cdot \frac{\sigma_{\rm pPb}^{\psi(2S)}}{\sigma_{\rm pPb}^{J/\psi}} \cdot \frac{\sigma_{\rm pp}^{J/\psi}}{\sigma_{\rm pp}^{\psi(2S)}} \tag{5.10}$$

The $R_{\rm pPb}^{\psi(2S)}$ is shown in Fig. 5.8 and has been compared with $R_{\rm pPb}^{J/\psi}$. In case of systematic on the double ratios, the difference in the $\sqrt{s}$ and y domains between p-Pb and pp is taken into account by the inclusion of the 8% systematic uncertainty as discussed in section 5.9.3. The other quoted uncertainties combine those from $R_{\rm pPb}^{J/\psi}$ [2] with those for the double ratio, avoiding a double counting of the J/ψ related uncertainties.

Fig. 5.8 indicates that the ψ(2S) suppression is much stronger than the one for J/ψ and reaches a factor $\sim$2 with respect to pp. The results are compared with theoretical calculations including either nuclear shadowing only [13, 14] or coherent energy loss, with or without a shadowing contribution [15]. For the former mechanism, the values correspond to calculations performed for the J/ψ. However, due to the relatively similar kinematic distributions of gluons that produce the $c\bar{c}$ pair which will then hadronize to a J/ψ or a ψ(2S), the shadowing effects are expected to be the same, within 2-3% [16, 17], for the two charmonium states. No sensitivity to the final quantum numbers of the charmonium state is expected for coherent energy loss [18], implying that the calculations shown in Fig. 5.8 are valid for both resonances. As a consequence, all three models would predict an almost identical suppression for the ψ(2S) and the J/ψ over the full rapidity range, with negligible theoretical uncertainties. This prediction is in strong disagreement with our data and clearly indicates that other mechanisms must be invoked in order to describe the ψ(2S) suppression in proton-nucleus collisions. The numerical values of the $R_{\rm pPb}^{\psi(2S)}$ are summarized in Table 5.7.

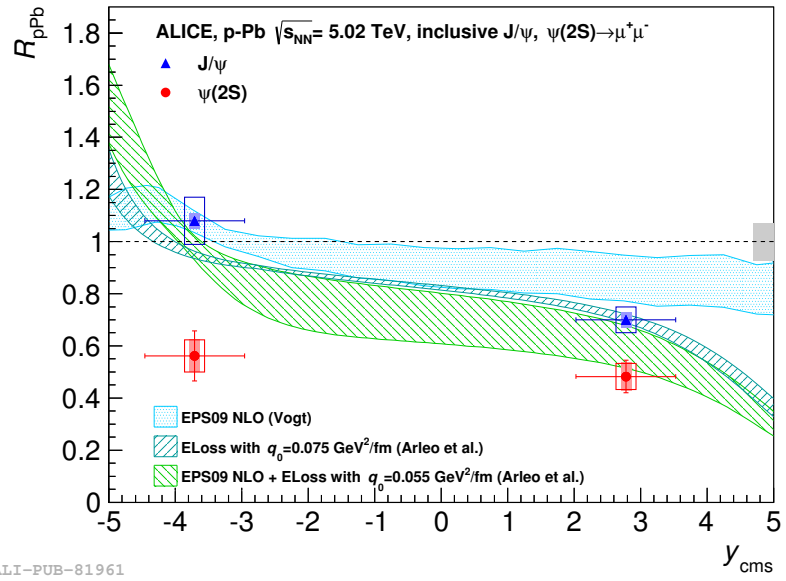

Figure 5.8: The nuclear modification factor for ψ(2S), compared to the corresponding quantity for J/ψ [2]. The horizontal bars correspond to the width of the rapidity regions under study. The vertical error bars correspond to statistical uncertainties, the boxes to uncorrelated systematic uncertainties, and the shaded areas to partially correlated uncertainties. The filled box on the right, centered on $R_{\rm pPb} = 1$, shows uncertainties that are fully correlated between J/ψ and ψ(2S). Model calculations tuned on J/ψ, and including nuclear shadowing [13] and coherent energy loss [15] are also shown. The corresponding calculations for ψ(2S) produce identical values for the coherent energy loss mechanisms and a 2-3% larger result for nuclear shadowing and therefore are not shown.

Collision Type	Rapidity Range	$R_{\rm pPb}$ Value ± stat. ± corr. ± uncorr.
p-Pb	$2.03 < y_{\rm cms} < 3.53$	$0.56 \pm 0.10 \pm 0.06 \pm 0.06$
Pb-p	$-4.46 < y_{\rm cms} < -2.96$	$0.48 \pm 0.06 \pm 0.06 \pm 0.05$

Table 5.7: The nuclear modification factor for ψ(2S) in p-Pb collisions. The first uncertainty is statistical, the second one is the correlated systematic and the third the uncorrelated systematic.

The break-up cross section of the final state resonance due to interactions with CNM is expected to depend on the binding energy of the charmonium and such a mechanism would be a natural explanation for the larger suppression of ψ(2S). However, this process becomes relevant only if the charmonium formation time $\tau_{\rm f}$ is smaller than the time $\tau_{\rm c}$ spent by the $c\bar{c}$ pair inside the nucleus. One can evaluate the average proper time $\tau_{\rm c}$ spent in CNM as $\tau_{\rm c} = \langle L \rangle / (\beta_z \gamma)$ [19], where $\langle L \rangle$ is the

average length of nuclear matter crossed by the pair, which can be calculated in the framework of the Glauber model [20], $\beta_z = \tanh y_{c\bar{c}}^{\rm rest}$ is the velocity of the $c\bar{c}$ along the beam direction in the nucleus rest frame, and $\gamma = E_{c\bar{c}}/m_{c\bar{c}}$. For $c\bar{c}$ pairs in the charmonium mass range emitted at $p_{\rm T} = 0$ in the forward acceptance, one gets $\tau_{\rm c} \sim 10^{-4}$ fm/c, while the corresponding value at backward rapidity is $\sim 7 \cdot 10^{-2}$ fm/c. Estimates for the formation time $\tau_{\rm f}$ range between 0.05 and 0.15 fm/c [19, 21]. In this situation, no break-up effects depending on the final charmonium state should be expected at forward rapidity, and even for backward production one has at most $\tau_{\rm f} \sim \tau_{\rm c}$ which would hardly accomodate the strong difference observed between ψ(2S) and J/ψ suppression. As a consequence, other final state effects should be considered, including the interaction of the $c\bar{c}$ pair with the final state hadronic system created in the proton-nucleus collision.

The $p_{\rm T}$ dependence of the ψ(2S) nuclear modification factor is shown in Fig. 5.9 and has been compared with the corresponding result for J/ψ [22]. The uncertainties are obtained with the procedure used in Fig. 5.8, and the results are compared to the same models quoted there. The numerical values of the $R_{\rm pPb}^{\psi(2S)}$ in $p_{\rm T}$ bins are summarized in Table 5.8.

$p_{\rm T}$ GeV/c	$R_{\rm pPb}$ $(2.03 < y_{\rm cms} < 3.53)$ Value $\pm$ stat. $\pm$ corr. $\pm$ uncorr. $\pm$ global	$R_{\rm Pbp}$ $(-4.46 < y_{\rm cms} < -2.96)$ Value $\pm$ stat. $\pm$ corr. $\pm$ uncorr. $\pm$ global
[0; 2]	$0.42 \pm 0.12 \pm 0.05 \pm 0.05 \pm 0.03$	$0.44 \pm 0.17 \pm 0.06 \pm 0.06 \pm 0.03$
[2; 3]	$0.46 \pm 0.15 \pm 0.05 \pm 0.05 \pm 0.03$	$0.64 \pm 0.22 \pm 0.07 \pm 0.07 \pm 0.04$
[3; 5]	$0.51 \pm 0.11 \pm 0.08 \pm 0.06 \pm 0.03$	$0.61 \pm 0.17 \pm 0.09 \pm 0.07 \pm 0.04$
[5; 8]	$0.53 \pm 0.13 \pm 0.07 \pm 0.04 \pm 0.03$	$0.99 \pm 0.21 \pm 0.14 \pm 0.10 \pm 0.06$

Table 5.8: The nuclear modification factor for ψ(2S) as a fuction of $p_{\rm T}$ in p-Pb (second column) and Pb-p (last column).

Within uncertainties, no $p_{\rm T}$ dependence of the double ratio can be seen, and consequently as a function of $p_{\rm T}$, $R_{\rm pPb}^{\psi(2S)}$ has qualitatively a similar shape as that exhibited by $R_{\rm pPb}^{\rm J/\psi}$, but systematically characterized by smaller values. Theoretical models, which in this case also yield the same prediction for J/ψ and ψ(2S), are in fair

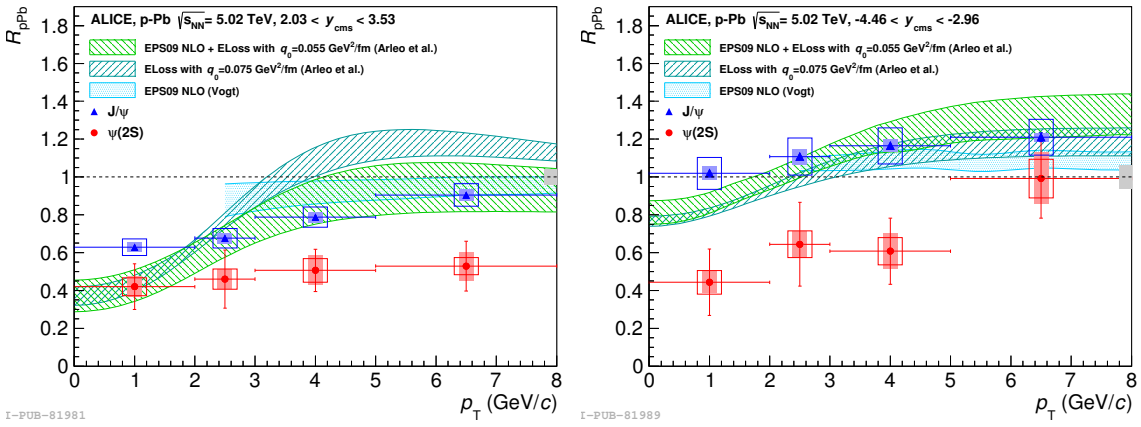

Figure 5.9: The nuclear modification factor for ψ(2S), compared to the corresponding quantity for J/ψ [22], as a function of p_{T}. Plots correspond to p-Pb (left) and Pb-p (right) collisions. The horizontal bars correspond to the width of the transverse momentum bins. For details on errors and model comparisons, see the caption of Fig. 5.8.

agreement with J/ψ results, but clearly overestimate the ψ(2S) nuclear modification factor values.

It is interesting to note that different values of transverse momentum for the resonances correspond to different τ_{c}, with the crossing times decreasing with increasing p_{T}. In particular, for backward production, τ_{c} varies by about a factor 2, between $\sim$0.07 (at $p_{\mathrm{T}} = 0$) and $\sim$0.03 fm/c (at $p_{\mathrm{T}} = 8$ GeV/c). As a consequence, a larger fraction of $c\bar{c}$ pairs may form the final resonance state inside CNM at low p_{T}, and one might expect smaller values of the double ratio in that transverse momentum region due to the weaker binding energy of ψ(2S). Although the results shown in Fig. 5.7 could be suggestive of such a trend, no firm conclusion can be reached due to the current experimental uncertainties.

5.10 Summary

In summary, the results on inclusive ψ(2S) production in proton-nucleus collisions at the LHC have presented. Measurements were performed with the ALICE Muon Spectrometer in the p-going ($2.03 < y_{\rm cms} < 3.53$) and Pb-going ($-4.46 < y_{\rm cms} < -2.96$) directions. The production cross sections, the double ratios with respect to the J/ψ in p-Pb and pp and the nuclear modification factors were estimated integrated and also differtially in $p_{\rm T}$. The results show that ψ(2S) is significantly more suppressed than J/ψ in both rapidity regions, and that no $p_{\rm T}$ dependence of this effect is found within uncertainties. This observation implies that initial state nuclear effects alone cannot account for the modification of the ψ(2S) yields, as also confirmed by the poor agreement of the ψ(2S) $R_{\rm pPb}$ with models based on shadowing and/or energy loss. Final state effects, such as the pair break-up by interactions with cold nuclear matter, might in principle lead to the observed effect, but the extremely short crossing times for the $c\bar{c}$ pair, in particular at forward rapidity, make such an explanation unlikely. Consequently, other final state effects should be considered, including the interaction of the $c\bar{c}$ pair with the final state hadronic system created in the proton-nucleus collision. It may be interesting to explore whether the present results are indicative of an additional color suppression in case of proton-nucleus collisions at LHC energies.

Bibliography

[1] B. Abelev *et al.*, (ALICE collaboration), "Suppression of ψ(2S) production in p-Pb collisions at $\sqrt{s_{\rm NN}}$ = 5.02 TeV," JHEP **12**, 073 (2014) [arXiv:1405.3796] [INSPIRE].

[2] B. Abelev *et al.*, (ALICE collaboration), "J/ψ production and nuclear effects in p-Pb collisions at $\sqrt{s_{\rm NN}}$ = 5.02 TeV," JHEP **02**, 073 (2014) [arXiv:1308.6726] [INSPIRE].

[3] R. Aaij *et al.*, (LHCb collaboration), "Measurement of J/ψ polarization in pp collisions at $\sqrt{s}$ = 7 TeV," Eur. Phys. J. C **73**, 2631 (2013) [arXiv:1307.6379] [INSPIRE].

[4] R. Aaij *et al.*, (LHCb collaboration), "Measurement of ψ(2S) meson production in pp collisions at $\sqrt{s}$ = 7 TeV," Eur. Phys. J. C **72**, 2100 (2012) [arXiv:1204.1258] [INSPIRE].

[5] S. Chatrchyan *et al.*, (CMS collaboration), "Measurement of the prompt J/ψ and ψ(2S) polarizations in pp collisions at $\sqrt{s}$ = 7 TeV," Phys. Lett. B **727**, 381 (2013) [arXiv:1307.6070] [INSPIRE].

[6] R. Aaij *et al.*, (LHCb collaboration), "Measurement of ψ(2S) polarisation in pp collisions at $\sqrt{s}$ = 7 TeV," Eur. Phys. J. C **74**, 2872 (2014) [arXiv:1403.1339] [INSPIRE].

[7] B. Abelev *et al.*, (ALICE collaboration), "Measurement of visible cross sections in proton-lead collisions at $\sqrt{s_{\rm NN}} = 5.02$ TeV in van der Meer scans with the ALICE detector," JINST **9**, P11003 (2014) [arXiv:1405.1849] [INSPIRE].

[8] B. Abelev *et al.*, (ALICE collaboration), "Measurement of quarkonium production at forward rapidity in pp collisions at $\sqrt{s} = 7$ TeV," Eur. Phys. J. C **74**, 2974 (2014) [arXiv:1403.3648] [INSPIRE].

[9] T. Aaltonen *et al.*, (CDF collaboration), "Production of ψ(2S) mesons in $p\overline{p}$ collisions at 1.96 TeV," Phys. Rev. D **80**, 031103 (2009) [arXiv:0905.1982] [INSPIRE].

[10] A. Adare *et al.*, (PHENIX collaboration), "J/ψ production versus transverse momentum and rapidity in p^+p collisions at $\sqrt{s} = 200$ GeV," Phys. Rev. Lett. **98**, 232002 (2007) [hep-ex/0611020] [INSPIRE].

[11] B. Abelev *et al.* and R. Aaij *et al.*, (ALICE and LHCb collaborations), "Reference pp cross-sections for J/ψ studies in proton-lead collisions at $\sqrt{s_{\rm NN}} = 5.02$ TeV and comparisons between ALICE and LHCb results," ALICE-PUBLIC-2013-002, CERN, Geneva Switzerland (2013) [LHCb-CONF-2013-013].

[12] A. Adare *et al.*, (PHENIX collaboration), "Nuclear modification of ψ', χ_c and J/ψ production in d+Au collisions at $\sqrt{s_{\rm NN}} = 200$ GeV," Phys. Rev. Lett. **111**, 202301 (2013) [arXiv:1305.5516] [INSPIRE].

[13] J.L. Albacete *et al.*, "Predictions for p+Pb collisions at $\sqrt{s_{\rm NN}} = 5$ TeV," Int. J. Mod. Phys. E **22**, 1330007 (2013) [arXiv:1301.3395] [INSPIRE].

[14] R. Vogt, private communication.

[15] F. Arleo and S. Peigne, "Heavy-quarkonium suppression in p-A collisions from

parton energy loss in cold QCD matter," JHEP **03**, 122 (2013) [arXiv:1212.0434] [INSPIRE].

[16] E.G. Ferreiro, F. Fleuret, J.P. Lansberg and A. Rakotozafindrabe, "J/ψ and ψ' production in proton(deuteron)-nucleus collisions: lessons from RHIC for the proton-lead LHC run," J. Phys. Conf. Ser. **422**, 012018 (2013) [arXiv:1211.4749] [INSPIRE].

[17] E.G. Ferreiro, private communication.

[18] F. Arleo, private communication.

[19] D.C. McGlinchey, A.D. Frawley and R. Vogt, "Impact parameter dependence of the nuclear modification of J/ψ production in d+Au collisions at $\sqrt{s_{\rm NN}} = 200$ GeV," Phys. Rev. C **87**, 054910 (2013) [arXiv:1208.2667] [INSPIRE].

[20] M.L. Miller, K. Reygers, S.J. Sanders and P. Steinberg, "Glauber modeling in high energy nuclear collisions," Ann. Rev. Nucl. Part. Sci. **57**, 205 (2007) [nucl-ex/0701025] [INSPIRE].

[21] F. Arleo and S. Peigne, "J/ψ suppression in p-A collisions from parton energy loss in cold QCD matter," Phys. Rev. Lett. **109**, 122301 (2012) [arXiv:1204.4609] [INSPIRE].

[22] B. Abelev *et al.*, (ALICE collaboration), "Rapidity and transverse momentum dependence of the inclusive J/ψ nuclear modification factor in p-Pb collisions at $\sqrt{s_{\rm NN}} = 5.02$ TeV," in preparation.

Chapter 6

Fractional double differential cross-section of J/ψ in pp and Pb-Pb collisions

The ALICE Collaboration has studied the differential production of J/ψ in the two rapidity ranges $2.5 < y < 4$ [1, 2] and $|y| < 0.9$ [2, 3] in Pb-Pb collisions. At the forward rapidities, a clear indication of J/ψ regeneration was observed for $p_{\rm T} <$ 3 GeV/c. On the other hand, the rapidity dependence of the regenerated J/ψ is not apparent from these studies.

In the present chapter, we report the measurement of fractional double differential cross-section (FDDC) of J/ψ at forward rapidity in pp and Pb-Pb collisions. The data presented in this chapter were collected by ALICE Collaboration at $\sqrt{s} = 7$ TeV in pp collisions and at $\sqrt{s_{\rm NN}} = 2.76$ TeV in Pb-Pb collisions. The data sample corresponds to an integrated luminosity $\mathcal{L}_{\rm int} = 1.35$ pb^{-1} and 68.8 μb^{-1} for pp and Pb-Pb collisions, respectively. This chapter is primarily aimed to study

the effect of the recombination on the rapidity distribution of J/ψ production. It may be noted that this is the first attempt to study the double differential cross-section of J/ψ at forward rapidity in ALICE.

6.1 Motivation

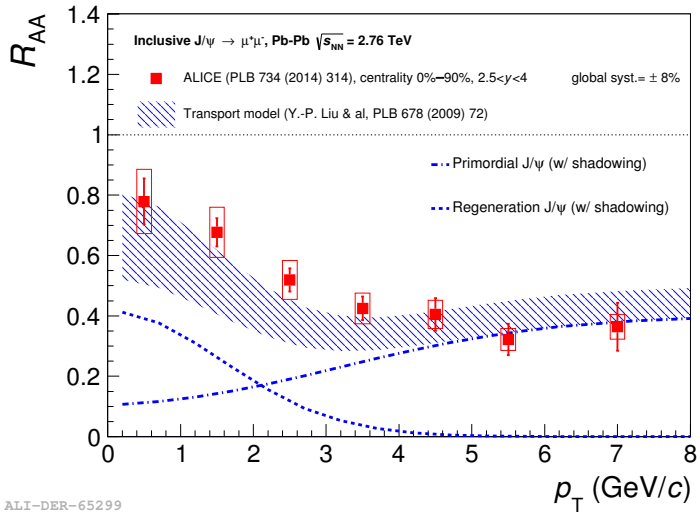

Figure 6.1: $R_{\rm AA}$ of J/ψ in Pb-Pb collisions.

In the Pb-Pb collisions [2], theoretical calculations indicate that the $p_{\rm T}$ of the regenerated J/ψs are small ($p_{\rm T} < 4$ GeV/c). On the other hand, the low $p_{\rm T}$ primordial J/ψ's are expected to be suppressed at LHC energies as shown in the Fig. 6.1. Thus, it may be interesting to study double differential cross-section in two $p_{\rm T}$ bins, namely $0 < p_{\rm T} < 3$ GeV/c and $p_{\rm T} > 3$ GeV/c as the origin and character of the J/ψs in these two bins are expected to be dominated by two different effects, regeneration and colour suppression, respectively. However, these delicate dependencies may be washed out by the CNM effects. Fig. 6.2 shows the $p_{\rm T}$ dependence of the $R_{\rm PbPb}$ and $R_{\rm pPb} \times R_{\rm Pbp}$ and their ratio ($S_{\rm J/\psi}$). It is observed from the figure that the $S_{\rm J/\psi}$ value changes rapidly from ~ 1.4 to ~ 0.4 for $p_{\rm T} < 3$ GeV/c while beyond $p_{\rm T} = 3$ GeV/c it remains nearly constant. This indicates that the CNM and recombination effects have

negligible contribution for $p_{\rm T} > 3$ GeV/c. Thus, it may be instructive to investigate the rapidity distribution of J/ψ production in the two $p_{\rm T}$ bins, namely $0 < p_{\rm T} < 3$ GeV/c and $p_{\rm T} > 3$ GeV/c.

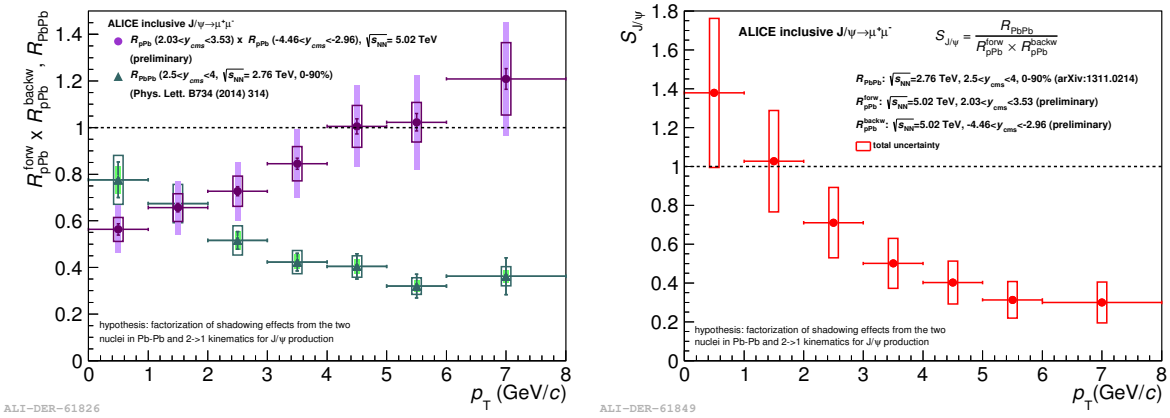

Figure 6.2: The inclusive J/ψ $R_{\rm PbPb}$ vs $p_{\rm T}$ compared to the product of $R_{\rm pPb} \times R_{\rm Pbp}$.

Any observation in Pb-Pb data needs to be normalized by the same in pp data. In the present thesis, I have reported a detail analysis of the pp data collected at $\sqrt{s} = 7$ TeV while the Pb-Pb data was collected at $\sqrt{s_{\rm NN}} = 2.76$ TeV.

In order to establish a variable which is indepenedent of $\sqrt{s}$, it was decided to study the fractional double differential cross-section (FDDC) for J/ψ. This assumption was tested on the published pp data collected at 2.76 [4] and 7 TeV [5] as a function of rapidity. It is evident from the Fig. 6.3 that the rapidity distribution of FDDC at the two center-of-mass energies agree bin by bin within 1σ. Therefore, in the present study it is possible to compare the rapidity distributions of J/ψ in pp and Pb-Pb collisions at $\sqrt{s} = 7$ and $\sqrt{s_{\rm NN}} = 2.76$ TeV, respectively.

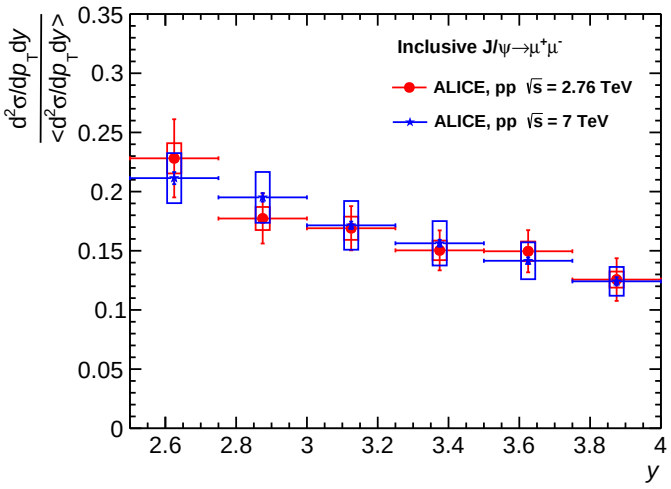

Figure 6.3: Fractional double differential cross-sections of J/ψ as functions of y in pp collisions at $\sqrt{s} = 2.76$ and 7 TeV.

6.2 Signal extraction

The signal extraction and systematic uncertainty measurements are similar to that described in chapter 4. Both in pp and Pb-Pb collisions, the J/ψ yields have been obtained by fitting the unlike-sign dimuon mass spectra with a combination of signal and background functions. For the J/ψ signals, Extended Crystal Ball (CB2) functions or NA60 functions have been used, while for the background a Variable Width Gaussian (VWG) function or a combination of a 4th order polynomial and exponential functions (Pol4 × Exp) has been adopted. The width of the ψ(2S) has been fixed to the ratio of their widths obtained in the MC. Alternative values of the ψ(2S) mass resolution have also been tested, allowing the ratio $(\sigma^{\rm MC}_{\psi(2S)}/\sigma^{\rm MC}_{J/\psi})$ to vary within 10%. For each combination of signal and background shape, the fitting range is also modified, to verify the stability of the fit.

The summary of the performed tests are bellow:

- CB2 signal shape and VWG for the background.

- CB2 signal shape and 4th order polynomial × exponential for the background.
- NA60 signal shape and VWG for the background.
- NA60 signal shape and 4th order polynomial × exponential for the background.

6.2.1 Fit results

Fig. 6.4 and 6.5 show the CB2+VWG fits to the y integrated dimuon mass spectrum in two p_{T} bins: $0 < p_{\mathrm{T}} < 3$ GeV/c and $p_{\mathrm{T}} > 3$ GeV/c in pp and Pb-Pb collisions, respectively. From the present data set, the J/ψ signals could be extracted in six and five rapidity bins for these two p_{T} bins for pp and Pb-Pb, respectively. Fig. 6.6 and 6.7 show the signal extraction with CB2+VWG in different rapidity bins for pp and Pb-Pb respectively, for each p_{T} bin.

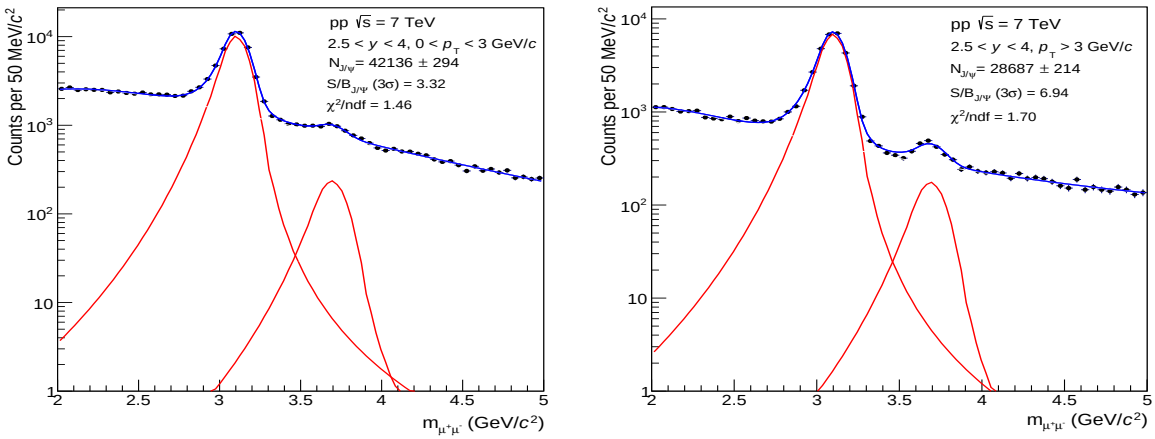

Figure 6.4: Opposite sign dimuon invariant mass distribution for integrated y ($2.5 \leq y \leq 4.0$), in two p_{T} bins, $0 < p_{\mathrm{T}} < 3$ GeV/c (left) and $p_{\mathrm{T}} > 3$ GeV/c (right) fitted with CB2+VWG in pp collisions.

Table 6.1 and 6.2 summarize the results of these fits for J/ψ for pp and Pb-Pb, respectively. In both the tables the $2.5 < y < 4$ bin correspond to the y integrated case.

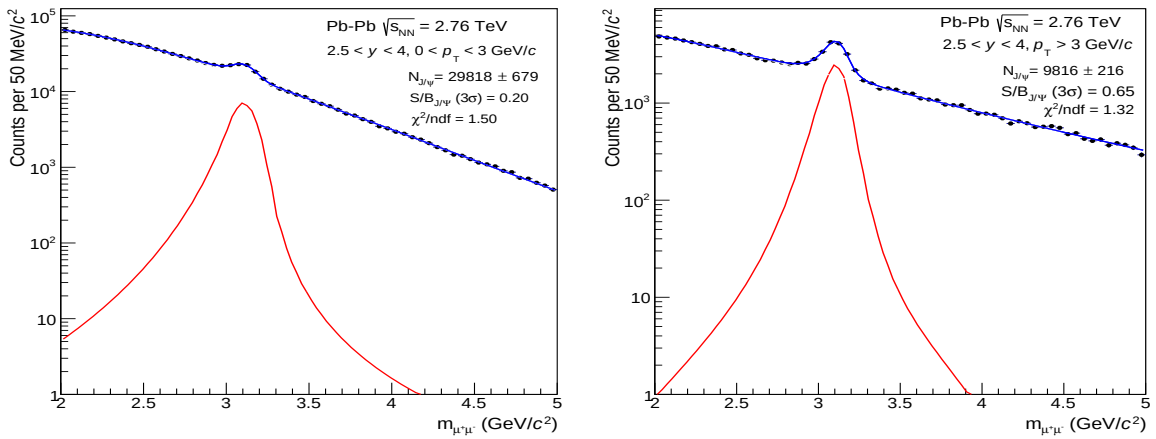

Figure 6.5: Same as Fig. 6.4 but for Pb-Pb collisions.

For pp, in the y integrated case, the significance for J/ψ is $\sim$ 174 and $\sim$ 153 for $0 < p_{\rm T} < 3$ GeV/c and $p_{\rm T} > 3$ GeV/c bin, respectively. In rapidity bins, the significance ranges between $\sim$ 40 ($\sim$ 32) and $\sim$ 88 ($\sim$ 80) for the bin $0 < p_{\rm T} < 3$ GeV/c ($p_{\rm T} > 3$ GeV/c), the maximum being reached in the middle of the covered rapidity range in both the $p_{\rm T}$ bins.

For Pb-Pb, in the y integrated case, the significance for J/ψ is $\sim$ 67 and $\sim$ 59 for $0 < p_{\rm T} < 3$ GeV/c and $p_{\rm T} > 3$ GeV/c bin, respectively. In rapidity bins, the significance ranges between $\sim$ 15 ($\sim$ 15) and $\sim$ 36 ($\sim$ 32) for the bin $0 < p_{\rm T} < 3$ GeV/c ($p_{\rm T} > 3$ GeV/c), in this case also the maximum being reached in the middle of the covered rapidity range in both the $p_{\rm T}$ bins.

	$0 < p_{\rm T} < 3$ GeV/c				$p_{\rm T} > 3$ GeV/c			
y bins	$N_{J/\psi}$ ± (stat)	S/B	Significance	χ^2/ndf	$N_{J/\psi}$ ± (stat)	S/B	Significance	χ^2/ndf
[2.5; 4.0]	42136 ± 294	3.32	173.94	1.46	28687 ± 214	6.94	153.05	1.70
[2.5; 2.75]	2391 ± 65	2.68	40.19	1.16	2299 ± 64	6.20	43.01	1.00
[2.75; 3.0]	8450 ± 138	2.87	76.52	1.42	6348 ± 106	7.22	72.18	1.29
[3.0; 3.25]	10900 ± 160	3.13	87.51	1.10	7756 ± 113	7.52	79.67	1.11
[3.25; 3.5]	10601 ± 150	3.50	87.78	0.76	6684 ± 105	6.65	73.68	1.41
[3.5; 3.75]	7361 ± 116	4.29	74.68	1.28	4383 ± 102	7.88	60.05	1.57
[3.75; 4.0]	2423 ± 85	5.11	43.34	1.54	1284 ± 47	6.77	32.33	1.35

Table 6.1: Fit results in rapidity bins for J/ψ in pp collisions.

	$0 < p_{\rm T} < 3$ GeV/c				$p_{\rm T} > 3$ GeV/c			
y bins	$N_{J/\psi}$ ± (stat)	S/B	Significance	χ^2/ndf	$N_{J/\psi}$ ± (stat)	S/B	Significance	χ^2/ndf
[2.5; 4.0]	29818 ± 679	0.20	67.46	1.50	9816 ± 216	0.65	59.17	1.32
[2.5; 2.75]	1875 ± 178	0.15	15.33	1.12	769 ± 62	0.43	14.63	1.11
[2.75; 3.0]	6670 ± 346	0.16	29.21	1.21	2424 ± 102	0.56	28.47	1.01
[3.0; 3.25]	8481 ± 353	0.20	35.56	1.37	2928 ± 132	0.63	32.36	1.39
[3.25; 3.5]	7048 ± 315	0.24	34.54	1.02	2377 ± 125	0.68	27.61	1.41
[3.5; 4.0]	6027 ± 211	0.38	34.93	1.13	1676 ± 84	0.73	25.58	1.21

Table 6.2: Fit results in rapidity bins for J/ψ in Pb-Pb collisions.

6.2.2 Systematic uncertainty

Table 6.3 and 6.4 summarizes the result on signal extraction together with the statistical and systematic errors of J/ψ in pp an Pb-Pb collisions, respectively.

For pp, in the y integrated case, the systematic uncertainty on signal extraction is $\sim 0.3\%$ and $\sim 0.2\%$ for $0 < p_{\rm T} < 3$ GeV/c and $p_{\rm T} > 3$ GeV/c bin, respectively. In rapidity bins, the systematic uncertainty is in the ranges $\sim 0.4\%$ ($\sim 0.1\%$) and $\sim 2\%$ ($\sim 1\%$) for the bin $0 < p_{\rm T} < 3$ GeV/c ($p_{\rm T} > 3$ GeV/c).

For Pb-Pb, in the y integrated case, the systematic uncertainty on signal extraction is $\sim 1.5\%$ and $\sim 1\%$ for $0 < p_{\rm T} < 3$ GeV/c and $p_{\rm T} > 3$ GeV/c bin, respectively. In rapidity bins, the systematic uncertainty is in the ranges $\sim 1\%$ ($\sim 0.3\%$) and $\sim 2\%$ ($\sim 5\%$) for the bin $0 < p_{\rm T} < 3$ GeV/c ($p_{\rm T} > 3$ GeV/c).

	$0 < p_{\rm T} < 3$ GeV/c	$p_{\rm T} > 3$ GeV/c
y bins	$N_{J/\psi}$ ± (stat.) ± (syst.)	$N_{J/\psi}$ ± (stat.) ± (syst.)
[2.5; 4.0]	42019 ± 299 ± 115	28697 ± 217 ± 59
[2.5; 2.75]	2395 ± 70 ± 50	2260 ± 63 ± 4
[2.75; 3.0]	8158 ± 138 ± 43	6524 ± 103 ± 30
[3.0; 3.25]	10842 ± 163 ± 47	7730 ± 114 ± 40
[3.25; 3.5]	10568 ± 153 ± 43	6698 ± 105 ± 9
[3.5; 3.75]	7406 ± 116 ± 123	4404 ± 92 ± 16
[3.75; 4.0]	2398 ± 74 ± 14	1274 ± 49 ± 11

Table 6.3: Results on signal extraction in rapidity bins for J/ψ in pp collisions.

	$0 < p_{\mathrm{T}} < 3$ GeV/c	$p_{\mathrm{T}} > 3$ GeV/c
y bins	$\mathrm{N}_{J/\psi} \pm$ (stat.) $\pm$ (syst.)	$\mathrm{N}_{J/\psi} \pm$ (stat.) $\pm$ (syst.)
$[2.5; 4.0]$	$29940 \pm 682 \pm 445$	$9926 \pm 219 \pm 97$
$[2.5; 2.75]$	$1940 \pm 186 \pm 97$	$771 \pm 65 \pm 7$
$[2.75; 3.0]$	$6601 \pm 350 \pm 71$	$2473 \pm 99 \pm 8$
$[3.0; 3.25]$	$8386 \pm 359 \pm 86$	$2908 \pm 125 \pm 21$
$[3.25; 3.5]$	$7074 \pm 318 \pm 43$	$2230 \pm 105 \pm 116$
$[3.5; 4.0]$	$6051 \pm 239 \pm 71$	$1653 \pm 87 \pm 35$

Table 6.4: Results on signal extraction in rapidity bins for J/ψ in Pb-Pb collisions.

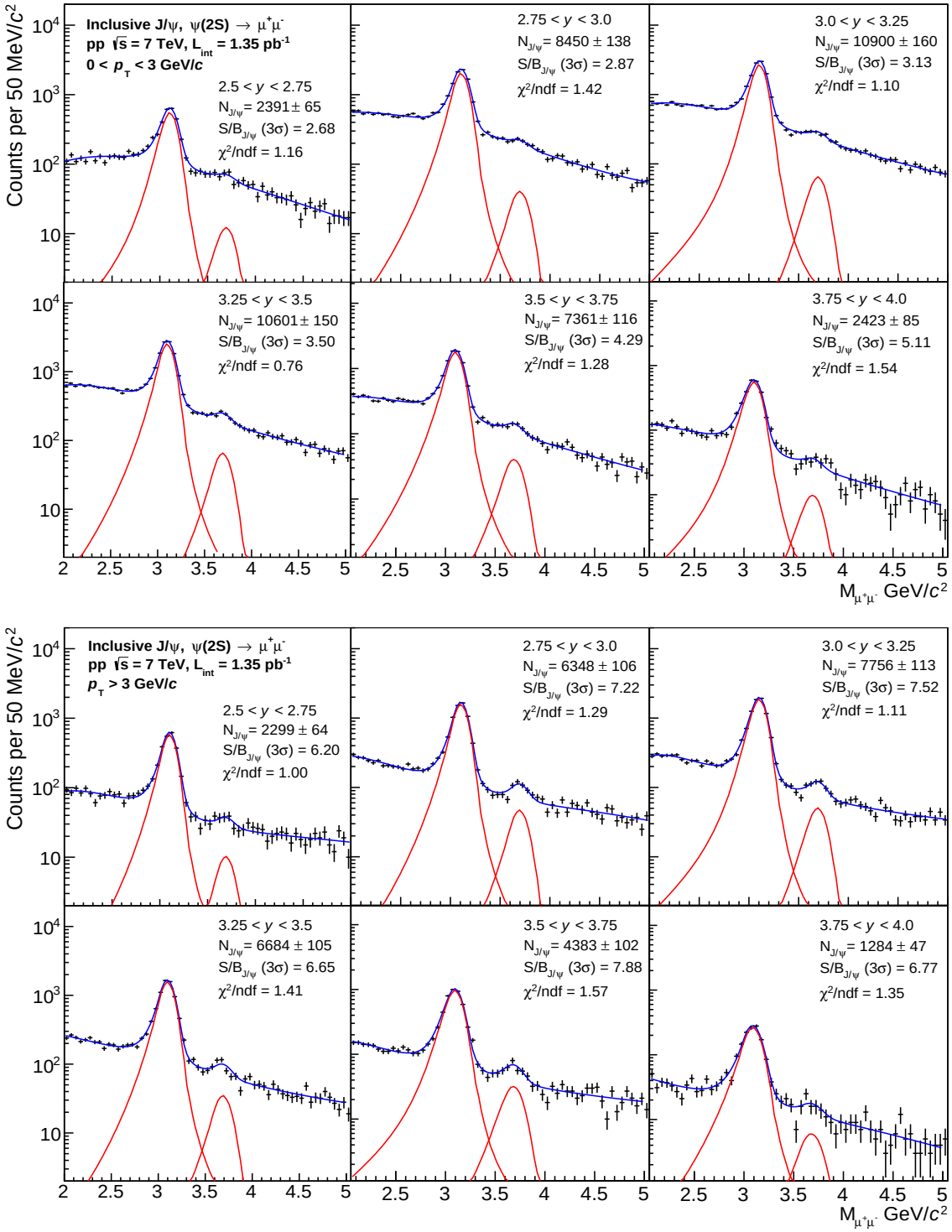

Figure 6.6: Invariant mass spectrum in six rapidity bins for $0 < p_{\mathrm{T}} < 3$ GeV/c (top) and $p_{\mathrm{T}} > 3$ GeV/c (bottom) fitted with CB2+VWG in pp collisions.

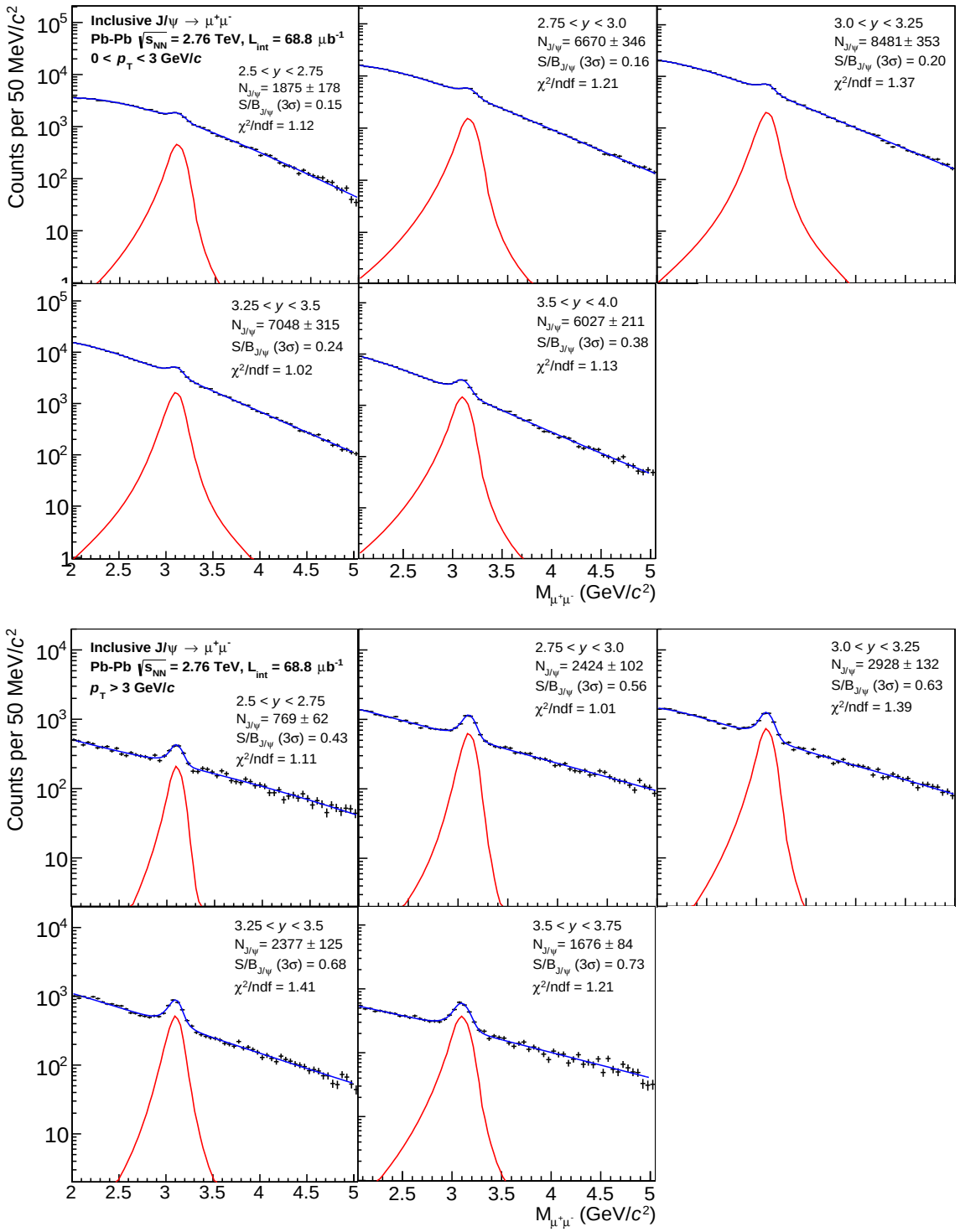

Figure 6.7: Invariant mass spectrum in five rapidity bins for $0 < p_{\mathrm{T}} < 3$ GeV/c (top) and $p_{\mathrm{T}} > 3$ GeV/c (bottom) fitted with CB2+VWG in Pb-Pb collisions.

6.3 Acceptance and efficiency corrections

The analysis procedures for the acceptance and efficiency corrections and its systematic uncertainty measurements for pp collisions is similar to that described in chapter 4. In the present case, the rapidity dependence and the uncertainties were estimated for specific p_{T} bins. The acceptance times efficiency (A$\times\epsilon$) has been determined by simulating J/ψ and ψ(2S) signals using p_{T} and y input distributions based on an interpolation of the LHC, CDF, and RHIC distributions. The signals are generated within a wider rapidity range ($2.0 \leq y \leq 4.5$) in order to account for the edge effects of the acceptance region. The A$\times\epsilon$ calculation has been performed on a run by run basis with a realistic MC simulation. It includes the experimental conditions (HV, LV and readout) of the Muon Spectrometer from Offline Calibration Data Base (OCDB). The A$\times\epsilon$ factor is determined as the ratio of the number of reconstructed signals over the generated events in the muon acceptance.

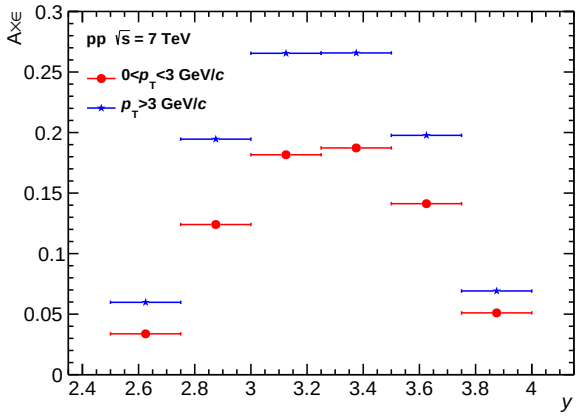

Figure 6.8: A$\times\epsilon$ of J/ψ as a functions of y in pp collisions.

The A$\times\epsilon$ for pp collisions in the six rapidity bins for $0 < p_{\mathrm{T}} < 3$ GeV/c and $p_{\mathrm{T}} > 3$ GeV/c is shown in Fig. 6.8. It may be noted that the A$\times\epsilon$ as a function of rapidity is lower in the low p_{T} bin as compared to the high p_{T} bin. This observation however, has a small effect on the present study since the variable FDDC depends on

the shape of the A×ϵ curve rather than on the absolute value.

For Pb-Pb collisions, the A×ϵ have been calculated from the Embedding Monte Carlo technique. The embedding Monte Carlo technique consisted of simulating a signal particle and embedding it with hits generated in the detector for a real MB event. Among MC techniques, the embedding provides the most realistic background conditions. Such a realistic description is necessary in the case of (most central) Pb-Pb collisions because of the high particle multiplicity environment which could alter the track reconstruction efficiency due to overlap of charge clusters in the cathode pad chambers. The J/ψ were generated according to realistic parametrization of their p_{T} and y distributions [6] and were forced to decay into dimuons. The detector response was provided by GEANT3 [7] taking into account the time dependence of the detector efficiency and the residual misalignment of the tracking chambers.

The A×ϵ for Pb-Pb collisions in five rapidity bins for $0 < p_{\mathrm{T}} < 3$ GeV/c and $p_{\mathrm{T}} > 3$ GeV/c is shown in Fig. 6.9.

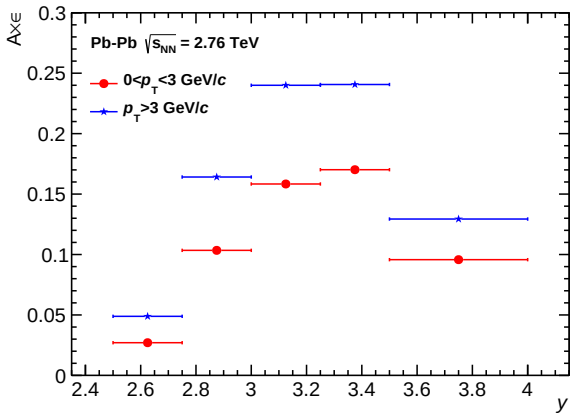

Figure 6.9: A×ϵ of J/ψ as a functions of y in Pb-Pb collisions.

6.4 Tracking and Trigger efficiency

The tracking and trigger efficiency and their systematic uncertainty measurements both for pp and Pb-Pb collisions are similar to that described in chapter 4. However, in this analysis, the determination of systematic uncertainty on the tracking and trigger efficiencies is not essential since they cancel out in the ratio.

6.5 Other systematic uncertainties

The other systematic uncertainties like the systematic uncertainty on the matching efficiency between the tracking and the trigger tracks, uncertainties due luminosity also cancelled out.

6.6 Results

The fractional double differential cross-section (FDDC) is defined as:

$$\frac{d^2\sigma/dp_{\rm T}dy}{(d^2\sigma/dp_T dy)_{\rm Total}} = \frac{N_{\rm J/\psi}}{({\rm A}\times\epsilon)_{\rm J/\psi}}.\frac{(({\rm A}\times\epsilon)_{\rm J/\psi})_{\rm Total}}{(N_{\rm J/\psi})_{\rm Total}} \tag{6.1}$$

The only systematic uncertainties in FDDC are due to the signal extraction and the A$\times\epsilon$ evaluation.

6.6.1 The rapidity dependence of FDDC

The FDDC of J/ψ as a function of y for two p_{T} ranges: $0 < p_{\mathrm{T}} < 3$ GeV/c and $p_{\mathrm{T}} > 3$ GeV/c are shown in the left and right panels of Fig. 6.10 for pp and Pb-Pb, respectively. For pp, the low p_{T} bin shows a smaller slope than the high p_{T} bin. The two distributions cross each other at the middle of our rapidity acceptance. On the other hand for Pb-Pb, the low p_{T} and high p_{T} distributions look quite similar in contrast to the pp case. This change of behaviour is striking and in order to establish these results, it was decided to compare them with the already published one.

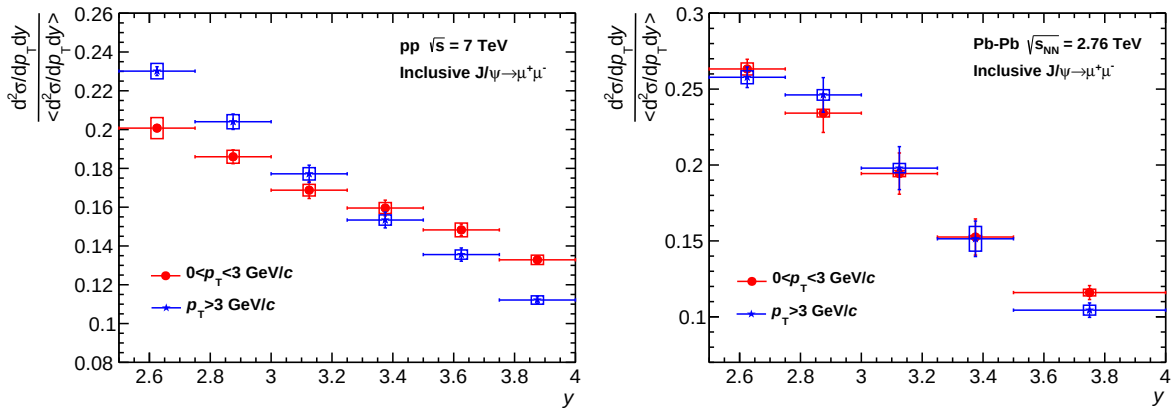

Figure 6.10: Fractional double differential cross-section of J/ψ as a function of y for pp (left) and Pb-Pb (right) collisions.

6.6.2 Comparison with the published results

This was done by adding the A×ϵ normalized counts in each rapidity bin for the low and high p_{T} bins. In this way the fractional differential cross-sections can be evaluated from the present analysis and can be compared with the published results at $\sqrt{s} = 7$ TeV [5] for pp and at $\sqrt{s_{\mathrm{NN}}} = 2.76$ TeV [2] for Pb-Pb. This comparisons is shown in the left and right panels of Fig. 6.11 for pp and Pb-Pb, respectively. It is observed that there is a good agreement between the two results for both the cases.

This check confirms the validity of the present analysis chain for FDDCs.

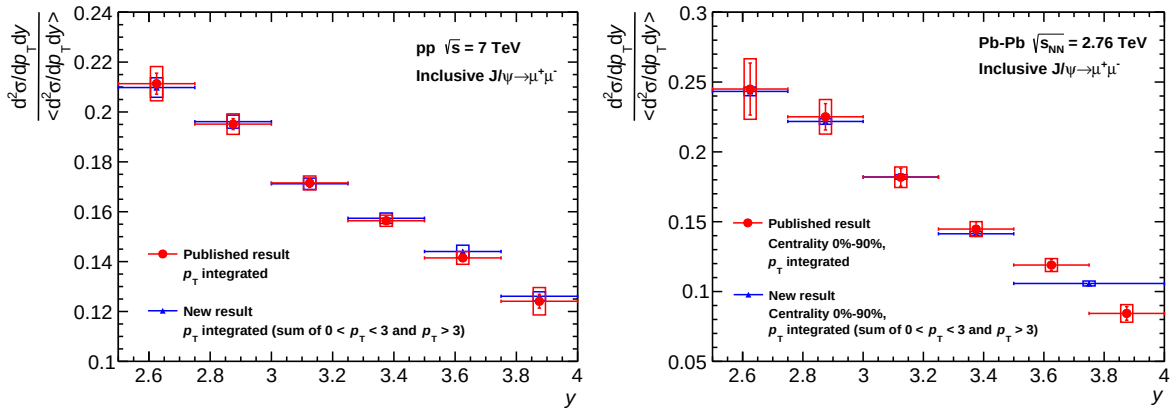

Figure 6.11: Fractional double differential cross-section of J/ψ compared with the published results at $\sqrt{s} = 7$ TeV [5] in pp collisions (left) and at $\sqrt{s_{\rm NN}} = 2.76$ TeV [2] in Pb-Pb collisions (right).

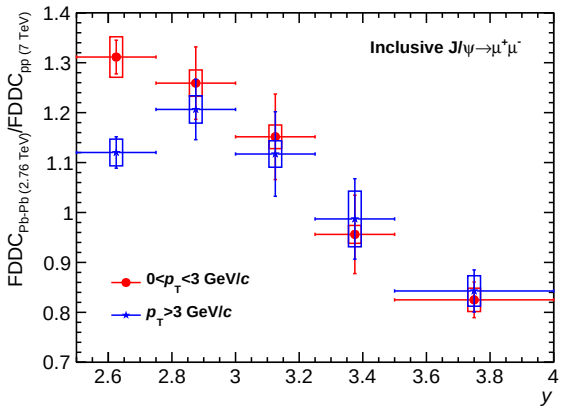

Figure 6.12: Ratio of the fractional double differential cross-section of J/ψ between Pb-Pb to pp as a function of y.

6.6.3 Discussion

The difference in the shapes of FDDC for pp and Pb-Pb results can be amplified by plotting the ratio $\mathrm{FDDC_{Pb-Pb}/FDDC_{pp}}$ (Fig. 6.12). It may be noted that the ratios are evaluated at two different center-of-mass energies but it has been demonstrated in Fig. 6.3 that this variable does not have an observable dependence on $\sqrt{s}$.

It is observed from Fig. 6.12 that there is a definitive excess of counts in the lowest rapidity bin $2.5 \leq y \leq 2.75$ for the low p_{T} bin compared to the high p_{T} bin. In the low p_{T} bin there are three competing contributions in Pb-Pb results compared to pp. They are (a) the colour suppression, (b) the CNM effects and (c) the recombination effects. The first two effects will lead to a decrease in J/ψ production while the third leads to an increase. Thus, the present observation seems to indicate a strong recombination effect in the $2.5 \leq y \leq 2.75$ bin. This may be quantitatively understood by noting that the density of the charge centres increases in the mid-rapidity region. This would imply a large recombination effect towards the mid rapidity direction.

It is also interesting to note from Fig. 6.10 that there is an indication of a saturation effect in FDDC value in Pb-Pb results for $p_{\mathrm{T}} > 3$ GeV/c in the low rapidity domain. This observation can be further explored theoretically within the framework of NRQCD which is successful in describing the pp cross-sections for $p_{\mathrm{T}} > 3$ GeV/c. The calculated pp cross-sections can be scaled with the glauber model to predict the cross-section for the Pb-Pb case. These results can be convoluted with the survival fraction (S(p_{T})) values based purely on the colour suppression model [8] as in this p_{T} domain the contribution of recombination and CNM effects are expected to be small. Such a comparison may indicate whether the fire-ball created in the Pb-Pb collisions is isotropic in temperature or not.

Bibliography

[1] B. Abelev *et al.* (ALICE Collaboration), "J/ψ Suppression at Forward Rapidity in Pb-Pb Collisions at $\sqrt{s_{\rm NN}} = 2.76$ TeV", Phys. Rev. Lett **109**, 072301 (2012).

[2] B. Abelev *et al.* (ALICE Collaboration), "Centrality, rapidity and transverse momentum dependence of J/ψ suppression in Pb-Pb collisions at $\sqrt{s_{\rm NN}} = 2.76$ TeV", Phys. Lett. B **734**, 314-327 (2014).

[3] B. Abelev *et al.* (ALICE Collaboration), "Inclusive, prompt and non-prompt J/ψ production at mid-rapidity in Pb-Pb collisions at $\sqrt{s_{\rm NN}} = 2.76$ TeV", arXiv:1504.07151.

[4] B. Abelev *et al.* (ALICE Collaboration), "Inclusive J/ψ production in pp collisions at $\sqrt{s} = 2.76$ TeV", Phys. Lett. B **718**, 295 (2012).

[5] B. Abelev *et al.*, (ALICE Collaboration), "Measurement of quarkonium production at forward rapidity in pp collisions at $\sqrt{s} = 7$ TeV," Eur. Phys. J. C **74**, 2974 (2014).

[6] F. Bossu, Z. C. del Valle, A. de Falco, M. Gagliardi, S. Grigoryan and G. Martinez Garcia, "Phenomenological interpolation of the inclusive J/ψ cross section to proton-proton collisions at 2.76 TeV and 5.5 TeV", arXiv:1103.2394 [nucl-ex].

[7] "GEANT - Detector description and simulation tool", CERN Program Library Long Write-up W5013, CERN Geneva.

[8] M.-C. Chu and T. Matsui, "Pattern of J/ψ suppression in ultrarelativistic heavy-ion collisions", Phys. Rev. D **37**, 1851 (1988).

Chapter 7

Quarkonia production cross-section calculation within the framework of NRQCD

7.1 Introduction

In this chapter the numerical calculations based on the non-relativistic quantum chromodynamics (NRQCD) framework is presented. These calculations have been performed during the course of this thesis and the results have been published in ref [1].

The understanding of the production of a heavy quarkonium has been a long-term effort both experimentally and theoretically. The different treatments of the non-perturbative evolution of the $Q\bar{Q}$ pair into a quarkonium lead to various theoretical models. There are mainly three models widely used to describe the production of quarkonium: the Colour Singlet Model (CSM), the Colour Evaporation Model (CEM)

and the non-relativistic quantum chromodynamics (NRQCD) framework.

The CSM, proposed right after the discovery of the J/ψ, assumes that the $Q\bar{Q}$ pair evolving into a quarkonium state is in a colour-singlet (CS) state and the quantum numbers, such as spin and angular momentum, are conserved after the formation of the quarkonium. The only inputs required in the model are the absolute value of the colour singlet $Q\bar{Q}$ wave function and its derivatives that can be determined from the data of decay processes. Once these quantities are provided, the CSM has no free parameters [2]. The CSM at leading-order, predicts well the quarkonium production cross-sections at relatively low energy [3], but fails to describe the data on charmonium production measured by the CDF experiment in $p - \bar{p}$ collisions [4] probably because it ignores the decays from higher states or B mesons, dominant at Tevatron energies [5]. Recently it has been revived, with the computation at higher orders in the strong coupling constant α_s expansion [6–8], since it was found to accommodate polarization results from Tevatron in a much better way as compared to NRQCD.

The CEM [9] is a phenomenologically successful model and was first proposed in 1977 [10]. In the CEM, the cross-section for a quarkonium state H is a fraction F_H of the cross-section of the produced $Q\bar{Q}$ pairs with invariant mass below the $M\bar{M}$ threshold, where M is the lowest mass meson containing the heavy quark Q. This cross-section has an upper limit on the $Q\bar{Q}$ pair mass but no constraints on the colour or spin of the final state. The $Q\bar{Q}$ pair is assumed to neutralize its colour by interaction with the collision-induced colour field via "colour evaporation". An important feature is that the fractions F_H are assumed to be universal so that, once they are determined by the data, they can be used to predict the cross-sections in other processes and in other kinematical regions. The most basic prediction of the CEM is that the ratio of the cross-sections for any two quarkonium states should be

constant, independent of the process and the kinematical region. However, variations in these ratios have been observed: for example the ratio of the cross-sections for χ_c and J/ψ are rather different in photoproduction and hadroproduction [11–14] and the ratio between different charmonium cross-sections measured at LHC is not constant as a function of p_T [15]. These variations represent a serious challenge to the status of the CEM as a quantitative phenomenological model for quarkonium production. However, the model is still widely used as simulation benchmark since, once the F_H fractions are determined, it can predict the cross-sections completely. However, it fails to predict the quarkonium polarization.

On the other hand, NRQCD can predict both the cross-section and the polarization of quarkonium production. In NRQCD, contributions to the quarkonium cross-section from the heavy-quark pairs produced in a colour-octet (CO) state are also taken into account, in addition to the colour-singlet (CS) contributions described above. The picture of the NRQCD [16] formalism is as follows. The orbital splittings in case of quarkonium bound states are smaller than the heavy quark mass m_Q, which suggests that all the other dynamical scales of these systems are smaller than m_Q. So, the relative velocity v between Q and $\bar{Q}$ is believed to be a small quantity, $v \ll 1$. Therefore, a hierarchy of scales, $m_Q \gg m_Q v \gg m_Q v^2$, as observed in a non-relativistic (NR) system, also holds for quarkonia. Here, m_Q fixes the distance range for $Q\bar{Q}$ creation and annihilation processes, the momentum $m_Q v$ is inversely proportional to the spatial size of the bound state and the kinetic energy $m_Q v^2$ determines the typical interaction time scale. These different distance scales make the study of quarkonium production interesting which is built in naturally in the NRQCD calculation.

Quarkonia production in NRQCD is calculated in two steps. At first, the creation of the $Q\bar{Q}$ pair in a hard scattering process at short distances is calculated perturbatively as an expansion in terms of the strong coupling constant α_s. Note

that $Q\bar{Q}$ states can be in a CS state [17–19] as well as in a CO state [20–22]. Then, the $Q\bar{Q}$ pair evolves into the quarkonium state with the probabilities that are given by the assumed universal non-perturbative long-distance matrix elements (LDMEs) which are estimated on the basis of the comparison with experimental measurements. For CO states, this evolution process also involves the non-perturbative emission of soft gluons to form CS states. The crucial feature of this formalism is that it takes into account the complete structure of the $Q\bar{Q}$ Fock space, which is spanned by the states $n = {}^{2S+1}L_J^{[i]}$, where S, L and J are the spin, orbital and total angular momenta, respectively and i is the colour multiplicity. A remarkable progress has been made in quarkonium production studies during the last decade based on the NRQCD formalism [23–30].

In recent times, the charmonium production in $p-p$ collisions has been measured at $\sqrt{s}$ = 2.76, 7 and 8 TeV by the ALICE [15, 31, 32], ATLAS [33], CMS [34] and LHCb [35–37] Collaborations at forward, near forward and mid rapidities. It may be noted here that ALICE, ATLAS, CMS and LHCb Collaborations report the prompt production cross-sections, while ALICE also measures the inclusive production cross-section at forward rapidity which includes the B feed-down to J/ψ and $\psi(2S)$ along with the prompt production.

In this thesis, the charmonium cross-sections have been calculated at $\sqrt{s} = 2.76$ and 7 TeV within the framework of LO NRQCD and compared with the available experimental data from LHC. The predictions for the production cross-sections of J/ψ and $\psi(2S)$ in $p-p$ collisions at $\sqrt{s} = 13$ TeV has been made as these collisions are foreseen at LHC in 2015. In addition, the calculations have also been performed at $\sqrt{s}$ = 5.1 TeV, which is the centre-of-mass energy for the forthcoming Pb-Pb run at the LHC. The FONLL [38, 39] formalism has been used to calculate the production cross-sections of J/ψ and $\psi(2S)$ from B meson decays. It is worthwhile

to mention that although the NLO calculations for quarkonium production exist in the literature [23–30], we have opted for the LO calculation as it reproduces all the existing data quite well for $p_T \geq 3 - 4$ GeV. Similar calculations have been carried out also for bottomonium.

7.2 Theoretical formalism

The factorization formalism of NRQCD provides a theoretical framework for studying heavy quarkonium production and decay. According to the NRQCD factorization formalism, the cross-section for direct production of a resonance H in a collision of particle A and B can be expressed as

$$d\sigma_{A+B\to H+X} = \sum_{a,b,n} \int dx_a dx_b G_{a/A}(x_a,\, \mu_F^2)\, G_{b/B}(x_b,\, \mu_F^2) \times d\sigma(a+b \to Q\bar{Q}(n)+X) < \mathcal{O}^H(n) > \tag{7.1}$$

where, $G_{a/A}(G_{b/B})$ is the parton distribution function (PDF) of the incoming parton $a(b)$ in the incident hadron $A(B)$, which depends on the momentum fraction $x_a(x_b)$ and the factorization scale μ_F. The tranverse mass of the resonance H is $m_T = \sqrt{p_T^2 + m_H^2}$, where $m_H \sim 2m_Q$ is the mass of the resonance H. The short distance contribution $d\sigma(a + b \to Q\bar{Q}(n) + X)$ can be calculated within the framework of perturbative QCD (pQCD). On the other hand, $< \mathcal{O}^H(n) >$ (the state $n = {}^{2S+1}L_J^{[i]}$) are non-perturbative LDMEs and can be estimated on the basis of comparisons with experimental measurements.

The differential cross-section for the short distance contribution i.e. the heavy quark pair production from the reaction of the type $a + b \to c + d$, where a, b refer to light incident partons, c refers to $Q\bar{Q}$ pair and d is the light final state parton, can

be written as [40]

$$\frac{d^2\sigma^{ab\to cd}}{dp_T\,dy} = \int dx_a\, G_{a/A}(x_a,\,\mu_F^2)\, G_{b/B}(x_b,\,\mu_F^2) \times 2p_T \frac{x_a\, x_b}{x_a - \frac{m_T}{\sqrt{s}} e^y} \frac{d\sigma}{d\hat{t}}(ab \to cd), \tag{7.2}$$

where $\sqrt{s}$ is the total energy in the centre-of-mass and y is the rapidity of the $Q\bar{Q}$ pair. In the present numerical computation, we have used CTEQ6L [41] for the parton distribution functions. The invariant differential cross-section is given by

$$\frac{d\sigma}{d\hat{t}} = \frac{|\mathcal{M}|^2}{16\pi\hat{s}^2}, \tag{7.3}$$

where $\hat{s}$ and $\hat{t}$ are the parton level Mandelstam variables and $\mathcal{M}$ is the Feynman amplitude for the process which contains α_s. We take the parametrization of α_s as [42] $\alpha_s = \frac{12\pi}{(33-2N_f)\ln(\mu_R^2/\Lambda^2)}$, where, μ_R is the renormalization scale and Λ is the non-perturbative scale of QCD.

The value of the momentum fraction x_b can be written as,

$$x_b = \frac{1}{\sqrt{s}} \frac{x_a\sqrt{s}\, m_T\, e^{-y} - m_H^2}{x_a\sqrt{s} - m_T\, e^y}. \tag{7.4}$$

The minimum value of x_a is

$$x_{a\min} = \frac{1}{\sqrt{s}} \frac{\sqrt{s}\, m_T\, e^y - m_H^2}{\sqrt{s} - m_T\, e^{-y}}. \tag{7.5}$$

The LDMEs are predicted to scale with a definite power of the relative velocity v of the heavy constituents inside $Q\bar{Q}$ bound states. In the limit $v \ll 1$, the production of quarkonium is based on the ${}^3S_1^{[1]}$ and ${}^3P_J^{[1]}$ (J = 0,1,2) CS states and ${}^1S_0^{[8]}$, ${}^3S_1^{[8]}$ and ${}^3P_J^{[8]}$ CO states. In our calculations, we used the expressions for the short distance CS

cross-sections given in Refs. [17–19] and the CO cross-sections given in Refs. [21, 22].

	LDMEs	Numerical value	NRQCD scaling order
Colour-Singlet	$<\mathcal{O}(Q\bar{Q}(\,^3S_1^{[1]}) \rightarrow J/\psi)>$	1.2 GeV^3	$m_c^3 v_c^3$
	$<\mathcal{O}(Q\bar{Q}(\,^3S_1^{[1]}) \rightarrow \psi(2S))>$	0.76 GeV^3	$m_c^3 v_c^3$
	$<\mathcal{O}(Q\bar{Q}(\,^3P_0^{[1]}) \rightarrow \chi_{c0})>/m_c^2$	0.054 GeV^3	$m_c^3 v_c^5$
	$<\mathcal{O}(Q\bar{Q}(\,^3P_1^{[1]}) \rightarrow \chi_{c1})>/3m_c^2$	0.054 GeV^3	$m_c^3 v_c^5$
	$<\mathcal{O}(Q\bar{Q}(\,^3P_2^{[1]}) \rightarrow \chi_{c2})>/5m_c^2$	0.054 GeV^3	$m_c^3 v_c^5$
Colour-Octet	$<\mathcal{O}(Q\bar{Q}(\,^3S_1^{[8]}) \rightarrow J/\psi)>$	0.0013 ± 0.0013 GeV^3	$m_c^3 v_c^7$
	$<\mathcal{O}(Q\bar{Q}(\,^3S_1^{[8]}) \rightarrow \psi(2S))>$	0.0033 ± 0.00021 GeV^3	$m_c^3 v_c^7$
	$<\mathcal{O}(Q\bar{Q}(\,^3S_1^{[8]}) \rightarrow \chi_{cJ})>/m_c^2$	0.00187 ± 0.00025 GeV^3	$m_c^3 v_c^5$
	$<\mathcal{O}(Q\bar{Q}(\,^1S_0^{[8]}) \rightarrow J/\psi)>$	0.018 ± 0.0087 GeV^3	$m_c^3 v_c^7$
	$<\mathcal{O}(Q\bar{Q}(\,^1S_0^{[8]}) \rightarrow \psi(2S))>$	0.0080 ± 0.00067 GeV^3	$m_c^3 v_c^7$
	$<\mathcal{O}(Q\bar{Q}(\,^3P_0^{[8]}) \rightarrow J/\psi)>/m_c^2$	0.018 ± 0.0087 GeV^3	$m_c^3 v_c^7$
	$<\mathcal{O}(Q\bar{Q}(\,^3P_0^{[8]}) \rightarrow \psi(2S))>/m_c^2$	0.0080 ± 0.00067 GeV^3	$m_c^3 v_c^7$

Table 7.1: The colour-singlet and colour-octet matrix elements with numerical values and NRQCD scaling order for charmonia.

The p_T distribution of J/ψ and $\psi(2S)$ in $p-p$ collisions at LHC energies has been calculated. For J/ψ production in $p-p$ collisions, contributions from three sources have been considered: (a) direct J/ψ production, (b) feed-down contributions to the J/ψ from the decay of heavier charmonium states, predominantly from $\psi(2S)$, χ_{c0}, χ_{c1} and χ_{c2} and (c) J/ψ from B hadron decays. The sum of the first two sources is called "prompt J/ψ" and the third source will be called "J/ψ from B". On the other hand, $\psi(2S)$ has no significant feed-down contributions from higher mass states. We call this direct contribution as "prompt $\psi(2S)$" to be consistent with the experiments. The other source to $\psi(2S)$ production is from B hadron decays and we call it "$\psi(2S)$ from B". The sum of the prompt $J/\psi(\psi(2S))$ and $J/\psi(\psi(2S))$ from B will be called "inclusive $J/\psi(\psi(2S))$".

The direct production cross-section of J/ψ can be written as the sum of the

contributions [21, 22],

$$\begin{aligned} d\sigma(J/\psi) = d\sigma(Q\bar{Q}(\ ^3S_1^{[1]})) < \mathcal{O}(Q\bar{Q}(\ ^3S_1^{[1]}) \to J/\psi) > \\ + d\sigma(Q\bar{Q}(\ ^1S_0^{[8]})) < \mathcal{O}(Q\bar{Q}(\ ^1S_0^{[8]}) \to J/\psi) > \\ + d\sigma(Q\bar{Q}(\ ^3S_1^{[8]})) < \mathcal{O}(Q\bar{Q}(\ ^3S_1^{[8]}) \to J/\psi) > \\ + d\sigma(Q\bar{Q}(\ ^3P_J^{[8]})) < \mathcal{O}(Q\bar{Q}(\ ^3P_J^{[8]}) \to J/\psi) > \\ +... \end{aligned} \tag{7.6}$$

Similar expression holds for direct $\psi(2S)$ production. The direct production cross-section for χ_{cJ} can be written as [21]:

$$\begin{aligned} d\sigma(\chi_{cJ}) = d\sigma(Q\bar{Q}(\ ^3P_J^{[1]})) < \mathcal{O}(Q\bar{Q}(\ ^3P_J^{[1]}) \to \chi_{cJ}) > \\ + d\sigma(Q\bar{Q}(\ ^3S_1^{[8]})) < \mathcal{O}(Q\bar{Q}(\ ^3S_1^{[8]}) \to \chi_{cJ} > \\ + ... \end{aligned} \tag{7.7}$$

Here, we have taken into account the contributions from all three χ_{cJ} (χ_{c0}, χ_{c1} and χ_{c2}) mesons to J/ψ.

To calculate the direct charmonia and feed-down contributions from heavier states as well as from B decays, we use the following branching ratios: $\mathcal{B}(J/\psi[\psi(2S)] \to \mu^+\mu^-)$=0.0593[0.0078], $\mathcal{B}(\psi(2S) \to J/\psi)$=0.603. $\mathcal{B}(\chi_{cJ} \to J/\psi)$=0.0130, 0.348, 0.198 for $J = 0,\ 1,\ 2$, respectively and $\mathcal{B}(B \to J/\psi[\psi(2S)])$=0.116[0.307] [43]. The LDMEs [44] for CS and CO which we have used for our calculations are given in Table 7.1. The central values of LDMEs are taken for our calculations.

In order to estimate the uncertainty on the calculated values, four possible sources have been considered, namely the perturbative scales, the mass of the charm

and bottom quark, the branching ratios for the feed-down to J/ψ and the PDFs. The largest uncertainty in the branching ratios is $\sim$7% which corresponds to $B \to \psi(2S)+X$ channel. The uncertainty due to the assumed PDF was estimated by performing the calculations with different PDFs, namely CTEQ6L and CTEQ6L1. The largest uncertainty was found to be about 10% at $3 < p_T < 4$ GeV. For the FONLL [38, 39, 45] calculations CTEQ6.6 is used for the PDFs and the PDF uncertainty in this case is about 10%. The uncertainty related to the choice of the heavy quark masses was estimated by varying them in the ranges $1.2 < m_c < 1.6$ GeV and $4.5 < m_b < 5$ GeV for NRQCD and FONLL, respectively. The largest uncertainty due to mass variation was found to be about 12% at $3 < p_T < 4$ GeV. We define the renormalization and factorization scales by $\mu_{R,F} = \xi_{R,F}\mu_0$, where μ_0 is $\sqrt{p_T^2 + 4m_c^2}$ and $\sqrt{p_T^2 + m_b^2}$ for NRQCD and FONLL, respectively. The central values of our predictions are obtained with $\xi_{R,F} = 1$, the mass of the charm quark $m_c = 1.4$ GeV and the mass of the bottom quark $m_b = 4.75$ GeV. To avoid the accidental compensation between the μ_F and μ_R dependence of the cross-section occurring when the two scales are kept equal, we compute the scale uncertainty by varying μ_F and μ_R independently over the range $0.5 < \xi_{R,F} < 2$, with the constraint $0.5 < \xi_R/\xi_F < 2$. The uncertainty due to this scale variation was found to be as large as 45% at $3 < p_T < 4$ GeV. Thus, this is the dominant source of uncertainy and in all the subsequent figures for the numerical values, the uncertainty bands correspond only to this source. This assumption is valid in case the four sources of uncertainties are considered to be independent, in which case the contributions are to be added in quadrature.

7.3 Results of charmonium calculations

The NRQCD calculations have been carried out for the differential cross-sections of J/ψ and $\psi(2S)$ as a function of p_T at $\sqrt{s} = 2.76$ and 7 TeV. The numerical results have been compared with the experimental data available from CMS ($|y| < 0.9$, $0.9 < |y| < 2.4$, $|y| < 1.2$ and $1.2 < |y| < 2.4$), ATLAS ($|y| < 0.75$ and $0.75 < |y| < 2.4$), LHCb ($2 < y < 4.5$) and ALICE ($|y| < 0.9$ and $2.5 < y < 4$). Thus, this detail study explores the validity of NRQCD calculations at mid, near forward and forward rapidities at LHC energies.

In Fig. 7.1, the numerical values from the NRQCD calculations for differential cross-section of J/ψ as a function of p_T have been compared with the experimental values obtained by the four experiments at LHC, namely ATLAS [33], CMS [34], LHCb [35] and ALICE [15, 32] at $\sqrt{s} = 7$ TeV. Note that the ALICE measurements of inclusive J/ψ at forward rapidity are compared with the sum of the prompt J/ψ from NRQCD and J/ψ from B-decay from FONLL. It is observed from Fig. 7.1, that the calculated values show a good agreement with all the experimental data for $p_T >$ 4 GeV. In a recent publication [46], it has been shown that the low p_T cross-section can be reproduced by an inclusion of Color Glass Condensate (CGC) effects within the NRQCD framework.

The calculated values of the differential cross-section of $\psi(2S)$ as a function of p_T using the NRQCD framework have been compared with CMS [34], LHCb [36] and ALICE [15] data and are shown in Fig. 7.2. It is important to note that for $\psi(2S)$ there is no contribution from the higher excited charmonium states. Thus, the prompt and direct production are the same. Also in this case, the ALICE data on inclusive $\psi(2S)$ are compared with the sum of direct $\psi(2S)$ from NRQCD and $\psi(2S)$ from B-decay using FONLL. The results of theoretical calculations for $\psi(2S)$ provide

a good description of the experimental measurements.

The numerical calculations for inclusive J/ψ production were also carried out for $\sqrt{s} = 2.76$ TeV and compared with the reported inclusive measurements from LHCb [37] and ALICE [31] in Fig. 7.3. In this case the calculated and measured values for J/ψ are in good agreement for $p_T > 3$ GeV.

The ALICE Collaboration has also reported the ratio of the differential cross-sections of $\psi(2S)$ to J/ψ at $\sqrt{s} = 7$ TeV [15]. The measured and calculated values are shown in Fig. 7.4. The agreement is reasonable for $p_T > 3$ GeV and the increasing trend of the ratio is described by the calculation. It is worth noting that the prediction for this ratio from CEM is independent of p_T.

This success of NRQCD calculations in describing the $p - p$ collision data at various rapidities and energies has prompted us to use our calculations to predict the production cross-sections at $\sqrt{s} = 2.76$, 5.1 and 13 TeV. These predictions are shown in Fig. 7.5 and 7.6. It will be interesting to test the applicability of these calculations at the much higher centre-of-mass energy of 13 TeV in 2015. On the other hand, the predictions at $\sqrt{s} = 2.76$ and 5.1 TeV may be used for comparison with the Pb-Pb collision data at these energies.

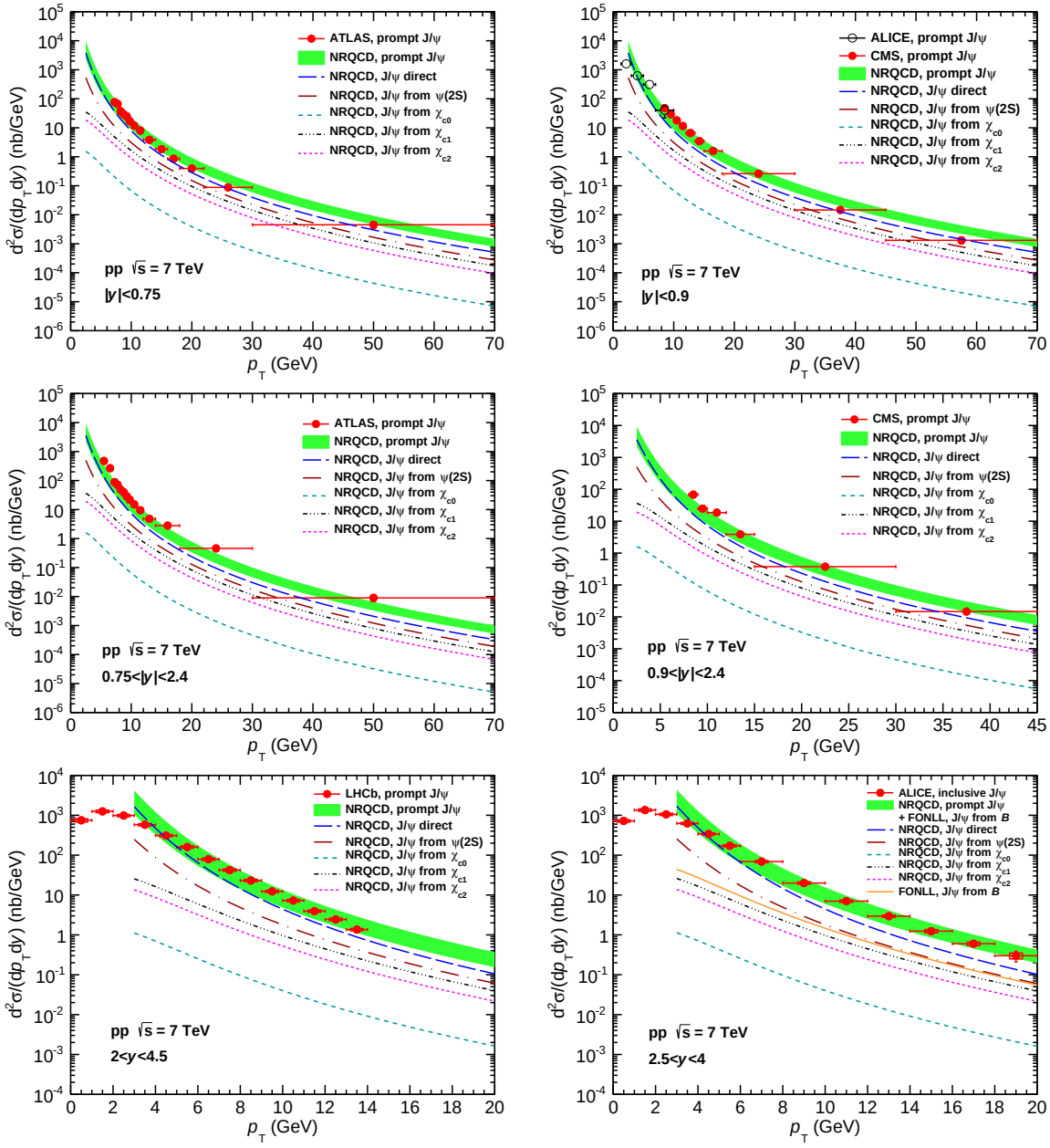

Figure 7.1: Differential production cross-section of J/ψ as a function of p_T compared with the ATLAS [33], CMS [34], LHCb [35] and ALICE [15, 32] data. The vertical error bars on the data points represent the statistical errors on the measurements, while the boxes correspond to the systematic uncertainties. The calculations corresponding to the sum of all contributions are shown as a green band. The direct and feed-down contributions to J/ψ are shown only by lines for the central values.

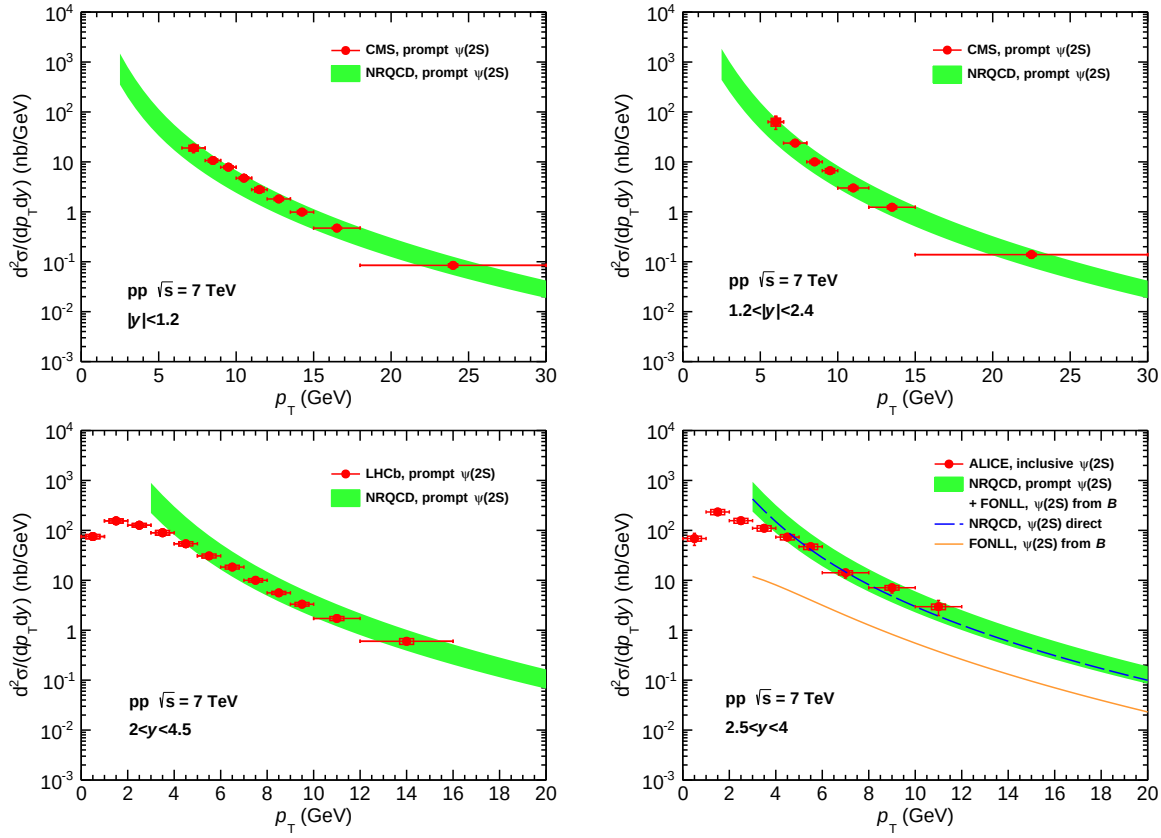

Figure 7.2: Differential production cross-section of $\psi(2S)$ as a function of p_T compared with the measurements by CMS [34], LHCb [36] and ALICE [15] data.

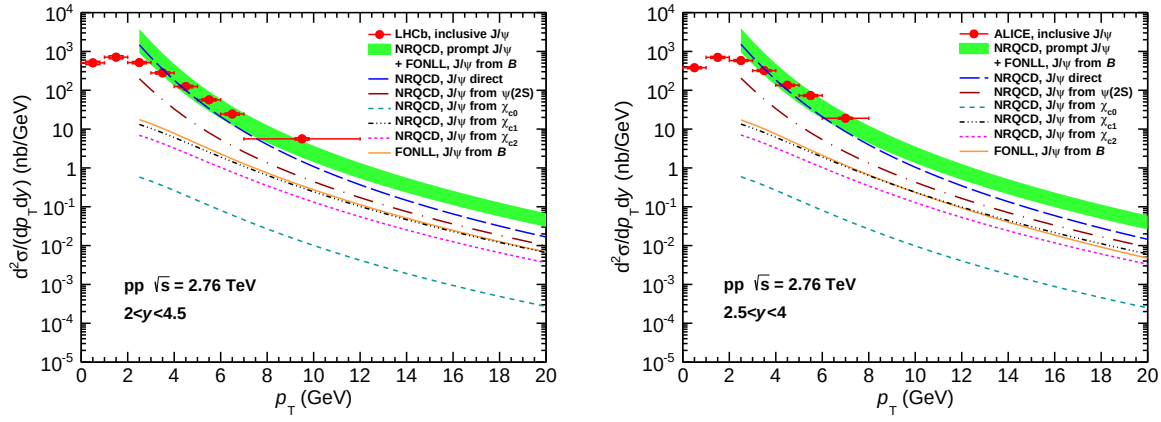

Figure 7.3: Differential production cross-section of inclusive J/ψ as a function of p_T compared with the measurements by LHCb [37] and ALICE [31].

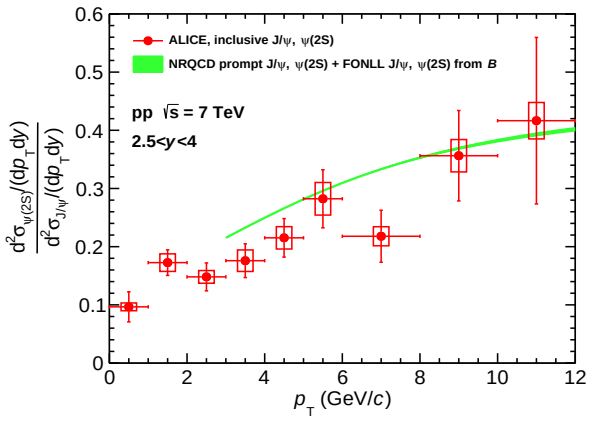

Figure 7.4: Inclusive $\psi(2S)$ to J/ψ production cross-section ratio as a function of p_T compared with the measurements by ALICE [15] data.

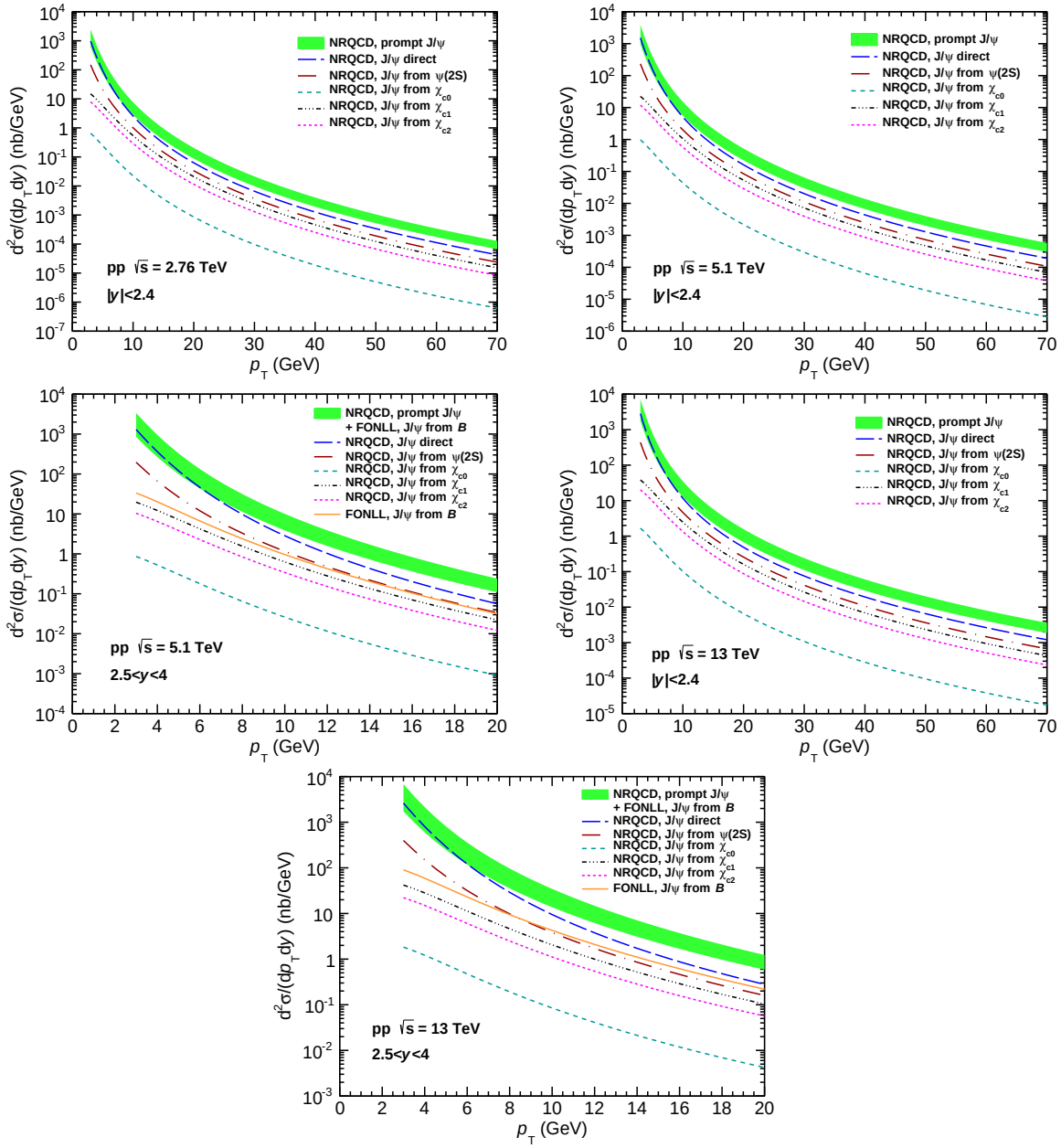

Figure 7.5: Theoretical predictions for the differential cross-section of J/ψ at $\sqrt{s} =$ 2.76, 5.1 and 13 TeV at mid and forward rapidity.

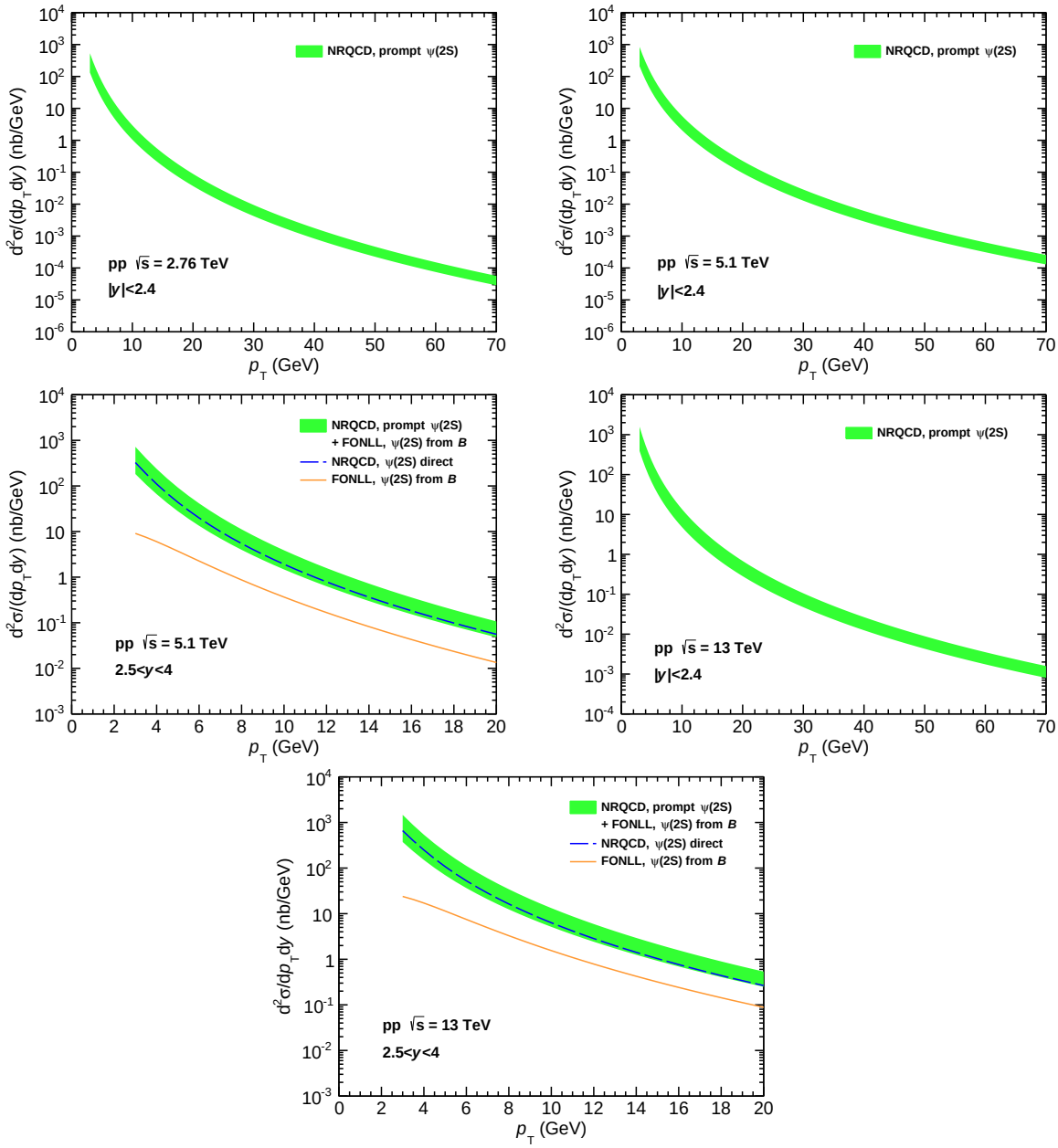

Figure 7.6: Theoretical predictions for the differential cross-section of $\psi(2S)$ at $\sqrt{s} =$ 2.76, 5.1 and 13 TeV at mid and forward rapidity.

7.4 Results of bottomonium calculations

The calculations based on the same framework have been carried out for the bottomonium production cross-sections at $\sqrt{s} = 7$ TeV and compared with the data from ATLAS [48], CMS [49], LHCb [50] and ALICE [15].

H	$\Upsilon(1S)$	$\Upsilon(2S)$	$\Upsilon(3S)$	$\chi_{b0}(1P)$	$\chi_{b1}(1P)$	$\chi_{b2}(1P)$	$\chi_{b0}(2P)$	$\chi_{b1}(2P)$	$\chi_{b2}(2P)$
$\mathcal{B}(H \to \mu^+\mu^-)(\%)$	2.48	1.93	2.18	$--$	$--$	$--$	$--$	$--$	$--$
$\mathcal{B}(H \to \Upsilon(1S))(\%)$	$--$	26.5	6.6	1.76	33.9	19.1	0.9	10.8	8.1
$\mathcal{B}(H \to \Upsilon(2S))(\%)$	$--$	$--$	10.6	$--$	$--$	$--$	4.6	19.9	10.6
M_H (GeV)	9.5	10.023	10.355	9.859	9.893	9.912	10.23	10.255	10.269

Table 7.2: Branching ratios and masses of bottomonia [43].

There are various feed-down contributions in Υ production and some of them are ignored in our calculations where the contribution are negligible. The feed-down contributions considered in the present calculations are: (i) for $\Upsilon(2S)$, feed-down contributions from $\Upsilon(3S)$ and $\chi_{bJ}(2P)$ are included; (ii) the feed-down contributions from $\Upsilon(2S)$, $\Upsilon(3S)$, $\chi_{bJ}(1P)$ and $\chi_{bJ}(2P)$ are included for $\Upsilon(1S)$. No feed-down contributions is included for $\Upsilon(3S)$. The branching ratios and masses of bottomonia [43] are summerized in Table 7.2.

The mass of the bottom quark is set to $m_b = M_H/2$ as an approximation, while M_H is the mass of the bottomonium H. The renormalization and factorization scales are defined by $\mu_{R,F} = \xi_{R,F}\mu_0$, where μ_0 is $\sqrt{p_T^2 + 4m_b^2}$. The LDMEs for CS and CO which we have used for our calculations are given in Table 7.3. The estimation of the uncertainty on the calculated values is similar to that of charmonium.

The results are shown in the Fig 7.7, Fig 7.8 and Fig 7.9 for $\Upsilon(1S)$, $\Upsilon(2S)$ and $\Upsilon(3S)$, respectively. These are in good agreement with the experimental results for $p_T > 5$ GeV.

	LDMEs	Numerical value	NRQCD scaling order
Colour-Singlet	$< \mathcal{O}(Q\bar{Q}(\ ^3S_1^{[1]}) \rightarrow \Upsilon(1S)) >$	10.9 GeV^3	$m_b^3 v_b^3$
	$< \mathcal{O}(Q\bar{Q}(\ ^3S_1^{[1]}) \rightarrow \Upsilon(2S)) >$	4.5 GeV^3	$m_b^3 v_b^3$
	$< \mathcal{O}(Q\bar{Q}(\ ^3S_1^{[1]}) \rightarrow \Upsilon(3S)) >$	4.3 GeV^3	$m_b^3 v_b^3$
	$< \mathcal{O}(Q\bar{Q}(\ ^3P_J^{[1]}) \rightarrow \chi_{bJ}(1P)) > /(2J+1)m_b^2$	0.100 GeV^3	$m_b^3 v_b^5$
	$< \mathcal{O}(Q\bar{Q}(\ ^3P_J^{[1]}) \rightarrow \chi_{bJ}(2P)) > /(2J+1)m_b^2$	0.036 GeV^3	$m_b^3 v_b^5$
Colour-Octet	$< \mathcal{O}(Q\bar{Q}(\ ^3S_1^{[8]}) \rightarrow \Upsilon(1S)) >$	- 0.0041 ± 0.0024 GeV^3	$m_b^3 v_b^7$
	$< \mathcal{O}(Q\bar{Q}(\ ^3S_1^{[8]}) \rightarrow \Upsilon(2S)) >$	0.0030 ± 0.0078 GeV^3	$m_b^3 v_b^7$
	$< \mathcal{O}(Q\bar{Q}(\ ^3S_1^{[8]}) \rightarrow \Upsilon(3S)) >$	0.0271 ± 0.0013 GeV^3	$m_b^3 v_b^7$
	$< \mathcal{O}(Q\bar{Q}(\ ^3S_1^{[8]}) \rightarrow \chi_{bJ}(1P)) > /(2J+1)m_b^2$	0.0127 ± 0.0016 GeV^3	$m_b^3 v_b^5$
	$< \mathcal{O}(Q\bar{Q}(\ ^3S_1^{[8]}) \rightarrow \chi_{bJ}(2P)) > /(2J+1)m_b^2$	0.0276 ± 0.0067 GeV^3	$m_b^3 v_b^5$
	$< \mathcal{O}(Q\bar{Q}(\ ^1S_0^{[8]}) \rightarrow \Upsilon(1S)) >$	0.1115 ± 0.0043 GeV^3	$m_b^3 v_b^7$
	$< \mathcal{O}(Q\bar{Q}(\ ^1S_0^{[8]}) \rightarrow \Upsilon(2S)) >$	0.0355 ± 0.0212 GeV^3	$m_b^3 v_b^7$
	$< \mathcal{O}(Q\bar{Q}(\ ^1S_0^{[8]}) \rightarrow \Upsilon(3S)) >$	- 0.0107 ± 0.0107 GeV^3	$m_b^3 v_b^7$
	$< \mathcal{O}(Q\bar{Q}(\ ^3P_0^{[8]}) \rightarrow \Upsilon(1S)) > /m_b^2$	- 0.0067 ± 0.0000 GeV^3	$m_b^3 v_b^7$
	$< \mathcal{O}(Q\bar{Q}(\ ^3P_0^{[8]}) \rightarrow \Upsilon(2S)) > /m_b^2$	- 0.0056 ± 0.0048 GeV^3	$m_b^3 v_b^7$
	$< \mathcal{O}(Q\bar{Q}(\ ^3P_0^{[8]}) \rightarrow \Upsilon(3S)) > /m_b^2$	0.0039 ± 0.0023 GeV^3	$m_b^3 v_b^7$

Table 7.3: The colour-singlet and colour-octet matrix elements with numerical values and NRQCD scaling order for bottomonia.

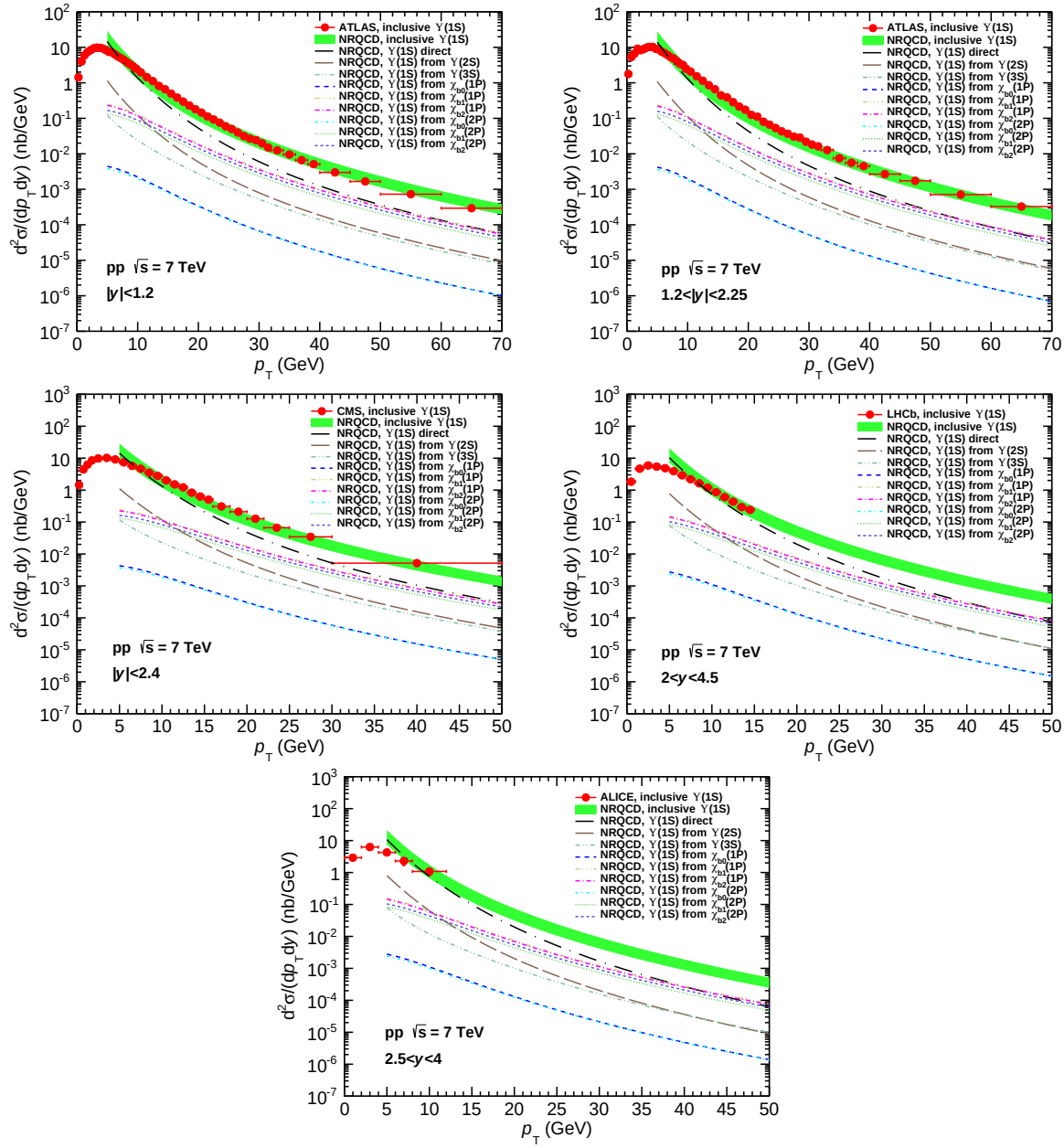

Figure 7.7: Differential production cross-section of $\Upsilon(1S)$ as a function of p_T compared with the measurements by ATLAS [48], CMS [49], LHCb [50] and ALICE [15] data.

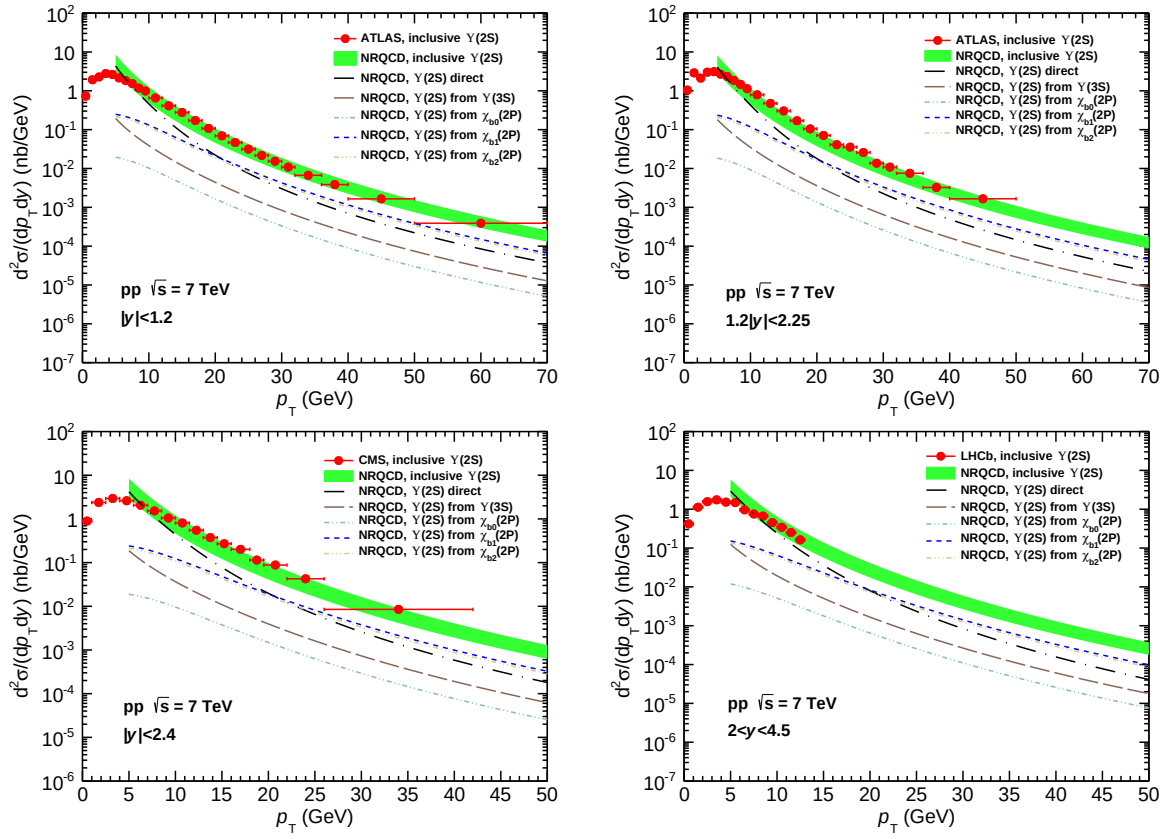

Figure 7.8: Differential production cross-section of $\Upsilon(2S)$ as a function of p_T compared with the measurements by ATLAS [48], CMS [49], LHCb [50].

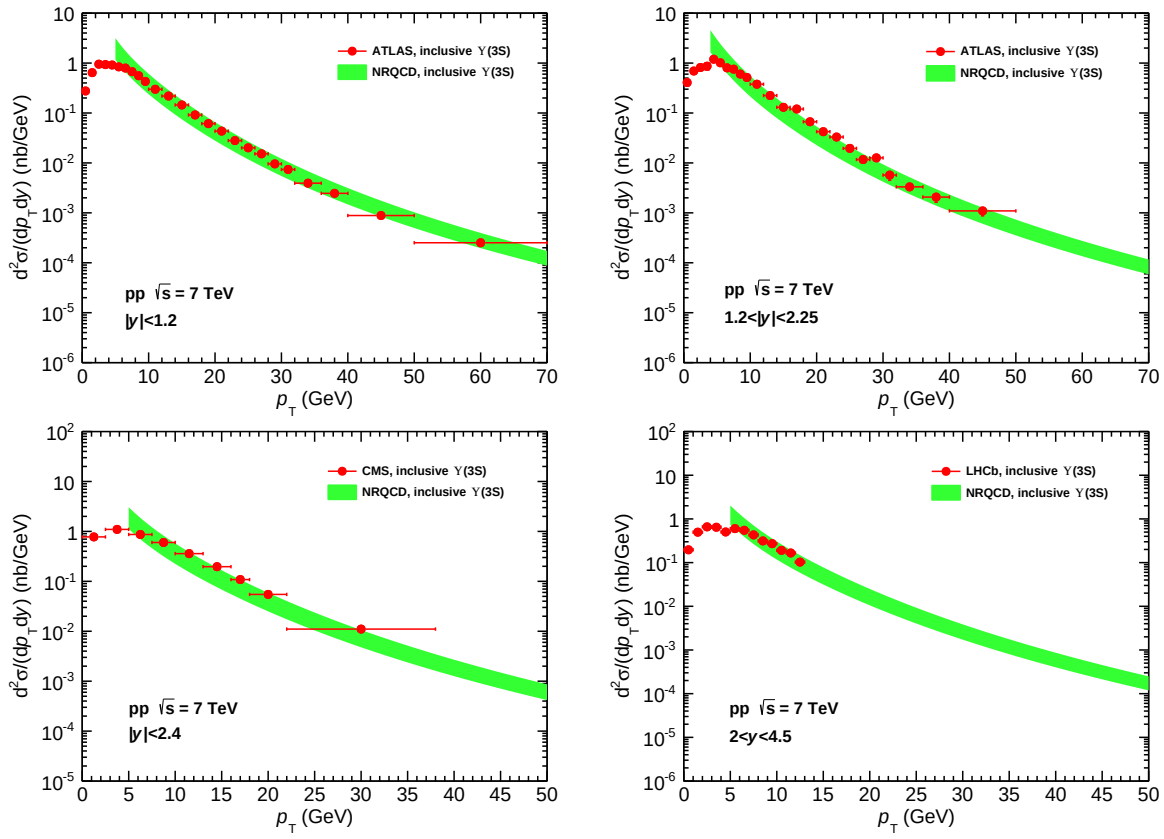

Figure 7.9: Differential production cross-section of $\Upsilon(3S)$ as a function of p_T compared with the measurements by ATLAS [48], CMS [49], LHCb [50].

7.5 Summary and outlook

In summary, the prompt and inclusive production cross-sections of J/ψ, $\psi(2S)$, $\Upsilon(1S)$, $\Upsilon(2S)$ and $\Upsilon(3S)$ at LHC energies have been calculated within the framework of LO NRQCD. These calculations include the contributions from direct production and from the decays of heavier charmonium and bottomoium states. The feed-down to J/ψ and $\psi(2S)$ from B meson decays has been implemented using the FONLL calculation. The comparisons with experimental data from LHC for different energies and rapidity intervals show that the LO NRQCD calculations give a good description of the production cross-sections of charmonium and bottomonium for $p_T > 3$ GeV and $p_T > 5$ GeV, respectively. The calculations for the production cross-sections of J/ψ and $\psi(2S)$ at $\sqrt{s} = 2.76$, 5.1 and 13 TeV have been carried out as well.

It may be noted that the fragmentation process contributes to the charmonium production at high p_T [30] and the inclusion of this process may further improve the calculations. It has been shown [46] that the production cross-sections in the low p_T interval ($p_T < 3$ GeV) can be described within the CGC+NRQCD formalism. In the future, we intend to adopt the CGC formalisms [46, 47] for quarkonium production in the low p_T region to cover the entire p_T range with the inclusion of all the feed-down contributions.

Bibliography

[1] Biswarup Paul, Mahatsab Mandal, Pradip Roy and Sukalyan Chattapadhyay, J. Phys. G: Nucl. Part. Phys. **42** 065101 (2015).

[2] C. Chao-Hsi, Nucl. Phys. B **172**, 425 (1980).

[3] G. A. Schuler, arXiv:hep-ph/9403387.

[4] F. Abe *et al.*, Phys. Rev. Lett. **69**, 3704 (1992).

[5] E. Braaten *et al.*, Phys. Rev. Lett. **71**, 1673 (1993).

[6] P. Artoisenet, J.P. Lansberg, and F. Maltoni, Phys. Lett. B **653**, 60 (2007).

[7] J. Campbell, F. Maltoni, and F. Tramontano, Phys. Rev. Lett. **98**, 252002 (2007).

[8] P. Artoisenet, J. Campbell, J. P. Lansberg, F. Maltoni, and F. Tramontano, Phys. Rev. Lett. **101**, 152001 (2008).

[9] N. Brambilla *et al.*, arXiv:hep-ph/0412158v2.

[10] H. Fritzsch, Phys. Lett. B **67**, 217 (1977).

[11] R. Aaij *et al.*, (LHCb Collaboration) Phys. Lett. B **718**, 431 (2012).

[12] S. Chatrchyan *et al.*, (CMS Collaboration), Eur. Phys. J. C **72**, 2251 (2012).

[13] R. Aaij *et al.*, (LHCb Collaboration) Phys. Lett. B **714**, 215 (2012).

[14] R. Aaij *et al.*, (LHCb Collaboration), JHEP **1310**, 115 (2013).

[15] B. Abelev *et al.*, (ALICE Collaboration) Eur. Phys. J. C **74**, 2974 (2014).

[16] G. T. Bodwin, E. Braaten, and G. P. Lepage, Phys. Rev. D **51**, 1125 (1995).

[17] R. Baier and R. Ruckl, Z. Phys. C **19**, 251 (1983).

[18] R. Gastmans, W. Troost and T. T. Wu, Nucl. Phys. B **291**, 731 (1987).

[19] B. Humpert, Phys. Lett. B **184**, 105 (1987).

[20] E. Braaten and S. Fleming, Phys. Rev. Lett **74**, 3327 (1995).

[21] P. L. Cho and A. K. Leibovich, Phys. Rev. D **53**, 6203 (1996).

[22] P. L. Cho and A. K. Leibovich, Phys. Rev. D **53**, 150 (1996).

[23] B. Gong and J. X. Wang, Phys. Rev. D **78**, 074011 (2008)

[24] B. Gong and J. X. Wang, Phys. Rev. Lett **100**, 232001 (2008).

[25] B. Gong, X. Q. Li and J. X. Wang, Phys. Lett. B **673**, 197 (2009).

[26] Y. Q. Ma, K. Wang and K. T. Chao, Phys. Rev. D **84**, 114001 (2011).

[27] Y. Q. Ma, K. Wang and K. T. Chao, Phys. Rev. Lett **106**, 042002 (2011).

[28] M. Butenschon and B. A. Kniehl, Phys. Rev. Lett **106**, 022003 (2011).

[29] B. Gong, L. P. Wan, J. X. Wang and H. F. Zhang, Phys. Rev. Lett **110**, 042002 (2013).

[30] G. T. Bodwin, H. S. Chung, U. R. Kim and J. Lee, Phys. Rev. Lett **113**, 022001 (2014).

[31] B. Abelev *et al.*, (ALICE Collaboration) Phys. Lett. B **718**, 295 (2012).

[32] B. Abelev *et al.*, (ALICE Collaboration) JHEP **11**, 065 (2012).

[33] G. Aad *et al.*, (ATLAS Collaboration) Nucl.Phys. B **850**, 387 (2011).

[34] S. Chatrchyan *et al.*, (CMS Collaboration) JHEP **02**, 011 (2012).

[35] R. Aaij *et al.*, (LHCb Collaboration) Eur. Phys. J. C **71**, 1645 (2011).

[36] R. Aaij *et al.*, (LHCb Collaboration) Eur. Phys. J. C **72**, 2100 (2012).

[37] R. Aaij *et al.*, (LHCb Collaboration) JHEP **02**, 041 (2013).

[38] M. Cacciari, M. Greco and P. Nason, JHEP **9805**, 007 (1998).

[39] M. Cacciari, S. Frixione and P. Nason, JHEP **0103**, 006 (2001).

[40] J. F. Owens Review of Modern Physics, Vol. **59**, 465 (1987).

[41] H. L. Lai. *et al.*, Phys. Rev. D **82**, 054021 (2010).

[42] Yu. L. Dokshitzer, G. Marchesini, B. R. Webber, Nucl. Phys. B **469**, 93 (1996).

[43] J. Beringer. *et al.* (Particle Data Group), Phys. Rev. D **86**, 010001 (2012) and 2013 partial update for the 2014 edition.

[44] R. Sharma and I. Vitev, Phys. Rev C **87**, 044905 (2013).

[45] M. Cacciari, private communication.

[46] Y. Q. Ma and R. Venugopalan, Phys. Rev. Lett **113**, 192301 (2014).

[47] Z. B. Kang, Y. Q. Ma and R. Venugopalan, JHEP **1401**, 056 (2014).

[48] G. Aad *et al.*, (ATLAS Collaboration) Phys. Rev. D **87**, 052004 (2013).

[49] S. Chatrchyan *et al.*, (CMS Collaboration) Phys. Lett. B **727**, 101 (2013).

[50] R. Aaij *et al.*, (LHCb Collaboration) Eur. Phys. J. C **72**, 2025 (2012).

Chapter 8

Summary and Outlook

This chapter Summerizes the results obtained in this thesis. The pp, p-Pb and Pb-Pb collisions data, collected by the ALICE Collaboration have been analyzed. The pp results were used to normalize the p-Pb and Pb-Pb results. The p-Pb and Pb-Pb data were analyzed to understand the cold and hot nuclear effects of the QCD matter on the J/ψ and ψ(2S) production, respectively. Theoretical calculations on cross-section using NRQCD framework in pp collisions provide an insight into the production mechanism of heavy-quark pair ($Q\bar{Q}$) production leading to the quarkonium formation.

8.1 J/ψ and ψ(2S) production in pp collisions

The inclusive production cross-section of J/ψ and ψ(2S) at forward rapidity ($2.5 < y < 4$) in pp collisions at a center of mass energy $\sqrt{s} = 7$ TeV as a function of the quarkonium transverse momentum and rapidity have been measured. For J/ψ, the measurements reported here represent an increase by a factor of about

80 in terms of luminosity with respect to the previously published ALICE results, whereas for the ψ(2S) state, this is the first ALICE measurements. The inclusive cross-sections, integrated over $p_{\rm T}$ and y are: $\sigma_{{\rm J}/\psi} = 6.69 \pm 0.04 \pm 0.63$ μb and $\sigma_{\psi(2{\rm S})} = 1.13 \pm 0.07 \pm 0.19$ μb, where the first uncertainty is statistical and the second is systematic (assuming no quarkonium polarization). Measuring both J/ψ and ψ(2S) cross-sections with the same apparatus and data set allows one to derive the fraction of inclusive J/ψ that come from ψ(2S) decay with reduced systematic uncertainties. It is: $f^{\psi(2{\rm S})} = 0.103 \pm 0.007 \pm 0.008$. Also, the inclusive ψ(2S) to J/ψ cross-section ratio provides the relative production of the two resonances as a function of $p_{\rm T}$ and y, integrated over $p_{\rm T}$ and y the value of this ratio is $\sigma_{\psi(2{\rm S})}/\sigma_{{\rm J}/\psi} = 0.170 \pm 0.011 \pm 0.013$.

These results are in good agreement with measurements from the LHCb experiment over similar $p_{\rm T}$ and y ranges. They are also in good agreement with NRQCD calculations for which the matrix elements have been fitted to data sets from Tevatron, RHIC and LHC, among others. In the CSM, both LO and NLO calculations underestimate the data at large $p_{\rm T}$ as was the case at lower energy. The addition of the leading-$p_{\rm T}$ NNLO contributions helps to reduce this disagreement at the price of larger theoretical uncertainties. LO calculations can reproduce qualitatively the data at low $p_{\rm T}$ and the rapidity dependence of the $p_{\rm T}$ integrated cross-sections.

8.2 ψ(2S) production in p-Pb collisions

The results on inclusive ψ(2S) production in proton-nucleus collisions at the LHC have presented. Measurements were performed with the ALICE Muon Spectrometer in the p-going ($2.03 < y_{\rm cms} < 3.53$) and Pb-going ($-4.46 < y_{\rm cms} < -2.96$) directions. The production cross sections, the double ratios with respect to the J/ψ in p-Pb and pp and the nuclear modification factors were estimated

integrated and also differentially in p_{T}. The results show that ψ(2S) is significantly more suppressed than J/ψ in both rapidity regions, and that no p_{T} dependence of this effect is found within uncertainties. This observation implies that initial state nuclear effects alone cannot account for the modification of the ψ(2S) yields. This is further confirmed by the poor agreement of the ψ(2S) R_{pPb} with models based on shadowing and/or energy loss. Final state effects, such as the pair break-up by interactions with cold nuclear matter, might in principle lead to the observed effect, but the extremely short crossing times for the $c\bar{c}$ pair, in particular at forward rapidity, make such an explanation unlikely. Consequently, other final state effects should be considered, including the interaction of the $c\bar{c}$ pair with the final state hadronic system created in the proton-nucleus collision. It may be interesting to explore whether the present results are indicative of an additional color suppression in case of proton-nucleus collisions at LHC energies.

8.3 Fractional double differential cross-section of J/ψ in pp and Pb-Pb collisions

In this thesis, the first study of the double differential cross-section of J/ψ has been presented using the Muon Spectrometer. The choice of a low p_{T}-bin ($0 < p_{\mathrm{T}} < 3$ GeV/c) was motivated by the fact that the recombination and the cold nuclear matter effects are mostly concentrated in the low p_{T} bin. Thus, it was decided to study the rapidity dependence of the production cross-section of J/ψ in the two p_{T} bins of $0 < p_{\mathrm{T}} < 3$ GeV/c and $p_{\mathrm{T}} > 3$ GeV/c. However these cross-sections were to be normalized with the pp data. In this thesis, the analysis of the 7 TeV pp data has been presented. Thus, we decided to use this data for the normalization of the 2.76 TeV Pb-Pb data. Since the center-of-mass energies were different, it was decided to

use the fractional differential cross-section (cross-section in a bin normalized by the total) as this quantity essentially depends on the shape of the rapidity distribution and it is expected that the shape of the $\mathrm{d}\sigma/\mathrm{d}y$ distribution does not change drastically between $\sqrt{s} = 2.76$ and 7 TeV. This assumption was tested with the published data and found to be correct.

It was found that there is a definitive excess of production of J/ψ in Pb-Pb compared to pp in the rapidity range of 2.5 to 2.75. This can be understood as the effect of recombination as it is expected that the number of charge centres increase towards the mid-rapidity. Thus, the probability of recombination also increases in the bins which are more central.

It is also interesting to note the observed distribution for high p_{T} bin is expected to be dominated by color suppression alone and devoid of recombination and CNM effects. A theoretical investigation in this direction may be carried out.

8.4 Quarkonium production cross-section calculation within the framework of NRQCD

The prompt and inclusive production cross-sections of J/ψ, $\psi(2S)$, $\Upsilon(1S)$, $\Upsilon(2S)$ and $\Upsilon(3S)$ in p-p collisions at LHC energies have been calculated within the framework of LO NRQCD. These calculations include the contributions from direct production and from the decays of heavier charmonium and bottomoium states. The feed-down to J/ψ and $\psi(2S)$ from B meson decays has been implemented using the FONLL calculation. The comparisons with experimental data from LHC for different energies and rapidity intervals show that the LO NRQCD calculations give a good description of the production cross-sections of charmonium and bottomonium for

$p_T > 3$ GeV and $p_T > 5$ GeV, respectively. The calculations for the production cross-sections of J/ψ and $\psi(2S)$ at $\sqrt{s} = 2.76$, 5.1 and 13 TeV have been carried out as well.

It may be noted that the fragmentation process contributes to the charmonium production at high p_T [1] and the inclusion of this process may further improve the calculations. It has been shown in [2] that the production cross-sections in the low p_T interval can be described within the CGC+NRQCD formalism. In future, we intend to adopt the CGC formalisms [2, 3] for quarkonium production in the low p_T region to cover the entire p_T range with the inclusion of all the feed-down contributions.

8.5 Outlook

The study of ψ(2S)/J/ψ ratio in pp collisions at $\sqrt{s} = 13$ TeV and 14 TeV will be interesting in order to extend the results obtained in Run 1 to higher energies. It is to be noted that color evaporation model (CEM) calculation predicts a flat distribution [4] for this ratio as a function of $\sqrt{s}$. Thus, this experimental investigation over a wide center-of-mass energy range will be an interesting check and any deviation might be an indication of multiparton interactions (MPI).

The ψ(2S) suppression in Pb-Pb collisions at extreme forward rapidities has been estimated in Run 1 [5], however the result is statistically limited. The ALICE result seems to follow a different trend as compared to the CMS result [6], although a direct comparison can not be done since two experiments have different kinematic ranges. Therefore, an analysis based on a high statistics data sample should be crucial to shed some light on the ψ(2S) behaviour. The projected integrated luminosity of 1 nb^{-1} at $\sqrt{s_{\rm NN}} = 5.1$ TeV and 5.5 TeV will be sufficient to carry out this experimental

investigation. In order to have a more precise understanding of the suppression and the feed-down from the excited charmonium states, we need the direct measurement of suppression of the excited states. In addition, finer centrality, rapidity and p_{T} binning with smaller uncertainties will also be possible, which in turn will further constrain the theoretical models. With the newly approved Muon Forward Tracker (MFT), one may also expect improvement of mass resolution due to precise vertex determination.

It may be noted that the nuclear modification factor in p-Pb collisions has been measured at $\sqrt{s_{\mathrm{NN}}} = 5.02$ TeV and upcoming Pb-Pb collisions will be at $\sqrt{s_{\mathrm{NN}}} =$ 5.1 TeV and 5.5 TeV, the center-of-mass energies of the two systems are almost the same, so the ratio of nuclear modification factor in p-Pb and Pb-Pb will be very interesting to shed some light on the different kind of mechanisms involved and it will be worthwhile to compare the observed nuclear modification factor and their ratio as a function of centrality, p_{T} and y with the predictions from the color suppression model.

The $\psi(2\mathrm{S})/\mathrm{J}/\psi$ ratio is predicted to be very sensitive to the QGP temperature and the double ratio $([\sigma_{\psi(2\mathrm{S})}/\sigma_{\mathrm{J}/\psi}]_{\mathrm{PbPb}}/[\sigma_{\psi(2\mathrm{S})}/\sigma_{\mathrm{J}/\psi}]_{\mathrm{pp}})$ is a useful quantity to compare directly the relative suppression of the two states. So, the measurement of the $\psi(2\mathrm{S})/\mathrm{J}/\psi$ ratio and the double ratio as a function of the collision centrality, transverse momentum and rapidity will be interesting.

The temperature produced in the Pb-Pb collisions at ALICE is ~ 500 MeV. This is quite high compared to the critical temperature ($\mathrm{T_c}$), which is ~ 170 MeV. The dissociation temperatures of $\psi(2\mathrm{S})$, J/ψ, $\Upsilon(3\mathrm{S})$, $\Upsilon(2\mathrm{S})$ and $\Upsilon(1\mathrm{S})$ are $\sim 1.2\ T_{\mathrm{c}}$, 1.6 T_{c}, 1.2 T_{c}, 1.6 T_{c} and 4 T_{c} respectively. So, it is expected that at LHC energies $\psi(2\mathrm{S})$, J/ψ, $\Upsilon(3\mathrm{S})$ and $\Upsilon(2\mathrm{S})$ production is suppressed except for the $\Upsilon(1\mathrm{S})$. However, as it is seen from the Pb–Pb data, the inclusive suppression of J/ψ is less than that of

the Υ(1S). This can be explained by considering the regeneration process, which is higher for the J/ψ due to high abundance of the $c\bar{c}$ pairs compared to $b\bar{b}$. However, it may be interesting to measure the ratio of $R_{\rm AA}$ of ψ(2S) and Υ(3S) as a function of centrality, since both their dissociation temperatures are similar. If their ratio is close to unity, it would imply that ψ(2S) production in Pb–Pb collisions does not have sizable contribution from recombination.

The future upgrades of ALICE during 2018 − 19, will improve the data quality substantially and the increased luminosity will ensure much higher statistics. Thus, in future the physics reach of ALICE will increase further.

The present thesis work is an indicator of a challenging future for probing the matter produced in ultra-relativistic heavy-ion collisions using heavy quark resonances.

Bibliography

[1] G. T. Bodwin, H. S. Chung, U. R. Kim and J. Lee, Phys. Rev. Lett **113**, 022001 (2014).

[2] Y. Q. Ma and R. Venugopalan, Phys. Rev. Lett **113**, 192301 (2014).

[3] Z. B. Kang, Y. Q. Ma and R. Venugopalan, JHEP **1401**, 056 (2014).

[4] A. Adare *et al.*, (PHENIX Collaboration) Phys. Rev. **D83**, 092004 (2012).

[5] R. Arnaldi *et al.* (ALICE Collaboration), arXiv:1211.2578, QM2012 proceedings.

[6] S. Chatrchyan *et al.* (CMS Collaboration), Phys. Rev. Lett **113**, 262301 (2014).

Appendix A

Effect of Front Absorber on Mass resolution

A.1 Motivation

To explore the effect of the front absorber on the mass resolution of Υ using the ALICE simulation framework, AliRoot. In its present form, the complete ALICE geometry along with different services, have been included in AliRoot.

A.2 Mass spectrum and p_{T} distribution of the dimuon decaying from J/ψ and Υ

The entire performance of ALICE can be studied through AliRoot framework. However in this study, only the J/ψ and Υ signal events decaying in dimuon channel have been studied (see also [3]), where all the features of the muon spectrometer have

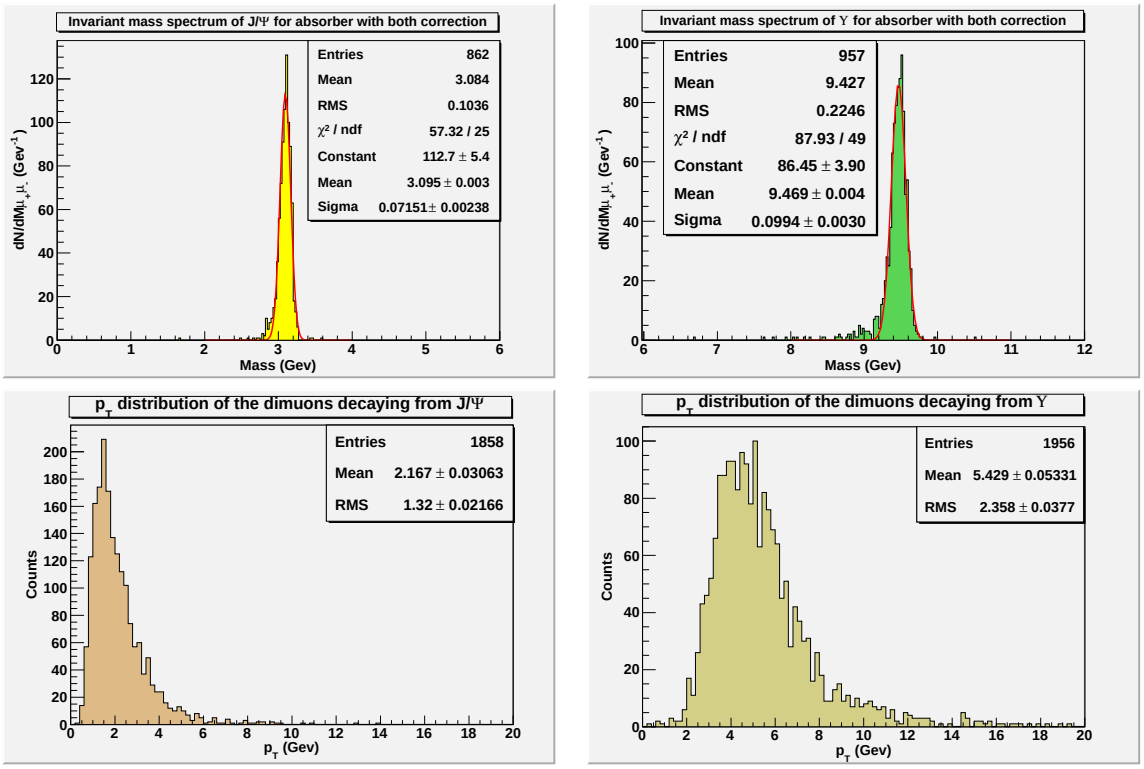

Figure A.1: The signal events for the muon spectrometer is (a) J/ψ (top-left) and (b) Υ (top-right),(c) p_{T} distribution of the dimuon, decaying from J/ψ (bottom-left) (d) p_{T} distribution of the dimuon, decaying from Υ (bottom-right) when all processes and corrections are applied.

been included. The probability of quarkonium decay to dimuon is very low ($\sim$5%) so the forced decay option of Pythia has been used. One can see from Fig. A.1(a) and A.1(b) that the mass resolution of J/ψ is $\sim$71 MeV but that of the Υ is $\sim$99 MeV. Here, the main assumption is that the Muon Tracking Stations are perfectly aligned and the front end electronics have a fixed gain with no distribution. The mass resolution of J/ψ is better than that of Υ. This can be understand from the fact that Muon spectrometer has low resolution for muons at high p_{T} and it can be seen from Fig. A.1(c) and A.1(d) that the p_{T} distribution of the dimuons decaying from J/ψ have lower p_{T} range than that of the dimuons decaying from Υ.

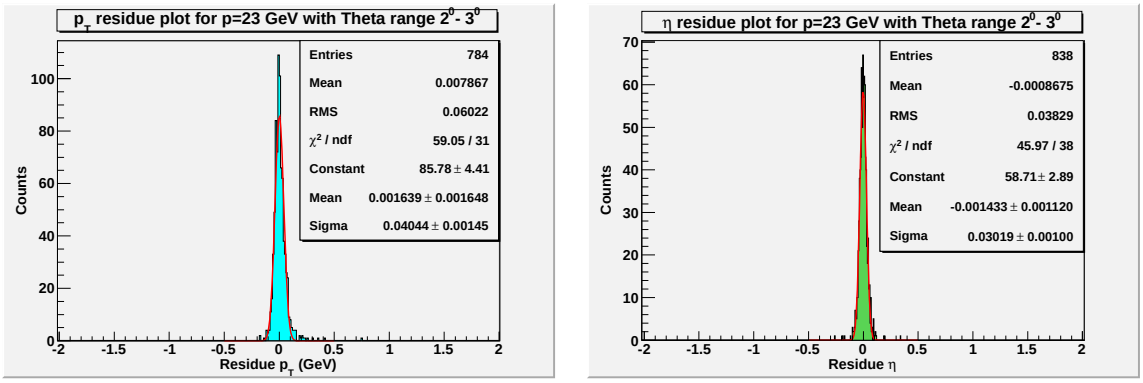

Figure A.2: (a) p_{T} residue plot at theta range $2^{\circ} - 3^{\circ}$ (left), (b) η residue plot at theta range $2^{\circ} - 3^{\circ}$ (right).

A.3 p_{T} and η resolution of Muon Spectrometer

It is to be noted that the invariant mass resolution depends on the p_{T} and η resolution alone. Therefore, the p_{T} and η resolutions have been calculated. To calculate the p_{T} and η resolution of the muon spectrometer, a single muon beam from the ALICE interaction point have been used. First, the emission angle have been fixed to a certain range ($2^{\circ} - 3^{\circ}$) and then by using a fixed value of p for the single muons, 10 simulations for each value of p_{T} (mean) from 1 GeV/c to 10 GeV/c have been performed. From these simulated files, the kinematic p_{T} (generated p_{T} at the event generator) and the recostructed p_{T} (p_{T} after passing through absorber and applying all processes and corrections) for each event have been calculated. From these two p_{T} values for each event, the p_{T} difference or p_{T} residue plot have been calculated. Each difference plot has been fitted with a gaussian distribution and the σ (width) of this disrtibution is a measure of the resolution. This process is shown in Fig. A.2(a) and A.2(b) for p_{T} and η, respectively. Plotting these widths along Y-axis and p_{T} (mean) along X-axis, the p_{T} resolution curve has been obtained. Similarly, from kinematic η and reconstructed η, the η resolution curve has been obtained. p_{T} and η resolution curves are shown in Fig. A.3(a) and A.3(b).

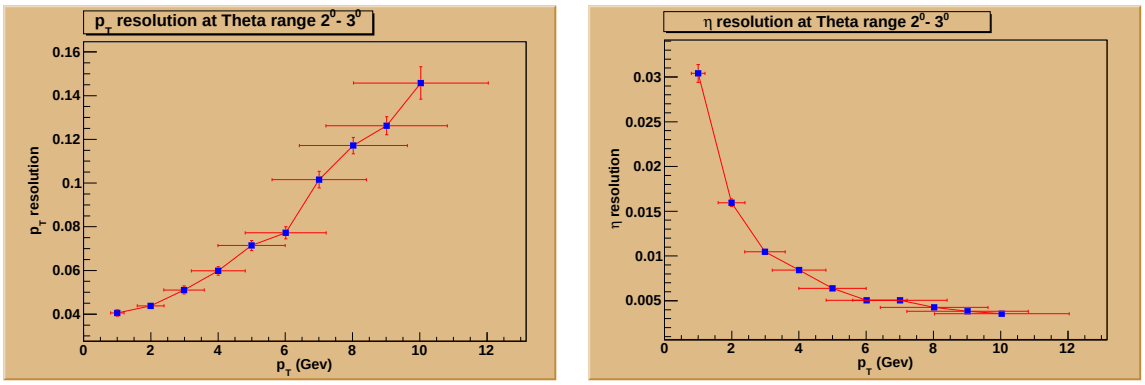

Figure A.3: (a) p_{T} resolution at emission angle range $2^{\circ} - 3^{\circ}$ (left), (b) η resolution at emission angle range $2^{\circ} - 3^{\circ}$ (right).

From Fig. A.3, one see that, the Muon spectrometer has better p_{T} resolution at low p_{T} range and as p_{T} increases the resolution worsens. This is due to the finite magnetic field of the bending magnet (3 Tm). The higher p_{T} tracks have less curvatures which lead to the detoriation of p_{T} resolution. However, the situation is reverse in case of η resolution, as one can see, the spectrometer has better η resolution at higher p_{T} and worse at low p_{T} range. This is the direct consequence for having the large forward absorber for ALICE Muon spectrometer. In order to investigate this issue the front absorber of the muon spectrometer has been studied in detail in the following section.

A.4 Can Υ mass resolution be better ?

The Front Absorber (FA) of the Muon Arm consists of a central cone within the acceptance of the spectrometer (2° to 9°), an outer shield to protect the central detectors of ALICE (otherwise the back scattering from the absorber may create undesirable backgrounds to the other detectors inside the L3 magnet) and an inner shield below 2° to absorb particles emanating from the beam-pipe. The front absorber reduces the forward flux of the charged particles by at least two orders of magnitude

and it has an additional responsibility to decrease the decay muon background, by limiting the free path of primary muonic decay of π's and K's toward the Muon Spectrometer. The low-Z materials are used for the front part and high-Z materials are placed in the rear part of the absorber. The length of the absorber is 10 $\lambda_{\rm int}$.

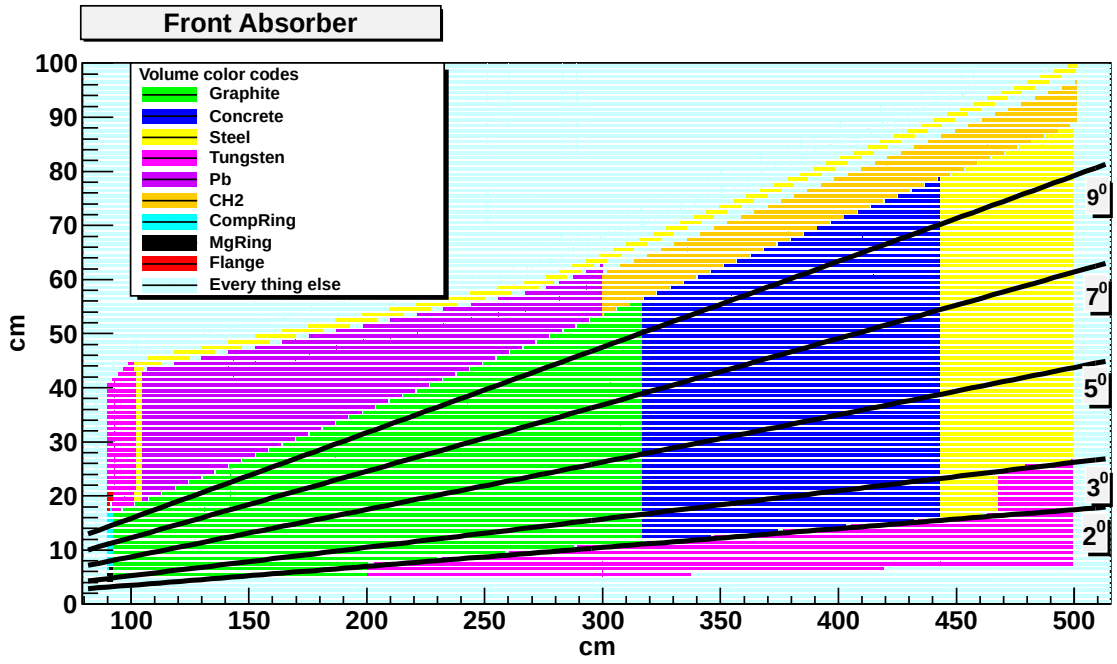

Figure A.4: A cross-sectional view of front absorber in y-z plane.

The material compositions and the placement of different materials of the front absorber was studied in detail. The present geometry of the absorber is shown in Fig. A.4. Here, the geometry package of ROOT have been used. A navigation pointer is propagated through the absorber from front part to rear region of the absorber in small steps. It keeps on recording the type of material in two dimensional histograms. Finally the two dimensional histograms are plotted on canvas, which produces the cross-sectional view of the upper half of y-z plane of the absorber as shown in Fig. A.4.

The muons interact electromagnetically with the absorber material and therefore, their energy loss is less. However, they will have a finite energy loss and staggering in the absorber in addition to the multiple coulomb scattering. Thus, these

effects have to be accounted properly in order to achieve a good mass resolution.

Energy loss

The energy loss is primarily [1] the ionization energy loss and radiative energy loss (direct e^+e^- pair production, Bremsstrahlung etc.). The radiative energy loss processes become more important than ionisation at sufficiently high energies. But at 100 GeV, which is the typical energy for muons from Upsilon decays the contribution from radiative processes is negligibe. Thus main contribution to the total energy loss is ionisation energy loss, which is calculated by Bethe-Bloch formula.

$$-\frac{dE}{dx} = \kappa z^2 \frac{Z}{A}\frac{1}{\beta^2}[ln\frac{2\gamma^2\beta^2 m_e c^2}{I} - \beta^2] \tag{A.1}$$

with,

$$\kappa = 4\pi N {r_e}^2 m_e c^2 \tag{A.2}$$

where N is the Avogadro number, z is the charge of the external particle in the absorber, r_e is the classical electron radius, m_e is the electron mass, Z is the atomic number of the absorber material, A is the atomic mass of the absorber material, I is the mean excitation energy of the material, and β and γ are the conventional relativistic parameters.

Multiple Coulomb scattering

Multiple Coulomb scattering is the scattering of the particles inside the Front Absorber. It is measured in terms of the angle (θ) between the track and the beam axis. However, if the invariant mass is calculated by assuming this scattering angle then the mass resolution gets worse. Therefore, a correction in the angular

measurement ($\Delta\theta^2{}_B$) is performed following the Branson correction.

$$\Delta\theta^2{}_B = \alpha^2(F_0 - \frac{F_1^2}{F_2}) \tag{A.3}$$

Where the quantities F_0, F_1 and F_2 are the 0^{th}, 1^{st} and 2^{nd} moment of z, respectively, calculated with the inverse radiation-length $X_0(z)$ distribution.

$$F_0 = \int_0^L \frac{dz}{X_0(z)} \tag{A.4}$$

$$F_1 = \int_0^L z\frac{dz}{X_0(z)} \tag{A.5}$$

$$F_2 = \int_0^L z^2\frac{dz}{X_0(z)} \tag{A.6}$$

and $\alpha(= 0.0136/p$, with p in Gev/c) is inversely proportional to the total momentum.

If the absorber is removed in simulation, we would observe the ideal mass resolution which is shown in Fig. A.5(a) where the position resolution is 55 MeV for Υ. The finite width is due to the finite position resolution of the tracking chambers and the magnetic field. On the other hand when absorber is present and no corrections are applied, the mass resolution has a width 280 MeV and the peak is shifted to 8.96 GeV instead of 9.4 GeV [Fig. A.5(b)] due to the energy loss and multiple coulomb scattering.

The effects of energy loss and multiple coulomb scattering processes described above which the muons experience in the Front absorber (see also Appendix C of [1]) have in the following way:

a) In the configuration file, all processes were switched off except multiple

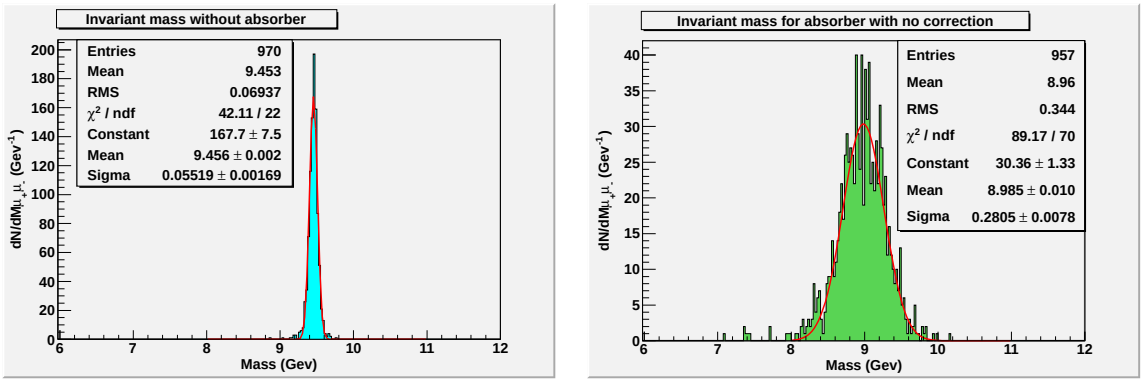

Figure A.5: Mass spectrum of Υ (a) without the absorber and all processes and corrections on (b) with absorber and all processes on but no correction.

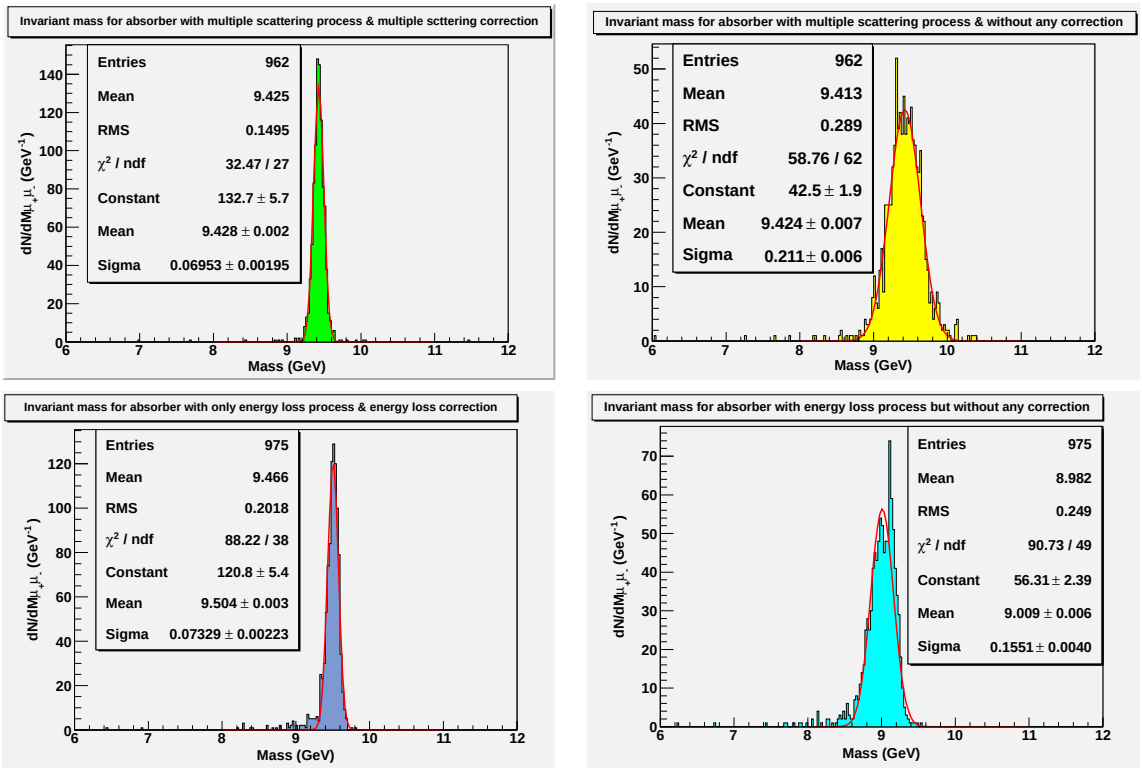

Figure A.6: Mass spectrum of Υ when (a) Multiple scattering process and multiple scattering correction are applied (top-left), (b) Multiple scattering is process applied but no corrections are applied(top-right),(c) Energy loss process and energy loss correction are applied (bottom-left) (d) Energy loss process is applied but no correction are applied (bottom-right).

scattering process and only multiple scattering correction is on, one can see from Fig. A.6(a), mass spectrum has width ∼69 MeV and peak at 9.4 GeV.

b) In the configuration file, when only multiple scattering process is on and no correction is applied, one can see from Fig. A.6(b), mass spectrum has width ∼211 MeV and peak is still at 9.4 GeV.

c) When only energy loss process is on and only energy loss correction is on, one can see from Fig. A.6(c), mass spectrum has width ∼73 MeV and peak at 9.4 GeV.

d) When only energy loss process is on and no correction is applied, one can see from Fig. A.6(d), mass spectrum has width ∼155 MeV and peak is shifted to 9.0 GeV instead of 9.4 GeV.

Thus, from above discussion, one see that multiple scattering correction has greater effect than energy loss correction in improving mass spectrum resolution.

A.5 Further studies

It is to be noted that there are more high-Z materials in the theta range $2^\circ - 3^\circ$ than $3^\circ - 9^\circ$ (Fig. A.4). So to find the dependence of resolution on the emission angle of absorber, the acceptance angle have been divided into several angle ranges ($2^\circ - 3^\circ$, $3^\circ - 5^\circ$, $5^\circ - 7^\circ$, $7^\circ - 9^\circ$) and the p_{T} and η residue plots have been plotted as shown in Fig. A.7. The value of p is chosen such that p_{T} range remains in p_{T} range of the dimuons decaying from Υ decay which is typically ∼4 GeV to 6 GeV. One can see from Fig. A.7, that the resolution is better in higher angle ranges.

In Fig. A.8, the p_{T} and η resolution curves for two theta ranges using the same method as described above have been shown. From the figures, one can see that p_{T} resolution is better at higher angle ($3^\circ - 4^\circ$) than that at lower angle ($2^\circ - 3^\circ$) and as

p_{T} increases the resolution worsen in both cases but resolution is still better at higher angle. In case of η resolution, it is evident that the correction for multiple scattering works much better and the η resolution at lower and higher angles are comparable.

The effect of emission angle on the mass resolution of Υ have been shown in Fig. A.9.

One can see that, the mass resolution is better at higher angle. The width of mass spectrum at theta range $2^{\circ} - 3^{\circ}$ is $\sim$111 MeV whereas that at range $3^{\circ} - 5^{\circ}$ is $\sim$94 MeV. This detoriation can surely be attributed to the detoriation of p_{T} resolution at low angles.

In summary, it has been observed that the resolution is about 20% worse at the low angle $(2^{\circ} - 3^{\circ})$ which can be largely attributed to the worsening of p_{T} resolution. This indicates that further improvement of the estimation of energy loss effects in the Front absorber may be achieved. This would involve detail GEANT based simulation studies.

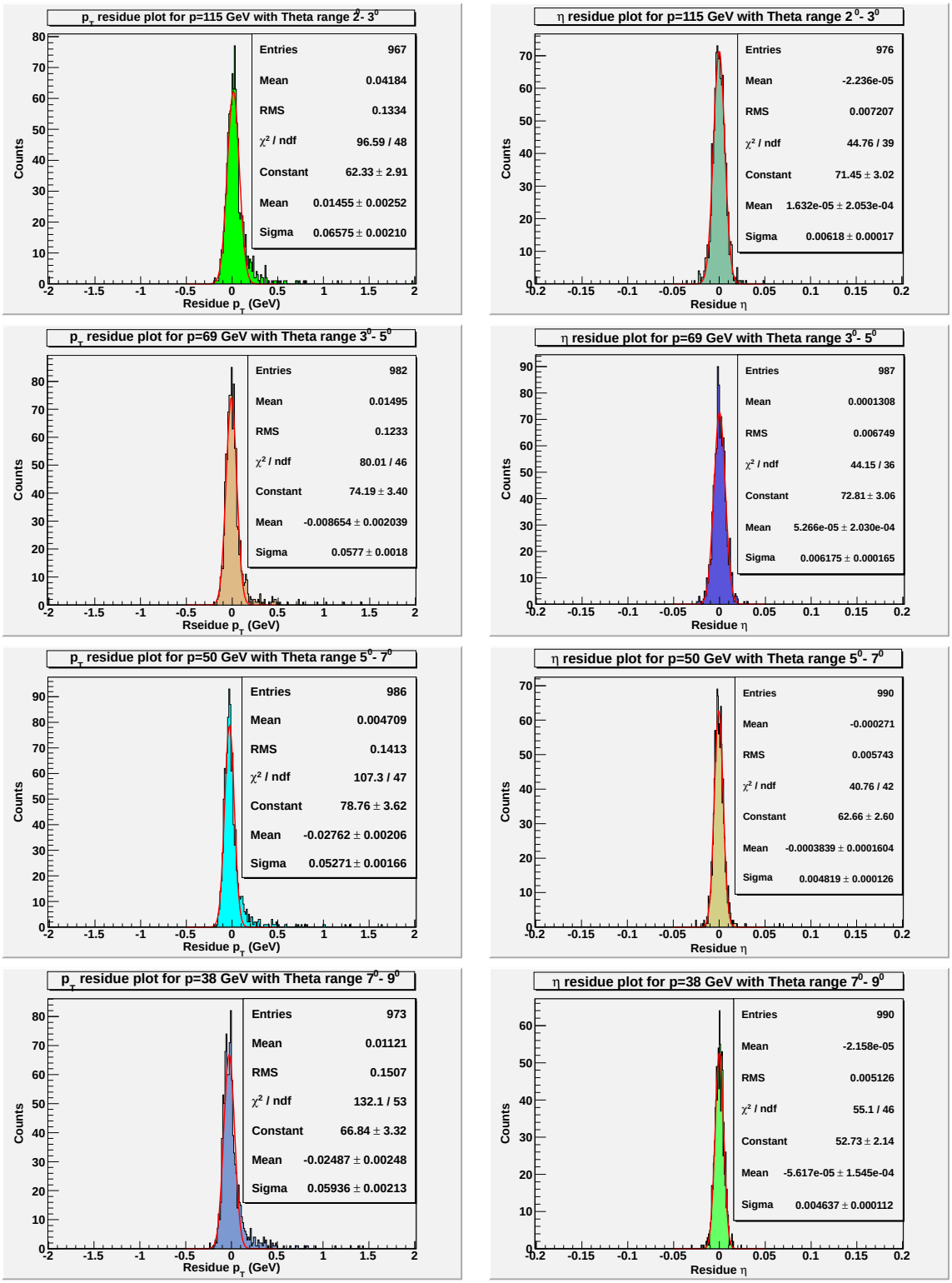

Figure A.7: p_{T} and η difference plots at different angle range keeping p_{T} in the Υ p_{T} range.

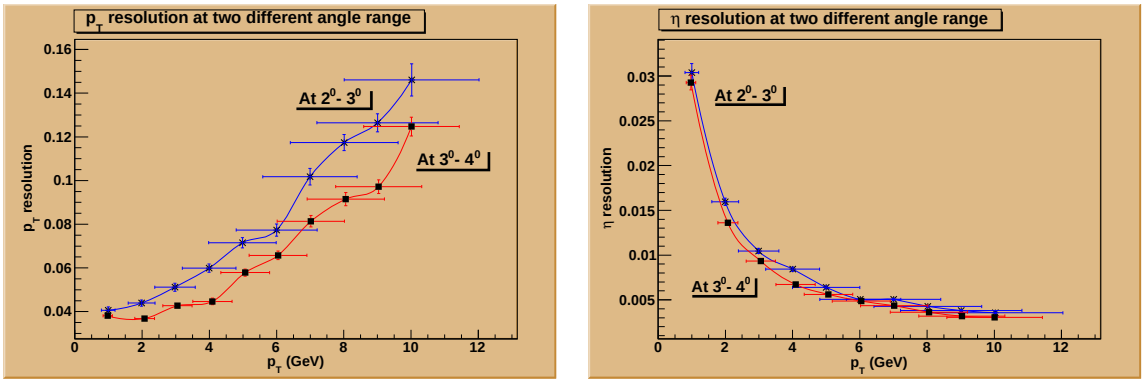

Figure A.8: (a) p_{T} resolution at two theta range $2^{\circ} - 3^{\circ}$ and $3^{\circ} - 4^{\circ}$, (b) η resolution at two theta range $2^{\circ} - 3^{\circ}$ and $3^{\circ} - 4^{\circ}$.

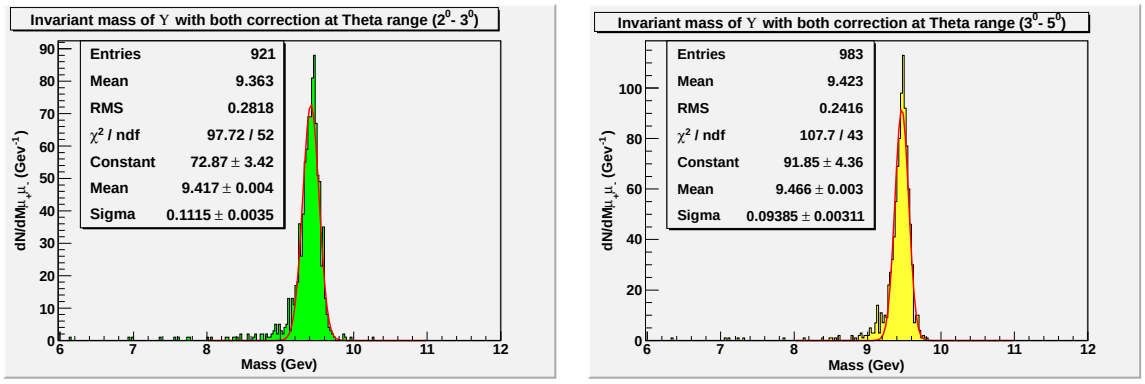

Figure A.9: Mass spectrum of Υ (a) at emission angle $2^{\circ} - 3^{\circ}$ (b) at emission angle $3^{\circ} - 5^{\circ}$.

Bibliography

[1] Ph.D. thesis, Indranil Das.

[2] "Introduction to High-Energy Heavy-Ion Collisions", Cheuk-Yin Wong.

[3] Homepage of Andreas Morsch

Appendix B

Fitting functions

B.1 Crystal Ball function

The Crystal Ball (CB) function is defined by the equation B.1. It consists of a Gaussian core portion and a power-law tail at low mass defined by the parameters α and n. The power-law part reproduces non Gaussian fluctuations due to energy loss processes.

$$f(x;\mu,\sigma,\alpha,n) = N.\begin{cases} e^{-\frac{(x-\mu)^2}{2\sigma^2}} & \text{for } \frac{x-\mu}{\sigma} > -\alpha \\ A.(B-\frac{x-\mu}{\sigma})^{-n} & \text{for } \frac{x-\mu}{\sigma} \leq -\alpha \end{cases} \tag{B.1}$$

$$A = \left(\frac{n}{|\alpha|}\right)^n .e^{-\frac{|\alpha|^2}{2}}$$

$$B = \frac{n}{|\alpha|} - |\alpha|$$

B.2 Extended Crystal Ball function or Double Crystal Ball function

The Extended Crystal Ball function (CB2) derives from the Crystal Ball function (CB). While the CB has only one power-law tail for low invariant masses, the CB2 has two power-law tails (one for higher masses, the other for lower ones). So it's a Gaussian core convoluted with two power-law tails. The CB2 is defined by the following equation:

$$f(x;\mu,\sigma,\alpha,n,\alpha',n') = N.\begin{cases} e^{-\frac{(x-\mu)^2}{2\sigma^2}} & \text{for } \alpha' > \frac{x-\mu}{\sigma} > -\alpha \\ A.(B - \frac{x-\mu}{\sigma})^{-n} & \text{for } \frac{x-\mu}{\sigma} \leq -\alpha \\ C.(D + \frac{x-\mu}{\sigma})^{-n'} & \text{for } \frac{x-\mu}{\sigma} \geq \alpha' \end{cases} \tag{B.2}$$

$$A = \left(\frac{n}{|\alpha|}\right)^n .e^{-\frac{|\alpha|^2}{2}}$$

$$B = \frac{n}{|\alpha|} - |\alpha|$$

$$C = \left(\frac{n'}{|\alpha'|}\right)^{n'} .e^{-\frac{|\alpha'|^2}{2}}$$

$$B = \frac{n'}{|\alpha'|} - |\alpha'|$$

B.3 NA60 function

This is a function adopted for charmonia in NA50 and NA60 experiments. It is basically a gaussian shape with variable sigma:

$$\sigma = \begin{cases} p_2 & \text{for } p_9 M_0 < M < p_{10} M_0 \\ p_2(1 + [p_3(p_9 M_0 - M)]^{[p_4 - p_5\sqrt{(p_9 M_0 - M)}]}) & \text{for } M < p_9 M_0 \\ p_2(1 + [p_6(M - p_{10} M_0)]^{[p_7 - p_8\sqrt{(M - p_{10} M_0)}]}) & \text{for } M > p_{10} M_0 \end{cases} \quad \text{(B.3)}$$

$$f(M) = N.e^{-\frac{(M-M_0)^2}{2\sigma^2}} \quad \text{(B.4)}$$

Right and left asymmetric tails are allowed. The function has 11 parameters. NA60 function better describes both right and left sides of the MC spectrum.

B.4 Variable Width Gaussian

For the background description a Gaussian with a width (σ) which varies as a function of the mass values has been adopted.

$$\sigma = \beta + \gamma \times ((x - \alpha)/\alpha) \quad \text{(B.5)}$$

$$f(x) = N.e^{-\frac{(x-\alpha)^2}{2\sigma^2}} \tag{B.6}$$

B.5 Exponential times 4th order ploynomial function

It is a function obtained by multiplying the exponential function and 4th order polynomial function.

$$f(x) = N.e^{\frac{x}{\alpha}} \times (a_0 + a_1 x + a_2 x^2 + a_3 x^3 + a_4 x^4) \tag{B.7}$$